Abstract of "Dynamic Shearing Resistance of HTPB, Sucrose and their Polymer-Bonded Energetic Simulant" by Pinkesh Malhotra, Ph.D., Brown University, February 2021.

Pressure-shear plate impact (PSPI) experiments have been performed on a polymer-bonded energetic material simulant and its constituents – a simulant crystal sucrose and an elastomeric binder HTPB. Dynamic response of each of the constituents is first investigated under a range of normal stresses (3-10 GPa) and high shear strain-rates ($10^5 - 10^6\ s^{-1}$). Shear strength of HTPB shows a highly pressure-dependent behavior, with the strength increasing from 120 MPa to 470 MPa as the normal stress increases nominally from 3 GPa to 9 GPa. Peak shear strength of sucrose, on the other hand, shows a relatively weak dependence on normal stress, with its shear strength increasing merely from an average value of 410 MPa to 465 MPa as the normal stress increases from 2.9 GPa to 9.5 GPa. Sucrose also exhibits pronounced strain softening under shear after reaching a peak value. A quasi-linear viscoelastic model with a pressure-dependent instantaneous elastic response is used to model HTPB. A thermodynamic framework is presented for constitutive modeling of sucrose. A finite deformation thermo-mechanical model, incorporating a complete Mie-Gruneisen equation of state, is used to model sucrose. Simulations show that the dramatic drop in shear strength of sucrose is a result of localized deformation in the form of adiabatic shear bands. PSPI experiments on the sucrose/HTPB composite show that the peak dynamic shearing resistance of the composite increases from 176 MPa to 453 MPa as the normal stress increases nominally from 3 GPa to 9.75 GPa. The shearing resistance builds up to a peak value before decreasing to a smaller non-zero value. Such a drop could be due to multiple factors like fracture of sucrose and/or HTPB,

delamination of HTPB from sucrose crystals, adiabatic shear band localization in the HTPB binder or sucrose crystals and friction between fractured surfaces.

Once a strong foundation for material response of constituents of a polymer-bonded simulant is laid, in-situ quantitative experimental investigation of deformation fields and mechanisms of hot-spot formation is desired. A high-speed microscopic imaging system, with a temporal resolution of 250 ns and a sub-micron spatial resolution has been built in pursuit of this goal.

Dynamic Shearing Resistance of HTPB, Sucrose and their Polymer-Bonded Energetic Simulant

by
Pinkesh Malhotra,
B.Tech, M.Tech, Indian Institute of Technology, Bombay, 2014
Sc.M., Brown University, 2016

Submitted in partial fulfillment of the requirements
for the Degree of Doctor of Philosophy in
Solid Mechanics at Brown University

Providence, Rhode Island
February 2021

This dissertation by Pinkesh Malhotra is accepted in its present form by
the School of Engineering as satisfying the dissertation requirement
for the degree of Doctor of Philosophy.

Date_____ _____
Pradeep R. Guduru, Ph.D. Advisor

Date_____ _____
Rodney J. Clifton, Ph.D. Advisor

Recommended to the Graduate Council

Date_____ _____
David L. Henann, Reader

Date_____ _____
Eric Chason, Reader

Approved by the Graduate Council

Date_____ _____
Andrew G. Campbell, Ph.D.
Dean of the Graduate School

Curriculum Vitae

Pinkesh Malhotra received a Dual Degree (Bachelors and Masters) in Mechanical Engineering from Indian Institute of Technology, Bombay in 2014. He joined Brown in 2014 and received a transitional Master of Science degree in Solid Mechanics in 2016.

Forthcoming Publications

1. Tong Jiao, Pinkesh Malhotra and Rodney Clifton. "IR temperature measurement in pressure-shear plate impact experiments". In: *AIP Conference Proceedings* (Vol. 1979, No. 1, p.160012), 2018.
2. Tong Jiao, Pinkesh Malhotra and Rodney Clifton. "Emissivity change in pressure-shear plate impact experiment". Accepted. In: *AIP Conference Proceedings* 2020.
3. Pinkesh Malhotra and Pradeep R. Guduru. "A Technique for High-Speed Microscopic Imaging of Dynamic Failure Events". Submitted to: *Experimental Mechanics*, 2019.
4. Pinkesh Malhotra, Tong Jiao, Rodney Clifton, Pradeep R. Guduru and David L. Henann. "Dynamic Shearing Resistance of Sucrose and HTPB: Experiments and Modeling". In preparation.
5. Pinkesh Malhotra, Tong Jiao, Rodney Clifton, Pradeep R. Guduru and David L. Henann. "Dynamic Shearing Behavior of a Polymer-Bonded Sugar: Experiments and Modeling". In preparation.

Conference Presentations

1. "High-Speed Microscopic Imaging of Dynamic Failure Events." *56th Annual Technical Meeting of the Society of Engineering Science,* Washington University, St. Louis, MO, USA (Oct. 2019)
2. "High-Speed Microscopic Imaging of Dynamic Failure Events." *New. Mech*, University of Massachusetts Amherst, Amherst, MA, USA (Oct. 2019)
3. "High-Speed Microscopic Imaging of Initiation and Propagation of Adiabatic Shear Bands." (Poster) *21st Biennial Conference of the APS Topical Group on Shock Compression of Condensed Matter*, Portland, OR, USA (June 2019)
4. "High-Speed Microscopic Imaging of Initiation and Propagation of Adiabatic Shear Bands." (Talk and Poster) *New. Mech*, Brown University, Providence, RI, USA (Oct. 2018)
5. "Dynamic Shearing Resistance of Constituents of Simulant of an Active Material." *75th Society for Experimental Mechanics Annual Conference*, Greenville, SC, USA (June 2018)
6. "High-Speed Microscopic Imaging of Initiation and Propagation of Adiabatic Shear Bands." *75th Society for Experimental Mechanics Annual Conference*, Greenville, SC, USA (June 2018)
7. "Dynamic Shearing Resistance of Constituents of an Active Material Simulant." (Poster) *New. Mech*, MIT, Boston, MA, USA (Oct. 2017)
8. "Dynamic Shearing Resistance of Constituents of an Active Material Simulant." *54th Annual Technical Meeting of the Society of Engineering Science,* Northeastern University, Boston, MA, USA (July 2017)
9. "Dynamic Shearing Resistance of Constituents of an Active Material Simulant." *20th Biennial Conference of the APS Topical Group on Shock Compression of Condensed Matter*, St Louis, MO, USA (July 2017)

Teaching Experience

- ENGN0310 Mechanics of Solids and Structures, *Fall 2015* (Undergraduate)
- ENGN0040 Dynamics and Vibrations, *Spring 2016* (Undergraduate)
- ENGN0310 Mechanics of Solids and Structures, *Fall 2016* (Undergraduate)
- ENGN2490 Crystal Structures and Crystallography, *Fall 2017* (Graduate)
- ENGN2210 Continuum Mechanics, *Fall 2019* (Graduate)
- ENGN2290 Plasticity, *Spring 2020* (Graduate)

Dedicated to my family

Acknowledgements

My graduate education at Brown University has been a wonderful learning experience. I joined Brown with a singular motive of learning experiments. I have not only achieved confidence in experimental solid mechanics but have also been provided an opportunity to work on the theoretical and computational fronts. All my learning has been a cooperative effort of many talented and kind people, who I would like to thank here.

First and foremost, I would like to thank my advisors Prof. Pradeep Guduru and Prof. Rodney Clifton, who have helped me develop a scientific temper towards research problems. My education under their guidance can be summarized in two keywords: *rigor* and *simplicity*. I would like to thank Pradeep for giving me an opportunity to build scientific equipment from scratch. Both Rod and Pradeep have been instrumental in helping me develop a patient and impartial approach towards problems. I have immensely benefitted from the company of Dr. Tong Jiao who taught me PSPI experiments. Her willingness to help and her great company made the Plate Impact Facility feel like home.

Several faculty at Brown have been very helpful. I would like to thank Prof. David Henann the most for his constant guidance, whether during the coursework or in performing simulations for the thesis. I would like to thank both Prof. Henann and Prof. Eric Chason for being on the committee and providing useful comments. My interactions with Prof. Allan

Bower, Prof. Haneesh Kesari and Prof. Sharvan Kumar have all been very enjoyable and memorable. I would also like to thank Prof. Kyung-Suk Kim for welcoming me in his lab in the first year.

I have been a constant customer of the machine shop for the past five years. Charles Vickers, Michael Packer and James Carroll have been instrumental in helping me build the new experimental facilities and have always managed to somehow find time for my machining jobs. Their company has made my experience at Brown very enjoyable. I am also very thankful to other members of staff, including Chris Bull, Brian Corkum, John Shilko and Anthony McCormick. The lightning speed with which Stephanie Gesualdi placed orders helped me carry out experiments at a brisk pace.

I would like to thank all my friends at Brown without whose support this endeavor would not have been possible. I would like to especially thank my friend, Harkirat Singh, who has provided immense emotional support during difficult times. I have been very lucky to have found good friends in Kaushik Vijaykumar, Srinivas Yadavalli, Sagar Wadhwa, Mrityunjay Kothari, Aakash Sane, Adriana Salazar and Srijan Neogi whose company I have enjoyed and who have stayed with me through thick and thin. My friendship with Sagar Wadhwa, Archita Agarwal, Apoorvaa Deshpande, Prachi Jain, Anshul Jain, Mohak Patel, Jay Sheth and Ravi Kumar has made my life at Brown memorable.

Above all, I would like to thank my parents and my family in being truly the pillars of support during my PhD life. Despite living on the other side of the world, they have constantly

guided me through tough situations. This endeavor would not have been possible without their continuous love and support.

Table of Contents

List of Tables

List of Illustrations

Chapter 1

Introduction

1.1 Background and Motivation

An energetic material is one with a large amount of stored chemical energy that can be released over a very short duration of time. Energetic materials have their origins in gunpowder, which can be traced back to 9^{th} century China. Gunpowder was accidentally developed by the Chinese monks in their search for a life-enhancing elixir. Gunpowder played an important role in military for several centuries until further developments in the explosive technology by Ascanio Sobrero and Alfred Nobel. In 1867, Alfred Nobel, the man behind instituting the famous Nobel prize, created an alternative to gunpowder, named dynamite. However, major developments in energetic materials have been made in the 20^{th} century with the invention of several energetic crystals such as RDX (1,3,5-Trinitro-1,3,5-triazinane), HMX (1,3,5,7-Tetranitro-1,3,5,7-tetrazoctane), TATB (1,3,5-Triamino-2,4,6-trinitrobenzene) and many more.

Even though energetic materials have found their primary application in military for a long time, today, they serve an important role in space applications and civil engineering. Energetic materials are routinely employed as a solid fuel in rocket propellants and in mining and construction. Shaped charges made out of conventional explosives are used to focus the explosive energy and find numerous applications such as perforating wells in the oil and gas industry.

Based on their applications, energetic materials can be classified as explosives, pyrotechnics and propellants. Explosives can be made in several forms like pressings of explosive crystals, casting and polymer-bonded explosives. The attention here is restricted to polymer-bonded explosives.

Polymer-Bonded Explosives (PBXs) are composites of energetic crystals held together by a very small fraction (usually 5-10% by weight) of a polymeric binder. These granular composites are widely used in military explosives, rocket propulsion and mining. Some of the commonly used energetic crystals are HMX, RDX and PETN (2,2-Bis[(nitroxy)methyl] propane-1,3-diyl dinitrate). Hydroxy-terminated polybutadiene (HTPB), Estane and Viton form the majority of polymeric binders used in PBXs. Using an elastomeric binder in a PBX reduces the sensitivity of these explosives to accidental detonation, thus making them ideal candidates for insensitive explosives (IE). The development of insensitive explosives has been a major undertaking of the U.S. Army after the unfortunate 1966 Palomares and 1968 Thule accidents. Following these accidents, the Los Alamos National Laboratory developed Insensitive High Explosives (IHEs) which preserve their effectiveness but reduce sensitivity to impact, thus making them safer. The reduced shock sensitivity of PBXs allows for safer transportation and minimizes the probability of accidental events such as sympathetic detonations. PBXs also have other desirable features like machinability and castability, which further enhance their role for IHEs. Most of the deformation in a PBX is taken up by the binder which prevents inter-granular friction between the crystals, thereby reducing the sensitivity of the PBX to external mechanical stimuli. Accurate prediction of the sensitivity of IHEs to imposed dynamic mechanical loading is essential but has been highly challenging. Since the impact sensitivity of the PBXs is closely

related to their mechanical behavior, composition and microstructure, it is imperative to study the mechanical response of PBXs and their constituents under loading scenarios of interest.

From the perspective of performance and safety, it is important to study ignition mechanisms in explosives. It is generally accepted that ignition in explosives begins in localized regions of high temperature, called 'hot-spots' (Bowden and Yoffe (1958), (1985)). These regions of high temperature are formed when localized mechanical energy is converted to heat. Consider the case of a shock wave passing through an explosive material. Material or geometric heterogeneities in the system are expected to lead to localization of energy and hot-spot formation. Once these hot-spots turn critical (i.e. can cause ignition), self-sustaining dissociation reaction fronts emanate from them, resulting in ignition. The exothermic chemical reactions lead to a thermal runway, melting and formation of gaseous products, resulting in a rapid increase in local pressures. Shock waves emanate from these spots, cause more hot-spots to form and ultimately an avalanche of hot-spots results in a detonation front being formed (Sewell and Menikoff (2004)). Ultimately, the detonation front surpasses the shock front at the Shock to Detonation Transition (SDT). Thus, in order to accurately model the response of energetic crystals to a shock stimulus, it is important to understand mechanisms leading to the initial hot-spot formation.

In the study of PBXs, energetic crystals like HMX and RDX are often replaced by simulant crystals such as sucrose, melamine and acetaminophen to prepare mock explosives. A simulant crystal is a molecular crystal that closely resembles an energetic crystal in terms of one or more relevant attributes such as crystal structure, density and mechanical properties. Due to their

inert nature simulants provide a safer way to investigate the mechanical behavior, making them suitable for laboratory settings. Another major advantage of studying energetic simulants is that they allow decoupling of mechanical and chemical responses of energetic crystals. Consequently, one can understand the dynamics of energy localization phenomenon such as pore collapse, adiabatic shear localization, fracture, granular friction, etc. (which together are known as "hot-spot mechanisms") without the additional complexity introduced by the associated chemical reactions in an actual energetic crystal.

A great deal of work has been done over the past few decades to understand the compressive response of PBXs (Funk et al. (1996), Gray III et al. (1998), Idar et al. (1998)) and their polymer-bonded simulants (PBSs) (Funk et al. (1996), Idar et al. (1998), Williamson et al. (2006), Siviour et al. (2008), Liu et al. (2011), Hu et al. (2015), Kendall and Siviour (2015)). It has been shown through quasi-static and split-Hopkinson bar testing that the compressive strength of the polymer-bonded composites of energetic/simulant crystals increases with increasing strain-rates and decreasing temperatures (Funk et al. (1996), Gray III et al. (1998), Drodge et al. (2007), Siviour et al. (2008)). For example, it was shown by Gray III et al. (1998) that the peak stress of PBX 9501, under nominal uniaxial stress loading, increases from a value of ~9 MPa at 10^{-3} s^{-1} and 27 ^{0}C to ~60 MPa at 2000-2500 s^{-1} and 17 ^{0}C. Similarly, the peak stress decreases from a value of ~125 MPa at -40 ^{0}C to ~35 MPa at 55 ^{0}C for a strain-rate in the range of at 2000-2500 s^{-1}. It is expected that the polymer binder being the more compliant component in a PBX would take up most of the strains and result in a dramatic dependence of compressive strength of the PBX on the strain rate and temperature. Wiegand and Reddingius

(2005), Ravindran et al. (2016), (2017) provide a quantitative validation of the fact that most of the strains are indeed concentrated in the binder regions of the composite.

It is observed that in quasi-static and high strain-rate testing, the compressive stress drops after reaching a peak and exhibits strain softening. The mode of failure changes with strain-rate and temperature. Siviour et al. (2008) show, through in-situ X-ray tomography, that for quasi-static loading rates, debonding between sucrose crystals and the binder is the reason behind the loss in mechanical strength of the composite. Ravindran et al. (2016), (2017) and carried out high-strain rate experiments in which deformation was imaged through in-situ digital image correlation (DIC) at the meso-scale. It was shown that deformation localizes in polymer-rich regions, resulting in failure primarily through binder fracture or binder delamination. Similarly, the failure mode of PBX 9501 and other composites under high strain-rate loading is found to change from a combination of binder debonding and trans-granular fracture of the explosive crystals (HMX in this case) at 20 ^{0}C to brittle trans-granular cracking of HMX and glassy fracture of the binder at -40 ^{0}C. This transition from a ductile to brittle failure occurs when the temperature of the PBX is decreased to a value below the glass transition temperature of the binder. Therefore, it can be concluded that strain-rate and temperature are important external Funk et al. (1996) parameters influencing the compressive stress-strain response and failure mechanisms of PBXs. Deformation behavior of PBXs is shown to depend on intrinsic factors as well, such as the particle size of the energetic/simulant crystals (Balzer et al. (2004), Siviour et al. (2004)), loading density (weight fraction of explosive crystals in the composite) and ageing of the polymer binder (Fuente and Rodríguez (2003)). Strength of the composite is shown to vary inversely with the square root of the particle size (Balzer et al. (2004)), i.e. larger crystal

size leads to a weaker PBX. Similarly, a larger crystal size is associated with larger impact sensitivity. It is demonstrated by Armstrong et al. (1990) that the drop-height for 50% probability of initiation of RDX crystals varies linearly with the inverse of the square root of particle size. Ageing of the polymer has been shown by Fuente and Rodríguez (2003) to reduce the damping capacity of HTPB-based rocket propellants, effectively reducing their service life.

It should be noted that in all the studies referenced above, PBXs/PBSs are subject to uniaxial stress testing, i.e. compression without any confinement. A lack of confinement results in very low pressures which may not be representative of the loading scenarios in several applications. Wiegand and Reddingius (2005) explored the effect of confinement on elastic and plastic behavior of polymer bonded simulants at quasi-static strain rates. They showed that the Young's modulus of PBS 9501 increases from 1.5 GPa at a confinement pressure of 0.1 MPa to ~7.5 GPa at a pressure of 138 MPa. Similarly, the flow stress is reported to increase from 8 MPa to ~65 MPa as the pressure is increased from 0.1 MPa to 138 MPa. It is shown that the primary mode of failure for an unconfined composite is fracture and debonding whereas it is plastic flow under confinement pressure. However, the range of pressures explored by Wiegand and Reddingius (2005) is very limited and the pressure values are very small. More generally, there has been a lack of experimental effort on studying the high-pressure, high strain-rate response of PBXs under these conditions

Plate impact has been a key experimental technique in attaining high pressures and high strain-rates simultaneously. Pressures ranging from a few GPa to hundreds of GPa and strain-rates of the order of 10^5-10^7 s^{-1} can be attained using plate impact techniques (See Figure 1.1 for

comparison with other techniques). Another advantage with plate impact experiments is the uniaxial strain loading as opposed to uniaxial stress in the Kolsky bar type experiments. An important class of plate impact techniques is the Pressure-Shear Plate Impact (PSPI) experiment. Pioneered by Clifton and Klopp (1985) at Brown University, PSPI experiments allow investigation of the shearing response of materials under high pressures, high shear strain-rates and high shear strains. The PSPI technique is described in detail in the next section. While plate impact techniques have been used for a long time to study the shock response of explosive crystals, no significant work has gone into studying the strength behavior under high pressures. This also holds true for PBXs. It is to be noted that the shear strength behavior of PBXs and their components is extremely critical in modeling their overall mechanical behavior under dynamic loading conditions. Accurate models incorporating shearing resistance are important to adequately model localization behavior like shear bands or phenomena like pore collapse, which lead to hot-spots, which provides strong motivation for PSPI experiments on PBXs. In the present work, dynamic shearing resistance measurements have been made on HTPB (elastomeric binder), sucrose (an energetic material simulant of β-HMX) and their composite, at pressures of 3-10 GPa and shear strain rates of 10^5-10^6 s^{-1}. The experimental results are described in Chapters 2, 3 and 6 respectively. To the best of our knowledge, these shear strength measurements are reported for the first time. Since HTPB and sucrose are vastly different types of materials, understanding their response to mechanical loading is imperative to lay a strong foundation for constitutive modeling of their composite. Therefore, PSPI experiments on the composite are preceded by PSPI experiments on HTPB and sucrose. It should also be noted at this point that the shear strength measurement of explosive crystals/simulants are extremely important to understand hot-spot formation for weak shocks

(i.e. the range of pressures considered here) and accidental impact. Initiation of hot-spots from weak shocks requires dissipative mechanisms in addition to shock heating (Sewell and Menikoff (2004)). Such a mechanism is provided by material heterogeneities and the strength considerations of the explosive become important.

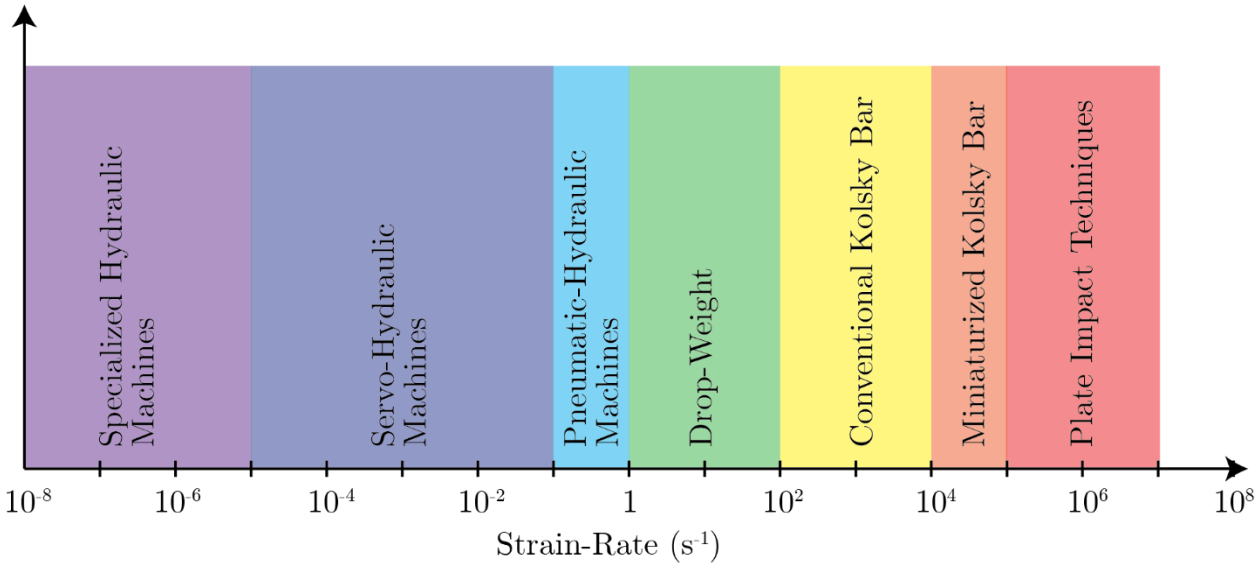

Figure 1.1 Experimental techniques for material testing at different strain rates

Considerable research effort has been spent towards studying the mechanisms behind hot-spot formation and propagation. A list of these mechanisms is provided by Field (1992), Field et al. (1992) :

(i) Formation of regions of large shear stresses, resulting in heating through plastic deformation. One such example is localization through formation of adiabatic shear bands (Winter and Field (1975), Field et al. (1992), Coffey and Sharma (2001), Sharma et al. (2001), Jaramillo et al. (2007), Cawkwell et al. (2008)).

(ii) Fracture in the bulk of explosive crystals or the binder, or debonding at binder/crystal interface.

(iii) Friction between explosive crystals or between fractured surfaces (Bowden and Yoffe (1985)).

(iv) Localized melting and subsequent viscous heating of the molten region.

(v) Pore-collapse, leading to adiabatic compression of trapped gas (Chaudhri and Field (1974), Bowden and Yoffe (1985), Dear et al. (1988)) and/or phenomena like jetting (Dear et al. (1988)).

These mechanisms have been studied in detail, primarily through numerical techniques and a few experimental techniques. On the experimental front, drop-weight impact, miniaturized Hopkinson bar, edge-on plate impact and micro-particle impact on explosive crystals have been utilized to study initiation and propagation of hot-spots. A variety of in-situ diagnostics have been used in these experiments. Since events like hot-spot formation occur over microsecond time-scales (Bowden and Yoffe (1958), (1985)), high-speed imaging is necessitated. In-situ high speed imaging in the visible spectrum and heat sensitive films have been used to capture the formation of features like adiabatic shear bands (Field et al. (1992)) and pore-collapse (Dear and Field (1988), Dear et al. (1988), Bourne and Field (1991), Swantek and Austin (2010)).

Bowden and Yoffe (1958), (1985) showed that for Deflagration to Detonation transition (DDT) to occur, hot spots should have sizes of 0.1-10 μm, durations of 10^{-5}-10^{-3} s and temperatures >700 K. Performing quantitative in-situ measurements of mesoscale deformation and temperature fields, at sub-micron spatio-temporal resolutions, during impact experiments has remained a challenge. Ravindran et al. (2016), (2017) made quantitative measurements of deformation fields in a polymer-bonded sugar, using in-situ imaging at spatial and temporal

resolutions of 20 μm and 10 μs respectively. Kannan et al. (2018) have reported a comparatively finer spatial resolution of 10 μm at frame rates of 5 million frames per second, to capture twinning in Magnesium. However, achieving micron scale spatial resolutions at such high framing rates remains a major challenge. Owing to the important need for high resolution in-situ measurements, a high-speed microscopic imaging system with sub-micron spatial and sub-microsecond temporal resolutions is developed in this work. The capability of the system is demonstrated by quantitative measurements of displacement and strain fields in and around a highly localized region of shear band in polycarbonate. Chapter 7 details the development of this experimental method and measurements of kinematic fields associated with shear band initiation under edge-on impact of a notched plate of polycarbonate.

At the same time, measurements of highly heterogeneous temperature fields have been lagging in the experimental literature. Such measurements are harder to make as there are hardly any high-speed thermal imaging systems that achieve the necessary time resolution. Zehnder et al. (2000) developed an infra-red high-speed camera to visualize the formation of adiabatic shear bands ahead of a crack-tip in Kalthoff-like (Kalthoff (1990)) impact experiments. Quantitative measurements of temperature fields were reported by (Guduru, Ravichandran, et al. (2001), Guduru, Rosakis, et al. (2001)). More recently, Keyhani et al. (2019) have reported simultaneous measurements of deformation fields of a sucrose aggregate in the visible and infrared spectra using high-speed imaging. At the same time, high-speed X-ray diagnostics are also emerging to capture deformations during dynamic loading. Escauriza et al. (2020) investigate the pore-collapse process in PMMA using X-rays. Such developments

highlight the recent drive towards capturing highly heterogenous two-dimensional deformation fields during high strain-rate experiments.

1.2 Introduction to Pressure Shear Plate Impact (PSPI) experiments

Pressure-Shear Plate Impact (PSPI) experiments have been used to study the dynamic behavior of materials under high pressures (~20 GPa), high shear strain rates (10^5-10^7 s^{-1}) and large shear strains (100-200%). Recently, the PSPI technique has been extended to pressures up to 50 GPa by Kettenbeil et al. (2020) . A variety of materials have been tested using this technique, for example, metals (Gilat and Clifton (1985), Tong et al. (1992), Frutschy and Clifton (1998), Grunschel (2009)), ceramics (Espinosa (1995), Sundaram (1999)), polymers (Clifton and Jiao (2015)), lubricants (Ramesh and Clifton (1987)) and glasses (Sundaram (1999)). In these experiments, a flyer plate impacts the target plate at an angle, θ generating both compressive longitudinal and shear waves. The angle, θ is usually kept below 20^0 to ensure that no slip occurs at the impact face. A 2.5" gas gun at the plate impact facility at Brown University is used for most experiments. The gun barrel has a keyway which facilitates oblique impact. One of the most common test configurations is a sandwich configuration as shown in Figure 1.2. In this configuration, a thin sample (typically 10-200 μm) is sandwiched between two hard elastic plates, hereafter, referred to as the front target plate and the rear target plate. The flyer and target plates are made from a hard material, like pure tungsten carbide or high strength steel, that remains elastic (or nearly so) in the range of loading pressures and strain rates reported herein. Upon impact of the flyer, a one-dimensional plane-wave loading is

obtained. This is one of the key advantages of PSPI experiments as it allows for an easy interpretation of stress-state achieved inside the specimen.

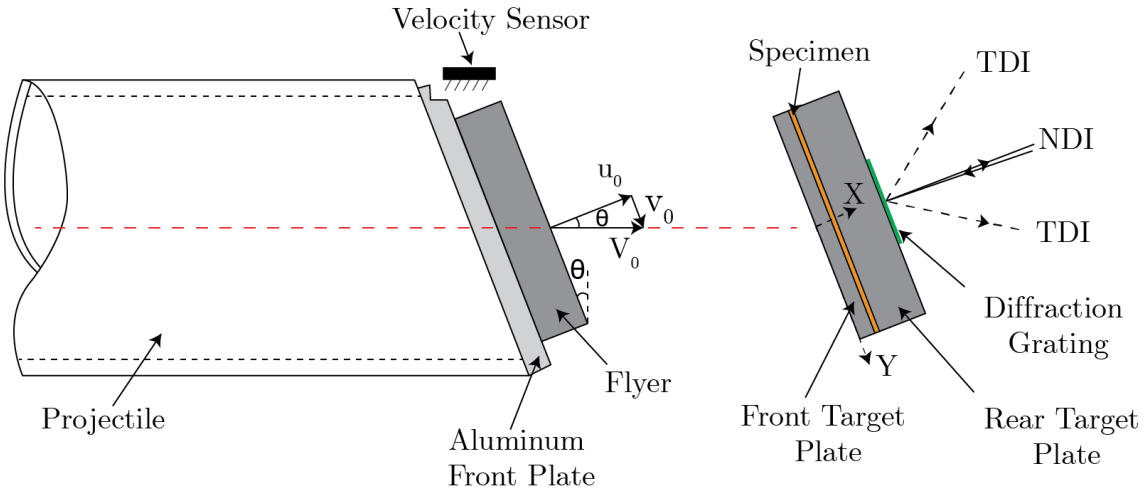

Figure 1.2 PSPI Experimental Set-up. The projectile is typically a light-weight fiberglass tube. A flyer plate is glued to an aluminum plate bonded to the front of the projectile. A flat step is made on the aluminum front plate perpendicular to the impact direction. This step is used to short out the pins of the velocity sensor that is used to measure the velocity of the projectile. The velocity sensor consists of five pins, placed at an angle of ~110^0 to the impact direction. Rotation of the projectile is prevented by a key, attached to the projectile and sliding in a keyway in the gun barrel. The flyer plate and the target assembly are aligned for impact of parallel plates with an angle, θ, between the normal to the impact plane and the direction of approach. Plane compressive and shear waves are generated at the impact face. A thin specimen, sandwiched between two hard elastic plates (target plates), is loaded by the forward propagating plane waves emanating from the impact plane. Particle velocities at the free surface are measured using a combined normal and transverse displacement interferometer (NDI & TDI). Measured transverse displacements are made possible by using interference of beams diffracted symmetrically by a diffraction grating deposited on the free surface of the rear target plate

The t-X plot for a typical PSPI experiment with sandwich configuration is shown in Figure 1.3. The impact occurs at X=0 and t=0, where X refers to the spatial coordinate along the thickness direction (as shown in Figure 1.2) in a reference configuration and t represents time. On impact, longitudinal and shear waves are sent through the front target plate and the

flyer. Due to low acoustic impedance of the specimen, these waves reverberate through the specimen before the stress state rings-up to a uniform value. Note that the thickness of the front target plate is chosen so that the compressive stress in the specimen has rung-up to a uniform value before the arrival of the shear wave. This facilitates he measurement of shear strength of the specimen at a state of constant normal stress.

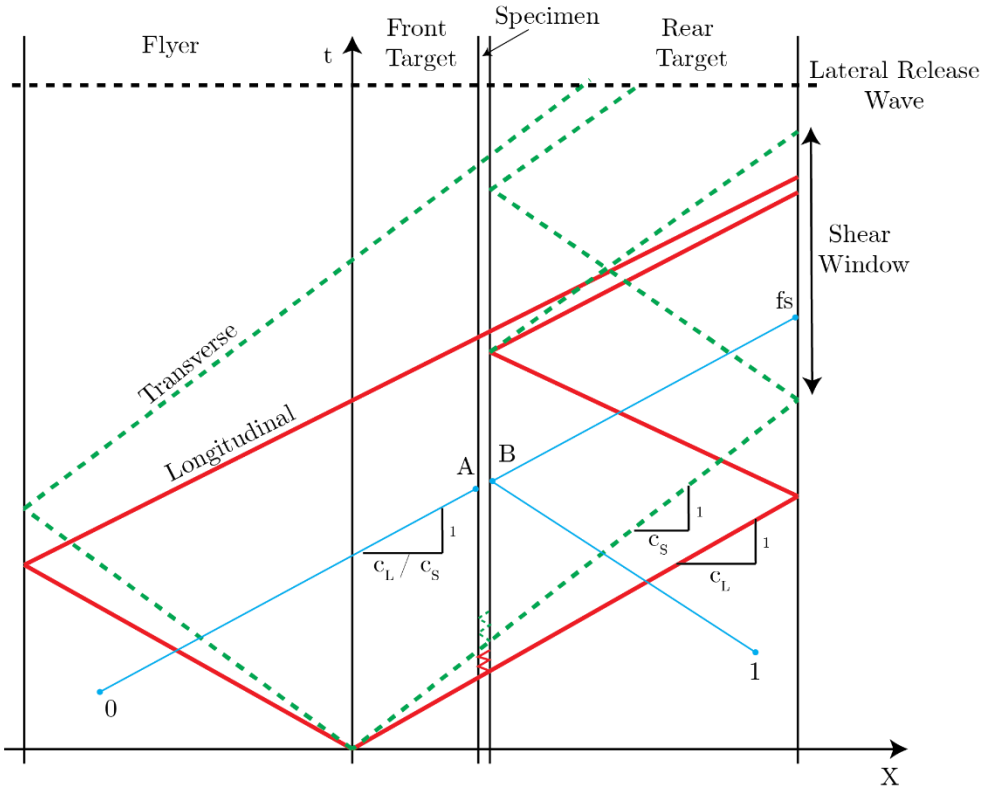

Figure 1.3 A typical t-X plot for a PSPI experiment. Solid red lines represent the longitudinal wave characteristics and dashed green lines represents the shear wave characteristics. Blue lines represent characteristics for either longitudinal or shear waves. Point 0 and Point 1: Before the arrival of longitudinal wave ($\sigma_0 = \tau_0 = 0,\ u_0 = V_0\, cos(\theta), v_0 = V_0\, sin\,(\theta)$ and $\sigma_1 = \tau_1 = u_1 = v_1 = 0$). Point A: Front Target/Specimen interface. Point B: Rear Target/Specimen interface. Point *fs*: Traction-free surface of Rear Target plate ($\sigma_{fs} = \tau_{fs} = 0$)

The time window of shear loading at a constant normal stress is cut short by the unloading wave from the free surface of the rear target plate, as shown in Figure 1.3. The thickness of the rear target plate and the flyer are chosen to maximize the shear window. Typically, a shear window of 0.75-1 μs is achieved, which allows large shear strains of 1-10 for shear strain rates of 10^6-10^7 s^{-1}. On impact, cylindrical unloading waves are generated at the circumference of the plates due to traction-free boundary conditions. When these waves reach the point being monitored on the free surface of the rear target plate, displacements can no longer be interpreted as caused by easily interpretable one-dimensional plane waves and the record is discarded beyond this point.

If the flyer and target plates respond elastically, velocities and tractions at the sample/rear target plate interface can be inferred from the free surface velocity measurements made on the rear target plate. For such a case, normal and shear stresses in the sample can be obtained using a characteristic analysis for one-dimensional elastic wave propagation. From Figure 1.3, the characteristic equations at the front-target plate/specimen interface are:

$$\sigma_A - \rho_0 c_L u_A = -\rho_0 c_L u_0 \tag{1.1}$$

$$\tau_A - \rho_0 c_S v_A = -\rho_0 c_S v_0 \tag{1.2}$$

Here, σ and τ represent normal and shear stress respectively, u and v represent normal and transverse velocities, c_L and c_S are longitudinal and shear wave velocities and ρ_0 is initial density of the target plate and flyer material. $u_0 = V_0 \cos(\theta)$ and $v_0 = V_0 \sin(\theta)$ where V_0 is the impact velocity. Note that a similar analysis can be carried out for plates made from different materials. Similarly, the characteristic equations satisfied at the specimen/rear-target plate interface are:

$$\sigma_B + \rho_0 c_L u_B = 0 \tag{1.3}$$

$$\tau_B + \rho_0 c_S v_B = 0 \tag{1.4}$$

$$\sigma_B - \rho_0 c_L u_B = -\rho_0 c_L u_{fs} \tag{1.5}$$

$$\tau_B - \rho_0 c_S v_B = -\rho_0 c_S v_{fs} \tag{1.6}$$

After a sufficient number of reverberations through the thickness of the specimen, a nominally uniform of stress is obtained in the sample, i.e. $\sigma_A = \sigma_B = \sigma_{sp}, \tau_A = \tau_B = \tau_{sp}$ and the normal velocity at the front and rear of the specimen is also the same, i.e. $u_A = u_B = u_{sp}$. The subscript '*sp*' stands for specimen and denotes the steady state. Combining equations (1.1) to (1.6), the following relations are obtained for a steady state:

$$\sigma_{sp} = -\frac{\rho_0 c_L u_{fs}}{2} \tag{1.7}$$

$$\tau_{sp} = -\frac{\rho_0 c_S v_{fs}}{2} \tag{1.8}$$

$$2u_S = u_{fs} = u_0 \tag{1.9}$$

$$v_B = \frac{v_{fs}}{2}; v_A = v_0 - v_B \tag{1.10}$$

Figure 1.4 depicts the reverberations inside the sample. After the ring-up is complete, the normal stress reaches a peak value of $\sigma_{sp} = -\frac{\rho_0 c_L u_0}{2}$ as given through equations (1.7) and (1.9). However, the shear stress may nor ring up to the peak value of $\tau_{sp} = -\frac{\rho_0 c_S v_0}{2}$ if the sample deforms plastically in shear. Then, the velocity difference between the front and back of the specimen leads to a shear strain rate given as:

$$\dot{\gamma} = \frac{v_A - v_B}{h} = \frac{v_0 - v_{fs}}{h} \tag{1.11}$$

The expression for strain rate in equation (1.11) is valid only after the specimen has reached a state of constant shear stress as shown in Figure 1.4 (b). The shear strain rate is integrated to yield the shear strain:

$$\gamma(t) = \int_0^t \dot{\gamma}(\tau) d\tau \tag{1.12}$$

The above analysis assumes an ideal condition of perfectly parallel impacting surfaces. However, there is always a finite amount of tilt between the flyer and the target plate. It is important to keep the tilt as low as possible, typically a value below *2 mrad* is desired. In order to achieve such low tilt angles, an extremely precise alignment technique was invented by Kumar and Clifton (1977) . Alignment of the flyer to the sandwich consists of two steps: a coarse alignment step and a fine alignment step. In the coarse-alignment step, the flyer and the sandwich are brought in contact and the degrees of freedom of the sandwich adjusted to ensure no gaps and a complete overlap of the impacting surfaces. This is followed by a fine alignment step that uses a partially-mirrored, 90^0 precision prism. The procedure is described in detail in Kumar and Clifton (1977) . It should be noted that an alignment precision as small as 0.02 mrad is achieved using this method.

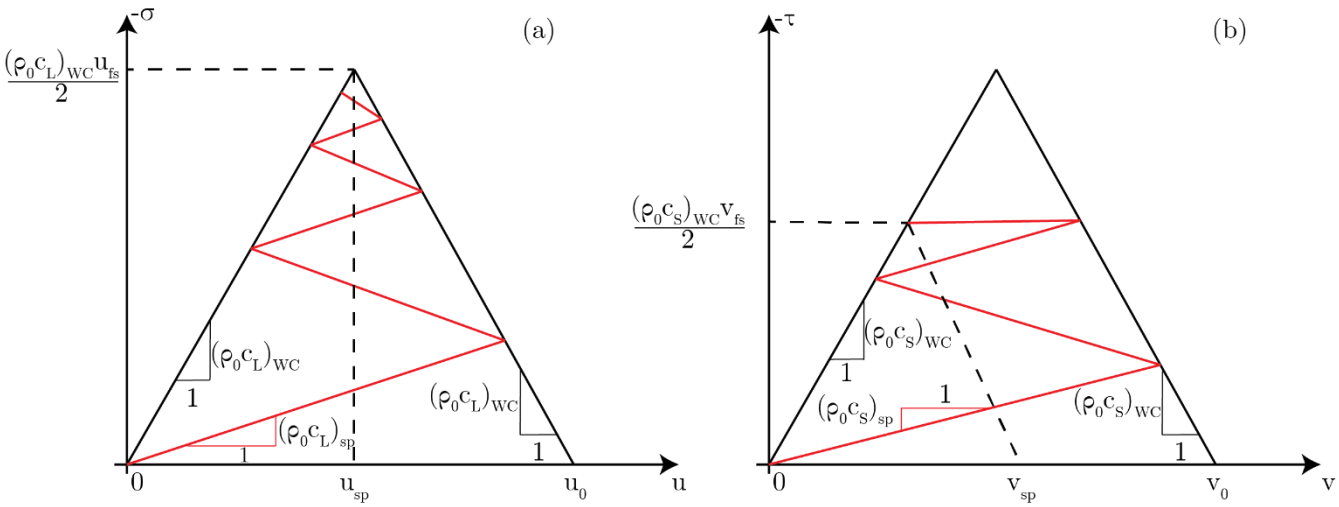

Figure 1.4 Stress- particle velocity plots for normal and shear waves. (a): Solid black lines with a slope equal to $+(\rho_0 c_L)_{WC}$ represent the allowable states for normal particle velocity and normal stress that can be achieved at the interface between the sample and the rear target plate, as characterized by equation (1.3). Solid black line with a slope equal to $-(\rho_0 c_L)_{WC}$ represent the allowable states for normal particle velocity and normal stress that can be achieved at the interface between the sample and the front target plate, as characterized by equation (1.1). The state of normal stress and normal particle velocity within the sample, which has a lower acoustic impedance than the target plates, is given by solid red lines with slopes $\pm(\rho_0 c_L)_{sp}$, and is shown to ring up to the peak normal stress value of $-\sigma = (\rho_0 c_L)_{WC} u_{fs}/2$. (b) A similar description, as for normal stress and normal velocity, holds true for the shear stress versus transverse particle velocity. If the sample responds elastically under shear, the shear stress rings up to the peak value of $-\tau = (\rho_0 c_s)_{WC} v_{fs}/2$. However, if the sample does not respond elastically up to the peak value of shear stress and deforms plastically, the transverse particle velocity is not uniform across the sample. A case where the difference between the transverse particle velocities at the front and back of the sample becomes constant, leading to a constant shear strain-rate, is shown

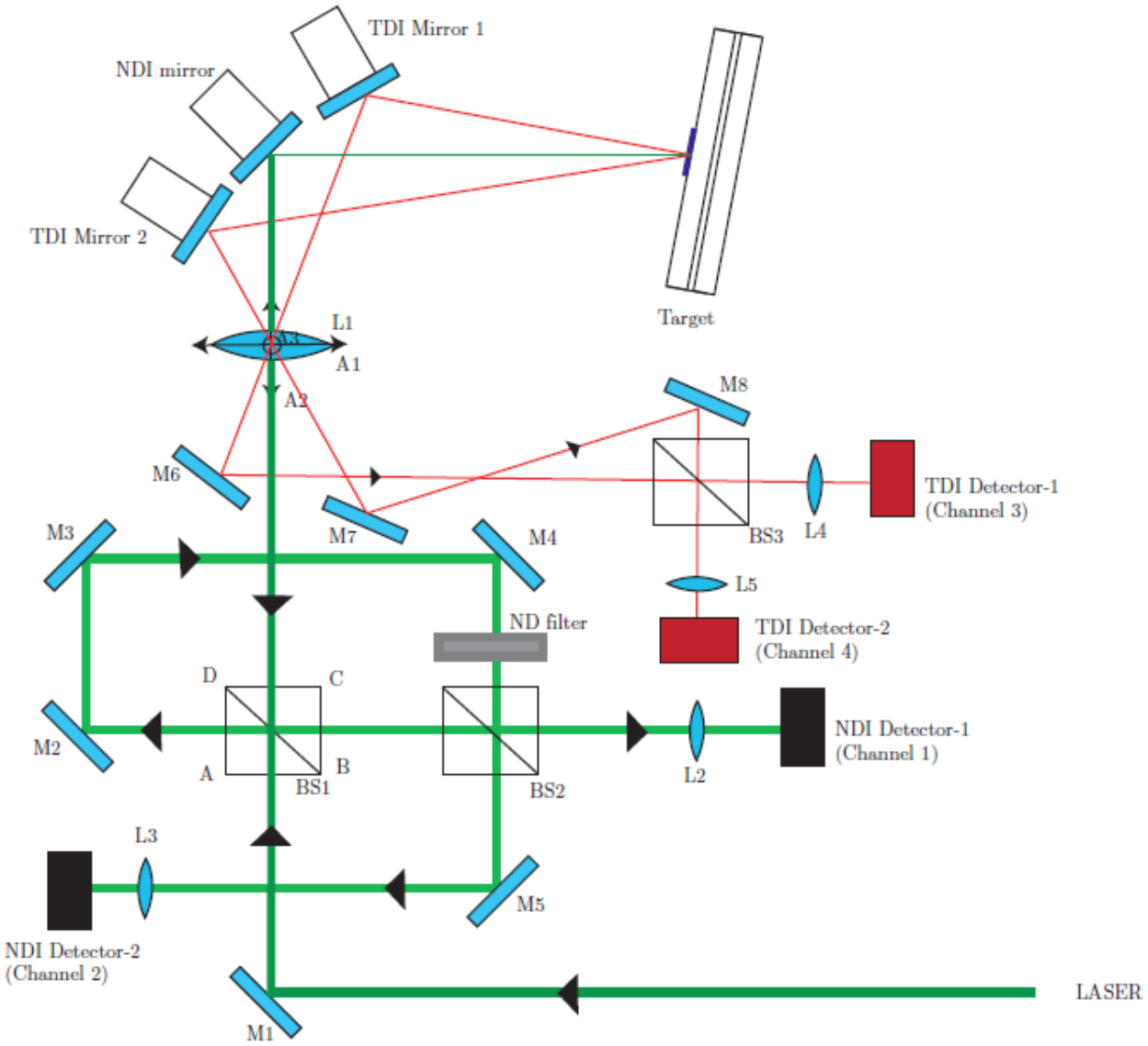

Figure 1.5 Optical set-up for NDI and TDI. A collimated laser beam ($\lambda = 532\,nm$) is aligned to fall normally on the diffraction grating on the back of the rear target. Lens L1, with a focal length of 500 mm, focuses the collimated beam to a focal spot of size ~100 μm on the grating. The reflected 0^{th} order beam is directed to beam-splitter BS2, where it interferes with the incident laser beam, to generate the NDI fringes. Two NDI photo-detectors (NDI Detector-1 and NDI Detector-2), each with a bandwidth of 1 GHz, are used to capture the fringe pattern. The reflected +1 and -1 order beams are directed to beam-splitter BS3, where they interfere to give TDI fringes. Two TDI photo-detectors (TDI Detector-1 and TDI-detector-2), each with a bandwidth of 350 MHz, are used to capture the TDI fringe pattern. Signals from the photo-detectors are captured by high bandwidth (≥ 1 GHz) and high sampling rate oscilloscopes ($\geq$ 2.5 GSa/s)

In order to confirm if a shot is valid, tilt measurement during the experiment is necessary. Four tilt pins flush with the impact surface measure the times of contact at different points on the circumference of the sandwich. Klopp and Clifton (1990) provide a detailed analysis of tilt in PSPI experiments. A program was written in Mathematica to calculate the closure velocity, V_{cl} and the closure angle, Ω (see Figure 2b in Klopp and Clifton (1990)) from contact times of the four tilt pins. The tilt angle, α can then be obtained as:

$$\sin(\alpha) = \frac{V_0 \cos(\theta)}{V_{cl}} \approx \alpha \tag{1.13}$$

A combined Normal Displacement Interferometer (NDI) and Transverse Displacement Interferometer (TDI) is used to measure rear surface velocities (more details by Kim et al. (1977)). The optical set-up for NDI and TDI is shown in Figure 1.5. The interferometers are facilitated by a diffraction grating deposited on the free surface of the rear target plate using photolithography. A diffraction grating with 625 lines/mm is used. It is important to have a good quality diffraction grating to get a TDI signal with adequate signal to noise ratio (see Appendix B in Frutschy (1997)). Normal and transverse displacement sensitivities obtained using the diffraction gratings are:

$$\Delta U = \frac{\lambda}{2} \tag{1.14}$$

$$\Delta V = \frac{d}{2n} \tag{1.15}$$

Where ΔU and ΔV are normal and transverse displacements per fringe respectively, λ is the wavelength of laser light used, d is the spacing between lines in the grating and n is the diffraction order. For $\lambda = 532$ nm, $d = 1.6\ \mu m$ and $n = 1$, $\Delta U = 0.266\ \mu m/fringe$ and $\Delta V = 0.8\ \mu m/fringe$ are obtained.

Displacements are obtained from phase change information of the interferometric records. The phase of an amplitude-corrected trace of a record is given as:

$$\Delta\psi(i) = 2\pi m + \pi(\alpha + 1) - \alpha \cos^{-1}\big(y(i)\big) - \psi_0 \tag{1.16}$$

where $\Delta\psi(i)$ is the change in phase at the i^{th} data point, m is an integer that is updated by 1 after every fringe, $y(i) \in [-1,1]$ is the trace value at the i^{th} data point and ψ_0 is the initial phase. $\alpha = 1$ for a positive slope $\alpha = -1$ for a negative slope of the trace. Hence, the normal and transverse displacements are given as:

$$U(i) = \frac{dU}{d\psi} \times \Delta\psi_{normal}(i) = \frac{\frac{\lambda}{2}}{2\pi} \times \Delta\psi_{normal}(i) \tag{1.17}$$

$$V(i) = \frac{dV}{d\psi} \times \Delta\psi_{transverse}(i) = \frac{\frac{d}{2n}}{2\pi} \times \Delta\psi_{transverse}(i) \tag{1.18}$$

Differentiating the displacements yields velocities. Consider an example of interferometric records for shot PM1603 on sucrose. Figure 1.6 shows the NDI trace while Figure 1.7 shows the TDI trace. Note that the amplitude of the traces does not remain constant. Hence, an amplitude-correction step is incorporated before extracting the phase information from the trace. Figure 1.8 shows the normal and transverse velocity profiles obtained from these traces.

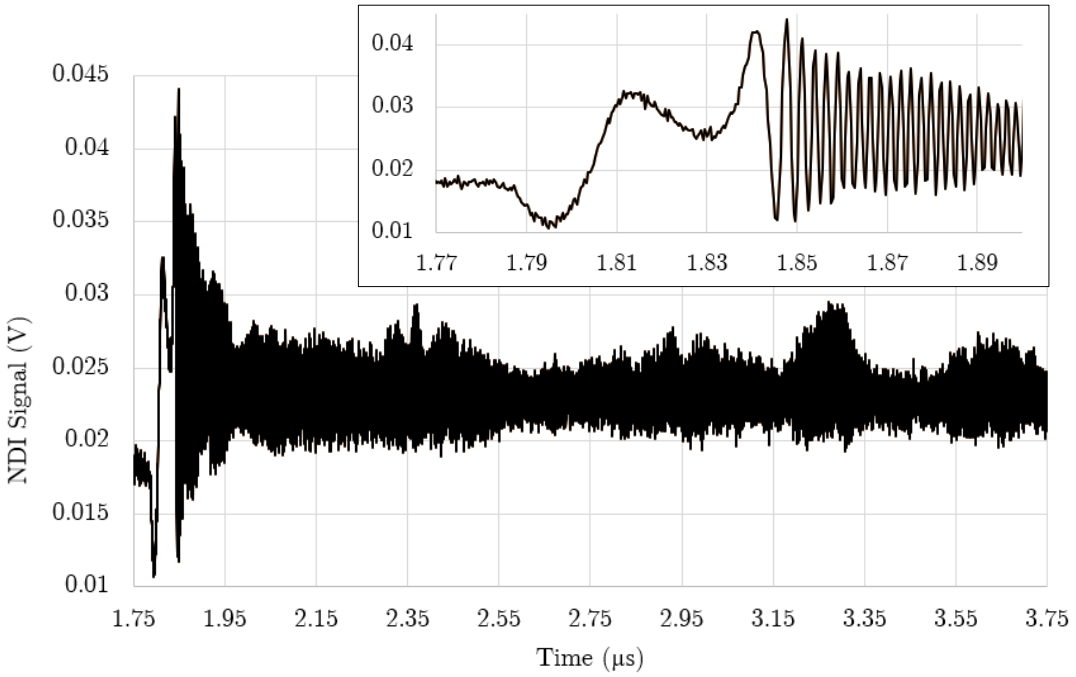

Figure 1.6 NDI trace for shot PM1603. The arrival of the normal wave at the free surface is marked by a sudden change in slope of the trace, at 1.78 μs, which is shown clearly in the inset

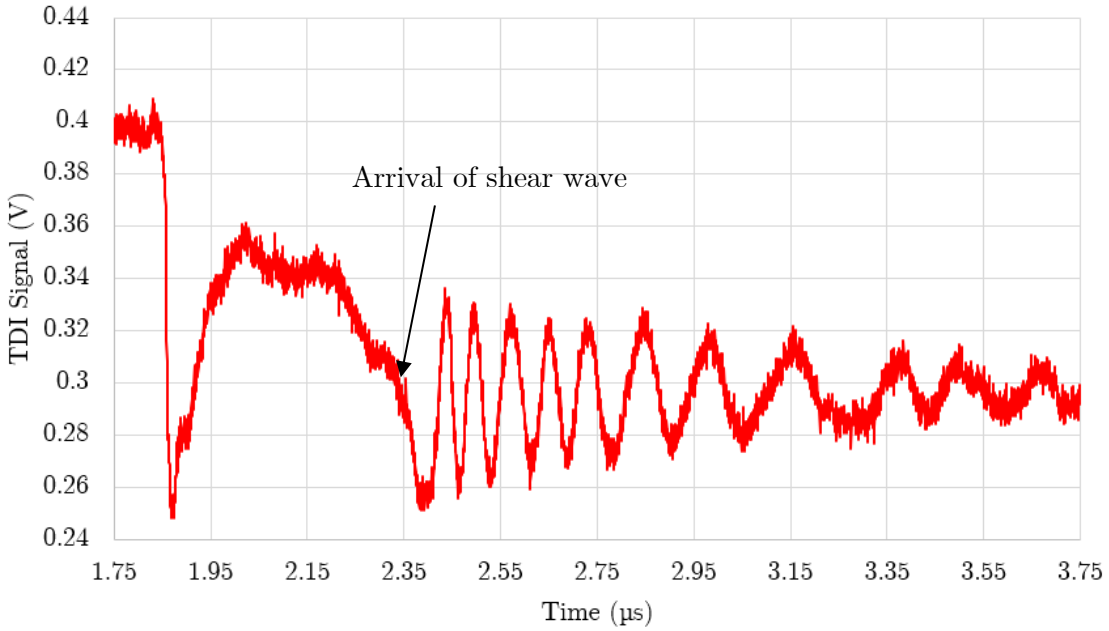

Figure 1.7 TDI trace for shot PM1603. The shear wave arrives at 2.3 μs as shown by the arrow. The arrival of shear wave is usually indicated by a sudden change of slope in the TDI trace. The portion of the trace before the arrival of shear wave is a result of tilt

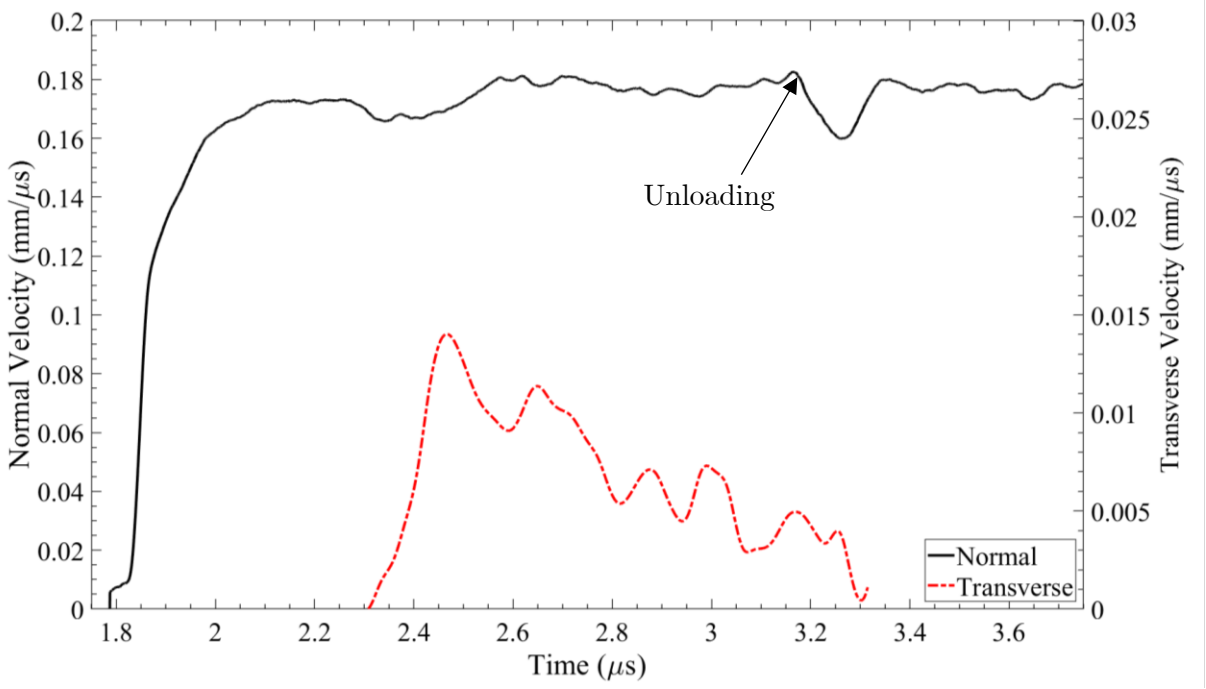

Figure 1.8 Normal and transverse velocity profiles for shot PM1603 on sucrose. The arrival of unloading longitudinal wave is indicated by the arrow. The velocity profiles are not considered beyond this time

1.3 Organization of Thesis

The thesis is divided into 8 chapters. Literature on polymer-bonded explosives and their mechanical behavior has been reviewed in the first chapter, followed by an introduction to the PSPI experimental technique of measuring dynamic behavior of materials. Chapters 2-5 are dedicated to PSPI experiments on the binder, HTPB and the energetic simulant, sucrose, and their constitutive modeling. All PSPI experiments are performed at large pressures (3-10 GPa), large shear strain-rates (10^5-10^6 s^{-1}) and large shear strains (0.25-2). Dynamic shear behavior of HTPB and its pressure dependence are explored through PSPI experiments in Chapter 2. A quasi-linear viscoelastic model is used to simulate such a behavior of the elastomeric binder. This is followed by three chapters on sucrose. The results of PSPI experiments on sucrose are

reported in Chapter 3, with focus on the shearing behavior. Chapter 4 lays the foundation of a thermodynamic framework for modeling a solid undergoing large deformation. A complete Mie-Gruneisen equation of state is derived, which allows for an adequate representation of the mechanical response of an energetic or simulant crystal subject to impacts and shocks. The thermodynamic framework is very generic and allows for the incorporation of large elastic deformations through higher order elastic constants, thermoelastic heating and thermo-viscoplasticity. The model is implemented in ABAQUS through a user-subroutine and the results are compared with experimental observations in Chapter 5. Chapter 6 details the PSPI experiments on the sucrose/HTPB composite for a given composition. Using the models for sucrose and HTPB developed in prior chapters, ABAQUS simulations are carried out on one-dimensional canonical microstructures and compared with experimental data. Chapters 2-6 lay a strong foundation for capturing material behavior of HTPB, sucrose and their composite, which sets the stage for exploring the mechanical response of the highly heterogeneous polymer-bonded simulants and their explosive counterparts. Since the eventual goal is to enable an understanding of the mechanisms leading to the formation of hot-spots in PBXs, a high-speed microscopic imaging capability is developed, with the necessary spatio-temporal resolution. Chapter 7 details the construction of such an imaging system and demonstrates its capability in capturing kinematic fields associated with adiabatic shear band formation in polycarbonate. At last, a summary of the work is presented in Chapter 8 and future work is described.

Chapter 2

HTPB: Experiments and Constitutive Modeling

2.1 Introduction

Hydroxy-terminated polybutadiene (HTPB) is one of the most widely used polymeric binders in Polymer-Bonded Explosives (PBXs) (Bourne and Milne (2004), Milne et al. (2007), Williams et al. (2013)) and solid rocket propellants. The main role of a polymer binder in a PBX is to cushion the explosive crystals from mechanical insults like shock and friction. At the same time, the binder improves the processability and provides tailorable properties while maintaining performance. In some cases, the binders also contribute to the explosive efficiency, like in the case of energetic binders with nitro and azido groups. HTPB has also been the most common binder for mock explosives, especially polymer-bonded sugars (PBSs) (Siviour et al. (2008), Hu et al. (2015), Kendall and Siviour (2015)). HTPB is also used in several other products like adhesives, foam insulation, bushings, surface coatings, elastomeric wheels and tires. The application of interest in this study is the role of a binder played by HTPB in PBXs and PBSs.

One of the key advantages of a polyurethane binder like HTPB is the ease with which its mechanical properties can be manipulated by varying the relative amounts of its constituents. Mechanical properties like Young's modulus, tensile strength, % elongation at break, loss tangent, storage and loss moduli can be altered in a controlled fashion by changing the type of

polyols or di-isocyanates and their relative fractions. Such behavior has been studied in detail by Jain et al. (1993), Desai et al. (2000), Sekkar et al. (2000) and Wingborg (2002) . Such a tuning capability makes HTPB an attractive choice as a binder. Wingborg (2002) shows that tensile strength of curable polyurethanes can be increased by use of symmetrical and rigid di-isocyanates in the hard-segments. It is demonstrated by Sekkar et al. (2000) that increasing the R-ratio (ratio of equivalent weights of -NCO and -OH groups) in an HTPB/Toluene Di-isocyanate (TDI) polyurethane increases the cross-link density, which further leads to an increase in Young's modulus and tensile strength and a decrease in % elongation at break. Similar results are obtained by Jain et al. (1993) by changing the polyol fraction. The glass transition temperature (T_g), however, is shown to remain unaffected by the R-ratio (Sekkar et al. (2000)). Another important knob for controlling binder stiffness is the amount of plasticizer. Jordan et al. (2016) show that increasing the fraction of plasticizer reduces the mechanical strength and also decreases the glass transition temperature. Change in T_g has implications on the working temperature range of the binder and hence the PBX/rocket propellant. Another property of concern is the pot life of the constituent mixture of a binder, especially from the perspective of sample preparation for propellants. Aliphatic di-isocyanates give a higher pot life than aromatic di-isocyanates and hence, are preferred for casting propellants.

There are only a limited number of studies on characterizing the mechanical behavior of HTPB. Cady et al. (2006) showed an increase in flow stress with increasing strain-rate and decreasing temperature. They also reported an increase in the apparent glass transition temperature, T_g with increasing strain-rate. The drop in flow stress with increasing temperature is also reported by Siviour et al. (2008) at strain rates of ~3000 s^{-1} through Kolsky bar

experiments. Such a drop in the flow stress is drastic around the glass transition temperature, falling from above 100 MPa at -80 ^{0}C to below 10 MPa at -40 ^{0}C. However, under shock loading, Meziere et al. (2004) and Millett et al. (2004) report that no changes occur in the T_g, decomposition temperature or crosslink density, as indicated by the Hugoniot measurements. It should be noted that these studies used different compositions of HTPB. Different compositions can result in very different mechanical behavior and hence varied results. Jordan et al. (2016) demonstrate such a variation in high strain-rate and shock properties of different compositions of HTPB. It is shown that increasing the plasticizer content reduces the strength, T_g and shock velocity in HTPB since an increased amount of plasticizer helps with a smoother movement of polymer chains.

While the normal response of the elastomeric binder is important and has been measured under uniaxial stress and uniaxial strain loading, it is crucial to characterize its shear strength. None of the prior studies have measured the shear strength of HTPB under high pressures and high shearing rates. Such measurements are critical for accurate modeling of the constitutive response of HTPB as well as prediction of localization and failure phenomena in PBXs. Shear strength measurements have been made for other polymers. For example, Clifton and Jiao (2015) report a comprehensive experimental study of polyurea, using PSPI experiments to determine its shear strength under a range of pressures and shear strain rates. It is shown that the shear strength of polyurea is highly pressure dependent and increases almost linearly with applied normal stress for normal stresses beyond ~3 GPa. Experimental measurements on polyurea further emphasize the importance of measuring shear behavior at high pressures. Apart from the PSPI experiments, shear strength has been measured for various polymers in normal

impact experiments through normal and lateral stress measurements. While most of the polymers like PMMA (Millett and Bourne (2000)), Estane, Kel-F-800 (Bourne and Gray III (2005)) and epoxy resin (Millett et al. (2002)) show an increasing shear strength with increasing normal stress, there exist deviations from this behavior as well. For example, polychloroprene exhibits an elastic-perfectly plastic behavior above a normal stress of 1 GPa. These lateral stress measurements also help identify the Hugoniot Elastic Limit (HEL) of the material. The present study uses one-dimensional plane wave pressure-shear plate impact (PSPI) experiments to measure the shearing resistance of HTPB under different pressures. To the best of our knowledge, these are the first measurements of the dynamic shear strength of HTPB.

There has also been a limited effort on constitutive model development of binder elastomers in polymer-bonded systems. Most of the studies use a strain-rate and temperature dependent linear viscoelastic formulation. For example, Barua and Zhou (2011) employ a generalized Maxwell model approach through a Prony series to model the viscoelastic relaxation of shear response while the volumetric response is modeled through a constant bulk modulus. The time and temperature dependence of the shear moduli are usually accounted for through the time-temperature superposition principle, with the assumption of a thermo-rheologically simple material. Similar modeling efforts employing the Prony series approach have been made byMas et al. (2002), Wang et al. (2016) and Hu et al. (2017) . However, such an approach is adequate for small to moderate strain ranges where linear viscoelasticity holds. For applications of interest where large normal and shear deformations are expected, non-linear hyperelasticity-based formulations are more effective. Many of these finite deformation viscoelastic and viscoplastic models are based on a Kroner-type decomposition of deformation gradient into elastic and

viscous/plastic parts, i.e. $\boldsymbol{F} = \boldsymbol{F^e F^v}$ and involve complicated formulations of the stress tensor (Bergström and Boyce (1998), Cho et al. (2013)). Most of such models also involve a large number of material parameters, which are difficult to determine especially in high strain-rate and high-pressure regimes due to the lack of experimental data. Another major drawback of these models is their inability to adequately capture the pressure-dependence of shear response of elastomers under dynamic loading conditions. It is shown, in this study, and for polyurea by Clifton and Jiao (2015) , that the Lagrangian shear wave speeds in an elastomer are highly pressure-dependent. The shear strength of polymers as discussed above, is also a strong function of pressure. To incorporate such a dependence of shear wave speed and shear strength on pressure, Clifton and Jiao (2015) propose a multiplicative decomposition of free energy density into dilatational and distortional terms. A quasi-linear viscoelastic framework is developed to relax the instantaneous pressure and deviatoric stresses separately. In the present work, such a quasi-linear viscoelastic formulation is used in order to capture the measured pressure-dependence of the shear strength of HTPB.

2.2 Specimen Preparation

The binder material of interest in this investigation consists of the following components: (a) HTPB prepolymer, (b) a plasticizer, (c) an anti-oxidant, (d) a curing agent, and (e) a catalyst, mixed in specific proportions to achieve a desired binder stiffness. Each component plays an integral role in the resulting properties of the binder and the polymer-bonded composite. The plasticizer reduces the stiffness of the binder and provides rubbery character to the binder/energetic crystal composite. The plasticizer also reduces viscosity for ease of casting

and enables higher loading (i.e. fraction) of solid components in the composite. An antioxidant inhibits the oxidation of the binder which results in higher cross-linking and hence a stiffer binder. The catalyst determines the curing time, reducing it from days to hours. Some of the other components used in a binder are wetting agents and cross-linkers. These components are excluded from the present study. Note that addition of these components will likely alter the mechanical properties of the binder to some extent; however, no loss of generality of the experimental measurements is expected from their inclusion.

As noted by Millett et al. (2004) and Jordan et al. (2016) , it is important to specify the composition of the individual components used in preparing the polymeric binder for a useful comparison of mechanical behavior with other studies. The composition of the HTPB binder studied here is shown in Table 2.1. The weight fractions are based on the work by Williams et al. (2013) . However, unlike Williams et al. (2013) , no bonding agent is used. The composition is very similar to that employed in PBXN-110 (88% HMX and 12% HTPB by weight) as reported by Blumenthal et al. (2002), Cady et al. (2006) . HTPB resin from CrayValley (a brand of Total Petrochemicals) with the commercial name, Poly bd® R-45HTLO, is used in this study. More information on the specifications of the product can be found in Appendix A. The rest of the binder components are bought from Sigma Aldrich. The stiffness of the binder can be changed easily by changing the relative fractions of the plasticizer Jordan et al. (2016) or curing agent or both. The resulting elastomeric binder is a block co-polymer with hard and soft domains (see Figure 2.1). The isocyanate (-NCO) on IPDI reacts with the hydroxyl (-OH) group on HTPB to form a urethane (-NHCOO) linkage, which cross-links with other urethanes using hydrogen bonds to form hard domains, as illustrated in Figure 2.1. The urethane linkages form

the hard domains while the long carbon chains of the polyol (HTPB pre-polymer) form the soft domains that give the binder its high elasticity. For a given amount of plasticizer, the NCO:OH ratio determines the stiffness of the resulting polymer; higher the ratio, stiffer the polymer Haska et al. (1997), Sekkar et al. (2000) . An NCO:OH ratio of 1.05 is used in the present study.

Table 2.1 Composition of the HTPB binder used in the present study

Component	Chemical used	% by weight
Pre-polymer	Hydroxyl-terminated polybutadiene (HTPB)	47.380
Plasticizer	Dioctyl adipate (DOA)	47.300
Antioxidant	2,2'-methylene-bis-(4-methyl-tert-butylphenol (AO-2246)	0.635
Catalyst	Dibutyltin dilaurate (DBTDL)	0.095
Curing Agent	Isophorone diisocyanate (IPDI)	4.632

For preparing a thin layer of the HTPB binder for the plate impact experiments, the components listed in Table 2.1 are mixed and degassed for 10 minutes. Since extremely small amounts of some components are involved, larger quantities of the mixture (usually more than 60 grams) are prepared for consistency of experimental results. The front target plate, binder and rear target plate sandwich is prepared inside a vacuum chamber. Specimen thickness is controlled using shims. The sandwich is cured on a hot-plate at 60 ^{0}C for 12-16 hours, until a Shore A hardness in the range of 3-5 is obtained. See Appendix A for a detailed description of the steps involved in sample preparation and the chemical reactions involved in the curing process. Since there is range of Shore A hardness that is chosen and due to the inherent stochasticity involved in sample fabrication, a mild variation in normal and shear response of HTPB is expected across different experiments.

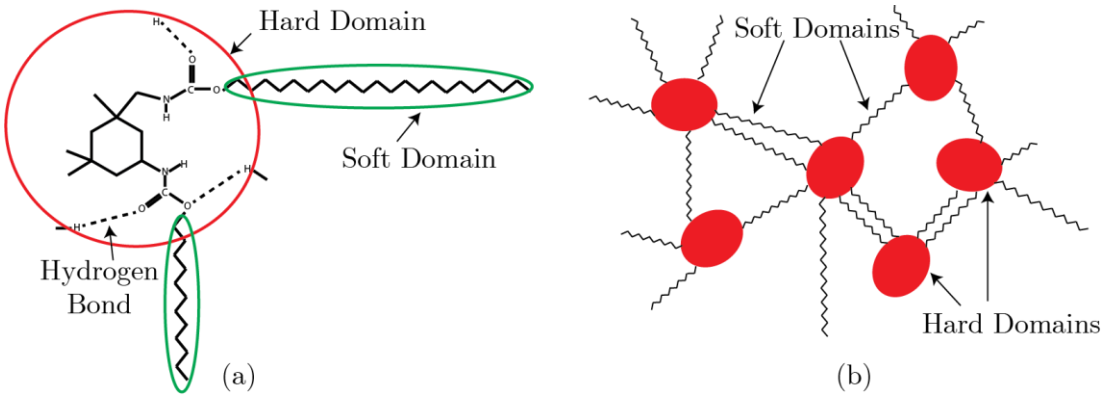

Figure 2.1 (a): Hard and soft domains of the elastomeric binder (a polyurethane); secondary hydrogen bonds enable cross-linking rather than the typically encountered covalent bonds. (b): Visualization of hard (red ellipses) and soft domains (zig-zag lines)

2.3 Experimental Results

A summary of the four shots conducted on HTPB is given in Table 2.2. Note that three different types of anvil materials are used: (a) WC504, (b) WC and (c) D2 Steel (heat treated to 62 HRC). WC504 is a commercial grade of tungsten carbide (obtained from Valenite) cemented with a cobalt binder. WC, procured from Basic Carbide Corporation, Lowber, PA has a lower percentage of the cobalt binder (~3%) and is hence, stiffer than WC504. Material properties of each of the anvil materials are presented in Table 2.3. While WC504 and WC are used for attaining higher normal stresses, D2 Steel is used for tests at lower normal stresses due to its lower yield strength. Impact velocities for each of the material are selected so that the normal stress is lower than the Hugoniot Elastic Limit (HEL) for the anvil material, except for WC. HEL for WC lies around 7 GPa, as shown by Kettenbeil et al. (2020) using symmetric PSPI experiments. Maximum normal stress attained using WC anvil plates is ~9 GPa (Table 2.2). Since the HEL of WC is very close to the maximum longitudinal stress imparted on the anvil plates, the deviation from elastic behavior for the range of normal stresses considered here is

minimal and an elastic wave characteristic analysis is therefore employed to obtain stresses in the sample from rear surface velocity measurements, as described in Chapter 1. In an ideal case, the constitutive response of the anvil material needs to be characterized beyond the elastic limit and an inverse analysis used to infer velocities and stresses at the sample/rear target plate interface from the experimentally measured free surface velocities at the rear target plate. Such an inverse analysis has been carried out by Clifton and Song (2019) .

Table 2.2 Summary of PSPI shots on HTPB

Shot No.	Target Material	h_S (μm)	h_F (mm)	h_{FT} (mm)	h_{RT} (mm)	Shore - A	θ	V_0 (m/s)	Tilt (mrad)	σ_{max} (GPa)	τ_{max} (GPa)	$\dot{\gamma}$ (s^{-1})
PM1601	WC504	237.6	4.065	4.039	4.045	4-5	0^0	191.7	3	9.1	NA	NA
PM1602	WC	108	6.417	2.929	5.856	4-5	18^0	175	0.4	8.84	470	$0.38x10^6$
PM1806	WC	130	6.432	2.886	5.967	3-4	18^0	126.75	2.43	6.32	360	$0.24x10^6$
PM1805	D2 Steel	145	6.902	2.946	6.388	5-6	18^0	132.48	1.03	2.84	120	$0.23x10^6$

h_S: sample thickness h_F: flyer thickness, h_{FT}: front target plate thickness, h_{RT}: rear target plate thickness, θ: angle of impact, V_0: impact velocity, σ_{max}: peak normal stress, τ_{max}: peak shear stress, $\dot{\gamma}$: average shear strain-rate

Table 2.3 Elastic material properties of different anvil materials used in PSPI shots

Material	WC 504	WC	D2 Steel
Density (g/cm^3)	13.800	15.400	7.787
Poisson's Ratio	0.22	0.2	0.29
Young's Modulus (GPa)	575	650	210
Longitudinal Wave Speed (mm/μs)	6.897	6.848	5.945
Shear Wave Speed (m/s)	4.132	4.193	3.233

Normal and transverse velocity profiles for the experiments are plotted in Figure 2.2 and Figure 2.3 respectively. The corresponding normal and shear stress profiles are plotted in Figure 2.4 and Figure 2.5 respectively. Note that in all the plots in this chapter, the velocity and stress profiles have been shifted in time and the beginning of a normal or transverse velocity/stress

profile does not indicate the time of arrival of longitudinal/shear wave. Since the acoustic impedance of HTPB is much lower than that of the target plates, normal stress profiles show distinct steps early-on as the normal velocity rings-up to the peak value. The steps in the normal velocity profiles are used to obtain normal stress-dependent Lagrangian longitudinal wave speeds in HTPB. The height of each step indicates the stress level while the step width indicates the transit time. Therefore, the Lagrangian wave speed is given as $2h_0/t$, where h_0 is the initial specimen thickness and t is the transit time.

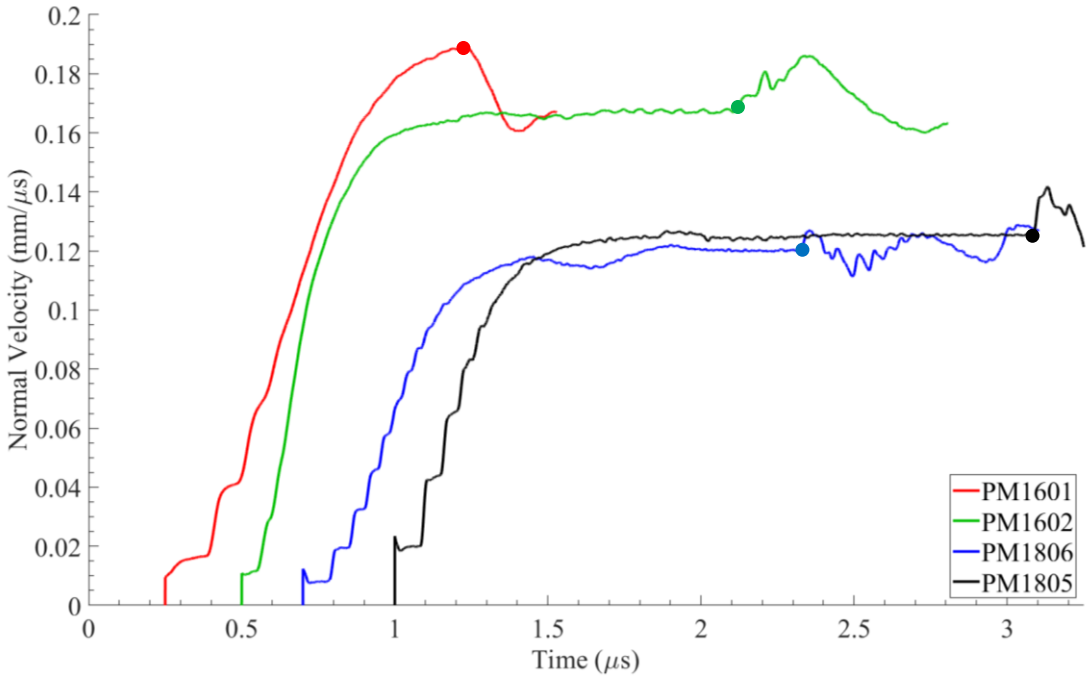

Figure 2.2 Normal velocity profiles for PSPI shots on HTPB. The arrival of the unloading wave at the sample/rear-plate interface is marked with dots

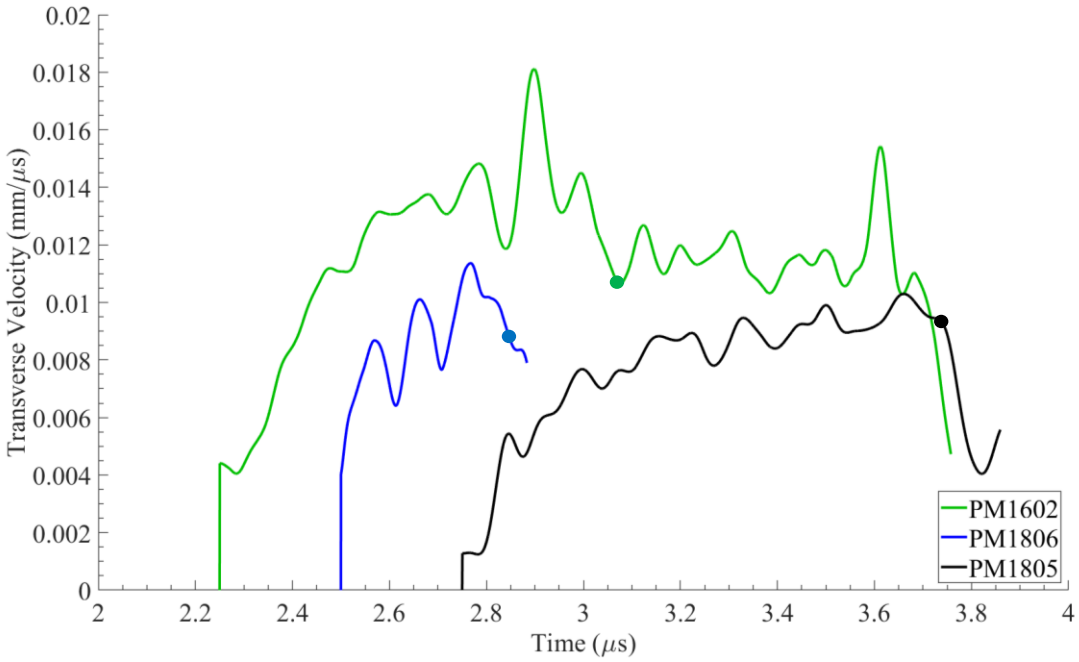

Figure 2.3 Transverse velocity profiles for PSPI shots on HTPB. The arrival of the unloading wave is marked with dots.

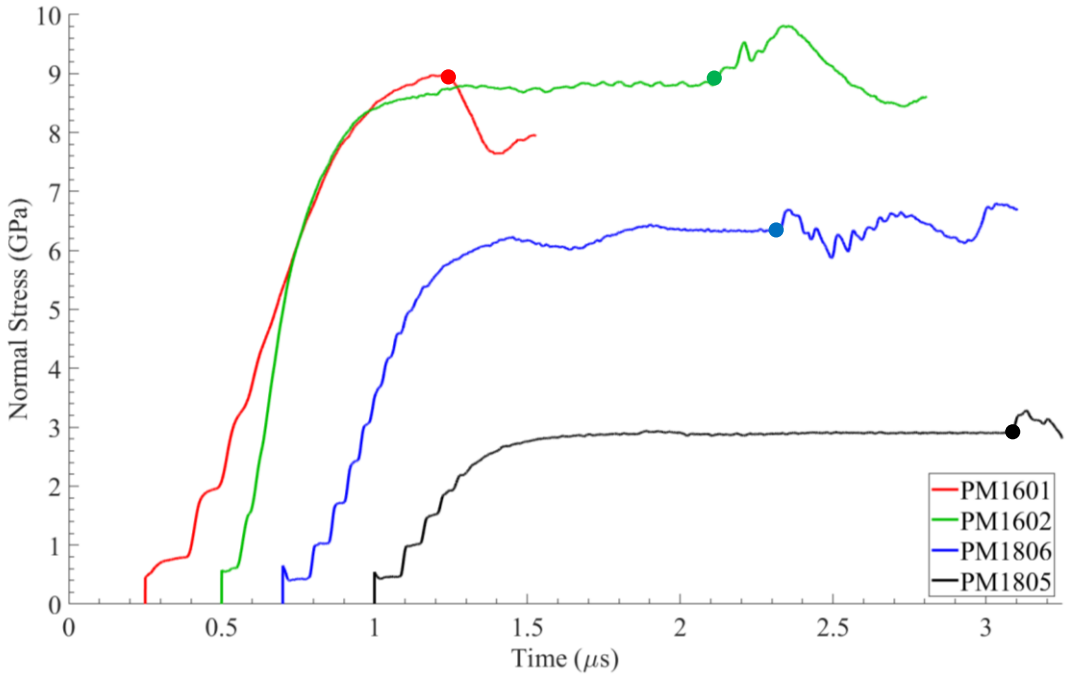

Figure 2.4 Normal stress profiles for PSPI shots on HTPB. The arrival of the unloading wave is marked with dots

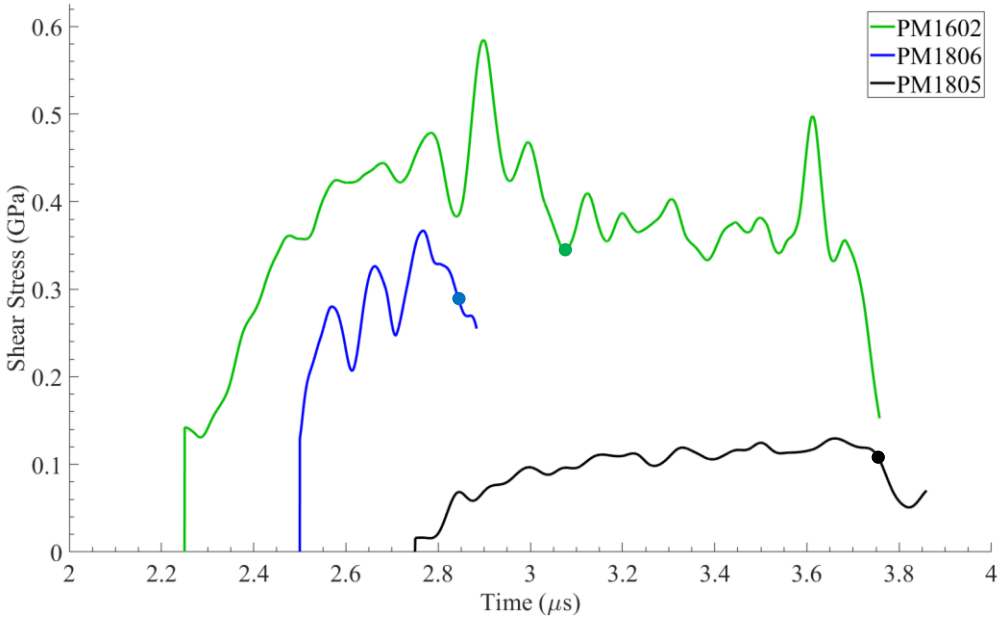

Figure 2.5 Shear stress profiles for PSPI shots on HTPB. The arrival of the unloading wave is marked by with dots

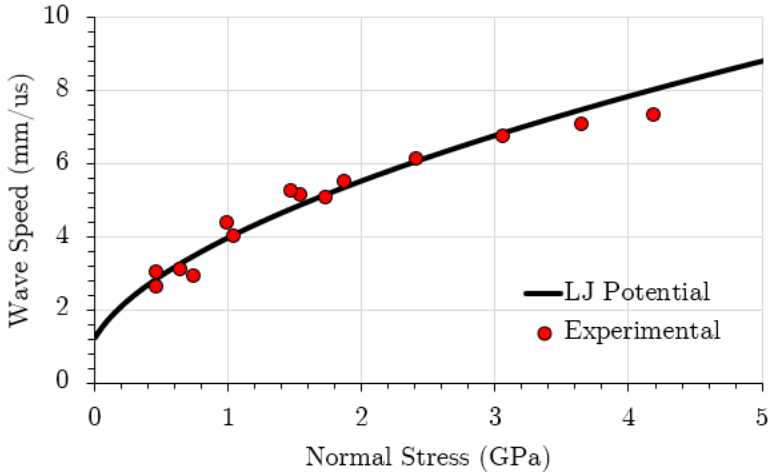

Figure 2.6 Lagrangian longitudinal wave speeds in HTPB as a function of normal stress. A Lennard Jones (LJ) potential is fit to the experimental wave speeds ($A = 0.4\ GPa, M = 6, N = 3$)

In Figure 2.6, the longitudinal wave speeds are plotted as a function of the normal stress. It can be observed that there is a pronounced stress-dependence of longitudinal wave velocity.

Also note that due to a small uncertainty associated with the weight ratios of some of the components of the binder mixture, some variation in specimen stiffness is expected across different shots. This results in some variability in the longitudinal wave speeds depicted in Figure 2.6.

During the ring-up process, the longitudinal wave can be regarded as a weak shock reverberating through the sample. Since the change in entropy across a weak shock wave is proportional only to pressure cubed (Davison et al. (2008)), the ring-up process can be considered as quasi-isentropic. The quasi-isentrope can be found by integrating the following stress-strain relation:

$$d\sigma = \rho_0 c^2(\sigma) d\epsilon \tag{2.1}$$

where σ is the normal stress, ρ_0 is the initial density, ϵ is the normal strain and $c(\sigma)$ is the Lagrangian wave speed as a function of normal stress. An equation of state with a form similar to Lennard-Jones potential has been proposed for block co-polymers by Porter (1995) , based on the concept of group interaction modeling of polymers. Pressure, P is related to the volume ratio $(J=v/v_0)$ through the following expression:

$$P = -A(J^{-N-1} - J^{-M-1}) \tag{2.2}$$

where $M = 6$, $N = 3$ and A is a constant chosen to fit the experimental longitudinal wave speed data, as shown in Figure 2.6. The quasi-isentrope for HTPB is plotted for $A = 0.4$ GPa in Figure 2.7. Note that the values of these constants obtained from such a fit of wave speeds using the Lennard-Jones potential are only preliminary and serve as a good starting point to fit experimental velocity profiles using the constitutive model described in the next section. It can

be observed from Figure 2.7 that large compressive strains, of the order of 0.4, are expected under a normal stress of about 10 GPa.

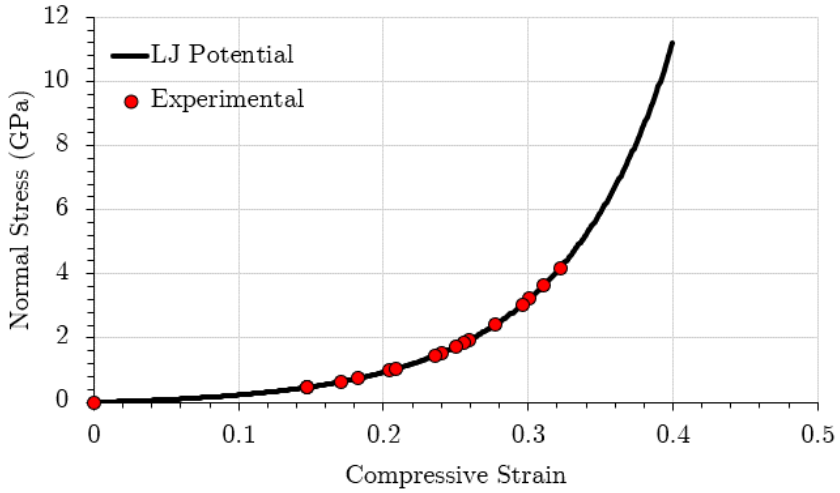

Figure 2.7 Quasi-isentrope of HTPB based on Lennard-Jones (LJ) potential

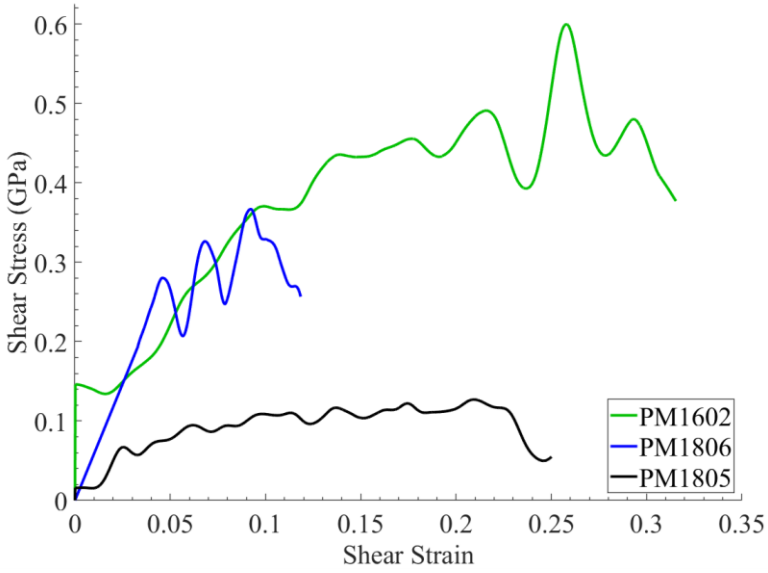

Figure 2.8 Dynamic shear stress vs shear strain plots for HTPB at a nominally similar shear strain rate of $2 \times 10^5 - 4 \times 10^5\ s^{-1}$and three different normal stresses: 2.84 GPa for PM1805, 6.32 GPa for PM1806 and 8.84 GPa for PM1602. The profiles are drawn for times before the arrival of unloading waves.

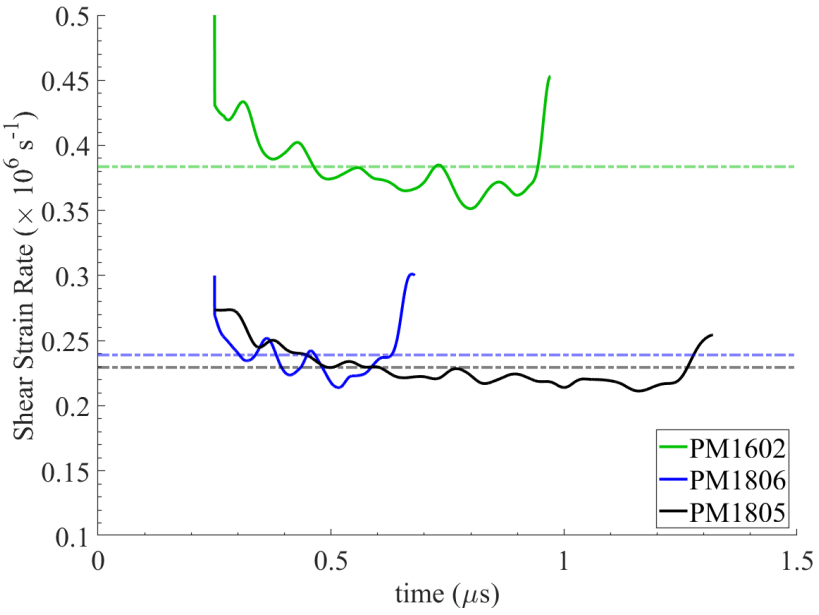

Figure 2.9 Shear strain-rate vs time plots for different PSPI shots on HTPB. The mean shear strain-rate values for each shot are indicated by the light-colored dotted lines

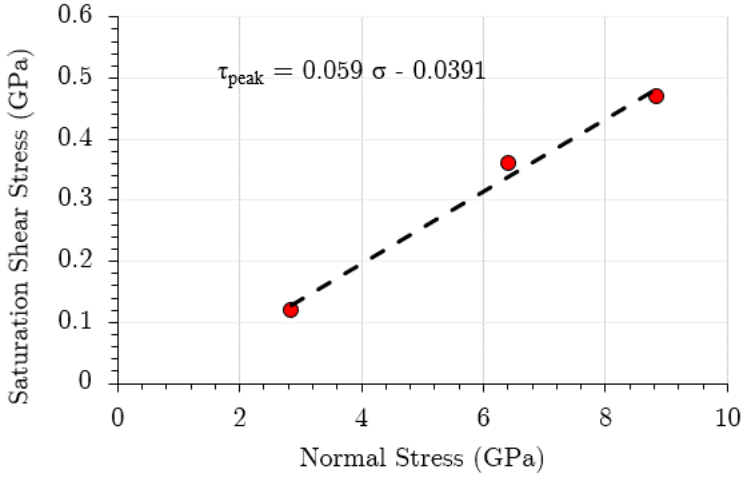

Figure 2.10 Saturation shear strength of HTPB as a function of normal stress, at a nominally similar shear strain rate of $2 - 4 \times 10^5\ s^{-1}$. The dashed line indicates a linear fit to the experimental data. The equation to the linear fit is displayed on the top left.

Figure 2.8 shows the dynamic shear stress vs shear strain curve of HTPB plotted at a nominally constant shear strain rate of $\sim 2 \times 10^5 - 4 \times 10^5\ s^{-1}$ (the shear strain-rates and their

mean values are plotted in Figure 2.9) and three different normal stresses. The shear stress is found to saturate to a steady value after the start of shearing deformation. The shear strength of HTPB is 120 MPa at a normal stress of 2.84 GPa and reaches as high as 470 MPa at a normal stress of 8.84 GPa. The saturation shear strength versus normal stress is plotted in Figure 2.10 and a linear fit through the experimental data indicates that the shearing resistance increases by approximately 59 MPa for every 1 GPa increase in normal stress. For comparison, shear strength behavior as a function of normal stress is compared for several polymers in Figure 2.11. It is evident that the shear strength of polyurea at various normal stresses closely resemble that of HTPB, suggesting polyurea as another potential candidate for a binder if similar shear strength properties are desired. Estane is another common binder and shows shear strength values very close to those of HTPB. Teflon and PMMA, on the other hand, show higher values for shear strength compared to those measured for HTPB. Shear strength of PMMA increases steeply with normal stress as compared to the rest of the polymers considered.

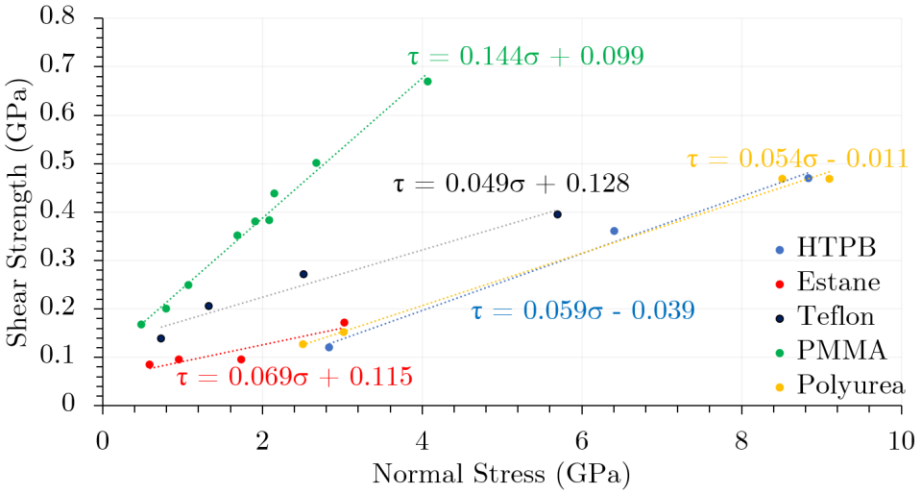

Figure 2.11 Shear Strength of various polymers as a function of normal stress. HTPB: Present work, Estane and Teflon: Bourne and Gray III (2005) , PMMA: Millett and Bourne (2000) and Polyurea: Clifton and Jiao (2015) . Linear equations have been fit to the experimental data

2.4 Constitutive Modeling

In this section, a quasi-linear viscoelastic model for an isotropic elastomeric binder is described. The model is based on the description by Clifton and Jiao (2015) .

2.4.1 Finite Deformation Kinematics for PSPI

As discussed in Chapter 1, the wave propagation is assumed to be in the X_1-direction while shearing deformation takes place in the X_2-direction, where X_1 and X_2 are coordinates in the undeformed configuration. The coordinates in the deformed configuration can be written as:

$$\begin{aligned} x_1 &= \lambda(t)X_1 \\ x_2 &= X_2 - \kappa(t)X_1 \\ x_3 &= X_3 \end{aligned} \tag{2.3}$$

where (x_1, x_2, x_3) are deformed configuration coordinates of point (X_1, X_2, X_3) at time t. $\lambda(t)$ and $\kappa(t)$ represent stretch and shear respectively. The deformation gradient can therefore be written as:

$$\boldsymbol{F} = \boldsymbol{\nabla x} = \begin{bmatrix} \lambda(t) & 0 & 0 \\ -\kappa(t) & 1 & 0 \\ 0 & 0 & 1 \end{bmatrix} \tag{2.4}$$

where the gradient, $\boldsymbol{\nabla}$ is taken with respect to the undeformed coordinates, $\boldsymbol{X}$. The Green-Lagrange strain tensor is then defined as:

$$\boldsymbol{E} \equiv \frac{\boldsymbol{F^T F - I}}{2} = \frac{1}{2}\begin{bmatrix} \lambda^2 + \kappa^2 - 1 & -\kappa & 0 \\ -\kappa & 0 & 0 \\ 0 & 0 & 0 \end{bmatrix} \tag{2.5}$$

2.4.2 Instantaneous Elastic Response

The instantaneous elastic response of an isotropic hyper-elastic material is specified through a strain energy density function, W as a function of the invariants (I_1, I_2, I_3) or equivalently, $(\bar{I_1}, \bar{I_2}, J)$ of the left Cauchy-Green tensor, $\boldsymbol{B} \equiv \boldsymbol{F}\boldsymbol{F}^T$. The invariants are defined as:

$$
\begin{aligned}
I_1 &\equiv tr(\boldsymbol{B}) = \lambda^2 + \kappa^2 + 2 \\
I_2 &\equiv \frac{1}{2}\left[\left(tr(\boldsymbol{B})\right)^2 - tr(\boldsymbol{B}^2)\right] = 2\lambda^2 + \kappa^2 + 1 \\
I_3 &\equiv J^2 = \det(\boldsymbol{B}) = \lambda^2
\end{aligned}
\tag{2.6}
$$

$$
\begin{aligned}
\bar{I_1} &\equiv J^{-\frac{2}{3}} I_1 = \lambda^{\frac{4}{3}} + \lambda^{-\frac{2}{3}}\kappa^2 + 2\lambda^{-\frac{2}{3}} \\
I_2 &\equiv J^{-\frac{4}{3}} I_2 = 2\lambda^{\frac{2}{3}} + \lambda^{-\frac{4}{3}}\kappa^2 + \lambda^{-\frac{4}{3}} \\
J &\equiv \det(\boldsymbol{F}) = \lambda
\end{aligned}
\tag{2.7}
$$

J represents ratio of current volume to initial volume and encompasses the volumetric behavior completely. $\bar{I_1}$ and $\bar{I_2}$ have constant values of 3 under dilatational deformation. Therefore, $(\bar{I_1} - 3, \bar{I_2} - 3)$ completely represent distortional deformation while $(J - 1)$ represents volume change. Using these invariants allows the separation of free energy density into volumetric and distortional terms.

A typically used form of free energy density is a generalized Mooney-Rivlin model Mooney (1940), Rivlin and Saunders (1997) :

$$
\bar{\psi}(\bar{I_1}, \bar{I_2}, J) = \sum_{i=j=0}^{N} C_{ij} (\bar{I_1} - 3)^i (\bar{I_2} - 3)^j + \sum_{p=1}^{P} D_p (J - 1)^{2p} \tag{2.8}
$$

where the first term corresponds to the distortional response and the second term describes the volumetric response. However, the above additive decomposition fails to capture the pressure-

dependence of longitudinal and shear wave speeds. In order to adequately capture the pressure-dependence, the following multiplicative decomposition of free energy density is proposed:

$$\bar{\psi}(\bar{I}_1, \bar{I}_2, J) = f(J)\, \hat{\psi}(\bar{I}_1, \bar{I}_2) \tag{2.9}$$

where $\hat{\psi}(\bar{I}_1, \bar{I}_2)$ is the distortional free energy and $f(J)$ is a pre-factor based on the modified Lennard-Jones potential suggested by Porter Jordan et al. (2016) such that $f(1) = 1$ and $N = M/2$:

$$f(J) = (J^{-M} - 2J^{-N}) + 2 \tag{2.10}$$

The first term of the generalized Mooney-Rivlin model in equation (2.8) is chosen to represent the distortional strain energy, $\hat{\psi}(\bar{I}_1, \bar{I}_2)$:

$$\hat{\psi}(\bar{I}_1, \bar{I}_2) = C_{00} + [C_{10}(\bar{I}_1 - 3) + C_{01}(\bar{I}_2 - 3)] \tag{2.11}$$

Since the symmetric 2nd Piola-Kirchhoff (P-K) stress is the energy conjugate of Green strain, the 2nd P-K stress can be written as a derivative of free energy density with respect to the Green strain.

$$\boldsymbol{\tau} = \frac{d\bar{\psi}(\bar{I}_1, \bar{I}_2, J)}{d\boldsymbol{E}} = \frac{\partial \bar{\psi}}{\partial \bar{I}_1}\frac{\partial \bar{I}_1}{\partial \boldsymbol{E}} + \frac{\partial \bar{\psi}}{\partial \bar{I}_2}\frac{\partial \bar{I}_2}{\partial \boldsymbol{E}} + \frac{\partial \bar{\psi}}{\partial J}\frac{\partial J}{\partial \boldsymbol{E}} \tag{2.12}$$

The derivatives of the invariants with respect to the Green strain tensor can be found to be

$$\begin{aligned} \frac{\partial \bar{I}_1}{\partial \boldsymbol{E}} &= -\frac{2}{3}\bar{I}_1 \boldsymbol{C^{-1}} + 2J^{-2/3}\boldsymbol{I} \\ \frac{\partial \bar{I}_2}{\partial \boldsymbol{E}} &= 2\bar{I}_1 J^{-2/3}\boldsymbol{I} - 2J^{-\frac{4}{3}}\boldsymbol{C} - \frac{4\bar{I}_2}{3}\boldsymbol{C^{-1}} \\ \frac{\partial J}{\partial \boldsymbol{E}} &= J\boldsymbol{C^{-1}} \end{aligned} \tag{2.13}$$

where $\boldsymbol{C} = \boldsymbol{F}^T\boldsymbol{F}$ is the right Cauchy-Green tensor. Thus, substituting the relations in equation (2.13) into equation (2.12) gives a general expression for the 2nd P-K stress for any free energy density function. The Cauchy stress, $\boldsymbol{T}$ can then be written as:

$$\boldsymbol{T} \equiv \frac{1}{J}(\boldsymbol{F}\boldsymbol{\tau}\,\boldsymbol{F}^T) = \frac{2}{J^{5/3}}\left(\frac{\partial\bar{\psi}}{\partial\bar{I}_1} + \bar{I}_1\frac{\partial\bar{\psi}}{\partial\bar{I}_2}\right)\boldsymbol{B} - \left(\frac{2}{J^{\frac{7}{3}}}\frac{\partial\bar{\psi}}{\partial\bar{I}_2}\right)\boldsymbol{B}^2 + \frac{1}{J}\left(-\frac{2}{3}\bar{I}_1\frac{\partial\bar{\psi}}{\partial\bar{I}_1} - \frac{4\bar{I}_2}{3}\frac{\partial\bar{\psi}}{\partial\bar{I}_2} + J\frac{\partial\bar{\psi}}{\partial J}\right)\boldsymbol{I} \tag{2.14}$$

A simplified form for the Cauchy stress can be obtained for PSPI, as shown in Appendix B.

2.4.3 Quasi-Linear Viscoelasticity

The instantaneous elastic stress response of the elastomeric binder to a steep change in strain is expected to relax to a lower state of stress. Consider a simple one-dimensional relaxation model based on work by Pipkin and Rogers (1968) and Fung (1972) , where the relaxed stress, $\bar{\sigma}(t)$ is related to the instantaneous elastic response, $\sigma^e(t)$ through a reduced relaxation function, $R(t)$:

$$\bar{\sigma}(t) = \sigma^e(t) + \int_0^t \sigma^e(t-t')\,\frac{dR(t')}{dt'}\,dt' \tag{2.15}$$

where the sample is loaded from $t' = 0$ to $t' = t$. For the Kelvin representation of a standard linear solid, the reduced relaxation function, $R(t)$ has the following form:

$$R(t) \equiv \frac{E(t)}{E(0)} = \frac{1 + S_0 e^{-t/t_R}}{1 + S_0} \tag{2.16}$$

where $E(t)$ is the relaxation function at time t, t_R is the relaxation time and the constant $S_0 = \frac{E_0}{E_\infty} - 1$. E_0 is referred to as the short-time glassy modulus and E_∞ is referred to as the long-time rubbery modulus. Instead of having one relaxation time, t_R, we assume a continuous distribution of relaxation times and replace S_0 with a distribution, $S(t')$. $S(t')$ is a weighting function for relaxation times between $(t', t' + dt')$. The reduced relaxation function can then be expressed as:

$$R(t) = \frac{1 + \int_0^\infty S(t')e^{-\frac{t}{t'}}dt'}{1 + \int_0^\infty S(t')dt'} \tag{2.17}$$

For the case of $S(t') = \delta(t' - t_R)$, the standard linear solid case (equation (2.16)) can be recovered. The following form for the continuous spectrum of relaxation times has been used by Fung (2013) and Becker and Foppl (1928) .:

$$S(t_R) = \begin{cases} \frac{c}{t_R} & t_1 < t_R < t_2 \\ 0 & otherwise \end{cases} \tag{2.18}$$

where c is a constant and t_1, t_2 are lower and upper limits on the relaxation times considered. Hence, there is no relaxation for $t_R < t_1$ or $t_R > t_2$. Such a choice can be justified on the basis that for relaxation times below t_1, the response is instantaneous elastic and relaxation times above t_2 are insignificant for the dynamic loading under PSPI. In this distribution, the shorter time scales are weighed heavier than the larger time scales, as investigated in detail by Neubert (1963) . Cut-offs (t_1 and t_2) are placed keeping in mind the application of interest. Combining equations (2.17) and (2.18), the reduced relaxation function is given as:

$$R(t) = \begin{cases} 1 & t = 0 \\ \dfrac{1 + c\left[E_1\left(\frac{t}{t_2}\right) - E_1\left(\frac{t}{t_1}\right)\right]}{1 + c\ ln\left(\frac{t_2}{t_1}\right)} & t \geq 0 \end{cases} \tag{2.19}$$

where $E_1(z) = \int_z^\infty \frac{e^{-t}}{t} dt$ is the exponential integral function. Therefore, in the above formulation, the constants (c, t_1, t_2) characterize the relaxation response. The effect of each of these constants is explored in Appendix C. The derivative of relaxation function needs to be substituted into equation (2.15) for the relaxed stress response and is calculated as:

$$\frac{dR(t)}{dt} = \left[\frac{c}{1 + c\ ln\left(\frac{t_2}{t_1}\right)}\right]\left(\frac{e^{-t/t_1} - e^{-t/t_2}}{t}\right) \tag{2.20}$$

Relaxation of instantaneous deviatoric stresses and pressure is treated with separate relaxation constants. Using equations (2.15) and (2.20), the deviatoric stress and pressure in an isotropic, quasilinear viscoelastic material are given as:

$$\begin{aligned} s_{ij}(t) &= s_{ij}^{e}(t) + \int_0^t s_{ij}^{e}(t-t')\,\frac{dR_d(t')}{dt'}\,dt' \\ &= s_{ij}^{e}(t) + \frac{c_d}{1+c_d\,ln\left(\frac{t_{d2}}{t_{d1}}\right)}\int_0^t s_{ij}^{e}(t-t')\left(\frac{e^{-t'/t_{d1}}-e^{-t'/t_{d2}}}{t'}\right)dt' \end{aligned} \tag{2.21}$$

$$\begin{aligned} p(t) &= p^{e}(t) + \int_0^t p^{e}(t-t')\,\frac{dR_p(t')}{dt'}\,dt' \\ &= p^{e}(t) + \frac{c_p}{1+c_p\,ln\left(\frac{t_{p2}}{t_{p1}}\right)}\int_0^t p^{e}(t-t')\left(\frac{e^{-t'/t_{p1}}-e^{-t'/t_{p2}}}{t'}\right)dt' \end{aligned} \tag{2.22}$$

where $s_{ij}(t)$ is the deviatoric stress and $p(t)$ is pressure. Subscript d represents deviatoric, subscript p represents pressure and superscript e indicates the instantaneous elastic behavior. A set of 6 constants $(c_d, t_{d1}, t_{d2}, c_p, t_{p1}, t_{p2})$ describes the relaxed response.

2.5 Finite Element Simulations

Finite element simulations are carried out in ABAQUS/Explicit to simulate the behavior of HTPB subject to PSPI loading. 4-noded bilinear plane strain quadrilateral elements with reduced integration and hourglass control (CPE4R) are used. Mesh size and time increment are chosen adequately to satisfy the CFL condition, i.e. the time increment should be smaller than the minimum element size divided by the longitudinal wave speed:

$$\Delta t \leq \min\left(\frac{L_{min}}{c_L}\right) \tag{2.23}$$

For a mesh size of 10 μm and longitudinal wave speeds up to 10,000 m/s, the time-step should be smaller than 1 ns. A time-step of 0.1 ns is used to err on the side of caution. The mesh for simulation of shot PM1601 is shown in Figure 2.12.The quasi-linear viscoelastic model is implemented in a VUMAT, a user-subroutine.

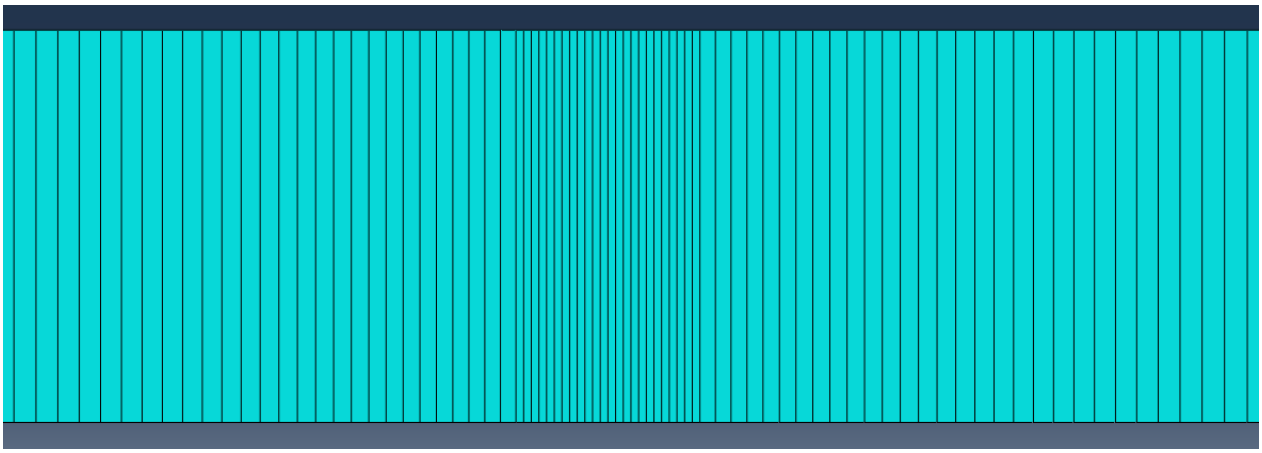

Figure 2.12 Mesh for simulation of shot PM1601. The HTPB sample, shown in the middle, has a mesh size of 10 μm while the target plates on either side have a mesh size increasing linearly from 20 μm (at the sample/target interface) to 75 μm (at the other end)

Table 2.4 Material parameters for quasi-linear viscoelastic model

ν	M	c_1 $(mm/\mu s)$	ρ_0 (kg/m^3)	C_{00} (GPa)	C_{10} (GPa)	C_{01} (GPa)	c_d	t_{d1} (ns)	t_{d2} (μs)	c_p	t_{p1} (ns)	t_{p2} (μs)
0.42	5	1750	1000	0.2	0.106	0.106	2	50	1	0.1	1	2

Table 2.4 lists the materials parameters used for the simulations. c_1 is the elastic longitudinal wave speed at zero pressure and is obtained from the intercept of the longitudinal wave speed versus normal stress plot in Figure 2.6. This value closely matches with the longitudinal wave speed derived from Hugoniot measurements of HTPB by Millett et al. (2004) . The value of M is chosen in such a way that the longitudinal wave speeds can be simulated to

match the experimental results, especially at high pressures. The Poisson's ratio, ν which is a measure of the change in shear strain relative to normal strain, is chosen to best fit the normal and shear velocity profiles obtained through the PSPI experiments. The first four material parameters in Table 2.4 characterize the instantaneous elastic response of HTPB. The parameters (C_{00}, C_{10}, C_{01}) in the Mooney-Rivlin model can be derived from the bulk modulus, K and shear modulus, G through the following relations:

$$K = (M^2 - 2N^2)C_{00} \tag{2.24}$$

$$G = 2(C_{01} + C_{10}) \tag{2.25}$$

where the bulk and shear moduli can be found using (ρ_0, c_1, ν). However, the experimental data are inadequate to determine the difference between C_{10} and C_{01}. So, the two moduli are taken to be the same and equal to $\mu/4$. The viscoelastic relaxation parameters are given in the last 6 columns. (t_{d1}, t_{d2}) and (t_{p1}, t_{p2}) indicate cut-offs on relaxation times for deviatoric stresses and pressure respectively. As shown in Appendix C, it is found that decreasing the cut-off of relaxation times on either end generates a quicker relaxation response and to a lower equilibrium stress state. The extent of relaxation of deviatoric stresses and pressure responses is also controlled by the pre-factors, c_d and c_p respectively. Note that the values for relaxation parameters are based on a limited search through the parameter space. A more comprehensive study based on the minimization of least squared errors can be undertaken for each parameter. Since our aim is to demonstrate the capability of the proposed constitutive model in capturing the viscoelastic behavior of HTPB, we restrict our search for relaxation parameters to a narrow range. It should also be kept in mind that the relaxation constants will vary with specimen composition and hence will require an update if a binder with a composition different than the

one used here is simulated. Even though pressure relaxation is included, the effect of relaxation on deviatoric stresses is much larger than that on pressure, with the relaxed stress values at t_2 for a unit step input to be $R(t_{d2}) = 0.206$ for the deviatoric stresses and $R(t_{d2}) = 0.581$ for pressure.

Figure 2.13 shows a comparison of experimental and simulated normal stress profiles for a constant set of material parameters. It is evident that the simulations can exactly replicate the normal stresses for the 2.84 GPa (PM1805) and 6.32 GPa (PM1806) shots. The agreement for the high-pressure shots (PM1601 and PM1602) is also very good. The slight discrepancy at high pressures can be explained by the fact that the anvil material (WC) reaches its Hugoniot elastic limit around 7 GPa, leading to a slight deviation in the experimental normal stress profile. Similarly, the agreement between the experimental and simulated shear stress profiles, as shown in Figure 2.14 is good. The shear stress values for the low and high-pressure shots (PM1805 and PM1602 respectively) agree very well. However, the simulation predictions for the intermediate shear stress levels fall below the experimentally determined values. Stress-strain behavior under simple shear when HTPB is subject to high pressures is shown in Figure 2.15. It should be noted that determining the exact shear strain from transverse velocity profiles in a sandwich configuration is not possible for the initial times when the shear stress has not yet equilibrated. Higher shearing rates are expected during the shear wave ring-up as compared to the equilibrium shear strain rate.

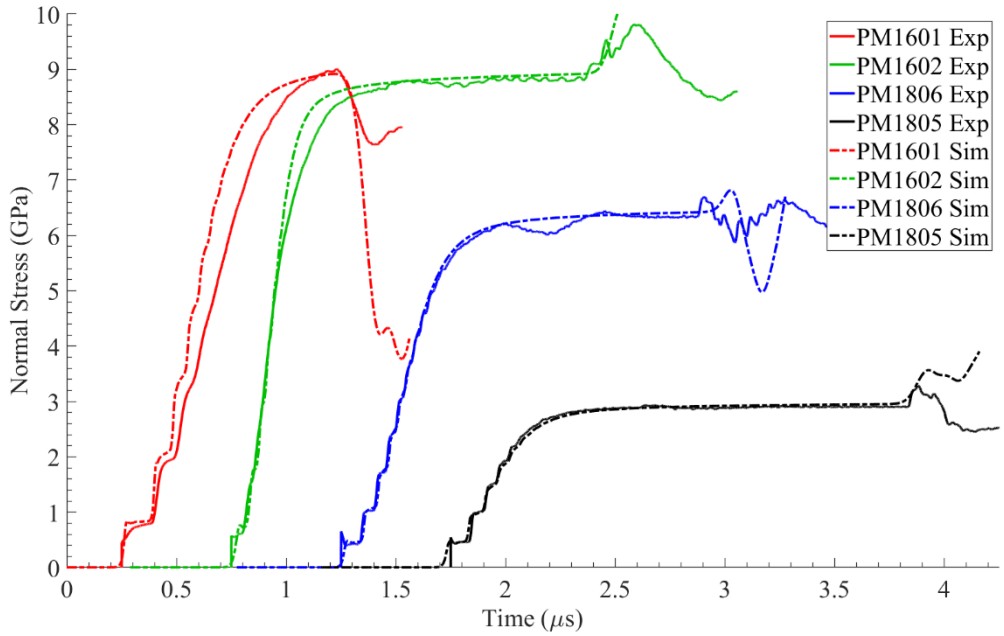

Figure 2.13 Comparison of experimental and simulated normal stress profiles for shots on HTPB

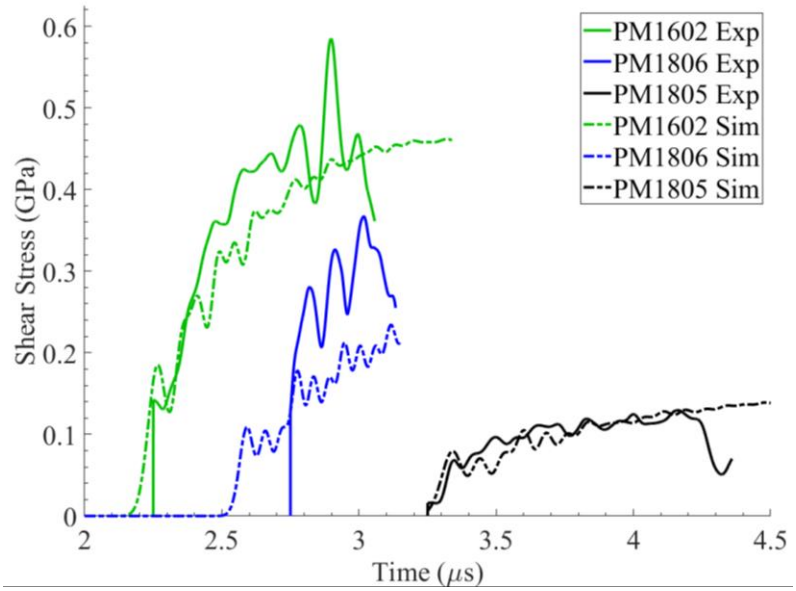

Figure 2.14 Comparison of experimental and simulated shear stress profiles for shots on HTPB

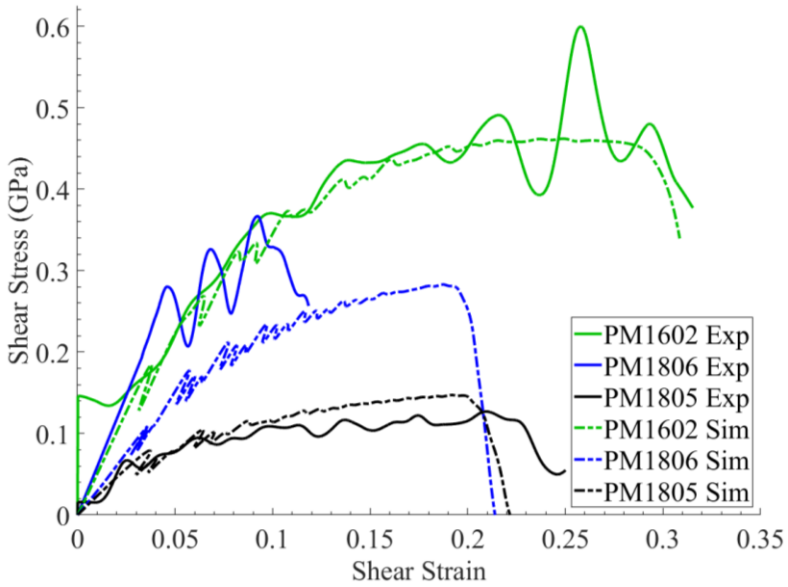

Figure 2.15 Comparison of experimental and simulated shear stress vs shear strain behavior of HTPB under dynamic loading

In Figure 2.16 and Figure 2.17, simulated stress profiles are compared with the experimental results (solid lines) for two cases: (a) Simulations without relaxation, i.e. instantaneous elastic response only (dotted lines), and (b) simulations with relaxation (dashed lines). For the case of normal stress, the instantaneous elastic response predicts higher levels of stress at each step, which is relaxed to match the experimental curves (see Figure 2.16). As mentioned above, simulations of quasi-linear viscoelasticity include a smaller amount of pressure relaxation compared to deviatoric stress relaxation. Since the shear stresses are extremely small when the specimen is loaded by the normal wave only, the effect of relaxation on normal stresses is minimal. Majority of the effect of relaxation can be observed in shear stress profiles in Figure 2.17. It can be observed that the instantaneous elastic response predicts much larger shear stresses than observed experimentally. The simulated shear stresses without relaxation also exhibit large steps which are not seen in experimental profiles. Another caveat of not including

relaxation is that the shear stresses continue to increase and do not show any signs of a plateau for the time scales of interest here. Therefore, a correct simulation of shear stresses under dynamic loading of the binder requires the inclusion of visco-elastic stress relaxation in the material model.

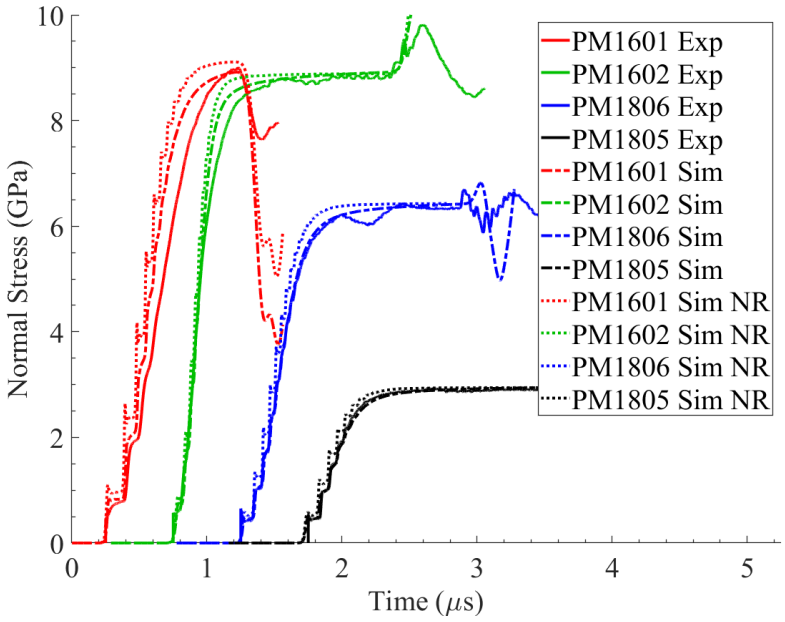

Figure 2.16 Comparison of normal stress profiles obtained from experiments and simulations, with and without relaxation. Relaxation leads to a closer agreement of simulations with experiments. 'NR' implies no relaxation

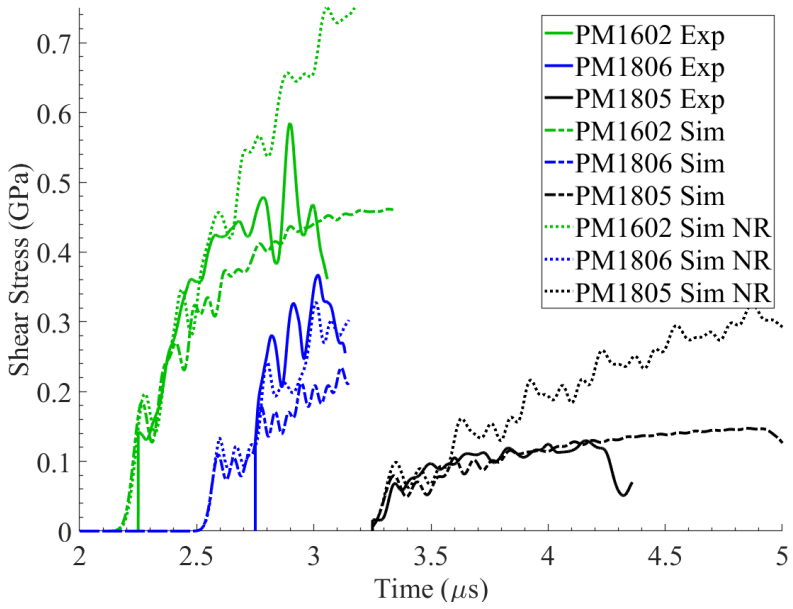

Figure 2.17 Comparison of shear stress profiles obtained from experiments and simulations, with and without relaxation. Simulations without relaxation lead to an always increasing shear stress profile and higher shear stress values than experimentally observed. Relaxation leads to a closer agreement of simulations with experiments. 'NR' implies no relaxation

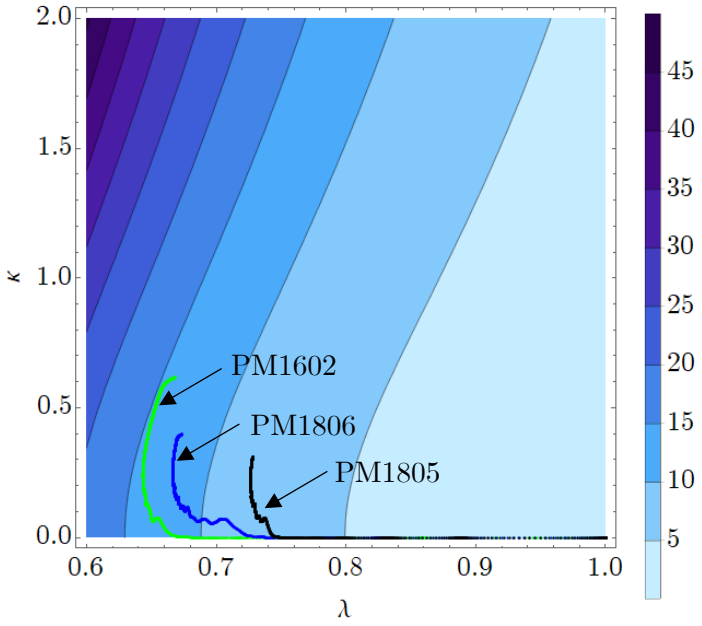

Figure 2.18 Contour plot of fast wave speed (in km/s) as a function of longitudinal compression, λ and shear, κ. Loading contour of simulations of different PSPI shots are also plotted. Note that the smallest value on the colorbar on the right is 1.75 km/s

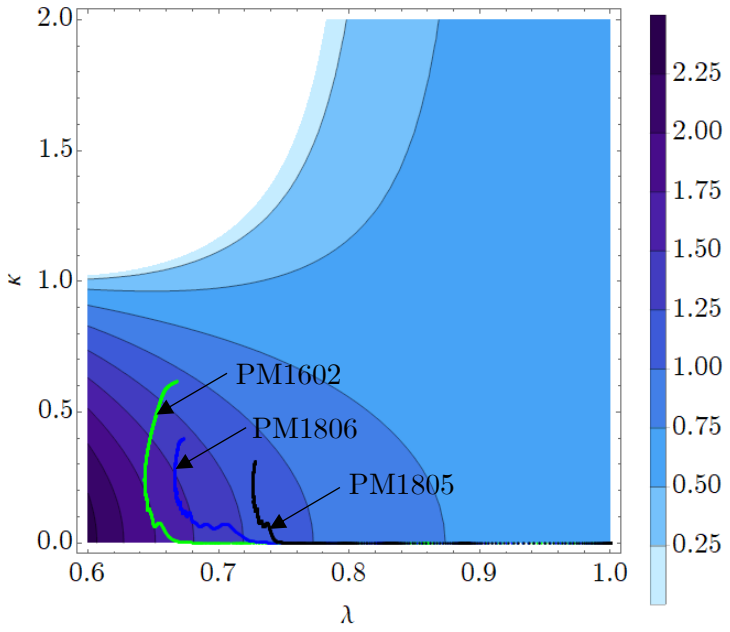

Figure 2.19 Contour plot of fast wave speed (in km/s) as a function of longitudinal compression, λ and shear, κ. Loading contour of simulations of different PSPI shots are also plotted.

It is important to ensure that the Lagrangian elastic wave speeds remain real and positive for the range of deformations encountered in the simulations. In order to ensure that, a wave analysis similar to the one in Clifton and Jiao (2015) is carried out. Contour plots of fast and slow wave speeds for material parameters given in Table 2.4 are drawn in Figure 2.18 and Figure 2.19. It can be observed that the fast wave speed (in this case, the normal wave speed) increases both with increasing compression (i.e. λ) and increasing shear (i.e. κ). The fast wave speed remains positive for the range of λ and κ inspected. The slow wave speed (in this case the shear wave speed), however, increases with increasing compression and decreases with increasing shear. There is also a limitation on the values of λ and κ beyond which the shear wave speed becomes imaginary, i.e. the wave equations no longer remain hyperbolic. The loading contours of simulated PSPI shots are plotted on the Lagrangian wave speed contour plots. It can be

observed that the λ and κ values for the simulations are far away from the region of zero wave-speeds, ensuring that the elastic wave speeds indeed remain real and positive for the range of deformations explored here.

2.6 Discussion

Dynamic shearing resistance measurements of HTPB, a common binder in PBXs and rocket propellants, are carried out using pressure-shear plate impact experiments. The experiments spanned a normal stress range of 3-9 GPa and nominal shear strain rates of $2\text{x}10^5 - 4\text{x}10^5$ s^{-1}. Longitudinal wave speeds are shown to increase non-linearly with increasing normal stress. The wave speeds are fit to a Lennard-Jones type potential, which enables the prediction of a quasi-isentrope for the material. It is found that the shearing strength of HTPB is highly pressure-dependent. Pressure-dependence of the binder is typically ignored in the material models used in energetic materials simulations in the literature. However, accounting for the large pressure-dependence reported here is expected to have important consequences in the prediction of energy localization mechanisms and hot-spots in PBXs. In this study, a quasi-linear viscoelastic model with pressure-dependent shear wave speeds and shearing resistance is used to describe the experimentally observed dynamic response of HTPB. The model consists of an instantaneous elastic response and a viscoelastic relaxation of the elastic response. Simulated profiles of normal and shear response are compared with experimental results and a good agreement is seen for a suitable choice of material parameters. The shear response of HTPB is compared with other elastomers and engineering polymers and is observed to be similar to that of polyurea.

2.7 Appendix A: HTPB sample preparation

The following steps are followed to prepare a binder mixture:

1. Decide on the total weight of the final polymer mixture. Usually more than 60 grams is prepared for consistency across different batches. This is because the fraction of curing agent (di-isocyanate) required is extremely small and even small percentage errors in pipetting can cause large changes in binder stiffness.
2. Wear a lab coat, disposable nitrile gloves and safety goggles. Keep a respirator and chemical resistant neoprene gloves ready for use when handling the catalyst, DBTDL and the curing agent, IPDI. All the chemicals must be stored inside the fumehood when being used and all operations should be performed inside the fumehood. DBTDL and IPDI are extremely hazardous (read Material Safety Data Sheets before use), so they should be handled carefully.
3. Take a plastic cup with a volume at least 3 times the volume of final mixture (assume the density of the final mixture to be $\sim 1 g/cm^3$). This is because degassing the mixture in the subsequent steps causes the polymer mixture to flow out of the cup. Place the cup on a weighing scale inside the fumehood.
4. Take out the required amount of HTPB (see Table 2.5 for component fractions) using a glass rod, into the plastic cup. HTPB resin is a clear, thick viscous liquid. Close lid of the HTPB container right after use to prevent oxidative reactions and ageing of HTPB resin.
5. Use a plastic disposable pipette to take out the plasticizer, DOA. DOA is a clear liquid, thinner than the HTPB resin. Do not mix yet.

6. Weigh the oxidizing agent, AO-2246 using Mettler Toledo balance, in a separate plastic cup. Keep it aside.
7. Put on the respirator and neoprene gloves.
8. Carefully open the DBTDL (catalyst) bottle and pour in the exact volume using a micro-pipette. Close the DBTDL bottle tightly and keep back in the pink tray in the fumehood.
9. Take out the curing agent, IPDI from the steel box and carefully pipette out the exact amount. Do not forget to change the disposable plastic pipettes every time you take out the liquid from the bottle.
10. Put in the AO-2246 powder. Mix well using a plastic/Teflon spoon.
11. Degass the mixture in a vacuum chamber for ~10 minutes until almost all the bubbles have died out.
12. Pour the required amount of degassed HTPB on the front target plate. Before beginning the sample preparation procedure, the front plate should be ready with shims on its periphery. The rear target plate should be stuck to a movable piston, whose height can be adjusted from outside the vacuum chamber. The remaining HTPB is then transferred in a rectangular plastic box and is used later as a reference to measure the Shore-A hardness of cured HTPB.
13. Degass again for ~2-3 minutes and slowly lower the rear target plate using the movable piston. Squeeze out the excess HTPB. Place a weight on top of the piston and keep for 5-10 minutes.
14. Detach the piston from the rear target plate and vent the vacuum chamber. Take out the sandwich (which is placed on a large steel substrate) and keep in the oven at 60 ^{0}C

for 12-16 hours. Place the rectangular box with excess HTPB under same conditions in the oven.

15. After 12 hours, check the Shore-A hardness of the excess HTPB sample. Heat for a longer time if needed.
16. After placing the sandwich in the oven, clean up the workspace. Put the disposable gloves, plastic cups, pipettes, etc. into a glass box. Close the glass box tightly and put an orange hazardous waste label on it.

Chemical Reactions involved

The two main components of the binder are: HTPB resin and the curing agent. HTPB is an oligo-polyol, i.e. it is an oligomer of butadiene terminated with a hydroxyl group (-OH) at each end of the chain (see Figure 2.20). IPDI is an aliphatic non-symmetric di-isocyanate, i.e. it has two isocyanate groups (-NCO) (see Figure 2.20).

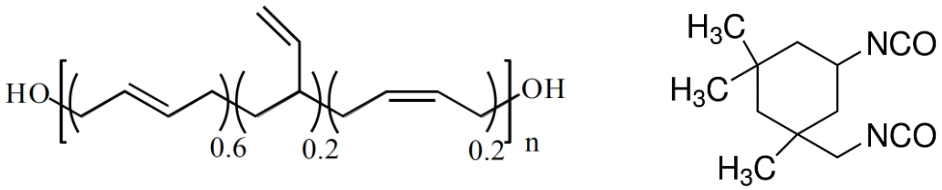

HTPB IPDI

Figure 2.20 Chemical structure of HTPB and IPDI

The basic reaction involved in the curing process is that between an isocyanate and an alcohol to give a urethane Ionescu (2005) , as shown below in Figure 2.21.

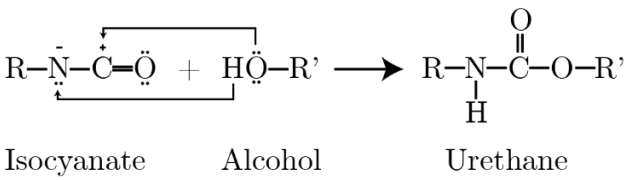

Figure 2.21 Reaction between an isocyanate and an alcohol leads to the formation of a urethane. The nucleophilic center of the alcohol (oxygen atom) attacks the electrophilic site of the isocyanate (carbon atom). The hydrogen atom on the alcohol adds on to the nitrogen atom of the isocyanate. The reaction is exothermic and generates a heat of 24 kcal/mol (Ionescu (2005))

To understand how to calculate the weight fractions of each component in the HTPB mixture, it is important to first define the following quantities.

1. Functionality (f): Number of hydroxyl groups per molecule of oligo-polyol.
2. Number average Molecular Weight (M_n): Number average molecular weight of a polymer is defined as:

$$M_n = \frac{\sum_i n_i M_i}{\sum_i n_i} \tag{2.26}$$

where n_i is the number of moles of i^{th} molecule and M_i is the molecular weight of i^{th} molecule.

3. Weight average Molecular Weight (M_w): Weight average molecular weight of a polymer is defined as:

$$M_n = \frac{\sum_i n_i M_i^2}{\sum_i n_i M_i} \tag{2.27}$$

4. Polydispersity Index (PDI)/Molecular Weight Distribution (MWD): PDI is the measure of heterogeneity of molecule sizes in a polymer and is defined as:

$$PDI = \frac{M_w}{M_n} \tag{2.28}$$

5. Hydroxyl Number (OH#): Milligrams of KOH equivalent for 1 gram of the sample (mg KOH/g).

$$OH\# = \frac{f \times 56100}{M_n} \tag{2.29}$$

where M_n is the number average molecular weight of the sample (g/mol) and $56100\,mg$ is the equivalent weight of KOH.

6. Equivalent Weight (EW): Equivalent weight is defined as:

$$EW = \frac{M_n}{f} = \frac{56100}{OH\#} \tag{2.30}$$

1 equivalent weight of polyol reacts with one equivalent weight of the di-isocyanate.

Table 2.5 Material parameters for Poly bd R-45HTLO from the data sheet

Hydroxyl functionality	2.4-2.6
Number average molecular weight	2800 g/mol
Polydispersity Index	2.5
Hydroxyl number	47.1 mgKOH/g
Specific gravity (23 ^{0}C)	0.901 g
Glass Transition Temperature	-75 ^{0}C

Case Study 1: For a simple 2-component system of a polyol and an isocyanate, percentage of each component required is:

$$\%\, component = \frac{EW_i}{\sum_i EW_i} \tag{2.31}$$

Consider a polymer bonded explosive with 10% binder content. It is given that DOA content is 5%, AO content is 0.01% and NCO:OH ratio is 1:1. Assuming no bonding agent, what is the % of HTPB (R-45 HT) and % of IPDI by weight? First, find the percentage of curatives (%C):

$$\%C = 10 - 5 - 0.01 = 4.99 \tag{2.32}$$

Now, to proceed further, the equivalent weights of HTPB and IPDI are required. $EW_{HTPB} = 1191$ is obtained from equation (2.30) by substituting the value of hydroxyl number (OH#) from Table 2.5. Similarly, with a molecular weight of 222 g/mol and a functionality of 2, the equivalent weight of IPDI is found to be 111. Therefore, the percentages of HTPB and IPDI are:

$$\%HTPB = \frac{1191}{1191 + 111} \times 4.99 = 4.56\% \tag{2.33}$$

$$\% IPDI = 4.99 - 4.56 = 0.43\% \tag{2.34}$$

Case Study 2: Consider an NCO:OH ratio of 1.2 in Case Study 1. This implies that there are 1.2 equivalents of IPDI for every equivalent of HTPB. Let the % of HTPB be x. Therefore,

$$x + 1.2x = 4.99 \tag{2.35}$$

$$\% HTPB = \frac{1\ EW\ HTPB}{1\ EW\ HTPB + 1.2\ EW\ IPDI} \times (\%C) = \frac{1191}{1191 + 1.2 \times 111} \times 4.99 = 4.49\% \tag{2.36}$$

$$\% IPDI = 8.6 - 7.81 = 0.5\% \tag{2.37}$$

Note that in the above case studies, HTPB resin and the IPDI curing agent are the only curatives. However, if other compounds like a cross-linking agent or bonding agent (for example Dantocol in Williams et al. (2013)) contribute to the NCO:OH ratio, they need to be accounted for in the curatives percentage as well.

2.8 Appendix B: Cauchy Stress for PSPI

The left Cauchy-Green tensor, $\boldsymbol{B} = \boldsymbol{F}^T\boldsymbol{F}$ can be found from the definition of $\boldsymbol{F}$ using equation (2.4):

$$\boldsymbol{B} = \begin{bmatrix} \lambda^2 & -\kappa\lambda & 0 \\ -\kappa\lambda & \kappa^2 + 1 & 0 \\ 0 & 0 & 1 \end{bmatrix} \tag{2.38}$$

Substituting the above expression in equation (2.14), the Cauchy stress is expressed below:

$$\begin{aligned} \boldsymbol{T} = 2f(\lambda)\left[\frac{C_{10}}{\lambda^{5/3}} + \frac{C_{01}\bar{I}_1}{\lambda^{5/3}}\right]\boldsymbol{M_1} - \frac{2C_{01}}{\lambda^{\frac{7}{3}}} f(\lambda)\boldsymbol{M_2} \\ + \left\{[C_{00} + C_{01}(\bar{I}_2 - 3) + C_{10}(\bar{I}_1 - 3)]f'(\lambda) - \frac{f(\lambda)}{\lambda}\left[\frac{2C_{10}\bar{I}_1}{3} + \frac{4C_{01}\bar{I}_2}{3}\right]\right\}\boldsymbol{I} \end{aligned} \tag{2.39}$$

where $\boldsymbol{I}$ is the identity tensor and the tensors $\boldsymbol{M_1}$ and $\boldsymbol{M_2}$ defined below:

$$\boldsymbol{M_1} = \begin{bmatrix} \lambda^2 & -\kappa\lambda & 0 \\ -\kappa\lambda & \kappa^2 + 1 & 0 \\ 0 & 0 & 1 \end{bmatrix} \tag{2.40}$$

$$\boldsymbol{M_2} = \begin{bmatrix} \lambda^2(\lambda^2 + \kappa^2) & -\kappa\lambda(1 + \kappa^2 + \lambda^2) & 0 \\ -\kappa\lambda(1 + \kappa^2 + \lambda^2) & (1 + \kappa^2)^2 & 0 \\ 0 & 0 & 1 \end{bmatrix} \tag{2.41}$$

For a linear elastic response, the constants (C_{00}, C_{01}, C_{10}) can be related to the bulk modulus, K and shear modulus, μ:

$$K = (M^2 - 2N^2)C_{00} \tag{2.42}$$

$$\mu = 2(C_{01} + C_{10}) \tag{2.43}$$

Assuming $C_{01} = C_{10} = \frac{\mu}{4}$, equation (2.39) can be further simplified:

$$\begin{aligned} \boldsymbol{T} = \frac{2f(\lambda)C_{10}}{\lambda^{\frac{5}{3}}}(1 + \bar{I}_1)\boldsymbol{M_1} - \frac{2C_{10}}{\lambda^{\frac{7}{3}}} f(\lambda)\boldsymbol{M_2} \\ + \left\{[C_{00} + C_{10}(\bar{I}_1 + \bar{I}_2 - 6)]f'(\lambda) - \frac{2f(\lambda)}{3\lambda}C_{10}(\bar{I}_1 + 2\bar{I}_2)\right\}\boldsymbol{I} \end{aligned} \tag{2.44}$$

2.9 Appendix C: Effect of relaxation constants on the relaxation function

From the figure below, it can be concluded that increased stress relaxation is observed with larger c, smaller t_1 and smaller t_2 for the range of time intervals considered here.

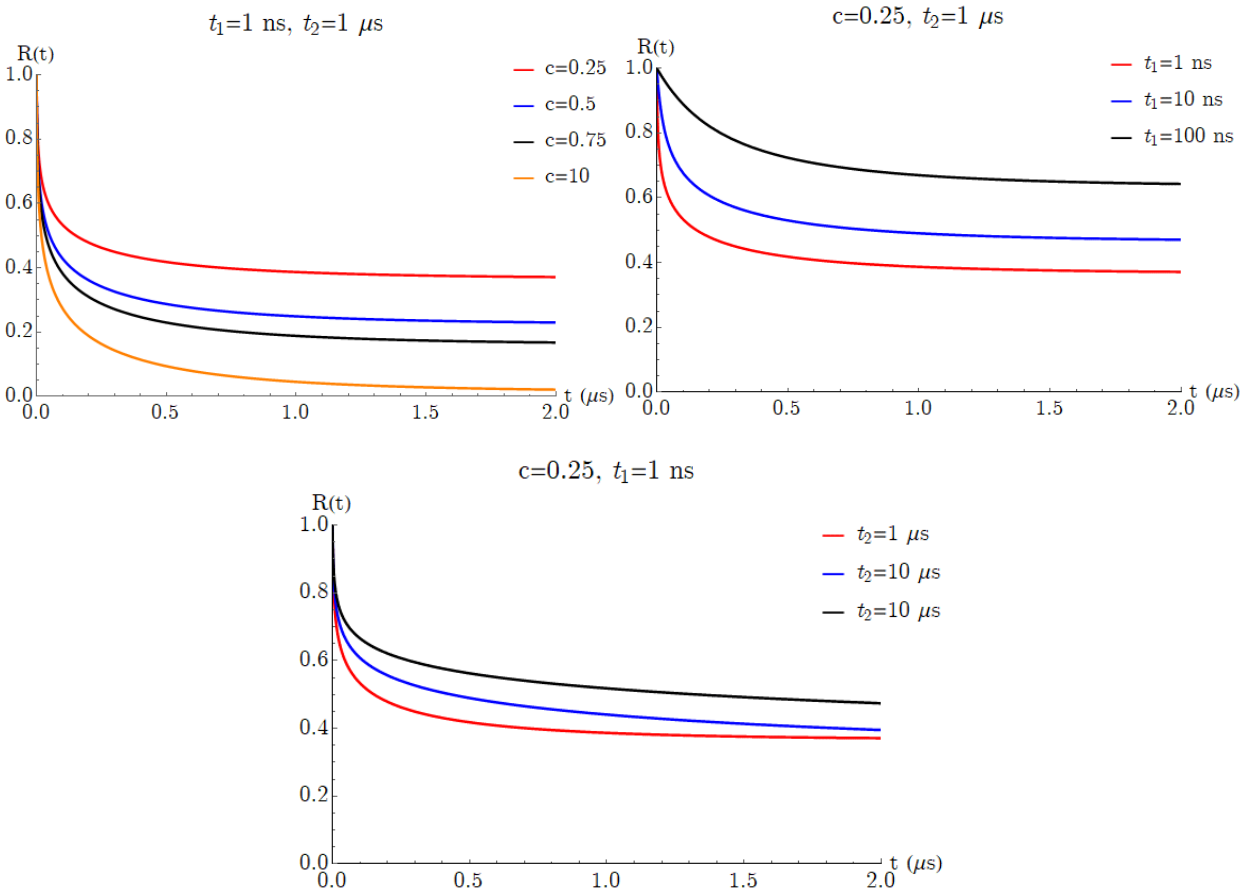

Figure 2.22 Effect of relaxation constants (c, t_1, t_2) on the relaxation function, R(t) for $0 \leq t \leq 2\ \mu s$

Chapter 3

Sucrose: Experiments

3.1 Introduction

An energetic simulant crystal is a molecular crystal that matches with an actual energetic crystal such as HMX, RDX, PETN, etc. in terms of one or more attributes that include crystal structure, density and mechanical properties. Several energetic simulant crystals have been explored in the past, such as, sucrose, acetaminophen and melamine. Sucrose and acetaminophen are simulants for HMX due to their similar monoclinic crystal structure. β-HMX crystals have $P2_1/c$ ($P2_1/n$) symmetry with cell dimensions of $a = 6.54$ Å$, b = 11.05$ Å$, c = 8.70$ Å$, \beta = 124.3^0$ (Miller and Garroway (2001)). Sucrose also belongs to the $P2_1$ space group with cell dimensions of $a = 10.89$ Å$, b = 8.69$ Å$, c = 7.77$ Å$, \beta = 103^0$ (Beevers et al. (1952)). Sucrose has also been shown to have mechanical behavior similar to that of HMX, RDX and PETN under drop-weight impact (Heavens and Field (1974)) and a similar shock Hugoniot as HMX (Sheffield et al. (1998)). These similarities have resulted in sucrose being widely used as an energetic material simulant. Sucrose has not only been used as a mock energetic crystal in the energetic materials industry, but also finds an important application in the pharmaceutical industry as a model material to study compaction processes (Duncan-Hewitt and Weatherly (1990)). Use of sucrose offers insights into fracture in chipping, capping and delamination in such compaction processes.

Due to their inert nature, energetic simulants provide a safe and cost-effective way to test the mechanical behavior of real energetic crystals, which makes them suitable for laboratory settings. Another major advantage of studying energetic simulants is that they allow decoupling of mechanical and chemical behaviors of energetic crystals so that one can understand the mechanical signatures of phenomena such as pore collapse, adiabatic shear localization, fracture and granular friction independent of the effects of the accompanying chemical reaction in an actual energetic material. Sheffield et al. (1998) showed how the dissociation reaction in HMX crystals affects particle velocity waveforms at the front and the rear ends of the sample and how the waveforms compare to an inert simulant (sucrose). This allowed them to visualize how waveforms in HMX would have looked if no chemical reaction took place. Moreover, it should be noted that several properties of energetic crystals are not adequately known, some of which are: (a) melt curve as a function of pressure, (b) thermal conductivity of the solid phase as a function of temperature and pressure, (c) specific heat capacity of the liquid phase as a function of pressure and temperature, (d) viscosity in the liquid phase as a function of pressure and temperature, and (e) anisotropy of yield surface. Some of these properties are hard to measure experimentally because of the onset of chemical decomposition and a subsequent reaction under extreme conditions. However, all the above properties are important for accurate modeling of mechanical behavior of energetic crystals under large deformations and accurate prediction of ignition from hot-spot formation. Simulant crystals like sucrose offer an opportunity to provide reference values and trends for relevant material properties of real energetic crystals.

Due to their mechanical and chemical fragility, characterization of molecular crystals using traditional testing methods is very difficult. Brittle molecular crystals such as RDX, HMX,

PETN, sucrose, etc. fracture prematurely because they cannot endure large strains. Moreover, characterization methods such as electron microscopy are difficult to use on these materials for quantitative assessment as they chemically dissociate under an electron beam. Hence, not much is known about the deformation behavior of molecular crystals and the underlying deformation mechanisms. As a result, researchers have been left with only a handful of experimental methods to characterize these materials at the quasi-static limit. Nano-indentation and atomic force microscopy (AFM) have been used to extract elastic moduli and hardness of sucrose on different planes. Ramos and Bahr (2007) have used nanoindentation on single crystals of sucrose and reported an elastic modulus of 38 GPa on the (100) planes and 33 GPa on the (001) planes. They found a hardness of ~1.5 GPa, suggesting a bulk yield strength of 500 MPa. Duncan-Hewitt and Weatherly (1989) report a hardness of 645 MPa using micro-indentation while Masterson and Cao (2008) report a value of 1.8-2.4 GPa using AFM nanoindentation. Hardness measurements suggest there is a significant variation in the results using different measurement techniques. Fracture toughness values of sucrose in the range of 0.07-0.1 MPa $\sqrt{m}$ were reported by Duncan-Hewitt and Weatherly (1989) . Apart from mechanical and chemical fragility, molecular crystals are difficult to analyze and characterize experimentally because of other unfavorable features such as anisotropy and phase transformations. For example, β-HMX has a monoclinic crystal structure with 13 elastic constants which have been measured experimentally by Zaug (1998) and Stevens and Eckhardt (2005) . Similar measurements of elastic constants of RDX by Haussühl (2001), Schwarz et al. (2005), Haycraft et al. (2006) show large anisotropy of elastic properties along different orientations. Anisotropy in crystallographic slip results in varying mechanical response when shocked in different orientations. Dick et al.

(2004) demonstrate the anisotropy in strength and elastic precursor decay of β-HMX single crystals when shocked in different orientations. The inelastic mechanisms of deformation are also shown to vary with orientation. Similarly, Hooks et al. (2006) show that elastic wave speeds, Hugoniots and plastic wave relaxation rates are highly anisotropic for shocked RDX single crystals. Such a large anisotropy in elastic and plastic properties of energetic crystals requires extensive experimental characterization for reliable constitutive models.

The mechanical response of molecular crystals such as HMX and RDX has been studied in sufficient detail under uniaxial strain through normal compression impact experiments (Dick et al. (2004), Hooks et al. (2006)). However, a systematic characterization of the shear strength of energetic crystals and their simulants such as sucrose has not been done so far. Trott et al. (2007) investigated the response of granular sugar under shock compression for different sample thicknesses, impact velocities and particle size distributions. A shock Hugoniot has also been reported by Sheffield et al. (1998) . However, these studies are insufficient to model the strength response of sucrose as a function of pressure and strain-rate. A detailed anisotropic elastic-viscoplastic model is not possible to build at this stage due to absence of sufficient experimental data. It is difficult to develop even a sufficiently robust isotropic model for polycrystalline sucrose or a sufficiently large aggregate of sucrose grains, which can adequately model large deformations under high pressures and high strain rates. The absence of any shear strength measurements makes it difficult to perform realistic simulations of deformation and phenomena such as pore-collapse, shear localization and friction that lead to hot-spot formation. Granularity of the specimen further hinders the ability to probe bulk material response of sucrose. The effect of granular nature of the specimen is brought out through very different normal velocity profiles

for same impact velocities observed by Trott et al. (2007) . For these reasons, we employ the PSPI technique in the present work to measure the material response of a uniform sucrose layer to normal and shear loading.

To add to the complexity of mechanical behavior of molecular solids, it has been reported that under high pressures, temperatures and shear strains, molecular solids can undergo phase transformations. Patyk et al. (2012) and Ciezak-Jenkins and Jenkins (2018) report an isostructural phase transformation in sucrose at a pressure of ~5 GPa, using a diamond anvil cell. Ciezak-Jenkins and Jenkins (2018) subject sucrose samples to large shear strains at high pressures using a rotational diamond anvil cell and show that amorphization occurs under such loading conditions. However, the diamond anvil cell studies do not quantify the shear strains and rates of loading and hence do not provide the necessary quantitative information to develop material models. Therefore, in the present work, we lay an experimental foundation using the PSPI experiments for the constitutive modeling of sucrose. In addition to being the first undertaking to study high pressure, high strain-rate strength of sucrose, the experimental results also reveal the propensity of sucrose to undergo shear localization. Such findings beg for more experimental effort on real energetic crystals such as HMX and RDX under PSPI loading.

3.2 Specimen Preparation

A uniform thin layer of crystalline sucrose is prepared on the front target plate by using spin-coating a super-saturated solution of sucrose in de-ionised water. Pure sucrose from Sigma Aldrich is used rather than commercial variety of sugar. An 80% w/w solution of sucrose in

water is prepared and degassed. The solution is spin-coated on the substrate at 4000 rpm. The substrate is placed on a hot plate at ~60 ^{0}C for ~12-16 hours until all water has evaporated and sucrose has crystallized. As shown in Figure 3.1, it is important to stay above the metastability limit (in Zone III) for crystallization to occur. Moist environment and rough substrate are found to favor grain nucleation and growth.

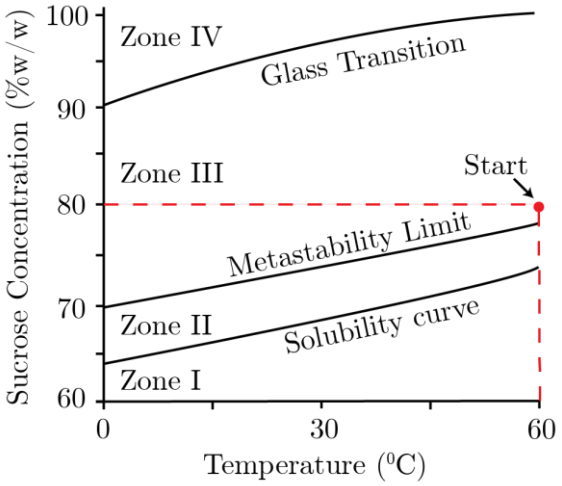

Figure 3.1 Sucrose concentration (% weight of solid) vs temperature (Shastry and Hartel (1996)). Zone I: Under-saturated solution, Zone II: Meta-stable solution, Zone III: Labile solution, Zone IV: Amorphous state. Sucrose crystallization begins above the metastability limit. So, for a solution heated at 60 ^{0}C, a starting solution concentration of 80% is chosen

A sample obtained by following the above preparation process is shown in Figure 3.2. The sample thickness is measured using a Dektak profilometer. A sucrose layer of 10-20 μm in thickness can be obtained by this method, which facilitates large shear strain rates of the order of 10^6 s^{-1}. Note that the specimens are not perfectly flat and have a surface roughness of the order of a micron. On cooling, cracks are observed on the sample, as shown in Figure 3.2 (b) and (c), due to a large mismatch between the coefficient of thermal expansion of the substrate

and that of sucrose. However, the width of these cracks is extremely small as indicated by the scale bar and would not be significant in the PSPI experiments. Another critical issue of interest is the crystallinity of the sucrose layer. To ensure that the sucrose layer prepared by the spin-coating method is crystalline, X-Ray Diffraction (XRD) studies are carried out on powdered crystalline sucrose and spin-coated sucrose layer (see Appendix A). An overlap of XRD peaks of the crystalline specimen and that of crystalline powdered sugar shows that the spin-coating method indeed yields a crystalline layer. Figure 3.2 (d) depicts a polycrystalline layer of a sucrose specimen with a grain size of the order of a few microns.

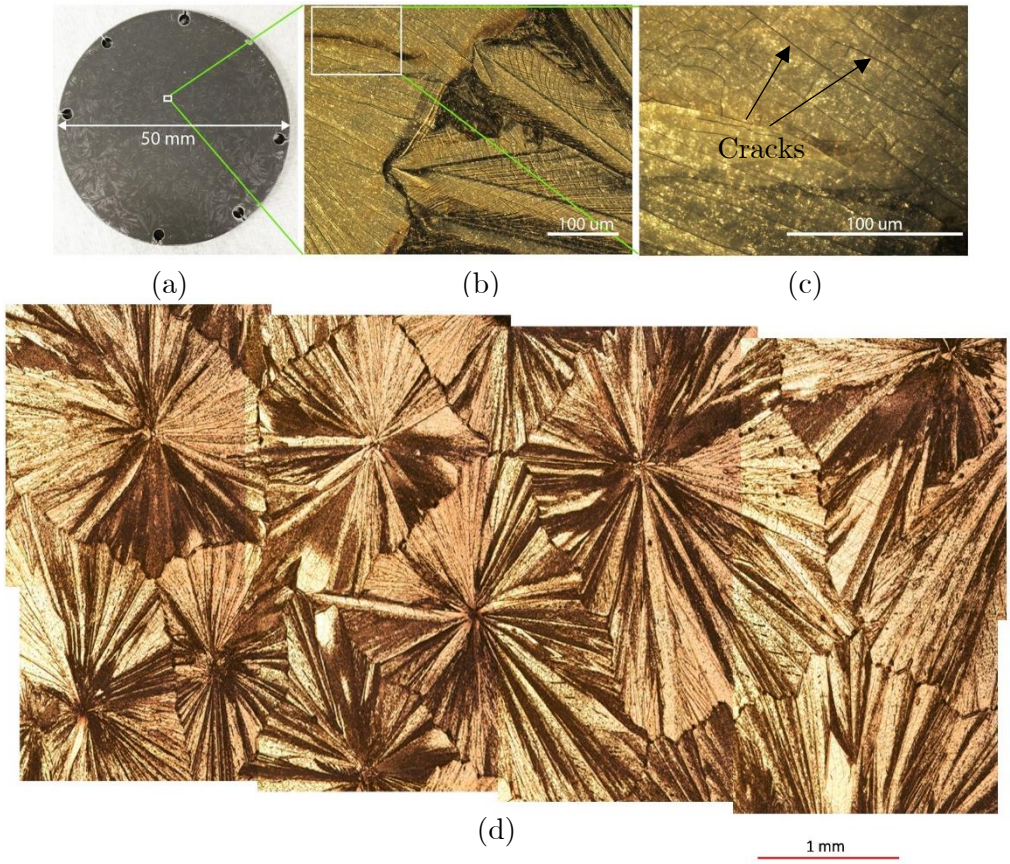

Figure 3.2 (a) WC front target plate (diameter = 50 mm) with a 15 μm thick uniform layer of sucrose spin-coated on top. (b), (c) magnified views of a spot on the sample, (d) a stitched version of microscope images indicating sucrose grain boundaries

3.3 Experimental Results

A total of 7 PSPI shots have been conducted on sucrose. A summary of the shots is provided in Table 3.1. D2 steel is used as the anvil material for the low normal stress (nominally 3 GPa) shots, while WC is used for the high normal stress (nominally 9.5 GPa) shots. Shear strain rates of the order of 10^6 s^{-1} are obtained as a result of using extremely small sample thicknesses of 10-20 μm.

Table 3.1 Summary of PSPI shots on sucrose

Shot No.	Target Material	h_S (μm)	h_F (mm)	h_{FT} (mm)	h_{RT} (mm)	θ	V_0 (m/s)	Tilt (mrad)	σ_{max} (GPa)	τ_{max} (GPa)	$\dot{\gamma}$ (s^{-1})
PM1802	D2 Steel	12.05	6.915	2.978	6.511	18^0	132.06	1.21	2.82	0.382	$1.95x10^6$
PM1803	D2 Steel	12.63	6.94	2.951	6.522	18^0	134	NA	2.9	0.442	$1.7x10^6$
PM1804	D2 Steel	16.97	6.965	2.944	6.571	18^0	133.46	1.02	2.93	0.404	$1.55x10^6$
PM1603	WC	17.6	6.443	2.886	5.872	18^0	187	0.5	9.1	0.460	$2.9x10^6$
PM1701	WC	16.91	6.324	2.855	5.986	18^0	194.5	0.8	9.75	0.288	$3.1x10^6$
PM1702	WC	13.58	6.369	2.937	5.934	18^0	191.9	0.37	9.64	0.580	$3.98x10^6$
PM1801	WC	18.24	6.335	2.914	5.940	18^0	188.52	0.97	9.47	0.530	$2.95x10^6$

h_S: sample thickness h_F: flyer thickness, h_{FT}: front target plate thickness, h_{RT}: rear target plate thickness, θ: angle of impact, V_0: impact velocity, σ_{max}: peak normal stress, τ_{max}: peak shear stress, $\dot{\gamma}$: average shear strain-rate

Figure 3.3 and Figure 3.4 show the normal and transverse velocity profiles for the low-pressure shots on sucrose. The normal and transverse velocity profiles for the high-pressure shots are plotted in Figure 3.5 and Figure 3.6 respectively. The normal velocity profiles show an elastic precursor as shown by the initial step. Following the elastic precursor, the normal velocity for the low-pressure shots rises steeply to the plateau, with a rise time of approximately 86 ns. For the high-pressure shots, the initial rise after the elastic precursor is steep but a bend is observed at a normal velocity of 120 m/s, which could be a result of the anvil material, WC

reaching its HEL. Moreover, no steps are observed in the normal velocity profiles despite the large acoustic impedance mismatch between anvil material and sucrose because sucrose layers are extremely thin. Instead, the normal velocity rises steeply to the saturation value. Normal stress profiles for low and high-pressure cases are plotted in Figure 3.7 and Figure 3.9 respectively. Saturation normal stresses of ~3 GPa and ~9.5 GPa are obtained nominally for the low and high velocity shot categories. Note that in all the plots in this chapter, the velocity and stress profiles have been shifted in time and the beginning of a normal or transverse velocity/stress profile does not indicate the time of arrival of longitudinal/shear wave at the point on the free surface of the rear target plate where velocity measurements are made.

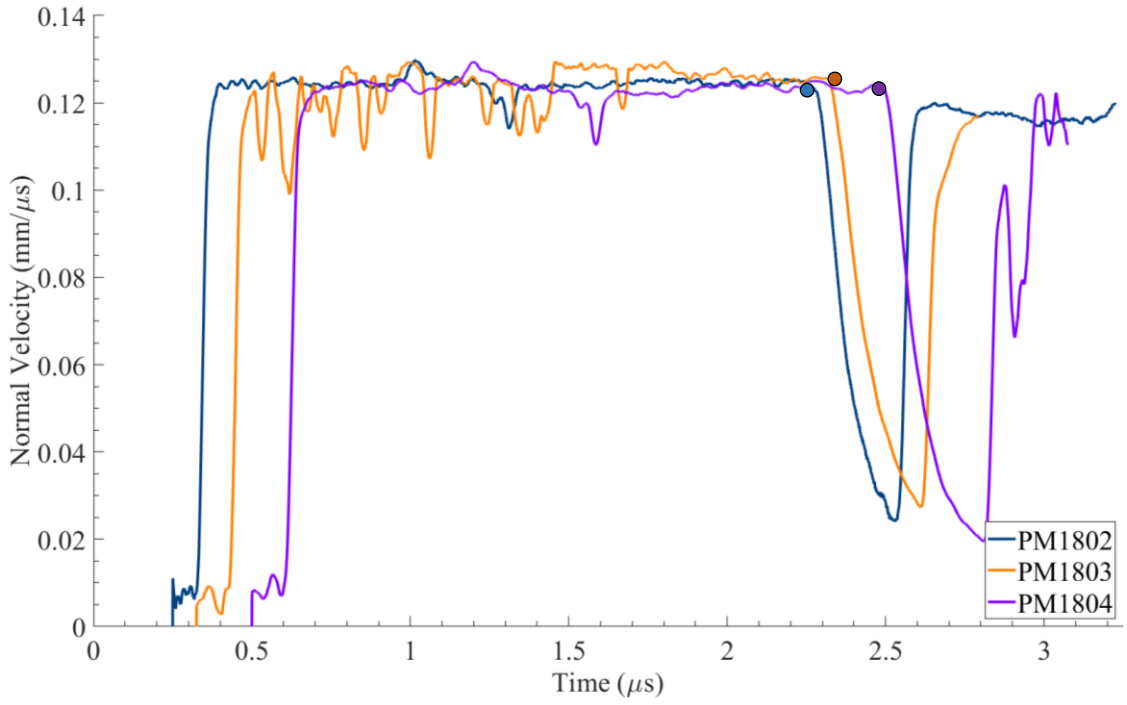

Figure 3.3 Normal velocity vs time profiles for low pressure shots conducted on sucrose. The arrival of unloading wave at the sample/rear-plate interface is indicated by dots. Note that the noise in the velocity profile of PM1803 is caused as a result of small NDI signal

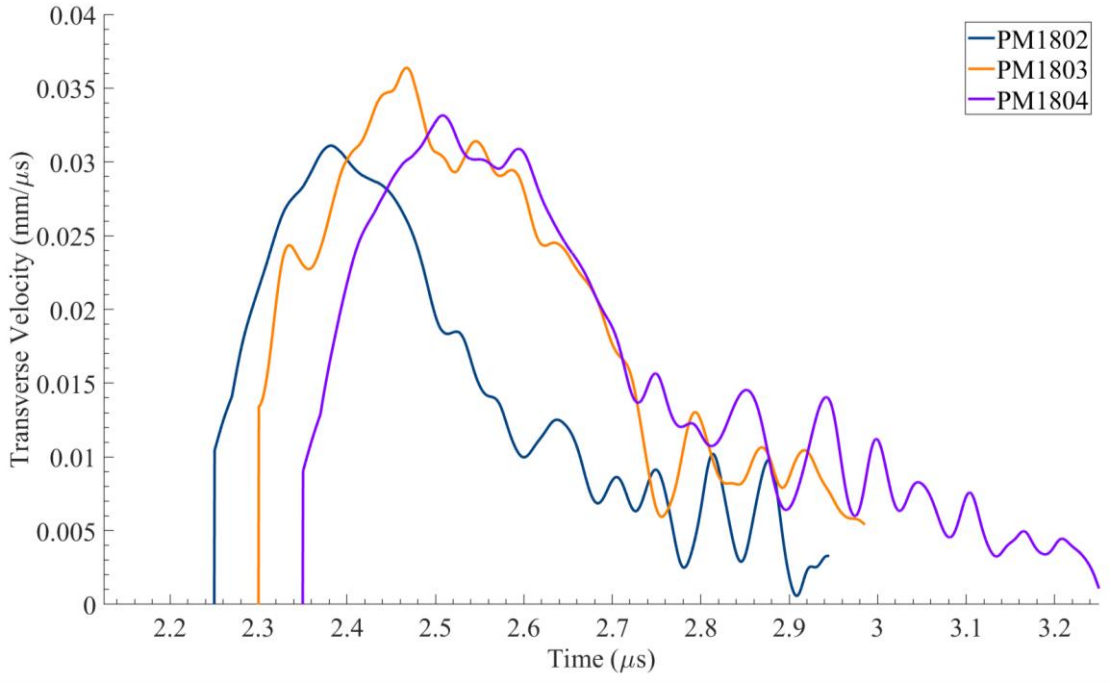

Figure 3.4 Transverse velocity vs time profiles for low pressure shots conducted on sucrose. The unloading longitudinal wave arrives at the sample/rear-plate interface later than the range of times plotted

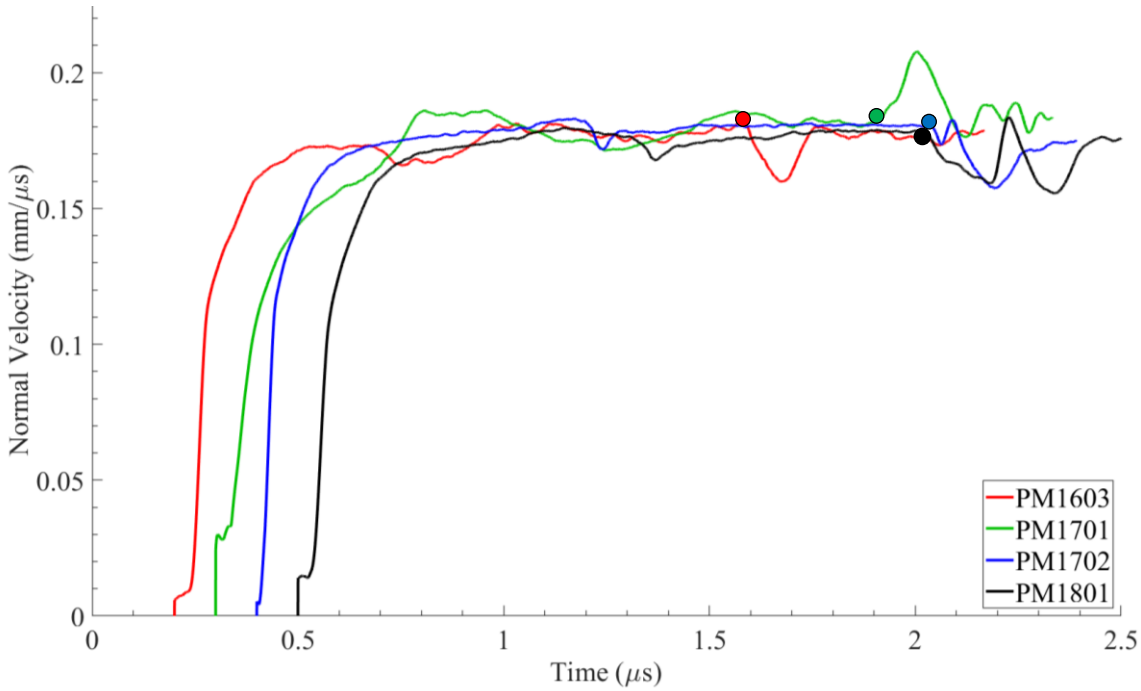

Figure 3.5 Normal velocity vs time profiles for high pressure shots on sucrose. Arrival of unloading wave at the sample/rear-plate interface is indicated by dots

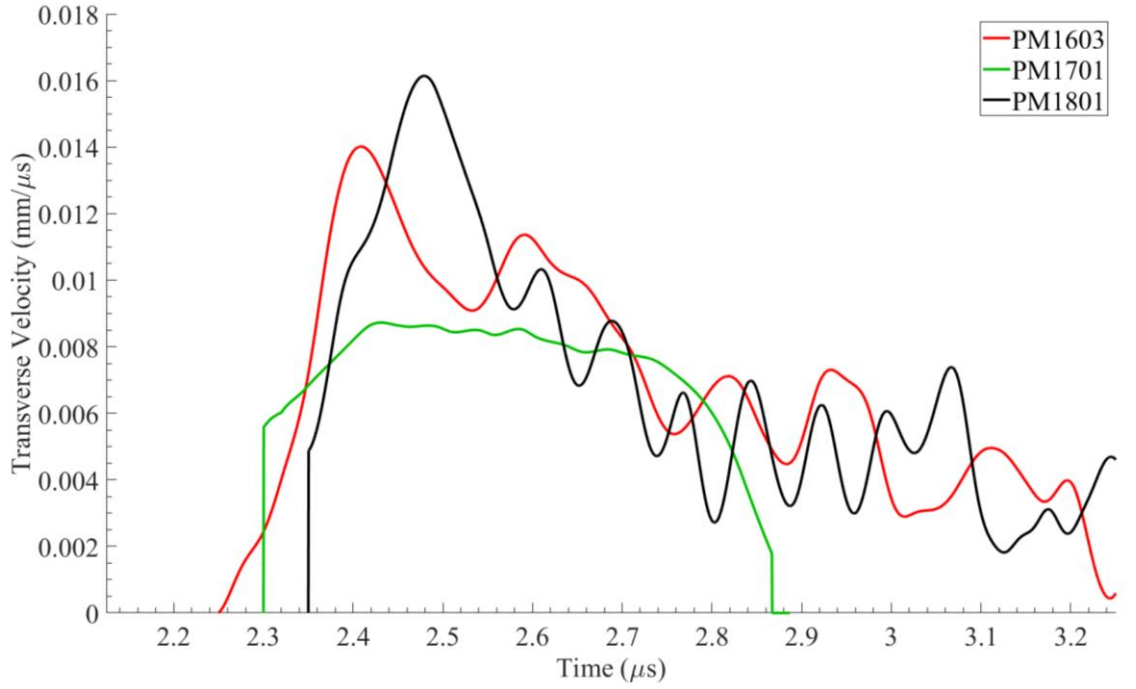

Figure 3.6 Transverse velocity vs time profiles for high pressure shots on sucrose

Similarly, the shear stress profiles are plotted in Figure 3.8 and Figure 3.10 for the low and high-pressure shots respectively. The shear behavior offers more interesting insights into the mechanical behavior of sucrose under high pressures and high shear strain-rates ($>10^6$ s^{-1}). The shear stress rises to a peak value followed by a pronounced strain softening. Under these loading conditions, sucrose loses its shearing resistance after accumulating a certain amount of shear strain. For the low-pressure case, the shear stress profiles are very repeatable. For the high-pressure case, two shots (PM1603 and PM1801) show almost identical shear behavior. However, for shot PM1701, the peak shear strength is much smaller than the other two shots and shows a complete loss in shear strength. Transverse velocity and shear stress profiles for PM1702 are not plotted since the data for that shot is very noisy due to the low TDI signal to noise ratio. Overall, the high-pressure shots exhibit more variability in the shear stress data as compared to

the low-pressure shots. However, both the cases show qualitatively similar behavior. Also note that as the transverse velocity reduces to a very small value after shear strain-softening, the transverse velocity and shear-stress profiles become noisy due to the low signal to noise ratio of TDI signal thereafter.

Normal stress profiles for all shots on sucrose are plotted in Figure 3.11. High and low-pressure shots are laid on top of each other for a better comparison and to demonstrate the consistency of the normal behavior across different shots. Similarly, shear stress profiles for all shots on sucrose are plotted in Figure 3.12.

The dramatic drop in shear strength of sucrose can be attributed to a thermo-viscoplastic instability leading to localized shearing deformation and possibly melting in the sucrose sample. Such behavior is modeled using an appropriate constitutive model in Chapter 4. A simple calculation of the amount of plastic work due to shear converted to heat ($= \int \beta \, \tau d\gamma$) suggests a significant increase in temperature. Here $\int \tau d\gamma$ is the amount of plastic work due to shearing deformation and β is the fraction of plastic work converted to heat. For example, assuming homogeneous deformation across the specimen in shot PM1603, $\beta = 0.9$ and ambient values of specific heat ($1244\ J/kgK$) and density of sucrose ($1580.5\ kg/m^3$), a temperature increase of approximately 286 ℃ is expected. The thermal softening eventually overtakes the strain and strain-rate hardening, leading to localized deformation. Such localized failure through the formation of adiabatic shear bands has been observed in molecular solids like RDX by Sharma and Coffey (1996), Sharma et al. (1996), Coffey and Sharma (2001) . Sharma and

Coffey (1996) and Sharma et al. (1996) use Atomic Force Microscopic (AFM) imaging to illustrate the lattice and molecular deformations in RDX resulting from drop-weight loading. AFM images of an RDX single crystal subject to an aquarium shock of 12.9 GPa magnitude by Sandusky et al. (1993) are shown in Coffey and Sharma (2001) . AFM images of recovered samples shows shear bands with width of several tens of microns form along crystal slip planes and extend for hundreds of microns. It is also shown that RDX melts locally within the shear bands, flows out of the bands and solidifies on the crystal surface. Molecular dynamics studies of shock-loaded HMX (Jaramillo et al. (2007)) and RDX (Cawkwell et al. (2008)) also show the formation of nano-shear bands at 45^0 to the direction of impact. However, quantitative measurements of peak shear stress at which shear bands form are not made in any of the above studies.

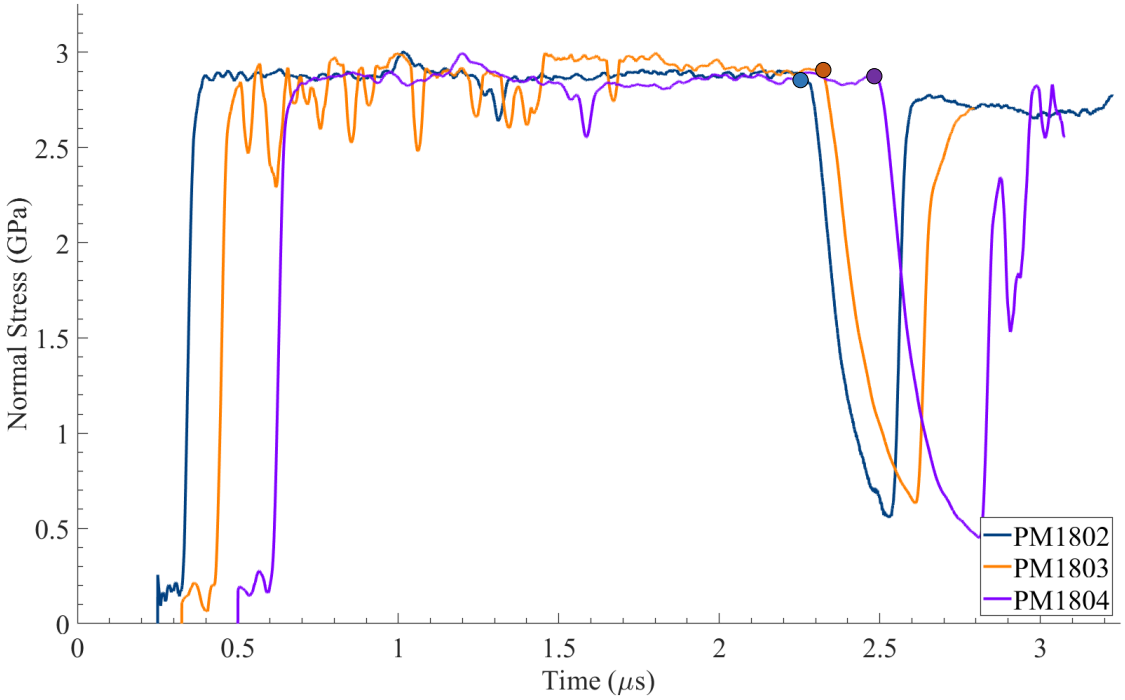

Figure 3.7 Normal stress vs time profiles for low pressure shots on sucrose

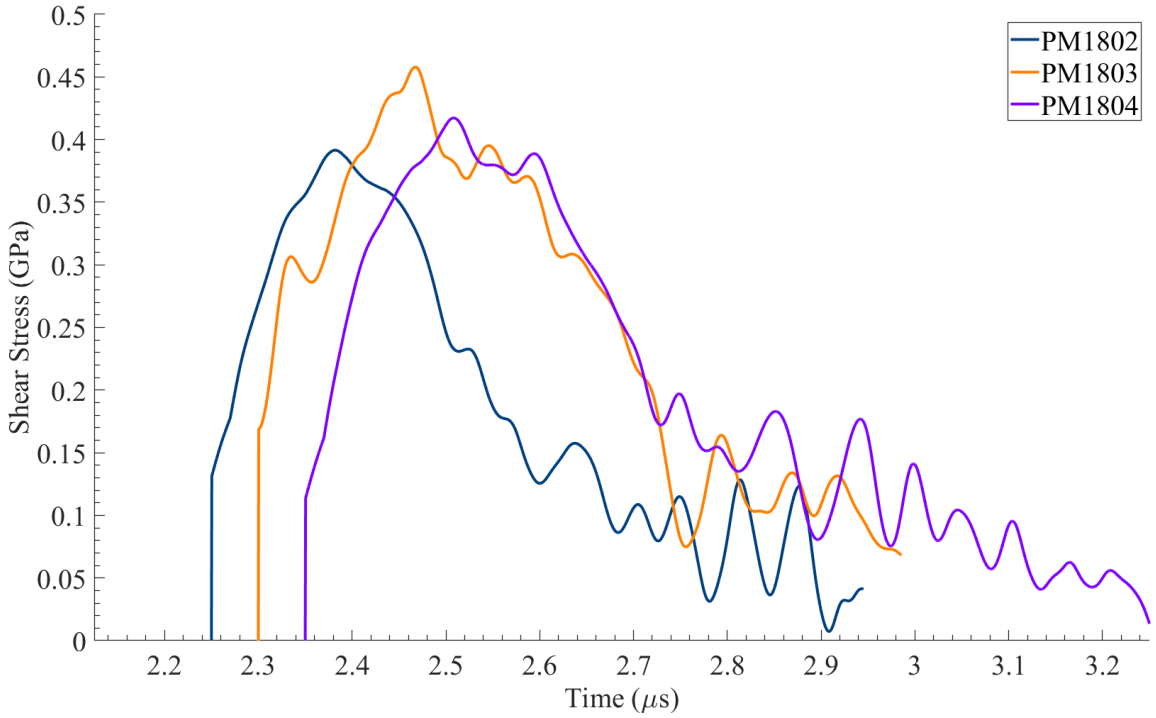

Figure 3.8 Shear Stress vs time profiles for low pressure shots on sucrose

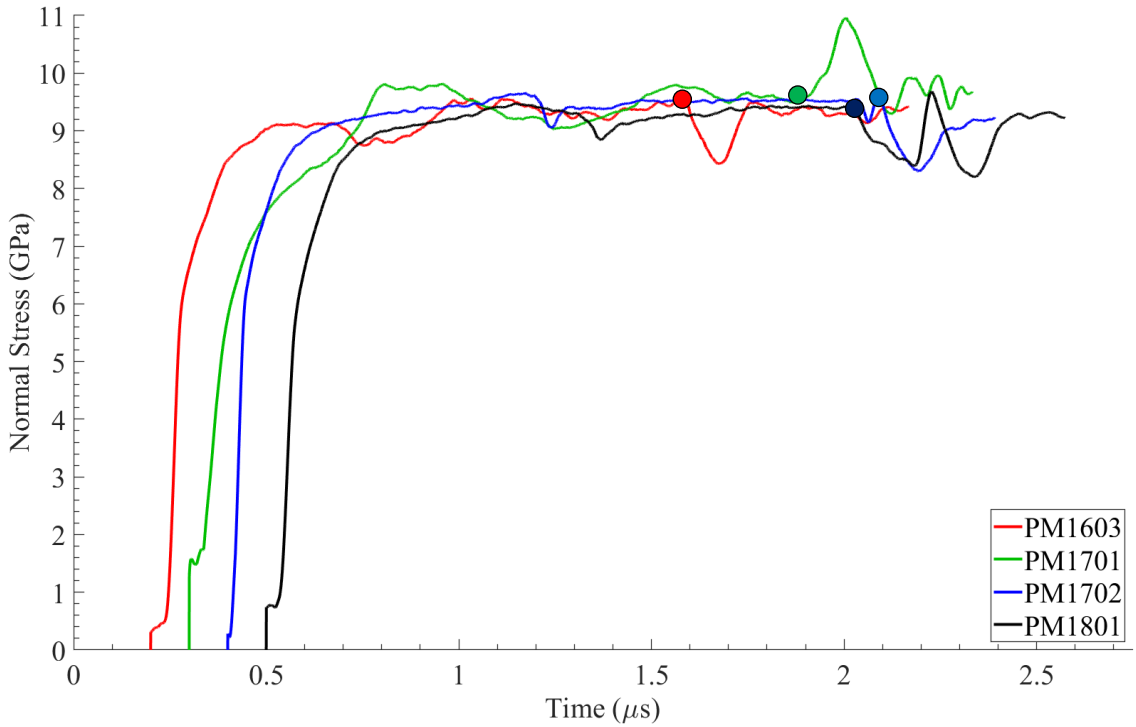

Figure 3.9 Normal stress vs time profiles for high pressure shots on sucrose

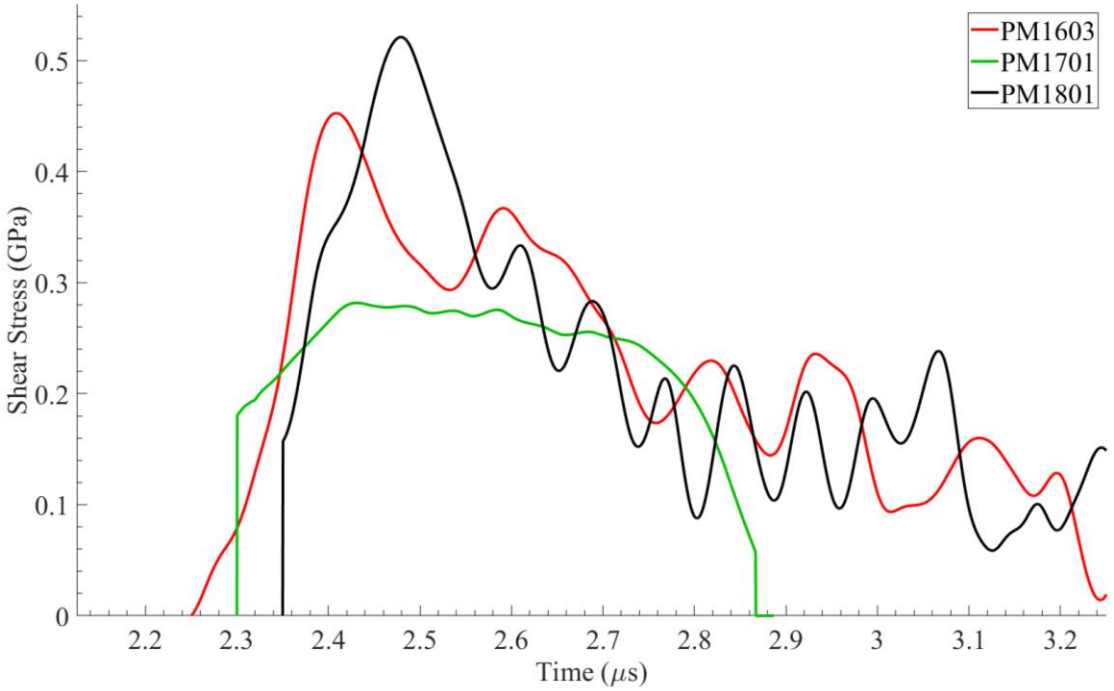

Figure 3.10 Shear stress vs time profiles for high pressure shots on sucrose

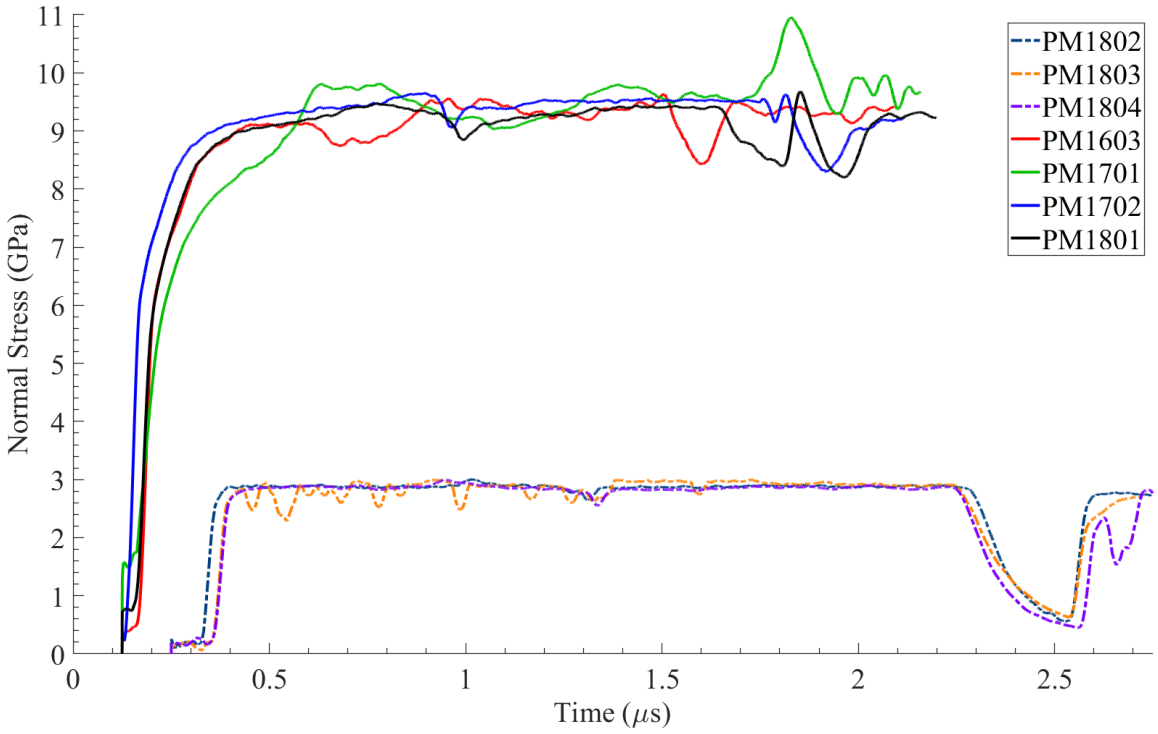

Figure 3.11 Normal stress vs time profiles for all shots on sucrose. Solid lines show the high-pressure shots while dotted lines show low-pressure shots.

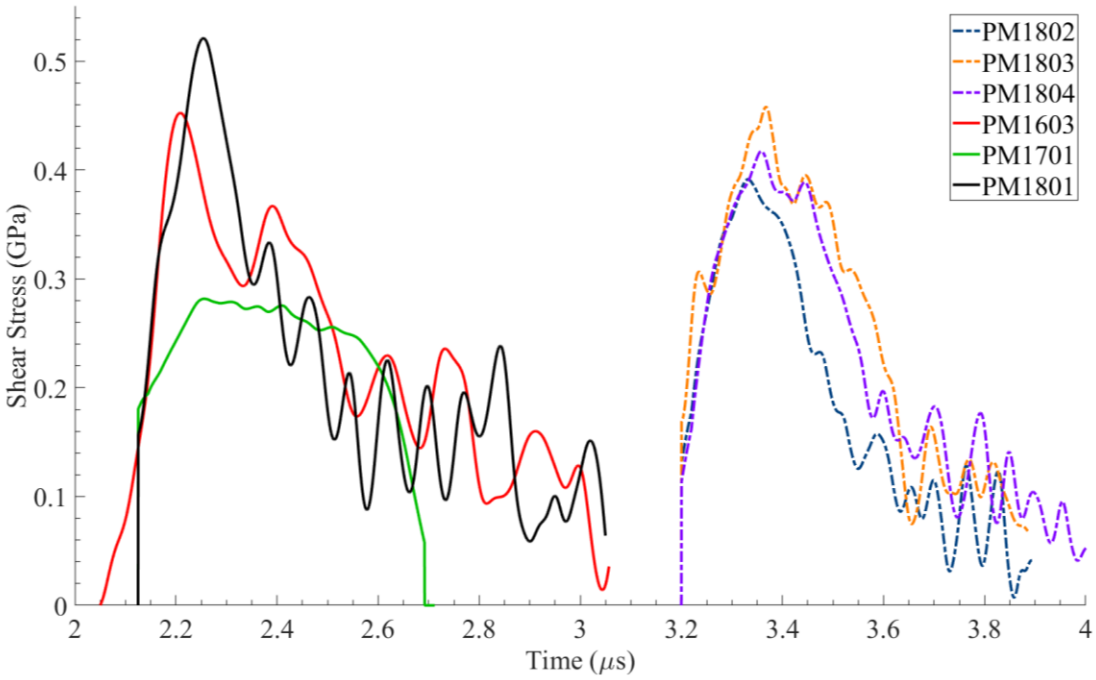

Figure 3.12 Shear stress vs time profiles for all shots on sucrose. Solid lines show the high-pressure shots while dotted lines show low-pressure shots. High and low-pressure shots are laid on top of each other for a better comparison and to demonstrate consistency of shear behavior across different shots

Peak shear stresses in sucrose exhibit some variability for a given normal stress. The variability is low for the low normal stress cases. However, in general, the peak shearing resistance of sucrose seems to be very weakly dependent on normal stress, as shown in Figure 3.13. In contrast, as presented in Chapter 2, the shearing resistance of HTPB is heavily pressure-dependent.

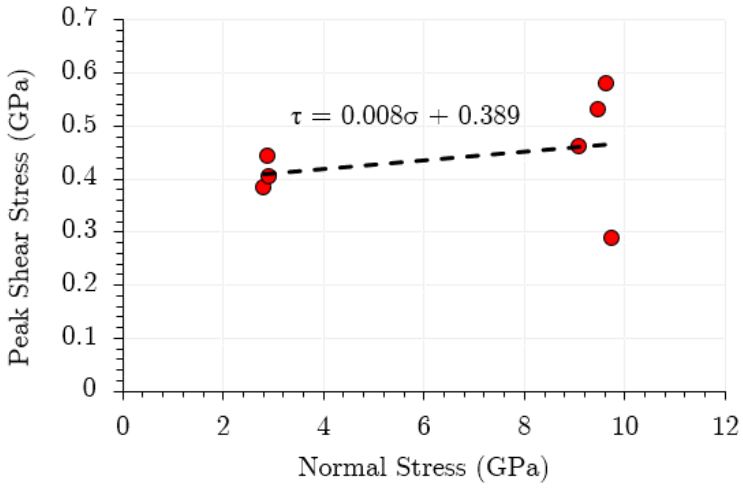

Figure 3.13 Peak shear stress of sucrose vs normal stress, at a nominally similar shear strain rate. The dashed line indicates a linear fit to the experimental data. The equation to the linear fit is displayed above the trendline. Note that the slope of the curve is very small $\left(\frac{d\tau}{d\sigma} = 0.008\right)$ as compared to that for HTPB $\left(\frac{d\tau}{d\sigma} = 0.059\right)$. Since substantial temperature increase is expected due to normal compression, peak shear stress is expected to depend on temperature as well. The plot therefore shows the coupled effect of normal stress and temperature rather than normal stress alone

Shear strain-rate curves are plotted for low and high-pressure shots on sucrose in Figure 3.14 and Figure 3.15 respectively. Mean shear strain-rate values for the low-pressure shots lie in the $\sim 1.5 \times 10^6 - 2 \times 10^6\ s^{-1}$ range while the mean shear strain-rates for high-pressure shots are slightly higher ($\sim 3 \times 10^6\ s^{-1}$). The shear strain-rate values calculated here should be taken with caution as they assume that deformation in the specimen is homogeneous and the shear stress has equilibrated. Due to the extremely small thickness of the specimen, shear stress equilibrium can be attained fairly quickly, However, strain localization is suspected inside the specimen after the fall in shear strength. For such inhomogeneous deformations, the shear strain-rate plots shown here do not represent the true dynamic stress-strain inside the specimen. So, the shear strain-rate and shear strain values are only nominal proxies of actual values. Shear stress versus

nominal shear strain behavior is plotted in Figure 3.16 and Figure 3.17 for low and high pressure shots respectively. It can be observed that shear stress falls around a nominal shear strain of ~0.2 for the low-pressure shots while the critical shear strain for high pressure shots is ~0.5, signalling the role of pressure in suppressing the onset of instability. Moreover, note that the fall in shear strength is faster in low-pressure shots compared to high-pressure shots, which again indicates that a superposed pressure slows the catastrophic failure caused by the onset of adiabatic shear localization.

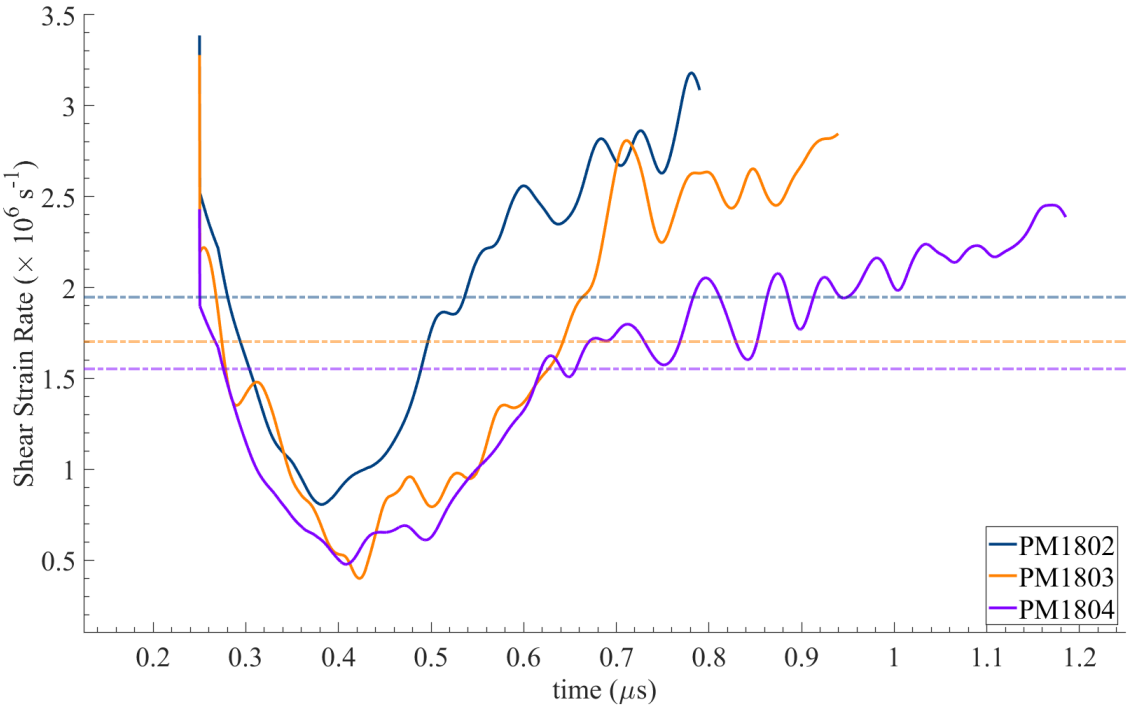

Figure 3.14 Shear strain-rates for low-pressure shots. The mean shear strain-rate values for each shot are indicated by the light-colored dotted lines

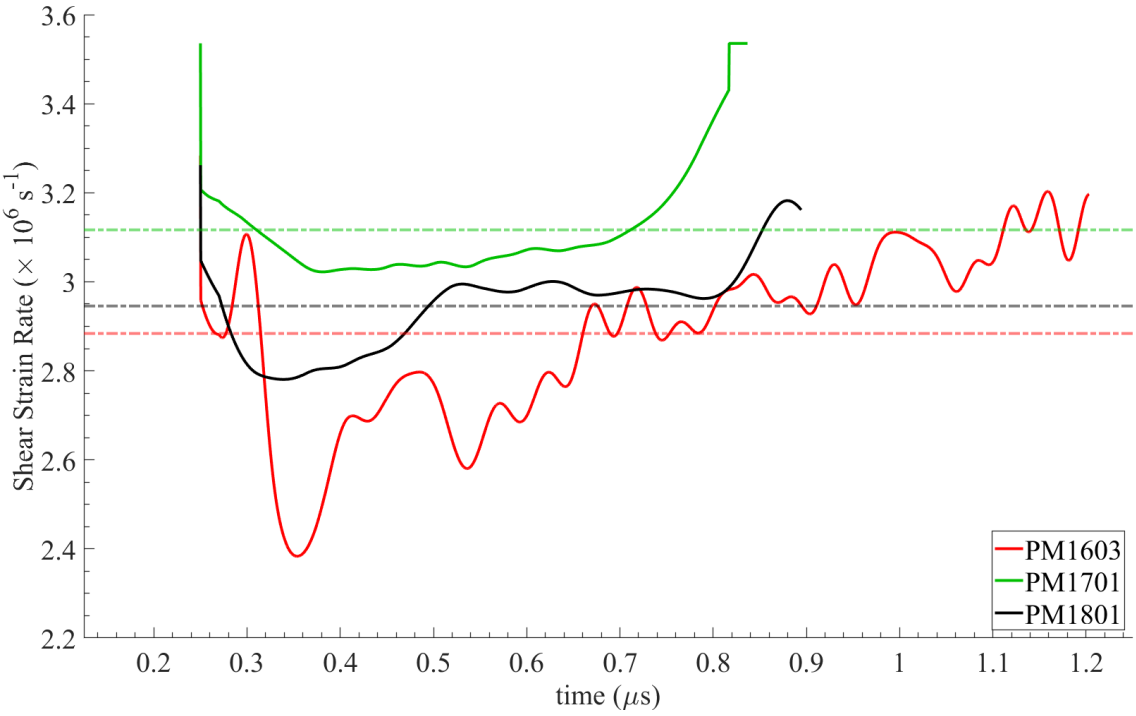

Figure 3.15 Shear strain-rates for high-pressure shots. The mean shear strain-rate values for each shot are indicated by the light-colored dotted lines

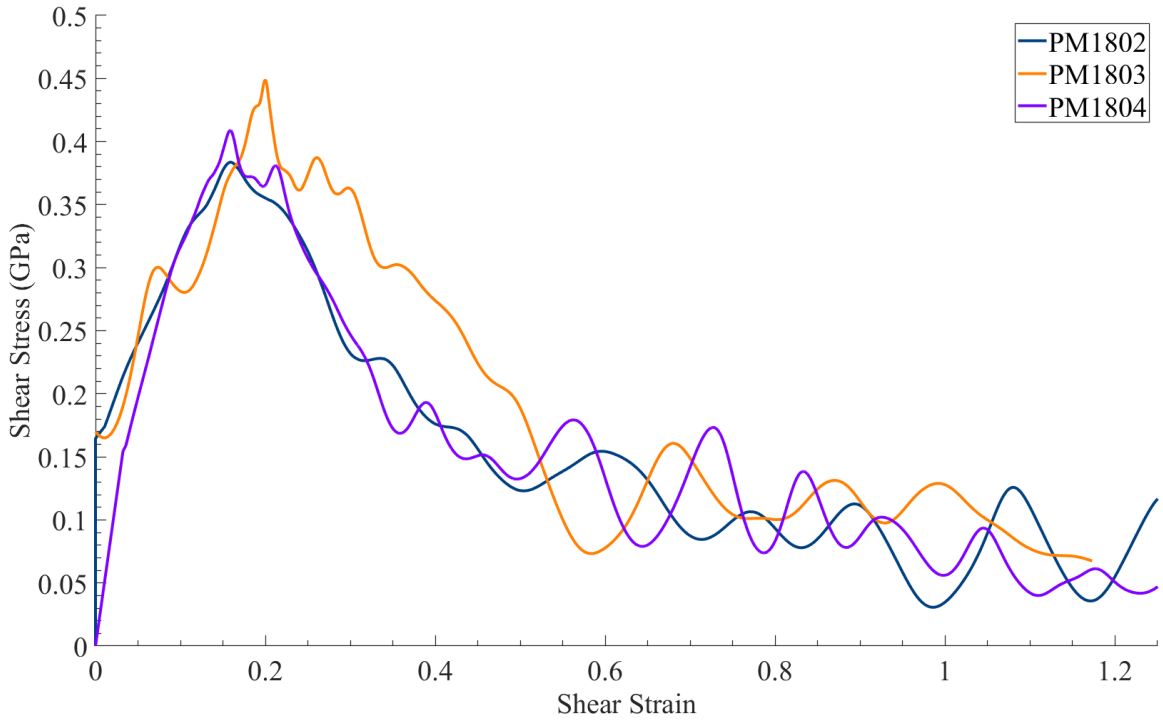

Figure 3.16 Shear stress vs shear strain for low pressure shots

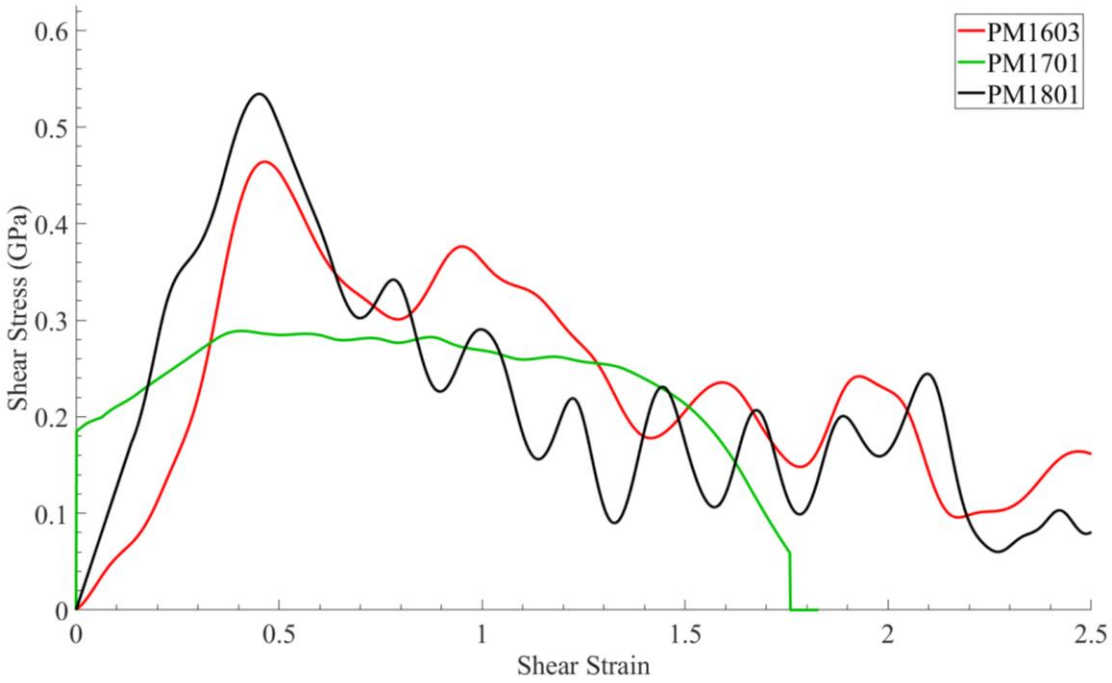

Figure 3.17 Shear stress vs shear strain for high pressure shots

3.4 Discussion

The shear strength of an energetic crystal simulant, i.e. sucrose has been investigated through pressure-shear plate impact experiments. To the best of our knowledge, this is the first investigation of its kind. Experiments have been performed at two different nominal normal stress values: 3 and 9.5 GPa, with nominal shear strain-rates of $1.5 - 2 \times 10^6\ s^{-1}$ and $3 \times 10^6\ s^{-1}$ for the low and high-pressure cases respectively. Normal stress shows an initial elastic precursor, followed by a sharp rise to the plateau. Unlike the HTPB experiments, no reverberations are picked up in the normal velocity profiles, due to extreme thinness of the samples. The shear strength of sucrose shows a peak value followed by a dramatic drop after reaching a critical strain. The peak shear stress and the shear stress drop are consistently observed at both low and high pressures, although the critical strain at which the drop occurs

varies with pressure. Such softening of the shear response of sucrose may be attributed to thermo-viscoplastic instabilities such as adiabatic shear bandings, which results in localized deformation of the specimen. It is worth noting that formation of adiabatic shear bands is a key mechanism of hot-spot formation in energetic crystals. The reported measurements on sucrose motivate the need to study the shear strength behavior of actual energetic crystals under high-pressures and strain-rates. It should also be noted that peak shear strength of sucrose is not very pressure-sensitive, which is in stark contrast to the HTPB binder. Moreover, the shear strength of HTPB is equivalent to that of sucrose at a nominal normal stress of 9 GPa and is expected to exceed that of sucrose for higher normal stresses, making sucrose softer of the two phases. Such a change in relative pressure-sensitivity of the two phases of a PBX can have potential implications for a change in deformation mechanisms, localization behavior and formation of hot-spots.

3.5 Appendix A: X-Ray diffraction studies of sucrose specimen

To make sure that the sucrose layer obtained using the spin-coating method is crystalline, an X-Ray Diffraction (XRD) study is conducted as shown in Figure 3.18. Figure 3.18 (a) shows that XRD intensity peaks for different spin-coated samples overlap, indicating consistency across different samples and different spots on the samples. It is evident from Figure 3.18 (b) that the spin-coated sample shows most of the peaks corresponding to powdered sucrose although with lower relative intensities. So, it is reasonable to believe that spin-coating gives a crystalline sample.

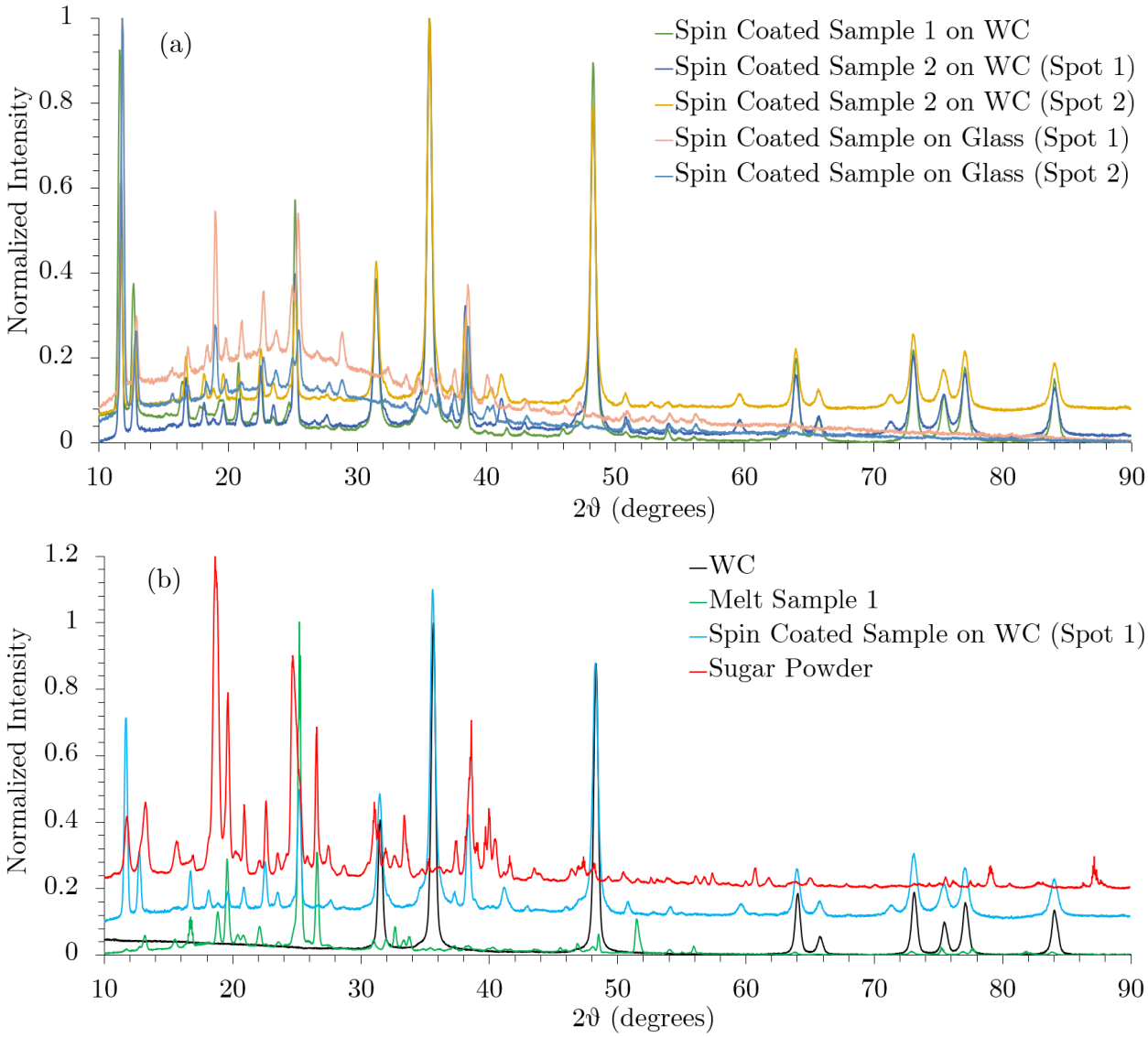

Figure 3.18 (a) XRD intensity plot for spin-coated sucrose samples. The agreement between the intensity peaks is good. (b) XRD intensity plot for WC, a melt sucrose sample, a spin-coated sucrose sample and sucrose powder. Spin-coated sample shows most of the peaks displayed by the crystalline sucrose powder, although at a lower intensity. Note that the thickness of sucrose for the spin-coated sample is ~18 μm while that for the melt sample is ~400 μm. Therefore, the spin-coated sample might show some peaks corresponding to the WC substrate

Chapter 4

Sucrose: Constitutive Modeling

4.1 Introduction

Energetic crystals such as HMX, RDX and PETN and their simulants such as sucrose are in general complex molecular crystals, characterized by anisotropic crystal structures and complex molecular arrangements. As a result, the response of such molecular crystals to mechanical loading is inherently complex. However, in order to model the material response and capture the physics behind phenomena such as pore collapse and subsequent chemical reactions, it is imperative to retain maximum features of a most generalized model albeit at the expense of complexity and computational resources expended. A general material model for such molecular crystals should incorporate: (a) a finite deformation framework, (b) non-linear anisotropic thermo-elasticity, i.e. have anisotropic elastic moduli which are dependent on pressure and temperature in general, and the ability to handle finite non-linear elastic deformations under large pressures through a complete equation of state, (c) plastic anisotropy, typically modeled using the crystal plasticity approach, and (d) thermo-elastic heat generation and plastic dissipation.

Multiple researchers have taken up the task of including one or more of the above-mentioned features into constitutive modeling of materials subject to extreme dynamic environments. Since the applications of interest involve large deformations, only finite

deformation models are reviewed here. Barton et al. (2009) employ an anisotropic thermo-elastic model coupled with crystal plasticity to model pore collapse in HMX although pressure and temperature-dependent moduli are not used and a constant specific heat capacity is assumed. Austin et al. (2015) extend the model by Barton et al. (2009) to incorporate temperature-dependent specific heat and couple chemical kinetics to simulate pore-collapse and consequent shear band formation. The effect of including crystal anisotropy and a rate-dependent model on shear band formation are analyzed and it is shown that a rate-independent model does not lead to shear band formation in the pore-collapse process, thus altering the mechanical signatures and subsequent chemical decomposition reactions. Use of pressure-dependent elastic moduli by Becker (2004), Luscher et al. (2013), Wang et al. (2016) enables them to capture large volumetric strains and evolution of shocks from steep pressure gradients. All the above references use crystal-plasticity to model the anisotropic plastic response. Clayton (2014) presents a thermodynamics-driven approach to modeling large deformations in hard anisotropic materials such as sapphire, diamond and quartz and incorporates all the aforementioned features of a general constitutive model. However, validating such a model requires a large number of experimentally characterized material constants which may not be feasible for all materials.

This chapter focuses on developing a thermodynamically consistent framework for finite deformation modeling of sucrose. The framework presented here is generic and can be used for any isotropic material subject to extreme dynamic environments involving high pressures, large strain-rates and strains, both in compressive and shear loading scenarios. In Section 4.2, a thermodynamics-based foundation for constitutive modeling of a solid is laid. This is followed by

a description of an isotropic thermoelastic, thermo-viscoplastic material model in section 4.3. An isotropic model of sucrose is presented for two main reasons, apart from its simplicity, (a) lack of characterization of anisotropic elastic constants of sucrose, and (b) use of polycrystalline samples in PSPI experiments. Logarithmic strains are employed in constitutive modeling because of its ease of additive decomposition of Cauchy stress into volumetric and deviatoric components even at finite strains, which is not possible with the Green-Lagrange strain tensor, as alluded to by Becker (2004) and Barton et al. (2008) . This makes it easier to handle volumetric and deviatoric responses separately and incorporate a complete equation of state into the framework. Since energetic crystals and their simulants are routinely subject to shock conditions, it is imperative to make material models that are able to faithfully represent mechanical and thermal behavior under these conditions. As a result, a complete Mie-Gruneisen equation of state, with a temperature-dependent specific heat capacity, is derived and implemented in section 4.4, to the lay a foundation for a temperature-coupled elastic behavior under large pressures. In section 4.2.5, it is shown that the temperature evolution equation involves two important terms, i.e. rate of thermo-elastic heating and rate of plastic dissipation, apart from thermal conduction. In section 4.5, an analytic expression for thermo-elastic heating is derived. Based on the complete equation of state, analytic expressions for different types of loading such as isothermal, isentropic and shock are derived without strength considerations in sections 4.6, 4.7 and 4.8 respectively and compared in section 4.9. The complete Mie-Gruneisen equation of state uses an isothermal 3^{rd}-order Birch Murnaghan equation of state as its reference curve. Section 10 presents a derivation for the Birch-Murnaghan equation of state using logarithmic strains, consistent with the constitutive modeling. Using logarithmic strains also has advantages at high pressures as shown by Anand (1979), (1986), Poirier and Tarantola

(1998) and Clayton (2014) . Note that the constitutive model for sucrose utilizes several material constants, not all of which are experimentally validated through PSPI experiments. Therefore, it is important to justify their choice based on experimental and theoretical observations of other researchers. The choice of material constants is discussed in detail in Chapter 5 where the results of simulations using material model laid out in this chapter are discussed.

In addition to the above, it must be noted that molecular crystals such as RDX, HMX and sucrose undergo complicated transformations like phase change and chemical decomposition under extreme environments. Adequate representation of such complex behaviors requires consideration of additional physics and multi-phase models, which are not the focus of present work.

4.2 Thermodynamics of a solid

4.2.1 Kinematics

Consider a body occupying a region of space, $\mathcal{B}_0$ in the reference/undeformed configuration. The body is then subjected to a motion, $\boldsymbol{x} = \boldsymbol{\chi}(\boldsymbol{X}, t)$ so that it now occupies a region of space, $\mathcal{B}_t$ at time t in the spatial/deformed configuration. The deformation gradient is then given as:

$$\boldsymbol{F} = \boldsymbol{\nabla}\boldsymbol{\chi} \tag{4.1}$$

where $\boldsymbol{\nabla}$ denotes gradient with respect to the material coordinates, $\mathbf{X}$ in the undeformed body. $\boldsymbol{F}$ can be multiplicatively decomposed into elastic and plastic parts, $\boldsymbol{F^e}$ and $\boldsymbol{F^p}$ respectively (commonly referred to as Kroner decomposition):

$$\boldsymbol{F} = \boldsymbol{F^e F^p} \tag{4.2}$$

Material coordinates are first transformed to an intermediate configuration by $\boldsymbol{F^p}$ and then to the deformed configuration by $\boldsymbol{F^e}$. It is assumed that only the elastic deformation can lead to a change in volume, i.e.

$$J^e \equiv det(\boldsymbol{F^e}) > 0 \tag{4.3}$$

and the plastic deformation is incompressible, i.e.

$$J^p \equiv det(\boldsymbol{F^p}) = 1 \tag{4.4}$$

The right Polar decomposition of $\boldsymbol{F^e}$ is given as:

$$\boldsymbol{F^e} = \boldsymbol{R^e U^e} \tag{4.5}$$

where $\boldsymbol{R^e}$ is the rotation tensor and $\boldsymbol{U^e}$ is a symmetric positive-definite tensor, called the elastic right stretch tensor. The spatial velocity gradient, $\boldsymbol{L}$ defined as:

$$\boldsymbol{L} \equiv \boldsymbol{grad}\, \boldsymbol{v} = \dot{\boldsymbol{F}}\boldsymbol{F^{-1}} \tag{4.6}$$

where $\boldsymbol{grad}$ represents the gradient in with respect to the spatial point, $\boldsymbol{x}$ in the deformed body. Substituting the Kroner decomposition of deformation gradient from equation (4.2) into equation (4.6), the velocity gradient can be decomposed as:

$$\boldsymbol{L} = \dot{\boldsymbol{F}}^{\boldsymbol{e}}\boldsymbol{F^{e-1}} + \boldsymbol{F^e}\dot{\boldsymbol{F}}^{\boldsymbol{p}}\boldsymbol{F^{p-1}F^{e-1}} = \boldsymbol{L^e} + \boldsymbol{F^e L^p F^{e-1}} \tag{4.7}$$

with $\boldsymbol{L^e} = \dot{\boldsymbol{F}}^{\boldsymbol{e}}\boldsymbol{F^{e-1}}$ and $\boldsymbol{L^p} = \dot{\boldsymbol{F}}^{\boldsymbol{p}}\boldsymbol{F^{p-1}}$. The rate of stretching ($\boldsymbol{D}$) and spin ($\boldsymbol{W}$) components of $\boldsymbol{L^e}$ and $\boldsymbol{L^p}$ are defined as:

$$\boldsymbol{D^e} \equiv sym(\boldsymbol{L^e}) \tag{4.8}$$

$$\boldsymbol{W^e} \equiv skw(\boldsymbol{L^e})$$

$$\boldsymbol{D^p} \equiv sym(\boldsymbol{L^p})$$

$$\boldsymbol{W^p} \equiv skw(\boldsymbol{L^p})$$

It is assumed that the plastic flow is irrotational, i.e.

$$\boldsymbol{W^p} = \boldsymbol{0} \tag{4.9}$$

so that $\boldsymbol{L^p} = \boldsymbol{D^p}$.

4.2.2 First Law of Thermodynamics

The First Law of Thermodynamics states that the change in internal energy of an isolated system is equal to the work done on the system plus the heat added to the system. In the reference configuration, the local form of first law is written as:

$$\dot{e_R} = \boldsymbol{T_0}: \dot{\boldsymbol{F}} - Div\,(\boldsymbol{q_R}) + r_R \tag{4.10}$$

where subscript 'R' indicates reference configuration. e_R is the internal energy per unit volume, $\boldsymbol{q_R}$ is the heat flux vector and r_R is the heat supply per unit volume. $\boldsymbol{T_0}$ is the unsymmetric 1st Piola-Kirchhoff stress tensor and $\boldsymbol{T_0}: \dot{\boldsymbol{F}}$ is the stress power. Stress power can also be written in terms of Cauchy stress as:

$$\boldsymbol{T_0}: \dot{\boldsymbol{F}} = J\boldsymbol{T}\boldsymbol{F^{-T}}: \dot{\boldsymbol{F}} = J^e\boldsymbol{T}: \dot{\boldsymbol{F}}\boldsymbol{F^{-1}} = J^e\boldsymbol{T}: \boldsymbol{L} \tag{4.11}$$

Hence, the first law can be re-written as:

$$\dot{e_R} = J\boldsymbol{T}: \boldsymbol{L} - Div\,(\boldsymbol{q_R}) + r_R \tag{4.12}$$

4.2.3 Second Law of Thermodynamics

The Second Law of Thermodynamics states that the net entropy production of an isolated system is non-negative. Therefore, the local form of the second law in the reference configuration is written as:

$$\delta_{\mathrm{R}} = \dot{\eta}_R + Div\left(\frac{\boldsymbol{q_R}}{\theta}\right) - \frac{r_R}{\theta} \geq 0 \tag{4.13}$$

where η_R is entropy per unit volume, δ_R is entropy production rate per unit volume, and θ is the temperature. The first term on the right is the rate of change of internal entropy of the system and the second and third terms on the right add up to the entropy flow into the system.

4.2.4 Free-energy Imbalance

The Helmholtz free energy is related to the internal energy and entropy through the following relation:

$$\psi_R = e_R - \eta_R\theta \tag{4.14}$$

where ψ_R is the Helmholtz energy per unit volume. Hence, the rate of change of free energy can be written as:

$$\dot{\psi_R} = \dot{e_R} - \dot{\eta_R}\theta - \eta_R\dot{\theta} \tag{4.15}$$

Substitute $\dot{e_R}$ from equation (4.12) and $\dot{\eta_R}$ from equation (4.13) into equation (4.15):

$$\dot{\psi_R} + \eta_R\dot{\theta} - J\boldsymbol{T}:\boldsymbol{L} + \frac{1}{\theta}\boldsymbol{q_R}.\boldsymbol{\nabla}\theta = -\theta\delta_R \leq 0 \tag{4.16}$$

Equation (4.16) is called the local free-energy imbalance inequality. $\theta\delta_R$ represents dissipation per unit volume and the free-energy imbalance states that dissipation is non-negative.

Two new stress measures are derived from the Cauchy stress tensor, T. Consider the stress power term $\boldsymbol{JT}:\boldsymbol{L}$. Using equation (4.7), the stress power can be decomposed into elastic and plastic terms:

$$\boldsymbol{JT}:\boldsymbol{L} = \boldsymbol{JT}:\boldsymbol{L^e} + \boldsymbol{JT}:\boldsymbol{F^e L^p F^{e-1}} = \boldsymbol{JT}:\boldsymbol{D^e} + \boldsymbol{JF^{eT} T F^{e-T}}:\boldsymbol{L^p} \tag{4.17}$$

Since the strains are defined in the reference configuration in terms of U, $\boldsymbol{D^e}$ is found in terms of $\dot{\boldsymbol{U}}^{\boldsymbol{e}}$ or $\dot{\boldsymbol{C}}^{\boldsymbol{e}}$. Consider the time derivative of the Right Cauchy Green tensor, $\dot{\boldsymbol{C}}^{\boldsymbol{e}}$:

$$\dot{\boldsymbol{C}}^{\boldsymbol{e}} = \overline{\boldsymbol{F^{e\dot{T}} F^e}} = \boldsymbol{F^{eT}}\left(\boldsymbol{L^e} + \boldsymbol{L^{eT}}\right)\boldsymbol{F^e} = 2\boldsymbol{F^{eT} D^e F^e} \tag{4.18}$$

$$\Longrightarrow \boldsymbol{D^e} = \frac{1}{2}\boldsymbol{F^{e-T}}\dot{\boldsymbol{C}}^{\boldsymbol{e}}\boldsymbol{F^{e-1}} \tag{4.19}$$

Substituting $\boldsymbol{D^e}$ from (4.19) into (4.17), we have:

$$\boldsymbol{JT}:\boldsymbol{L} = \left(\boldsymbol{JF^{e-1} T F^{e-T}}\right):\frac{\dot{\boldsymbol{C}}^{\boldsymbol{e}}}{2} + \left(\boldsymbol{JF^{eT} T F^{e-T}}\right):\boldsymbol{L^p} \tag{4.20}$$

At this juncture, two new stress measures are defined:

$$\boldsymbol{T^e} = \boldsymbol{JF^{e-1} T F^{e-T}} \tag{4.21}$$

$$\boldsymbol{M^e} = \boldsymbol{JF^{eT} T F^{e-T}} = \boldsymbol{C^e T^e} \tag{4.22}$$

where $\boldsymbol{T^e}$ is the symmetric elastic 2nd Piola-Kirchhoff stress, and $\boldsymbol{M^e}$ is the Mandel stress. Hence, the stress power can be re-written as:

$$\boldsymbol{JT}:\boldsymbol{L} = \boldsymbol{T^e}:\frac{\dot{\boldsymbol{C}}^{\boldsymbol{e}}}{2} + \boldsymbol{M^e}:\boldsymbol{L^p} \tag{4.23}$$

Re-writing the first law from equation (4.12) in terms of the two new stress measures introduced above:

$$\dot{e_R} = \boldsymbol{T^e}:\frac{\dot{\boldsymbol{C}}^{\boldsymbol{e}}}{2} + \boldsymbol{M^e}:\boldsymbol{L^p} - Div\left(\boldsymbol{q_R}\right) + r_R \tag{4.24}$$

The constitutive laws for e_R, ψ_R, $\boldsymbol{T^e}$, $\boldsymbol{M^e}$ are assumed to be functions of the same set of variables $(\boldsymbol{C^e}, \theta, \boldsymbol{\nabla\theta}, \boldsymbol{\xi})$ where $\boldsymbol{\xi}$ represents the list of internal state variables.

$$
\begin{aligned}
e_R &= \hat{e}_R(\boldsymbol{C^e}, \theta, \boldsymbol{\nabla}\theta, \boldsymbol{\xi}) \\
\psi_R &= \hat{\psi}_R(\boldsymbol{C^e}, \theta, \boldsymbol{\nabla}\theta, \boldsymbol{\xi}) \\
\eta_R &= \hat{\eta}_R(\boldsymbol{C^e}, \theta, \boldsymbol{\nabla}\theta, \boldsymbol{\xi}) \\
\boldsymbol{T^e} &= \widehat{\boldsymbol{T^e}}(\boldsymbol{C^e}, \theta, \boldsymbol{\nabla}\theta, \boldsymbol{\xi}) \\
\boldsymbol{M^e} &= \widehat{\boldsymbol{M^e}}(\boldsymbol{C^e}, \theta, \boldsymbol{\nabla}\theta, \boldsymbol{\xi})
\end{aligned}
\tag{4.25}
$$

Taking the time derivative of the free energy,

$$
\dot{\psi_R} = \frac{\partial \hat{\psi}_R}{\partial \boldsymbol{C^e}} : \dot{\boldsymbol{C^e}} + \frac{\partial \hat{\psi}_R}{\partial \theta}\dot{\theta} + \frac{\partial \hat{\psi}_R}{\partial \boldsymbol{\nabla}\theta} . \dot{\overline{\boldsymbol{\nabla}\theta}} + \frac{\partial \hat{\psi}_R}{\partial \boldsymbol{\xi}} * \dot{\boldsymbol{\xi}} \tag{4.26}
$$

where '$*$' denotes the appropriate scalar product considering the order of $\boldsymbol{\xi}$. Using equation (4.16), the rate of change of free energy can also be written as:

$$
\dot{\psi_R} = \boldsymbol{T^e} : \frac{\dot{\boldsymbol{C^e}}}{2} + \boldsymbol{M^e} : \boldsymbol{L^p} - \eta_R\dot{\theta} - \frac{1}{\theta}\boldsymbol{q_R} . \boldsymbol{\nabla}\theta - \theta\delta_R \tag{4.27}
$$

Combining equations (4.26) and (4.27),

$$
\begin{aligned}
&\left(\frac{\partial \hat{\psi}_R}{\partial \boldsymbol{C^e}} - \boldsymbol{T^e}\right) : \dot{\boldsymbol{C^e}} + \left(\frac{\partial \hat{\psi}_R}{\partial \theta} + \eta_R\right)\dot{\theta} + \frac{\partial \hat{\psi}_R}{\partial \boldsymbol{\nabla}\theta} . \dot{\overline{\boldsymbol{\nabla}\theta}} + \left(\frac{\partial \hat{\psi}_R}{\partial \boldsymbol{\xi}} * \dot{\boldsymbol{\xi}} + \frac{1}{\theta}\boldsymbol{q} . \boldsymbol{\nabla}\theta - \boldsymbol{M^e} : \boldsymbol{L^p} + \theta\delta_{\mathrm{R}}\right) \\
&\qquad = 0
\end{aligned}
\tag{4.28}
$$

Using the Coleman-Noll procedure, one can deduce the following definitions for stress and entropy:

$$
\boldsymbol{T^e} = 2\frac{\partial \hat{\psi}_R}{\partial \boldsymbol{C^e}} \tag{4.29}
$$

$$
\eta_R = -\frac{\partial \hat{\psi}_R}{\partial \theta} \tag{4.30}
$$

$$
\frac{\partial \hat{\psi}_R}{\partial \boldsymbol{\nabla}\theta} = \boldsymbol{0} \tag{4.31}
$$

In view of the above relations, the second law reduces to:

$$
\frac{\partial \hat{\psi}_R}{\partial \boldsymbol{\xi}} * \dot{\boldsymbol{\xi}} + \frac{1}{\theta}\boldsymbol{q_R} . \boldsymbol{\nabla}\theta - \boldsymbol{M^e} : \boldsymbol{L^p} = -\theta\delta_{\mathrm{R}} \leq 0 \tag{4.32}
$$

4.2.5 Temperature Evolution Equation

In this section, a partial differential equation that dictates the evolution of temperature during a thermally-coupled mechanical deformation is derived. Consider the time derivative of internal energy and use the thermodynamic relations derived in equations (4.29) and (4.30).

$$\begin{aligned}
\dot{e}_R &= \dot{\psi}_R + \theta\dot{\eta}_R + \dot{\theta}\eta_R \\
\dot{e}_R &= \frac{\partial\hat{\psi}_R}{\partial \boldsymbol{C}^e} : \dot{\boldsymbol{C}}^{\boldsymbol{e}} + \frac{\partial\hat{\psi}_R}{\partial\theta}\dot{\theta} + \frac{\partial\hat{\psi}_R}{\partial\boldsymbol{\xi}} * \dot{\boldsymbol{\xi}} - \theta\overline{\frac{\partial\dot{\hat{\psi}}_R}{\partial\theta}} + \dot{\theta}\eta_R \\
\dot{e}_R &= \frac{\boldsymbol{T}^{\boldsymbol{e}}}{2} : \dot{\boldsymbol{C}}^{\boldsymbol{e}} + \frac{\partial\hat{\psi}_R}{\partial\boldsymbol{\xi}} * \dot{\boldsymbol{\xi}} - \frac{\theta}{2}\frac{\partial\boldsymbol{T}^{\boldsymbol{e}}}{\partial\theta} : \dot{\boldsymbol{C}}^{\boldsymbol{e}} - \theta\frac{\partial^2\hat{\psi}_R}{\partial\theta^2}\dot{\theta} - \theta\frac{\partial^2\hat{\psi}_R}{\partial\boldsymbol{\xi}\partial\theta} * \dot{\boldsymbol{\xi}} \\
\dot{e}_R &= \frac{\boldsymbol{T}^{\boldsymbol{e}}}{2} : \dot{\boldsymbol{C}}^{\boldsymbol{e}} - \frac{\theta}{2}\frac{\partial\boldsymbol{T}^{\boldsymbol{e}}}{\partial\theta} : \dot{\boldsymbol{C}}^{\boldsymbol{e}} + \left(\frac{\partial\hat{\psi}_R}{\partial\boldsymbol{\xi}} - \theta\frac{\partial^2\hat{\psi}_R}{\partial\boldsymbol{\xi}\partial\theta}\right) * \dot{\boldsymbol{\xi}} - \theta\frac{\partial^2\hat{\psi}_R}{\partial\theta^2}\dot{\theta}
\end{aligned} \tag{4.33}$$

Substituting $\dot{e}_R$ from the first law (equation (4.24)) and rearranging terms,

$$-Div\,(\boldsymbol{q_R}) + r_R + \underbrace{\left(\frac{\theta}{2}\frac{\partial\boldsymbol{T}^{\boldsymbol{e}}}{\partial\theta} : \dot{\boldsymbol{C}}^{\boldsymbol{e}}\right)}_{\dot{q}^e} + \underbrace{\left[\boldsymbol{M}^{\boldsymbol{e}} : \boldsymbol{L}^{\boldsymbol{p}} - \left(\frac{\partial\hat{\psi}_R}{\partial\boldsymbol{\xi}} - \theta\frac{\partial^2\hat{\psi}_R}{\partial\boldsymbol{\xi}\partial\theta}\right) * \dot{\boldsymbol{\xi}}\right]}_{\dot{q}^p} = \underbrace{-\theta\frac{\partial^2\hat{\psi}_R}{\partial\theta^2}\dot{\theta}}_{c_R\dot{\theta}} \tag{4.34}$$

$$-Div\,(\boldsymbol{q_R}) + r_R + \dot{q}^e + \dot{q}^p = c_R\dot{\theta} \tag{4.35}$$

where $\dot{q}^e$ is rate of heating due to thermo-elasticity, $\dot{q}^p$ represents rate of inelastic heating and c_R is the referential specific heat capacity, defined at constant strain and constant internal variables. More specifically, c_R is specific heat capacity times the reference density. Equation (4.34) is the evolution equation for temperature. The first term in the expression for $\dot{q}^p$, i.e. $\boldsymbol{M}^{\boldsymbol{e}} : \boldsymbol{L}^{\boldsymbol{p}}$ represents rate of plastic work while the remainder of $\dot{q}^p$ represents the rate of change of internal energy of cold work ($\left(\frac{\partial\hat{\psi}_R}{\partial\boldsymbol{\xi}} - \theta\frac{\partial^2\hat{\psi}_R}{\partial\boldsymbol{\xi}\partial\theta}\right) * \dot{\boldsymbol{\xi}}$) (Rosakis et al. (2000)). A parameter, β, is defined as follows which quantifies the amount of plastic work converted to heat, i.e.

$$\beta = \frac{\dot{q_p}}{\boldsymbol{M}^{\boldsymbol{e}} : \boldsymbol{L}^{\boldsymbol{p}}} \tag{4.36}$$

β is often called the Taylor-Quinney coefficient. β is dependent on the evolution of internal variables that describe density of defects such as dislocations. Trial experiments on metals by Hodowany et al. (2000) show that β increases with increasing plastic strain and becomes constant after a saturation is achieved in dislocation density. However, due to difficulty of experimental characterization of β, a constant value is typically assumed in literature.

A new measure of thermomechanical coupling, called the Gruneisen tensor, is defined:

$$\boldsymbol{\Gamma}_{\mathrm{R}} = -\frac{1}{c_R}\left(\frac{\partial \boldsymbol{T}^{\boldsymbol{e}}}{\partial \theta}\right)_{\boldsymbol{C}^{\boldsymbol{e}},\boldsymbol{\xi}} \tag{4.37}$$

Fourier's Law of heat conduction gives the following relation between heat flux and temperature gradient:

$$\boldsymbol{q_R} = -k\boldsymbol{\nabla}\theta \tag{4.38}$$

where k is the thermal conductivity. Ideally, the thermal conductivity is a tensor dependent on temperature. However, thermal isotropy and no dependence of thermal conductivity on temperature are assumed, which may be justified for moderate temperature changes.

Substituting relations from equations (4.36), (4.37) and (4.38) into equation (4.34) and ignoring the heat supply term (i.e. $r_R = 0$),

$$k\nabla^2\theta - \frac{c_R\theta}{2}\boldsymbol{\Gamma}_{\mathrm{R}}\colon \dot{\boldsymbol{C}}^{\boldsymbol{e}} + \beta \boldsymbol{M}^{\boldsymbol{e}}\colon \boldsymbol{L}^{\boldsymbol{p}} = c_R\dot{\theta} \tag{4.39}$$

Assuming plastic irrotationality (equation (4.9)), we have $\boldsymbol{L}^{\boldsymbol{p}} = \boldsymbol{D}^{\boldsymbol{p}}$. Using a co-directional flow rule, the plastic stretch-rate, $\boldsymbol{D}^{\boldsymbol{p}}$ can be written as:

$$\boldsymbol{D}^{\boldsymbol{p}} = \frac{3}{2}\,\dot{\bar{\epsilon}}^{p}\,\frac{\boldsymbol{M}_{\boldsymbol{0}}^{\boldsymbol{e}}}{\bar{\sigma}} \tag{4.40}$$

where $\boldsymbol{M_0^e}$ is the deviatoric portion of Mandel stress, $\dot{\epsilon}^p$ is the effective plastic strain rate and $\bar{\sigma}$ is the effective stress, defined below:

$$\dot{\epsilon}^p = \sqrt{\frac{2}{3}}|\boldsymbol{D^p}| \tag{4.41}$$

$$\bar{\sigma} = \sqrt{\frac{3}{2}}\,|\boldsymbol{M_0^e}| \tag{4.42}$$

Hence, the rate of plastic work can be simplified as:

$$\boldsymbol{M^e}\!:\boldsymbol{L^p} = \boldsymbol{M^e}\!:\boldsymbol{D^p} = \bar{\sigma}\dot{\epsilon}^p \tag{4.43}$$

The temperature evolution can then be put into a simplified form below:

$$k\nabla^2\theta - \frac{c\theta}{2}\boldsymbol{\Gamma}_{\mathrm{R}}\!:\dot{\boldsymbol{C}}^{\boldsymbol{e}} + \beta\bar{\sigma}\dot{\epsilon}^p = c_R\dot{\theta} \tag{4.44}$$

If the first and second laws of thermodynamics are expressed spatially, the temperature evolution equation can be derived to be the following expression:

$$-\boldsymbol{div}\,(\boldsymbol{q}) + r + \underbrace{\left(\frac{\theta}{2J}\frac{\partial \boldsymbol{T^e}}{\partial\theta}\!:\dot{\boldsymbol{C}}^{\boldsymbol{e}}\right)}_{\dot{q}^e} + \underbrace{\left[\frac{1}{J}\boldsymbol{M^e}\!:\boldsymbol{L^p} - \rho\left(\frac{\partial\psi}{\partial\boldsymbol{\xi}} - \theta\frac{\partial^2\psi}{\partial\boldsymbol{\xi}\partial\theta}\right) * \dot{\boldsymbol{\xi}}\right]}_{\dot{q}^p} = \underbrace{-\rho\theta\frac{\partial^2\psi}{\partial\theta^2}\dot{\theta}}_{\rho c\dot{\theta}} \tag{4.45}$$

where $\boldsymbol{q}$ is the heat flux, r is the heat supply per unit volume, ψ is the Helmholtz free energy per unit mass and c is the specific heat in J/kg K. All the quantities are expressed spatially. $\boldsymbol{div}$ represents divergence in spatial coordinates. Using Fourier's Law ($\boldsymbol{q} = -k\,\boldsymbol{grad}\theta$), the temperature evolution equation can be re-written as:

$$k\,\boldsymbol{grad}^2\theta + r + \dot{q}^e + \dot{q}^p = \rho c\dot{\theta} \tag{4.46}$$

4.3 Constitutive Modeling

The constitutive model is defined in terms of a logarithmic strain in the intermediate configuration. It is defined below, in terms of the right stretch tensor, $\boldsymbol{U^e}$.

$$\boldsymbol{E^e} \equiv ln(\boldsymbol{U^e}) \tag{4.47}$$

Logarithmic strains are used because they facilitate an additive decoupling of volumetric and deviatoric strains under large pressures which is not possible with Green-Lagrange Strains. Furthermore, with the use of a correct invariant basis, the stress terms can also be decomposed into pressure and deviatoric response terms, as shown below. Such a decomposition is very helpful in a direct incorporation of a complete equation of state, which is typically measured through a separate set of experiments. Moreover, logarithmic strains require fewer higher order constants to fit the experimental data under high pressures, as shown by Poirier and Tarantola (1998) and Clayton (2014) .

Assuming that the material is isotropic, the constitutive response of sucrose is defined though an elastic free energy per unit volume, ψ_R. In general, ψ_R is a function of the elastic Right Cauchy-Green tensor, $\boldsymbol{C^e}$ and temperature, θ but for an isotropic material, the free energy can be represented in terms of 3 principal stretches ($\psi_R = \tilde{\psi}_R(\lambda_1^e, \lambda_2^e, \lambda_3^e, \theta)$) or 3 principal invariants of $\boldsymbol{C^e}$, ($\psi_R = \tilde{\psi}_R(I_1, I_2, I_3, \theta)$) where $I_1 = tr\boldsymbol{C^e}$, $I_2 = 0.5\left[(tr\boldsymbol{C^e})^2 + tr\boldsymbol{C^{e^2}}\right]$ and $I_3 = \det \boldsymbol{C^e} = J^{e^2}$. Note that the dependence of free energy on internal variables is not considered as the elastic response does not typically depend on the history of plastic response, as is the case with metals. With the (I_1, I_2, I_3) principal invariant based free energy, it is not possible to isolate the effect of each invariant due to the non-orthogonality of different stress response terms, i.e.

$\frac{\partial I_i}{\partial \boldsymbol{C}^e} : \frac{\partial I_j}{\partial \boldsymbol{C}^e} \neq 0$ for $i, j = 1,2,3$ and $i \neq j$. Therefore, the free energy density is written in terms of a new set of logarithmic strain invariants (K_1, K_2, K_3), as proposed by Criscione et al. (2000) . With each of these invariants, one can associate specific aspects of deformation and isolate the effect of each. The first invariant, K_1, defined below represents the volume change.

$$K_1 = tr(\boldsymbol{E}^e) = \ln(J^e) \tag{4.48}$$

where the superscript 'e' represents elastic. The second invariant, K_2 represents the distortional response of the material under constant volume and is defined as the magnitude of deviatoric portion of logarithmic strain.

$$K_2 = |\boldsymbol{E}_0^e| \tag{4.49}$$

Since, $\boldsymbol{E}^e = \frac{K_1}{3}\boldsymbol{I} + \boldsymbol{E}_0^e$, a tensorial direction can be associated with this deviatoric strain invariant:

$$\boldsymbol{N} = \frac{\partial K_2}{\partial \boldsymbol{E}^e} = \frac{\boldsymbol{E}_0^e}{|\boldsymbol{E}_0^e|} \tag{4.50}$$

where $\boldsymbol{N}$ is a unit tensor. Hence, the strain can be written as $\boldsymbol{E}^e = \frac{K_1}{3}\boldsymbol{I} + K_2\boldsymbol{N}$. The third invariant, K_3 represents the mode of distortion and is defined below:

$$K_3 = 3\sqrt{6}\,\det(\boldsymbol{N}) \tag{4.51}$$

It can be noted that $K_1 > 0$ for dilatation and $K_1 < 0$ under compression. $K_2 \geq 0$ always holds whereas $-1 \leq K_3 \leq 1$. $K_3 = 1$ in simple tension, $K_3 = -1$ in simple compression and $K_3 = 0$ in simple shear.

Let $\tilde{\psi}_R(K_1, K_2, K_3, \theta)$ be the free energy density. It can be shown that Mandel stress and logarithmic strain in the intermediate configuration are power conjugates. Hence,

$$\boldsymbol{M^e} = \frac{\partial \tilde{\psi}_R}{\partial \boldsymbol{E^e}} = \left(\frac{\partial \tilde{\psi}_R}{\partial K_1}\frac{\partial K_1}{\partial \boldsymbol{E^e}} + \frac{\partial \tilde{\psi}_R}{\partial K_2}\frac{\partial K_2}{\partial \boldsymbol{E^e}} + \frac{\partial \tilde{\psi}_R}{\partial K_3}\frac{\partial K_3}{\partial \boldsymbol{E^e}}\right) = \left(\frac{\partial \tilde{\psi}_R}{\partial K_1}\boldsymbol{I} + \frac{\partial \tilde{\psi}_R}{\partial K_2}\boldsymbol{N} + \frac{\partial \tilde{\psi}_R}{\partial K_3}\boldsymbol{Y}\right) \tag{4.52}$$

$$\boldsymbol{Y} = 3\sqrt{6}\boldsymbol{N^2} - \sqrt{6}\boldsymbol{I} - 3K_3\boldsymbol{N} \tag{4.53}$$

Since the tensors, $\boldsymbol{C^e}$ and $\boldsymbol{T^e}$ coaxial, i.e. have the same principal directions, Cauchy stress can be found using the definition of Mandel stress in equation (4.22),

$$\boldsymbol{T} = \frac{1}{J}\boldsymbol{R^e}\boldsymbol{M^e}\boldsymbol{R^{eT}} = \frac{1}{J}\left(\frac{\partial \tilde{\psi}_R}{\partial K_1}\boldsymbol{I} + \frac{\partial \tilde{\psi}_R}{\partial K_2}\boldsymbol{N'} + \frac{\partial \tilde{\psi}_R}{\partial K_3}\boldsymbol{Y'}\right) \tag{4.54}$$

where $\boldsymbol{N'} = \boldsymbol{R^e}\boldsymbol{N}\boldsymbol{R^{eT}}$ and $\boldsymbol{Y'} = \boldsymbol{R^e}\boldsymbol{Y}\boldsymbol{R^{eT}}$. Note that $\boldsymbol{N'}:\boldsymbol{I} = \boldsymbol{0}, \boldsymbol{Y'}:\boldsymbol{I} = \boldsymbol{0}$ and $\boldsymbol{N'}:\boldsymbol{Y'} = \boldsymbol{0}$, i.e. the Cauchy stress is composed of three mutually orthogonal terms and each term is dependent on derivative of a different stress invariant. This is facilitated by using a logarithmic strain measure and an appropriate set of invariants for logarithmic strain. So, it is possible to easily isolate the three response terms by contracting with $\boldsymbol{I}, \boldsymbol{N'}$ and $\boldsymbol{Y'}$. Specifically, the first term in (4.54) corresponds to the pressure term while the other two terms add up to give the deviatoric stress.

$$\frac{\boldsymbol{T}:\boldsymbol{I}}{3} = -P = \frac{1}{J}\frac{\partial \tilde{\psi}_R}{\partial K_1} \tag{4.55}$$

So, the pressure term can be isolated from the deviatoric response easily, while retaining the its dependence on all three invariants and temperature, i.e. $P(K_1, K_2, K_3, \theta)$.

The free energy density, $\tilde{\psi}_R(K_1, K_2, K_3, \theta)$ can be additively decomposed into three parts: (a) purely volumetric, $f_1(K_1, \theta)$, (b) purely distortional, $f_2(K_2, K_3, \theta)$ and (c) coupled-volumetric/distortional, $f_3(K_1, \theta)f_4(K_2, K_3, \theta)$, where the temperature dependence is retained in each portion of the free energy density.

$$\tilde{\psi}_R(K_1, K_2, K_3, \theta) = f_1(K_1, \theta) + f_2(K_2, K_3, \theta) + f_3(K_1, \theta)f_4(K_2, K_3, \theta) \tag{4.56}$$

For the purpose of modeling sucrose, consider a simple form of free energy of the following form:

$$\tilde{\psi}_R(K_1, K_2, K_3, \theta) = f_1(K_1, \theta) + G(K_1, \theta)K_2^2 \tag{4.57}$$

where $G(K_1, \theta)$ is the temperature and volumetric strain-dependent shear modulus. The dependence of free energy on K_3 is dropped for simplicity. The first term in the free-energy expression leads to pressure through $P(K_1, \theta) = -\frac{1}{J}\frac{\partial f_1}{\partial K_1} - \frac{1}{J}\frac{\partial G}{\partial K_1}K_2^2$. Pressure is found through a complete equation of state as described in section 4. Generally, the contribution of shear-induced pressure ($-\frac{1}{J}\frac{\partial G}{\partial K_1}K_2^2$) is very small due to small elastic distortional strains and can therefore be ignored. Therefore, the Mandel stress and Cauchy stress for such a free energy density function can be calculated as:

$$\boldsymbol{M^e} = -P(K_1, \theta)J\boldsymbol{I} + 2G(K_1, \theta)K_2\boldsymbol{N} \tag{4.58}$$

$$\boldsymbol{T}(K_1, K_2, \theta) = -P(K_1, \theta)\boldsymbol{I} + \frac{2}{J}G(K_1, \theta)K_2\boldsymbol{N'} \tag{4.59}$$

Typically, the shear modulus is written as a function of pressure and temperature, i.e. $G(P, \theta)$. One of the most commonly used forms of shear modulus is a linear variation with both pressure and temperature, as described by Steinberg et al. (1980) :

$$G(P, \theta) = G_0 + \frac{\partial G}{\partial P}\frac{P}{\left(\frac{\rho}{\rho_0}\right)^{1/3}} + \frac{\partial G}{\partial \theta}(\theta - \theta_0) \tag{4.60}$$

where G_0 is the shear modulus at ambient pressure and temperature. The derivatives of shear modulus with respect to pressure and temperature, i.e. $\frac{\partial G}{\partial P}$ and $\frac{\partial G}{\partial \theta}$ respectively are assumed to be constant by Steinberg et al. (1980) for fitting experimental data of several metals. However, the shear modulus behaviour near melt is not very well known, especially for energetic materials. It is expected that the shear modulus drops to zero after melt. A drastic drop in shear modulus at melt is observed through shear wave measurements by Nadal and Le Poac (2003) . The

Steinberg model in equation (4.60) doesn't necessarily give a zero shear modulus at melt and does not consider the variation of the slope of the shear modulus-temperature curve, i.e. $\frac{\partial G}{\partial \theta}$ with pressure, near the melting point. These issues are addressed by Nadal and Le Poac (2003) who propose the following form of shear modulus based on Lindemann theory at the melting point:

$$G(P,\theta) = \frac{1}{\Im(\theta/\theta_m)}\left[G_0 + \frac{\partial G}{\partial P}\frac{P}{\left(\frac{\rho_S}{\rho_{S0}}\right)^{\frac{1}{3}}}\left(1-\frac{\theta}{\theta_m}\right) + \frac{\rho_S}{Cm}k\theta\right] \tag{4.61}$$

$$\Im\left(\frac{\theta}{\theta_m}\right) \equiv 1 + \exp\left[\frac{\frac{\theta}{\theta_m}-1}{\zeta\left\{1-\frac{\theta}{\theta_m(1+\zeta)}\right\}}\right]; \frac{\theta}{\theta_m} \in [0,1+\zeta] \tag{4.62}$$

where the pre-factor $\Im\left(\frac{\theta}{\theta_m}\right)$ allows fulfilment of the condition that $G = 0$ for $\theta = \theta_m(1+\zeta)$. $\zeta \ll 1$ is a material parameter, ρ_s is the density in solid state, k is the Boltzman constant, m is atomic mass, $C = \frac{(6\pi^2)^{2/3}}{3}f^2$ and f is the Lindemann constant. The linear drop in pressure and temperature away from melting point, as originally proposed by Steinberg et al. (1980) is retained in this model. The material constants in the model can be determined by shear wave velocity measurements at different pressures and temperatures.

Since $\boldsymbol{L^p} = \boldsymbol{D^p}$ and $\boldsymbol{L^p} = \boldsymbol{\dot{F}^p F^{p-1}}$, the evolution of plastic distortion, $\boldsymbol{F^p}$ is given through the following equation:

$$\boldsymbol{\dot{F}^p} = \boldsymbol{D^p F^p} \tag{4.63}$$

The plastic stretching, $\boldsymbol{D^p}$ is then given through a codirectional flow rule, $\boldsymbol{D^p} = \frac{3}{2}\dot{\epsilon}^p \frac{\boldsymbol{M_0^e}}{\bar{\sigma}}$ (equation (4.40)). The effective plastic strain-rate and the equivalent stress are related through a strain-rate and temperature-dependent constitutive law. The Johnson-Cook model is used here:

$$\bar{\sigma} = [A + B(\bar{\epsilon}^p)^n]\left[1 + C\ln\left(\frac{\dot{\bar{\epsilon}}^p}{\dot{\bar{\epsilon}}_0}\right)\right](1 - \hat{\theta}^m) \tag{4.64}$$

where $(A, B, n, C, \dot{\bar{\epsilon}}_0, m)$ are material parameters, $\hat{\theta}$ is a function of temperature, θ and pressure, P defined below:

$$\hat{\theta} = \frac{\theta - \theta_{ref}}{\theta_m(P) - \theta_{ref}} \tag{4.65}$$

θ_{ref} is the reference temperature (usually taken to be the room temperature) and θ_m is the melt temperature.

Since high pressures are applied in the experiments and temperatures are expected to go beyond melting, the dependence of melting temperature on pressure is taken into account. Moreover, the melting point of large organic molecules such as HMX and sucrose is highly dependent on pressure. Numerical simulations of deformation of energetic crystals widely use the Lindemann Law of melting:

$$\theta_m = \theta_{m0}\exp\left[2\Gamma_0(1 - J) + \frac{2}{3}ln(J)\right] \tag{4.66}$$

where θ_{m0} is melting temperature at ambient pressure, Γ_0 is the Gruneisen parameter at ambient pressure and temperature, and $J = \frac{v}{v_0}$ is the compression ratio. v is the final specific volume and v_0 is the initial specific volume. At times, a linearized version of the Lindemann Law in volume, called the Kraut-Kennedy relation is also used.

$$\theta_m = \theta_{m0}\left(1 + a\frac{\Delta v}{v_0}\right) \tag{4.67}$$

where Δv is the reduction in specific volume under compression and a is a constant defined as:

$$a = 2\left(\Gamma_0 - \frac{1}{3}\right) \tag{4.68}$$

However, molecular dynamics simulations on HMX (Kroonblawd and Austin (2020)) indicate that the Lindemann Law grossly underestimates the melting point as a function of temperature. An alternative empirical form obtained by Simon and Glatzel (1929) is then used:

$$\theta_m = \theta_{m0}\left(1 + \frac{P - P_{ref}}{P_0}\right)^{1/d} \tag{4.69}$$

where (P_{ref}, P_0, d) are fitting parameters. The consequences of making a choice between the two forms of melt curve are discussed in detail in Chapter 5.

For completeness of the continuum model, two more issues need to be addressed: (a) phase transition from solid to liquid, and (b) constitutive model of the liquid. One way to model the solid-liquid phase transition is by introducing an order parameter, i.e. a phase-field parameter, as done by Fried and Gurtin (1993) . The stress response of the liquid phase can be decomposed into pressure and deviatoric stress components. While the pressure of the fluid can be described through an appropriate equation of state, the deviatoric stress now depends on the strain-rate through a pre-factor, called the shear viscosity of the liquid. The shear viscosity of the liquid phase is generally a function of pressure and temperature. Both phase transitions and material model for the liquid phase are not a part of the current work but are however important for the prediction of chemical reactions in melt. Since the yield strength in the material model drops rapidly at melt, the strain-rates tend to climb exponentially and become unreasonably large. In the present framework, the shear strain-rates after melt are set to reach an upper limit beyond which they are assumed to stay constant, as done by Grunschel (2009) . See Chapter-5 for more details. The focus of present work remains on the solid phase and its

constitutive modelling. Next, we consider the development of a complete equation of state for the solid.

4.4 Complete Mie-Gruneisen Equation of State

The Mie-Gruneisen equation of state has been one of the most commonly used forms of an equation of state for a solid subjected to shock loading. It is often encountered in hydrocodes, for solids under pressures up to a few megabar. In this section, a derivation of a complete equation of state is presented, i.e. with a temperature dependent specific heat capacity, on line with the work by Menikoff (2016) . It should be noted that the equation of state is derived in the spatial/deformed configuration as opposed to the intermediate configuration used in Section 2 and Section 3. In deriving the equation of state, a state of purely volumetric deformation is assumed.

The Gruneisen model can be derived from the definition of the Gruneisen parameter, Γ:

$$\Gamma \equiv v\left(\frac{\partial P}{\partial e}\right)_{v} \tag{4.70}$$

where the Gruneisen scalar parameter defined above is the volumetric part of the spatial Gruneisen tensor, i.e. $\Gamma = \frac{1}{3} tr(\boldsymbol{\Gamma})$. The spatial Gruneisen tensor is defined below:

$$\boldsymbol{\Gamma} = -\frac{v}{c}\left(\frac{\partial \boldsymbol{T}}{\partial \theta}\right)_{\boldsymbol{C}^{e},\xi} \tag{4.71}$$

$\boldsymbol{T}$ is Cauchy stress and c is the specific heat capacity. If the Gruneisen parameter is assumed to be independent of pressure and specific internal energy, equation (4.70) can be integrated to obtain the usually encountered form of Mie-Gruneisen equation of state.

$$P - P_{ref} = \frac{\Gamma}{v}(e - e_{ref}) \tag{4.72}$$

where P_{ref} and e_{ref} lie on a reference curve.

To specify a complete equation of state, consider the thermodynamic variables like η, e, ψ and P as functions of v and θ, i.e.

$$\begin{aligned} \eta &= \eta(v, \theta) \\ e &= e(v, \theta) \\ \psi &= \psi(v, \theta) \\ P &= P(v, \theta) \end{aligned} \tag{4.73}$$

Starting with an initial state characterized by the set of thermodynamic variables $(v_0, \theta_0, \eta_0, e_0, \psi_0, P_0)$. Let the final thermodynamic state be represented by $(v, \theta, \eta, e, \psi, P)$. Since a complete equation of state should be independent of the thermodynamic path connecting the initial and final states, we choose a path shown in Figure 4.1. The path consists of 2 segments: an isotherm at $\theta = \theta_0$ followed by an isochore at $v = v$.

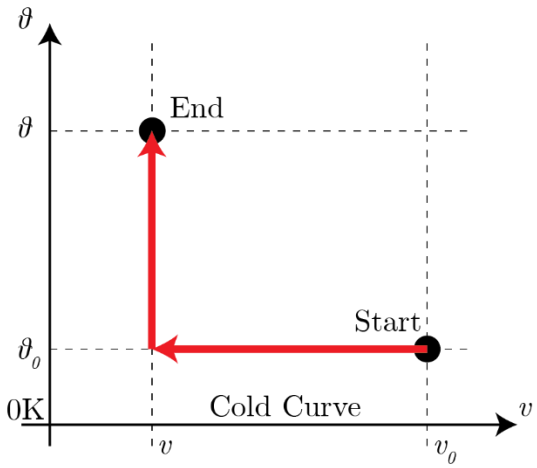

Figure 4.1 A thermodynamic path connecting the initial and final states.

A differential change in entropy can be written as:

$$d\eta = \left(\frac{\partial \eta}{\partial v}\right)_{\theta} dv + \left(\frac{\partial \eta}{\partial \theta}\right)_{v} d\theta \tag{4.74}$$

where subscripts denote the independent variables that are held constant when partial derivatives are taken. The partial derivatives of entropy can be written in terms of known/measurable thermodynamic quantities, Γ and c_v. The specific heat capacity, c_v is defined as:

$$c_v = \left(\frac{\partial e}{\partial \theta}\right)_{v} \tag{4.75}$$

From the first law of thermodynamics, we have,

$$de = -Pdv + \theta d\eta \tag{4.76}$$

If (v, η) are taken as independent variables, then the differential of specific internal energy, $e = e(v, \eta)$, can be written as:

$$de = \left(\frac{\partial e}{\partial v}\right)_{\eta} dv + \left(\frac{\partial e}{\partial \eta}\right)_{v} d\eta \tag{4.77}$$

Since dv and $d\eta$ are arbitrary, pressure and temperature can be defined in terms of partial derivatives of specific internal energy, from equations (4.76) and (4.77).

$$P = -\left(\frac{\partial e}{\partial v}\right)_{\eta} \tag{4.78}$$

$$\theta = \left(\frac{\partial e}{\partial \eta}\right)_{v} \tag{4.79}$$

If (v, θ) are instead chosen as free variables, the differential of specific internal energy and specific entropy can be written as:

$$de = \left(\frac{\partial e}{\partial v}\right)_{\theta} dv + \left(\frac{\partial e}{\partial \theta}\right)_{v} d\theta = \left(\frac{\partial e}{\partial v}\right)_{\theta} dv + c_v d\theta \tag{4.80}$$

$$d\eta = \left(\frac{\partial \eta}{\partial v}\right)_\theta dv + \left(\frac{\partial \eta}{\partial \theta}\right)_v d\theta \tag{4.81}$$

Substituting $d\eta$ from (4.81) into (4.77),

$$de = \left[-P + \theta\left(\frac{\partial \eta}{\partial v}\right)_\theta\right] dv + \left[\theta\left(\frac{\partial \eta}{\partial \theta}\right)_v\right] d\theta \tag{4.82}$$

Comparing (4.80) and (4.82),

$$\left(\frac{\partial e}{\partial v}\right)_\theta = \left[-P + \theta\left(\frac{\partial \eta}{\partial v}\right)_\theta\right] \tag{4.83}$$

$$c_v = \theta\left(\frac{\partial \eta}{\partial \theta}\right)_v \tag{4.84}$$

Using Maxwell's relations, we have

$$\left(\frac{\partial \eta}{\partial v}\right)_\theta = \left(\frac{\partial P}{\partial \theta}\right)_v \tag{4.85}$$

From equations (4.70), (4.84) and (4.85), one can show that

$$\Gamma c_v = v\left(\frac{\partial P}{\partial \theta}\right)_v = v\left(\frac{\partial \eta}{\partial v}\right)_\theta \tag{4.86}$$

Substituting the above relation into equation (4.83), it can be shown that

$$\left(\frac{\partial e}{\partial v}\right)_\theta = \left[-P + \frac{\Gamma c_v \theta}{v}\right] \tag{4.87}$$

Now, the aim is to find a differential change in entropy from equation (4.81) in terms of measurable quantities. Substituting expressions for partial derivatives from equations (4.84) and (4.86) into (4.81):

$$d\eta = \frac{\Gamma c_v}{v} dv + \frac{c_v}{\theta} d\theta \tag{4.88}$$

Integrating the above equation along the thermodynamic path in Figure 4.1, entropy at the final state can be written as:

$$\eta(v,\theta) = \eta_0 + \int_{v_0}^{v} \frac{\Gamma(v',\theta_0)c_v(v',\theta_0)}{v'}dv' + \int_{\theta_0}^{\theta} \frac{c_v(v,\theta')}{\theta'}d\theta' \tag{4.89}$$

where the Gruneisen parameter, Γ and specific heat capacity, c_v are considered as functions of (v,θ). Similarly, consider specific Helmholtz free energy, $\psi(v,\theta)$. Differential change in free energy is given as:

$$d\psi = -Pdv - \eta d\theta \tag{4.90}$$

where

$$P = -\left(\frac{\partial\psi}{\partial v}\right)_\theta \tag{4.91}$$

$$\eta = -\left(\frac{\partial\psi}{\partial\theta}\right)_v \tag{4.92}$$

Integrate equation (4.90) and substitute the expression for entropy, $\eta(v,\theta)$ from equation (4.89).

$$\begin{aligned}\psi(v,\theta) = \psi_0 &- \int_{v_0}^{v} P(v',\theta_0)dv' \\ &- \int_{\theta_0}^{\theta}\left[\eta_0 + \int_{v_0}^{v}\frac{\Gamma(\mathrm{v}',\theta_0)c_v(v',\theta_0)}{v'}dv' + \int_{\theta_0}^{\theta'}\frac{c_v(v,\theta'')}{\theta''}d\theta''\right]d\theta'\end{aligned} \tag{4.93}$$

Integrating the last term in equation (4.93) by parts, one can obtain a general expression for specific free energy:

$$\begin{aligned}\psi(v,\theta) = \psi_0 - \eta_0(\theta-\theta_0) &- \int_{v_0}^{v}\left[P(v',\theta_0) + (\theta-\theta_0)\frac{\Gamma(\mathrm{v}',\theta_0)c_v(v',\theta_0)}{v'}\right]dv' \\ &- \int_{\theta_0}^{\theta}\frac{(\theta-\theta')}{\theta'}c_v(v,\theta')d\theta'\end{aligned} \tag{4.94}$$

Pressure can be obtained from specific free energy, using equation (4.91):

$$P(v,\theta) = -\left(\frac{\partial\psi}{\partial v}\right)_\theta = P(v,\theta_0) + (\theta-\theta_0)\frac{\Gamma(v,\theta_0)c_v(v,\theta_0)}{v} + \int_{\theta_0}^{\theta}\frac{(\theta-\theta')}{\theta'}\frac{\partial c_v(v,\theta')}{\partial v}d\theta' \tag{4.95}$$

Compatibility condition: The Gruneisen coefficient and specific heat are not fully independent. They must obey the thermodynamic compatibility equation derived below.

$$\frac{\partial}{\partial v}\left(\frac{\partial^2 \psi}{\partial \theta^2}\right) = \frac{\partial}{\partial \theta}\left(\frac{\partial^2 \psi}{\partial \theta \partial v}\right) \tag{4.96}$$

To move further, a few thermodynamic identities need to be proved. Internal energy can be written in terms of specific free energy as:

$$e = \psi + \theta\eta \tag{4.97}$$

Therefore, the specific heat is given as (using equation (4.84)):

$$c_v = \left[\frac{\partial(\psi + \theta\eta)}{\partial \theta}\right]_v = \left(\frac{\partial \psi}{\partial \theta}\right)_v + \eta + \theta\left(\frac{\partial \eta}{\partial \theta}\right)_v \tag{4.98}$$

Using the definition of entropy from equation (4.92), equation (4.98) can be re-written as:

$$c_v = -\theta\frac{\partial^2 \psi}{\partial \theta^2} \tag{4.99}$$

Substituting the definition of entropy from equation (4.92) into equation (4.86),

$$\Gamma c_v = -v\frac{\partial^2 \psi}{\partial \theta \partial v} \tag{4.100}$$

Using relations in (4.99) and (4.100), the compatibility condition in equation (4.96) takes the following form.

$$v\frac{\partial c_v}{\partial v} = \theta\frac{\partial(\Gamma c_v)}{\partial \theta} \tag{4.101}$$

Equation (4.101) is called the compatibility condition and relates specific heat to the Gruneisen coefficient.

Using the compatibility condition, the third term in the expression for pressure in (4.95) can be simplified.

$$\int_{\theta_0}^{\theta} \frac{(\theta-\theta')}{\theta'} \frac{\partial c_v(v,\theta')}{\partial v} d\theta' = \int_{\theta_0}^{\theta} \frac{(\theta-\theta')}{v} \frac{\partial [\Gamma(v,\theta')c_v(v,\theta')]}{\partial \theta'} d\theta' \tag{4.102}$$

Apply integration by parts to equation (4.102),

$$\begin{aligned} \int_{\theta_0}^{\theta} \frac{(\theta-\theta')}{\theta'} \frac{\partial c_v(v,\theta')}{\partial v} d\theta' &= \left\{ \frac{(\theta-\theta')}{v} \Gamma(v,\theta')c_v(v,\theta') \right\}_{\theta_0}^{\theta} + \int_{\theta_0}^{\theta} \frac{\Gamma(v,\theta')c_v(v,\theta')}{v} d\theta' \\ &= -(\theta-\theta_0)\frac{\Gamma(v,\theta_0)c_v(v,\theta_0)}{v} + \int_{\theta_0}^{\theta} \frac{\Gamma(v,\theta')c_v(v,\theta')}{v} d\theta' \end{aligned} \tag{4.103}$$

Substitute (4.103) into equation (4.95) to get a simplified form for pressure:

$$P(v,\theta) = P(v,\theta_0) + \frac{1}{v}\int_{\theta_0}^{\theta} \Gamma(v,\theta')c_v(v,\theta')\, d\theta' \tag{4.104}$$

Equation (4.104) is called the complete equation of state and has been obtained without any assumptions so far. To find pressure from this relation, knowledge of the following three items is required:

(1) Isotherm at θ_0, i.e. $P(v,\theta_0)$

(2) Gruneisen parameter, $\Gamma(v,\theta)$

(3) Specific heat, $c_v(v,\theta)$

Equation (4.104) can be further simplified if an assumption on the form of Gruneisen parameter, $\Gamma(v,\theta)$ is made. Let us assume that the Gruneisen parameter is a function of specific volume only, $\Gamma = \Gamma(v)$. As mentioned by Grady (2017) , "*Both theoretical arguments and experience suggest that* Γ *is not sensitive to reasonable excursions of internal energy, E for many materials, and is usually assumed to be a volume-dependent only function,* $\Gamma(v)$*.*" For such a class of materials, the compatibility relation in (4.101) can be written as a hyperbolic partial differential equation in c_v:

$$v\frac{\partial c_v}{\partial v} = \theta\Gamma(v)\frac{\partial c_v}{\partial \theta} \tag{4.105}$$

Therefore, the characteristic curves for the above PDE are a solution to the following ODE:

$$\frac{d\theta}{dv} = -\frac{\Gamma(v)\theta}{v} \tag{4.106}$$

The characteristic curve that passes through the initial state (v_0, θ_0) is $\theta = \theta_0\phi(v)$ and corresponds to an isentrope (shown in section 4.6 below), where the integrating factor, $\phi(v)$ is given as:

$$\phi(v) = \exp\left(-\int_{v_0}^{v}\frac{\Gamma(v')}{v'}dv'\right) \tag{4.107}$$

Specific heat capacity is constant along the characteristic curve, i.e.

$$c_v(v,\theta) = c_v(v_0,\theta_0) = c_v\left(v_0, \frac{\theta}{\phi(v)}\right) = \widetilde{c_v}\left(\frac{\theta}{\phi(v)}\right) = \widetilde{c_v}(\tilde{\theta}) \tag{4.108}$$

where the tilde signifies the scaled temperature, $\tilde{\theta} = \frac{\theta}{\phi(v)}$. Hence, for the class of materials with $\Gamma = \Gamma(v)$, specific heat is a function of single scaled temperature. Therefore, a further simplified form of pressure can be written as:

$$P(v,\theta) = P(v,\theta_0) + \frac{\Gamma(v)\phi(v)}{v}\int_{\tilde{\theta}_0}^{\tilde{\theta}}\widetilde{c_v}(\tilde{\theta}')\,d\tilde{\theta}' \tag{4.109}$$

The derivative of the integrating factor in equation (4.108) is:

$$\frac{d\phi(v)}{dv} = -\frac{\phi(v)\Gamma(v)}{v} \tag{4.110}$$

Substituting (4.110) into (4.109),

$$P(v,\theta) = P(v,\theta_0) - \frac{d\phi(v)}{dv}\int_{\tilde{\theta}_0}^{\tilde{\theta}}\widetilde{c_v}(\tilde{\theta}')\,d\tilde{\theta}' \tag{4.111}$$

Expressions for other thermodynamic quantities are derived for the case of $\Gamma = \Gamma(v)$. Entropy can be re-written using equation (4.89):

$$\eta(v,\theta) = \eta_0 + \int_{v_0}^{v} \frac{\Gamma(v')\tilde{c_v}(\tilde{\theta}_0)}{v'}\,dv' + \int_{\tilde{\theta}_0}^{\tilde{\theta}} \frac{\tilde{c_v}(\tilde{\theta}')}{\tilde{\theta}'}\,d\tilde{\theta}' \tag{4.112}$$

Now, the expressions for Helmholtz specific free energy and specific internal energy can be simplified to the following relations:

$$\begin{aligned}\psi(v,\theta) = \psi_0 - \eta_0(\theta-\theta_0) - \int_{v_0}^{v}\left[P(v',\theta_0) + (\theta-\theta_0)\frac{\Gamma(v')\tilde{c}_v(\tilde{\theta}_0)}{v'}\right]dv' \\ - \phi(v)\int_{\tilde{\theta}_0}^{\tilde{\theta}} \frac{(\tilde{\theta}-\tilde{\theta}')}{\tilde{\theta}'}\tilde{c}_v(\tilde{\theta}')d\tilde{\theta}'\end{aligned} \tag{4.113}$$

$$\begin{aligned}e(v,\theta) &= \psi(v,\theta) + \theta\eta(v,\theta) \\ &= e_0 - \int_{v_0}^{v}\left[P(v',\theta_0) - \theta_0\frac{\Gamma(\mathrm{v}')\tilde{c_v}(\tilde{\theta}_0)}{v'}\right]dv' + \phi(v)\int_{\tilde{\theta}_0}^{\tilde{\theta}} \tilde{c_v}(\tilde{\theta}')\,d\tilde{\theta}'\end{aligned} \tag{4.114}$$

where $e_0 = \psi_0 + \theta_0\eta_0$.

At this juncture, it is worth noting that if $T_0 = 0K$ is chosen as the reference temperature, specific heat and entropy go to zero, i.e. $c_v(v,T_0) \to 0$ and $\eta_0 = 0$. The expressions above then simplify to:

$$P(v,\theta) = P_c(v) - \frac{d\phi(v)}{dv}\int_0^{\tilde{\theta}} \tilde{c_v}(\tilde{\theta}')\,d\tilde{\theta}' \tag{4.115}$$

$$\eta(v,\theta) = \int_0^{\tilde{\theta}} \frac{\tilde{c_v}(\tilde{\theta}')}{\tilde{\theta}'}\,d\tilde{\theta}' \tag{4.116}$$

$$\psi(v,\theta) = \psi_0 - \int_{v_0}^{v} P_c(v')dv' - \phi(v)\int_0^{\tilde{\theta}} \frac{(\tilde{\theta}-\tilde{\theta}')}{\tilde{\theta}'}\tilde{c}_v(\tilde{\theta}')d\tilde{\theta}' \tag{4.117}$$

$$e(v,\theta) = e_0 - \int_{v_0}^{v} P_c(v')dv' + \phi(v)\int_0^{\tilde{\theta}} \tilde{c_v}(\tilde{\theta}')\,d\tilde{\theta}' \tag{4.118}$$

Even though using the cold curve isotherm makes the expressions for thermodynamic entities compact, relations (4.111)-(4.114) are preferred for ease of obtaining material properties at temperatures other than the absolute zero.

4.5 Thermoelastic Heating

Heating due to severe elastic deformation is important in applications where a material is subject to impacts and shocks. Large pressures of the order of several GPa can be generated under such loading conditions in a very short amount of time, typically tens of nanoseconds. Therefore, adiabatic conditions combined with large compressibility of several materials can result in a significant temperature increase. Such an increase is especially important in the case of fragile molecular crystals like the energetic materials whose mechanical and chemical behavior is extremely temperature sensitive. Moreover, the melting points of energetic materials and their simulants are relatively low, compared to metals, which means that not a lot of thermal heating is required to melt. Therefore, it is important to accurately assess temperature of such materials under dynamic loads. In the PSPI experiments, normal compression can significantly raise the temperature and affect the strength of the material under subsequent shear loading. So, it is important to quantify the thermo-elastic heating.

In section 2.5, it was shown that the rate of heat generation due to elastic processes is given as:

$$\dot{q}^e = \left(\frac{\theta}{2}\frac{\partial \boldsymbol{T}^{\boldsymbol{e}}}{\partial \theta} : \dot{\boldsymbol{C}}^{\boldsymbol{e}}\right) \tag{4.119}$$

The above relation can be written in terms of Mandel stress:

$$\dot{q}^e = \frac{\theta}{2}\, \boldsymbol{C^{e-1}}\, \frac{\partial \boldsymbol{M^e}}{\partial \theta} : \dot{\boldsymbol{C}}^{\boldsymbol{e}} = \frac{\theta}{2}\, \frac{\partial \boldsymbol{M^e}}{\partial \theta} : \boldsymbol{C^{e-T}}\dot{\boldsymbol{C}}^{\boldsymbol{e}} \tag{4.120}$$

From equation (4.58), the derivative of Mandel stress with respect to temperature can be calculated as:

$$\frac{\partial \boldsymbol{M^e}}{\partial \theta} = -\frac{\partial P}{\partial \theta} J^e \boldsymbol{I} + 2\frac{\partial G}{\partial \theta}\boldsymbol{E_0^e} \tag{4.121}$$

Let us consider writing the right Cauchy-Green tensor in the right principal basis, $(\boldsymbol{r_1^e}\otimes\boldsymbol{r_1^e}, \boldsymbol{r_2^e}\otimes\boldsymbol{r_2^e}, \boldsymbol{r_3^e}\otimes\boldsymbol{r_3^e})$ in terms of right elastic stretches, $(\lambda_1^e, \lambda_2^e, \lambda_3^e)$.

$$\boldsymbol{C^e} = \sum_{i=1}^{3} (\lambda_i^e)^2\, \boldsymbol{r_i^e}\otimes\boldsymbol{r_i^e} \tag{4.122}$$

The term $\boldsymbol{C^{e-T}}\dot{\boldsymbol{C}}^{\boldsymbol{e}}$ in equation (4.120) can then be simplified as:

$$\boldsymbol{C^{e-T}}\dot{\boldsymbol{C}}^{\boldsymbol{e}} = \sum_{i=1}^{3} \frac{2\dot{\lambda_i^e}}{\lambda_i^e}\, \boldsymbol{r_i^e}\otimes\boldsymbol{r_i^e} \tag{4.123}$$

Similarly, the deviatoric part of elastic logarithmic strain tensor can be expressed in the right principal basis:

$$\boldsymbol{E_0^e} = \boldsymbol{E^e} - \frac{tr(\boldsymbol{E^e})}{3}\boldsymbol{I} = \sum_{i=1}^{3} \ln(\lambda_i^e)\, \boldsymbol{r_i^e}\otimes\boldsymbol{r_i^e} - \frac{\ln(J^e)}{3}\boldsymbol{I} \tag{4.124}$$

Thus, from equations (4.120), (4.121), (4.123) and (4.124), thermoelastic heating can be written in matrix form as:

$$\dot{q}^e = \theta \frac{\partial G}{\partial \theta} \begin{bmatrix} \ln\left[\frac{\lambda_1^e}{(J^e)^{1/3}}\right] & 0 & 0 \\ 0 & \ln\left[\frac{\lambda_2^e}{(J^e)^{1/3}}\right] & 0 \\ 0 & 0 & \ln\left[\frac{\lambda_3^e}{(J^e)^{1/3}}\right] \end{bmatrix} : \begin{bmatrix} 2\frac{\dot{\lambda_1^e}}{\lambda_1^e} & 0 & 0 \\ 0 & 2\frac{\dot{\lambda_2^e}}{\lambda_2^e} & 0 \\ 0 & 0 & 2\frac{\dot{\lambda_3^e}}{\lambda_3^e} \end{bmatrix}$$

$$-\frac{\theta}{2}\frac{\partial P}{\partial \theta} J^e \begin{bmatrix} 1 & 0 & 0 \\ 0 & 1 & 0 \\ 0 & 0 & 1 \end{bmatrix} : \begin{bmatrix} 2\frac{\dot{\lambda_1^e}}{\lambda_1^e} & 0 & 0 \\ 0 & 2\frac{\dot{\lambda_2^e}}{\lambda_2^e} & 0 \\ 0 & 0 & 2\frac{\dot{\lambda_3^e}}{\lambda_3^e} \end{bmatrix} \tag{4.125}$$

$$\Rightarrow \dot{q}^e = \theta \frac{\partial G}{\partial \theta} \sum_{i=1}^{3} \ln\left[\frac{\lambda_i^e}{(J^e)^{\frac{1}{3}}}\right]\left(2\frac{\dot{\lambda_i^e}}{\lambda_i^e}\right) - \frac{\theta}{2}\frac{\partial P}{\partial \theta} J^e \sum_{i=1}^{3}\left(2\frac{\dot{\lambda_i^e}}{\lambda_i^e}\right) \tag{4.126}$$

Since $J^e = \lambda_1^e \lambda_2^e \lambda_3^e$ and hence, $\frac{\dot{J^e}}{J^e} = \sum_{i=1}^{3} \frac{\dot{\lambda_i^e}}{\lambda_i^e}$, we have:

$$\dot{q}^e = \theta \frac{\partial G}{\partial \theta} \sum_{i=1}^{3} \ln\left[\frac{\lambda_i^e}{(J^e)^{\frac{1}{3}}}\right]\left(2\frac{\dot{\lambda_i^e}}{\lambda_i^e}\right) - \theta \frac{\partial P}{\partial \theta} \dot{J^e} \tag{4.127}$$

The first term in equation (4.127) requires knowledge of principal elastic stretches and stretch rates in all 3 principal directions. However, due to small deviatoric elastic strains, the contribution of the first term to the thermoelastic heat generation is small and can therefore be neglected. The second term, on the other hand, is easy to compute from the complete equation of state given through equation (4.111). The derivative of pressure with respect to temperature is given through a simple expression as follows:

$$\frac{\partial P}{\partial \theta} = -\frac{d\phi}{dv}\frac{d\tilde{\theta}}{d\theta}\,\tilde{c_v}(\tilde{\theta}) = \frac{\Gamma(v)}{v}\tilde{c_v}(\tilde{\theta}) \tag{4.128}$$

It is easy to verify that equation (4.127) holds for the special case of linear thermo-elasticity.

In the next few sections, analytic expressions for different thermodynamic curves such as the isentrope, isotherm and Hugoniot are derived using the complete equation of state. Plotting these curves for sucrose is expected to provide insights into material behavior under different types of loading.

4.6 Isentrope

The normal loading under pressure-shear plate impact can be considered as being close to an isentrope, i.e. the PSPI experiments load the specimen quasi-entropically. Pressure along an isentrope can be found using the Mie-Gruneisen EOS in (4.72) in terms of the reference curve:

$$P^{(\eta)}(v) - P^{ref}(v) = \frac{\Gamma(v)}{v}[e^{(\eta)}(v) - e^{ref}(v)] \tag{4.129}$$

where the superscript η specifies quantities along the isentrope. However, the specific internal energy, $e^{(\eta)}(v)$ remains unknown. If $e = e(v, \eta)$, pressure is defined as (equation (4.78)):

$$P(v, \eta) \equiv -\left(\frac{\partial e}{\partial v}\right)_{\eta} = -\frac{de^{(\eta)}}{dv} \tag{4.130}$$

Substitute (4.130) into (4.129) to obtain an ODE in $e^{(\eta)}(v)$:

$$\frac{de^{(\eta)}(v)}{dv} + \frac{\Gamma(v)}{v}e^{(\eta)}(v) = -\left[P^{ref}(v) - \frac{\Gamma(v)}{v}e^{ref}(v)\right] \tag{4.131}$$

Using the integrating factor $\phi(v)$ defined in equation (4.107), the ODE can be written as:

$$\frac{d}{dv}\left(\frac{e^{(\eta)}(v)}{\phi(v)}\right) = -\frac{1}{\phi(v)}\left[P^{ref}(v) - \frac{\Gamma(v)}{v}e^{ref}(v)\right] \tag{4.132}$$

So, the internal energy associated with an isentrope passing through the initial state (v_0, e_0) is given as:

$$e^{(\eta)}(v) = \phi(v)\left\{e_0 - \int_{v_0}^{v} \frac{1}{\phi(v')}\left[P^{ref}(v') - \frac{\Gamma(v')}{v'}e^{ref}(v')\right]dv'\right\} \tag{4.133}$$

Substituting the above expression for specific internal energy into equation (4.129), the expression for pressure along an isentrope can be obtained.

Since the temperature change during normal loading, which precedes the shear loading in a PSPI experiment, influences the shear strength of the material, it is necessary to calculate the temperature change during isentropic loading. Consider an alternative definition of the Gruneisen parameter:

$$\Gamma \equiv v\left(\frac{\partial P}{\partial e}\right)_v = -\frac{v}{\theta}\left(\frac{\partial \theta}{\partial v}\right)_\eta \tag{4.134}$$

The second relation in equation (4.134) can be obtained from equations (4.84) and (4.86). Integrating the above relation gives the temperature variation along an isentrope as a function of specific volume.

$$\theta^{(\eta)} = \theta_0 \exp\left(-\int_{v_0}^{v} \frac{\Gamma(v')}{v'}dv'\right) = \theta_0\phi(v) \tag{4.135}$$

Since equation (4.135) represents a characteristic curve for the hyperbolic PDE in equation (4.105), it implies that $c_v = constant$ along any isentrope. This is a consequence of the assumption that Gruneisen parameter is a function of specific volume only. The calculated isentrope for sucrose is plotted in Figure 4.2. It is assumed that $\frac{\Gamma(v)}{v} = \frac{\Gamma_0}{v_0}$ where $\Gamma_0 = \Gamma(v_0)$. A 3rd order Birch-Murnaghan equation of state is chosen as the reference curve:

$$P = K_{\theta 0}\left(\frac{v_0}{v}\right)\ln\left(\frac{v_0}{v}\right)\left[1 + \frac{K'_{\theta 0} - 2}{2}\ln\left(\frac{v_0}{v}\right)\right] \tag{4.136}$$

where $K_{\theta 0}$ and $K'_{\theta 0}$ are elastic bulk modulus and the first derivative of elastic bulk modulus with respect to pressure respectively. The derivation of this equation of state is presented in section 10. The material properties of sucrose used for plotting the curves are given in Table 4.1.

Table 4.1 Material parameters for sucrose

ρ_0	Initial density	1580.5 $\mathrm{kg/m^3}$
Elastic Parameters		
G_0	Shear Modulus at ambient	8.58 GPa
G_θ	Temperature coefficient of shear modulus	0
G_P	Pressure coefficient of shear modulus	0
ν	Poisson's ratio	0.25
$K_{\theta 0}$	Isothermal bulk modulus at ambient	14.3 GPa
$K'_{\theta 0}$	Derivative of Bulk modulus with respect to pressure	3.75
Γ_0	Gruneisen parameter at ambient	1.09
Thermal parameters		
c_p^*	Specific heat capacity at ambient	1244 J/kgK
k	Thermal conductivity	0.486 W/mK
α	Coefficient of thermal expansion	0.486 W/mK
c_0	Specific heat capacity, $c_v(\theta) = \frac{\theta^3}{c_0 + c_1\theta + c_2\theta^2 + c_3\theta^3}$	7.095 x 10^3 $\mathrm{kgK^4/J}$
c_1		2.230 x 10^1 $\mathrm{kgK^3/J}$
c_2		4.180 x 10^{-3} $\mathrm{kgK^2/J}$
c_4		3.050 x 10^{-4} kgK/J
a_1	$\int_0^\theta c_v(\theta)d\theta \approx (a_1\theta + a_2\theta^2)\frac{J}{kg}$	−133.647 J/kgK
a_2		2.082 $\mathrm{J/kgK^2}$

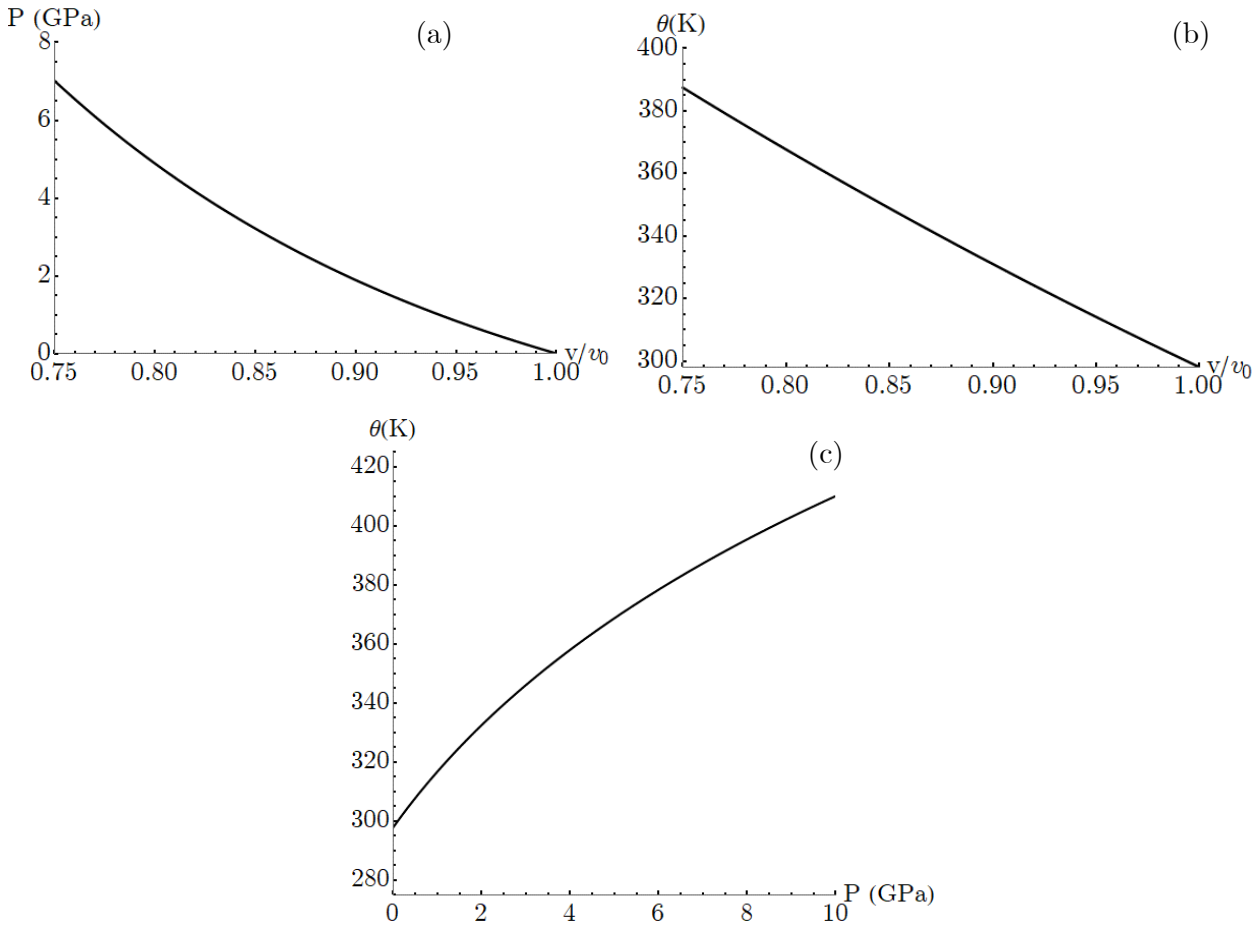

Figure 4.2 Isentrope curves for sucrose. Initial state is characterized by $v_0 = 1/\rho_0$, $P_0 = 0$, $\theta_0 = 298\,K$ and $e_0 = 0$, where ρ_0 is the initial density of sucrose

4.7 Isotherm

Pressure along an isotherm can be obtained from equation (4.111) by substituting the isotherm temperature, $\theta = \theta_i$.

$$P(v,\theta_i) = P(v,\theta_0) - \frac{d\phi(v)}{dv}\int_{\tilde{\theta}_0}^{\tilde{\theta}_i} \tilde{c_v}(\tilde{\theta}')\, d\tilde{\theta}' \tag{4.137}$$

Similarly, the expressions for specific internal energy, specific free energy and specific entropy can be obtained by substituting the isotherm temperature in equations (4.112)-(4.114). The 3rd order Birch-Murnaghan equation of state is chosen as the reference isotherm. The values for

these constants can be found in Table 4.1. Figure 4.3 shows isotherms for sucrose at different temperatures.

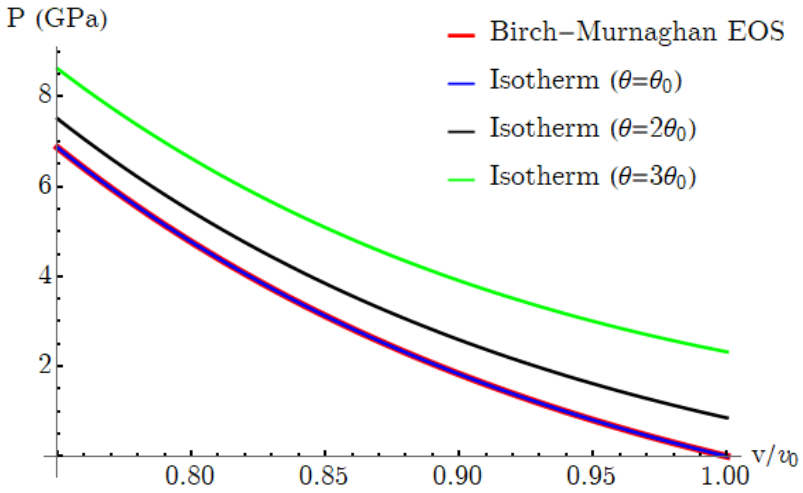

Figure 4.3 Isotherms for sucrose at different temperatures. $\theta_0 = 298\,K$.

4.8 Hugoniot

One of the problems of interest to the energetic materials community is the ability to predict detonation in energetic material aggregates when subjected to a shock wave. Consider the case of a shock wave traveling through a solid that subjects the material to a high pressure. Under such high pressures, the shear strength of the solid is negligible with respect to the pressure applied. So, the normal stress jump across the shock wave can be approximated to be equal to the pressure jump. Then, the specific internal energy of the solid for shock compression from an initial state of $(e_0, P_0, \theta_0, v_0)$ is given through the following Rankine-Hugoniot relation:

$$e^{(H)}(v) = e_0 + \frac{1}{2}\left(P^{(H)}(v) + P_0\right)(v_0 - v) \tag{4.138}$$

Pressure along a Hugoniot requires another piece of information. Usually, that is provided in terms of a shock speed-particle speed relation (example $u_s = c_0 + su_p$). Another way to find the pressure on a Hugoniot is by using a reference curve and then substituting into the complete equation of state, which is represented in the present case as the Mie-Gruneisen equation of state.

$$P^{(H)}(v) - P(v, \theta_0) = \frac{\Gamma(v)}{v}[e^{(H)}(v) - e(v, \theta_0)] \tag{4.139}$$

Internal energy along an isotherm can be found from equation (4.114):

$$e(v, \theta_0) = e_0 - \int_{v_0}^{v} \left[P(v', \theta_0) - \theta_0 \frac{\Gamma(\mathrm{v}')\widetilde{c_v}(\tilde{\theta}_0)}{v'} \right] dv' \tag{4.140}$$

Substituting the expressions for internal energy from equations (4.138) and (4.140) into equation (4.139), pressure along a Hugoniot can be written as:

$$P^{(H)}(v) = \frac{\frac{\Gamma(v)}{v} P_0(v_0 - v) + P(v, \theta_0) + \frac{\Gamma(v)}{v} \left\{ \int_{v_0}^{v} \left[P(v', \theta_0) - \theta_0 \frac{\Gamma(\mathrm{v}')\widetilde{c_v}(\widetilde{\theta_0})}{v'} \right] dv' \right\}}{1 - \frac{\Gamma(v)}{2v}(v_0 - v)} \tag{4.141}$$

Consider internal energy as a function of volume and entropy, $e(v, \eta)$. Change in internal energy can be written using the first law of Thermodynamics (equation (4.76)) as $de = -Pdv + \theta d\eta$. Consider $\eta = \eta(v, \theta)$. From equation (4.88), change in entropy can be written as $d\eta = \frac{\Gamma c_v}{v} dv + \frac{c_v}{\theta} d\theta$. Hence, the first law of thermodynamics can be written as:

$$de = \left(-P + \frac{\Gamma c_v \theta}{v} \right) dv + c_v d\theta \tag{4.142}$$

In a differential form, equation (4.142) can be written as:

$$de^{(H)} = \frac{1}{2}(v_0 - v) dP^{(H)} - \frac{1}{2}\left(P^{(H)} + P_0\right) dv \tag{4.143}$$

Equating right hand sides of equations (4.142) and (4.143):

$$\left(-P^{(H)} + \frac{\Gamma c_v \theta^{(H)}}{v}\right) dv + c_v d\theta^{(H)} = \frac{1}{2}(v_0 - v) dP^{(H)} - \frac{1}{2}\left(P^{(H)} + P_0\right) dv \tag{4.144}$$

A first-order ODE in $\theta^{(H)}$ is obtained by rearranging the terms,

$$c_v \frac{d\theta^{(H)}}{dv} + \frac{\Gamma c_v}{v}\, \theta^{(H)} = \underbrace{\frac{1}{2}(v_0 - v)\frac{dP^{(H)}(v)}{dv} + \frac{1}{2}\left(P^{(H)}(v) - P_0\right)}_{h(v)} \tag{4.145}$$

The right hand side of equation (4.145) is a function of specific volume and can be abbreviated into a function $h(v)$. $P^{(H)}$ can be substituted from equation (4.141). The derivative of the scaled temperature, $\tilde{\theta} = \theta/\phi(v)$, with respect to v is given by:

$$\phi(v)\frac{d\tilde{\theta}}{dv} = \frac{d\theta}{dv} + \frac{\Gamma(v)}{v}\theta \tag{4.146}$$

Substitute equation (4.146) into equation (4.145):

$$\widetilde{c_v}\left(\tilde{\theta}^{(H)}\right)\frac{d\tilde{\theta}^{(H)}}{dv} = \frac{h(v)}{\phi(v)} \tag{4.147}$$

Equation (4.147) gives temperature change along a Hugoniot. In its most generic form, the temperature relation above is a non-linear ODE and needs to be solved numerically. The special case of a constant specific heat can be solved easily. Hugoniot curves for sucrose are shown in Figure 4.4.

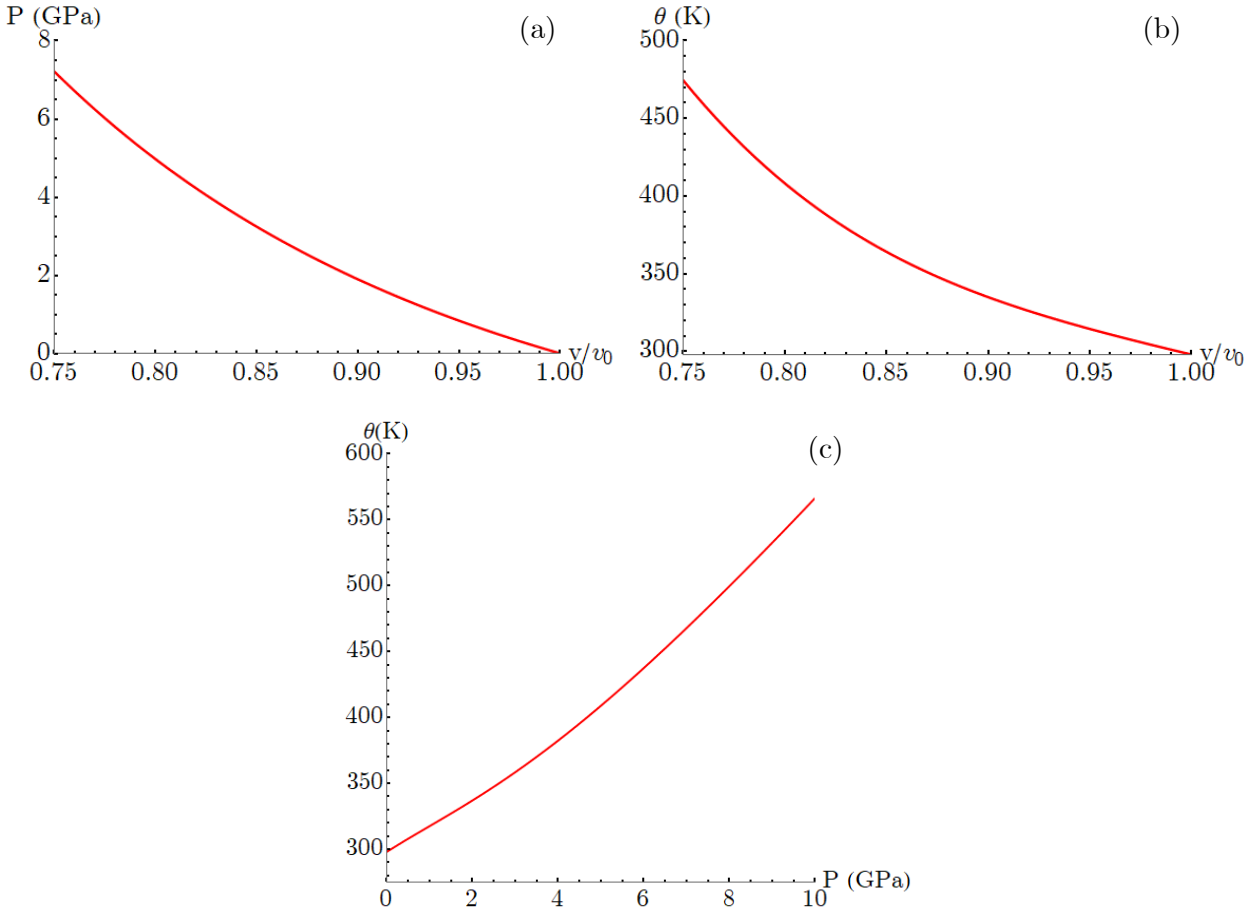

Figure 4.4 Hugoniot curves for sucrose.

4.9 Comparison of the Thermodynamic Curves

At this point, it is instructive to compare the pressure-volume-temperature (P, v, θ) response under different types of commonly encountered loading. Figure 4.5 shows a three-dimensional surface of a complete Mie-Gruneisen equation of state for sucrose in the (P, v, θ) space. An isotherm, an isentrope and a Hugoniot are plotted simultaneously. Figure 4.5 clearly illustrates the substantial difference between the three curves along the temperature axis.

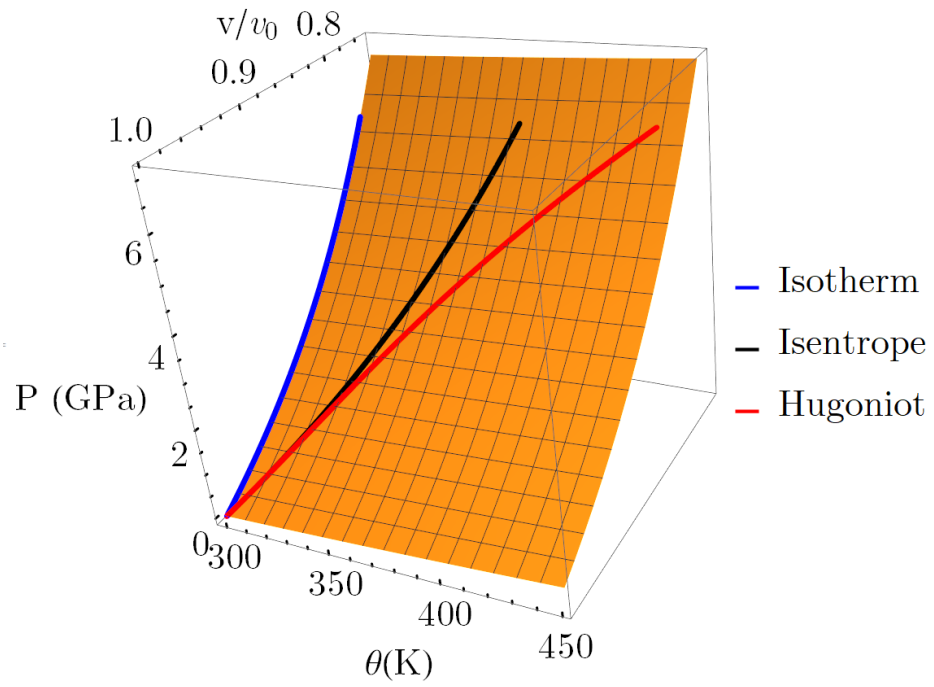

Figure 4.5 Pressure-Volume-Temperature curve for a complete Mie-Gruneisen equation of state for sucrose (Orange grid). Blue: Isotherm, Black: Isentrope and Red: Hugoniot, all passing through the initial state, $P_0 = 0, v_0, \theta_0 = 298K$.

For more illustrative comparison, the thermodynamic curves are compared on two-dimensional plots. Figure 4.6 shows that in the pressure, P vs compression ratio, v/v_0 ratio, the Hugoniot lies at the top and the isotherm lies at the bottom of the three curves. However, for the volume compression ratios considered here, the difference between the curves is relatively modest. The main difference between the isotherm, the isentrope and the Hugoniot lies in the temperature response of the material, as shown in Figure 4.7 and Figure 4.8. While the temperature rise along an isentrope is almost linear with volume compression ratio, temperature along the Hugoniot quickly diverges from the isentrope and leads to a much higher temperature rise. It is to be noted that while the temperature rise along an isentrope slows down with increasing pressure (Figure 4.8), the temperature rise along a Hugoniot quickens with increasing

pressure as indicated by the concave up curve. These differences in the material response to different types of thermodynamic loading has far reaching consequences for energetic materials. For example, a ramp wave with an isentropic pressure loading is much less likely to cause hot spots as compared to a shock wave.

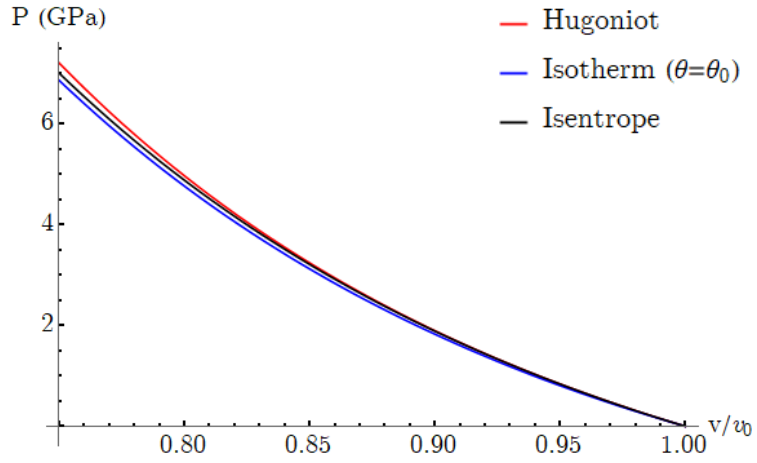

Figure 4.6 Pressure, P vs compression ratio, v/v_0 plots for sucrose, for a Hugoniot, an isentrope and an isotherm, all passing through the same initial point, i.e. $P_0 = 0, \frac{v}{v_0} = 1, \theta_0 = 298\ K$

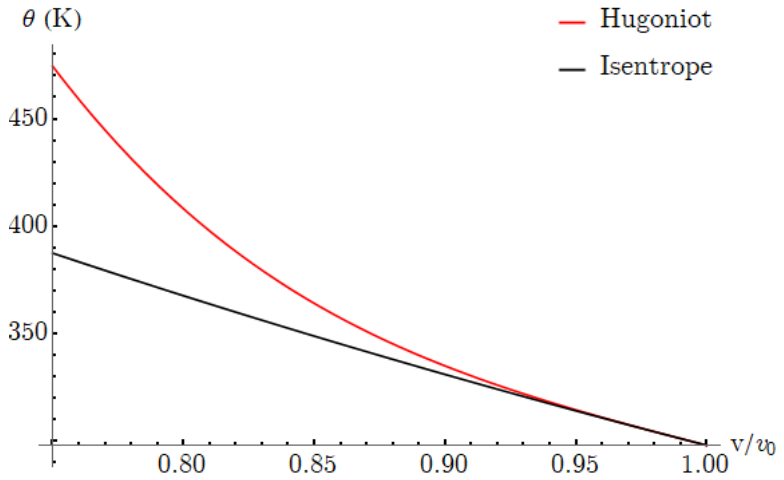

Figure 4.7 Temperature, θ vs compression ratio, v/v_0 plots for sucrose, for a Hugoniot and an isentrope

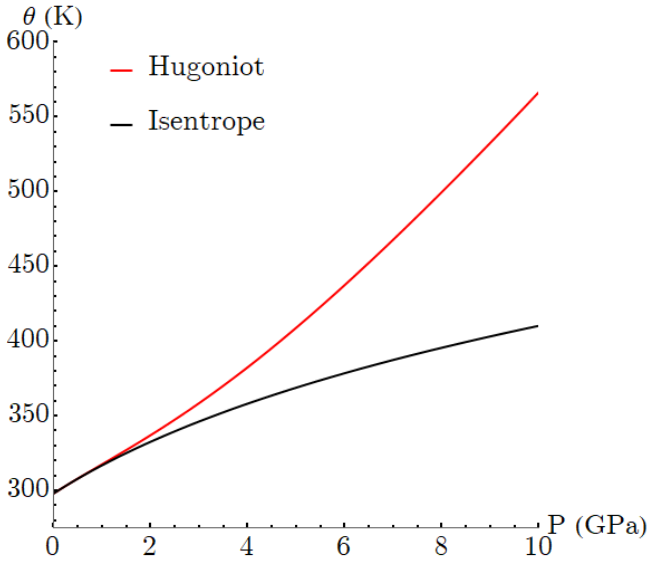

Figure 4.8 Temperature, θ vs pressure, P plots for sucrose, for a Hugoniot and an isentrope

From the preceding discussion, it is worth highlighting the importance of using a complete equation of state with a temperature dependent specific heat. As noted by Menikoff and Sewell (2002), Sewell and Menikoff (2004) , incorporating temperature dependence of specific heat in an equation of state is extremely important to accurately predict hot-spot temperatures and hence the consequent chemical reaction kinetics. Let us compare the thermodynamic response of sucrose for two cases: (a) Temperature dependent specific heat, and (b) Constant specific heat capacity, evaluated at $\theta = \theta_0$. Figure 4.9 shows that the choice of temperature-dependent vs temperature-independent specific heat does not have a substantial effect on the pressure-volume response of sucrose, for all the three kinds of loading.

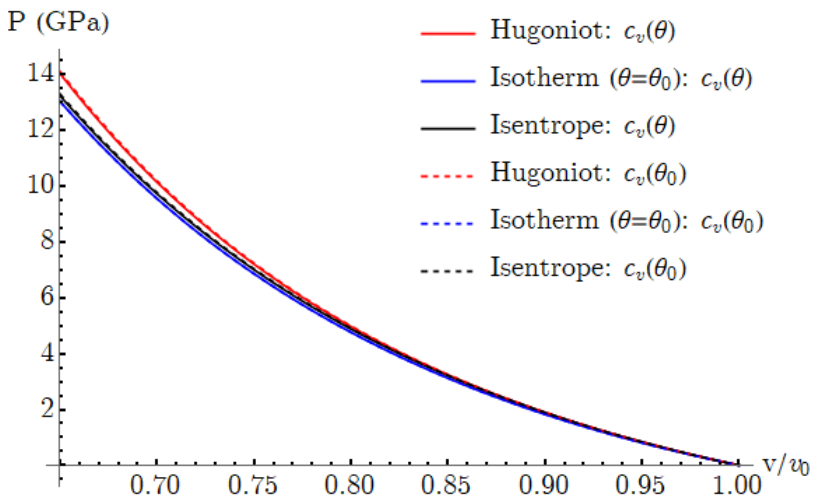

Figure 4.9 Pressure-volume response of sucrose for a temperature-dependent specific heat capacity (solid lines) vs temperature-independent specific heat capacity evaluated at $\theta = \theta_0$ (dashed lines)

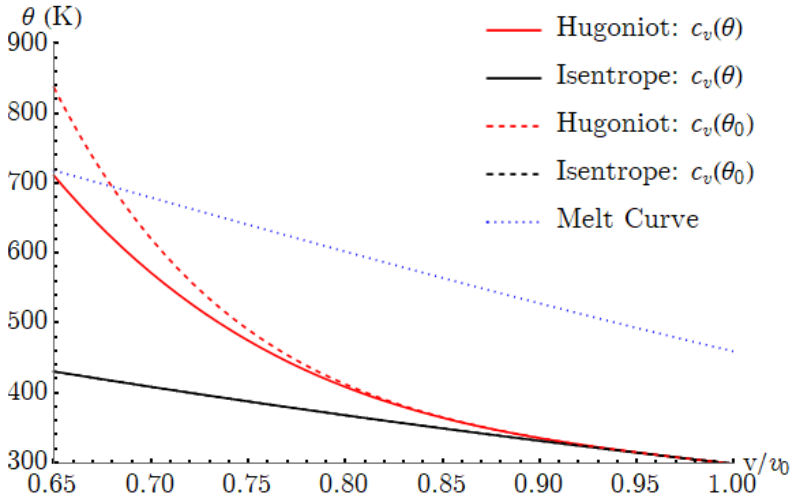

Figure 4.10 Effect of specific heat capacity on temperature rise along a Hugoniot and an isentrope with increasing compression, for sucrose. The pressure-dependent melt curve for sucrose is also shown. Note that the melt curve is based on Lindemann Law which is discussed in detail in Chapter 5

Figure 4.10 shows the difference arising in the temperature response due to the form of specific heat chosen. As expected, the temperature along the isentrope should be unaffected by

the choice of specific heat capacity because the specific heat capacity remains constant along an isentrope. However, there is a substantial difference in the temperature rise along a Hugoniot. Using the temperature-dependent specific heat, $c_v(\theta)$ results in a lower temperature increase with compression as compared to using a constant specific heat, $c_v(\theta_0)$, with the difference between the two cases increasing as the compression ratio increases. Such a comparison emphasizes the role played by the choice of specific heat capacity for shock wave loading of explosive/simulant crystals. Thus, proper representation of the temperature dependence of specific heat has consequences for accurately simulating the mechanical, thermal and chemical response of energetic materials. For example, the comparison of the Hugoniots in Figure 4.10 with the pressure-dependent melt curve for sucrose shows that beyond a compression ratio of ~0.67, the Hugoniot with a constant specific heat capacity predicts melting while using a complete equation of state does not. Such differences have a potentially significant impact on the accuracy of predicting deformation localization and formation of hot-spots due to adiabatic shear bands and the likelihood of such hot-spots turning critical, leading to ignition.

At this juncture, one may pose the following question: If a constant specific heat were to be used for simplicity, in a material model for sucrose, at what temperature should it be evaluated? To answer this question, the temperature along a Hugoniot is plotted for constant specific heat (dashed curves) at different temperatures and compare them with the case of temperature-dependent specific heat (solid curve). From Figure 4.11, it becomes clear that for the range of pressures considered, $c_v = c_v(1.5\theta_0)$ works the best in this scenario.

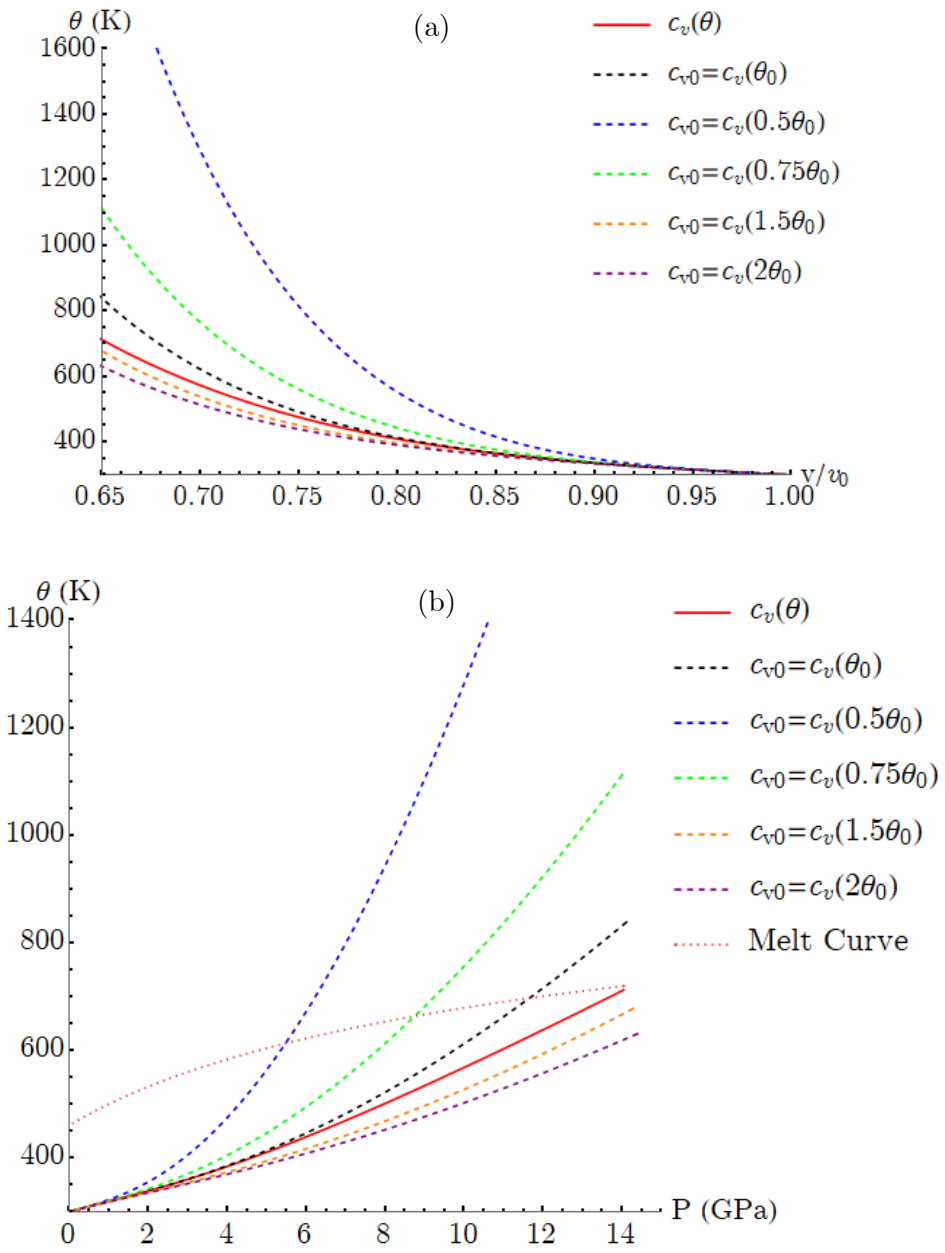

Figure 4.11 Temperature along a Hugoniot for sucrose for different specific heat capacities. Note that the melt curve shown above is based on the Lindemann Law which is discussed in detail in Chapter 5

4.10 Derivation of 3rd order Birch-Murnaghan equation of state

A 3rd order free-energy function is used to derive an isothermal equation of state. Note that the final form of the equation of state depends on the strain measure used. The $P - v$ relation based on the Euler-Almansi strain is the most commonly encountered form in shock physics and geophysics applications and is as follows:

$$P = \frac{3}{2}K_{\theta 0}\left[\left(\frac{v_0}{v}\right)^{\frac{7}{3}} - \left(\frac{v_0}{v}\right)^{\frac{5}{3}}\right]\left[1 + \frac{3}{4}(K'_{\theta 0} - 4)\left\{\left(\frac{v_0}{v}\right)^{\frac{2}{3}} - 1\right\}\right] \tag{4.148}$$

However, since the constitutive model is built using logarithmic strains, it is important to be consistent and use the same strain measure.

Consider a cube of an isotropic material subjected to pressure. The deformation gradient for such a deformation is given below:

$$\boldsymbol{F} = \lambda \boldsymbol{I} \tag{4.149}$$

Volumetric logarithmic strain is given as:

$$E_v = tr(\boldsymbol{E^e}) = \ln(\lambda^3) = \ln\left(\frac{v}{v_0}\right) \tag{4.150}$$

Now consider a polynomial expansion of Helmholtz free energy per unit volume in the reference configuration, as a function of magnitude of volumetric strain:

$$\psi_R(E_v) = A_0 + A_1 E_v + A_2 E_v^2 + A_3 E_v^3 \ldots \tag{4.151}$$

Pressure inside the solid is given as:

$$P = -\frac{tr(\boldsymbol{T})}{3} = -\frac{1}{\rho_0}\frac{\partial \psi_R}{\partial v} \tag{4.152}$$

where $\boldsymbol{T}$ is the Cauchy stress. Assume that the free energy and pressure are zero in the reference configuration, i.e. $A_0 = 0$ and $A_1 = 0$. Then the expression for pressure can be simplified in terms of A_2 and A_3:

$$P = -\frac{1}{\rho_0}\frac{\partial \psi_R}{\partial v} = -\frac{1}{\rho_0}\frac{\partial \psi_R}{\partial E_v}\frac{\partial E_v}{\partial \lambda}\frac{\partial \lambda}{\partial v} = -E_v\left(\frac{2A_2 + 3A_3E_v}{\lambda^3}\right) \tag{4.153}$$

Constants A_2 and A_3 need to be expressed in terms of measurable material parameters such as the isothermal bulk modulus, $K_{\theta 0}$ and its first pressure derivative, $K'_{\theta 0}$. The subscript '0' refers to the reference state of $(v_0, P_0 = 0, \theta_0 = 298\,K)$. $K_{\theta 0}$ and $K'_{\theta 0}$ are defined below:

$$K_{\theta 0} = -v\frac{\partial P}{\partial v} \tag{4.154}$$

$$K'_{\theta 0} = \frac{\partial K_{\theta 0}}{\partial P} \tag{4.155}$$

Using equations (4.153), (4.154) and (4.155), A_2 and A_3 can be found in terms of $K_{\theta 0}$ and $K'_{\theta 0}$:

$$A_2 = \frac{K_{\theta 0}}{2} \tag{4.156}$$

$$A_3 = \frac{K_{\theta 0}}{6}(2 - K'_{\theta 0}) \tag{4.157}$$

Substituting the above relations into equation (4.153), the 3rd-order Birch-Murnaghan equation of state in terms of logarithmic strains (Poirier and Tarantola (1998)) is written as:

$$P = K_{\theta 0}\left(\frac{v_0}{v}\right)\ln\left(\frac{v_0}{v}\right)\left[1 + \frac{K'_{\theta 0} - 2}{2}\ln\left(\frac{v_0}{v}\right)\right] \tag{4.158}$$

A comparison of the 3rd order Birch-Murnaghan EOS using the 3 different strain measures is shown in the plot below (Figure 4.12). Derivation of the EOS for the Green-Lagrange and Euler-Almansi strain tensors is given in Appendix A. It is evident that the Green-Lagrange strain leads to the most compliant behavior at the same volumetric compression while the Euler-Almansi form leads to the stiffest behavior. The Birch-Murnaghan forms for the logarithmic

strain and Euler-Almansi strain are in extremely close approximation of each other even for finite volumetric strains. All the 3 forms show excellent agreement at small strains which is to be expected.

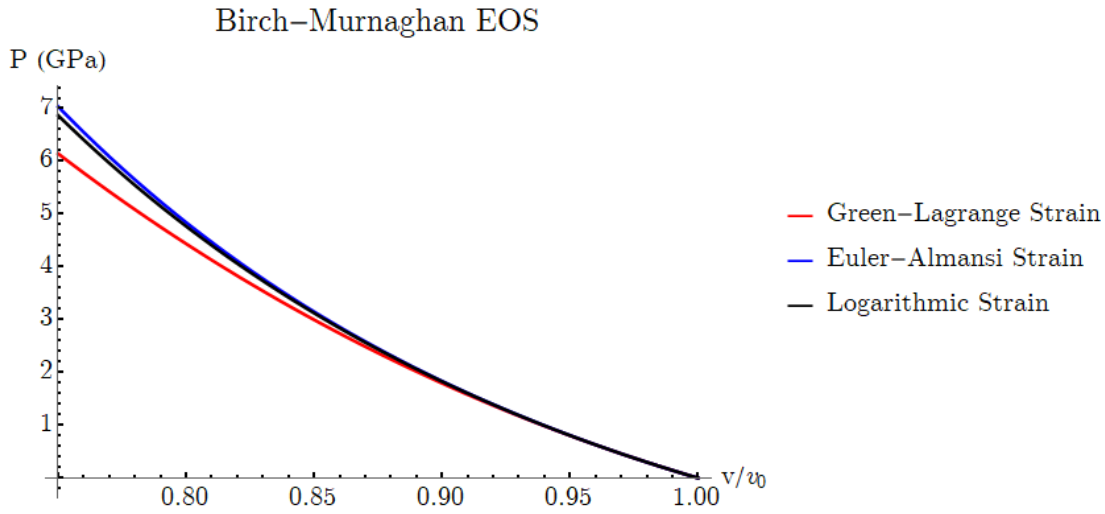

Figure 4.12 3rd order Birch-Murnaghan equation of state using 3 different strain measures

4.11 Discussion

Molecular crystals such as HMX, RDX and sucrose are complex materials to model under quasi-static and dynamic loads. The complexity arises on several fronts: (a) anisotropic elastic properties, (b) thermo-elastic coupling, (c) complex thermo-viscoplastic response, (d) low melting points, (e) strong dependence of material properties on temperature and pressure, such as the elastic moduli, specific heat, melt curve and viscosity of molten fluid to name a few, and (d) the added complexity of chemical reactions. Moreover, lack of experimental data on melt curves and temperature and pressure-dependencies of shear viscosities of melt for energetic crystals makes determination of material parameters an arduous task.

In this chapter, a thermodynamic framework for thermo-mechanical modeling of sucrose is presented, with focus on the solid phase before melting takes place. A complete Mie-Gruneisen equation of state is derived with the incorporation of a temperature-dependent specific heat capacity. The complete equation of state requires the knowledge of a reference isotherm, which is fulfilled through the derivation of a third-order Birch Murnaghan equation of state. It is shown that it is important to have a temperature dependent specific heat capacity for accurate prediction of deformation behavior and hot-spot formation in energetic crystals.

The framework also allows the incorporation of higher order elastic constants with dependencies on pressure and temperature. Plasticity is modeled using the Johnson-Cook Model which accounts for strain-hardening, strain-rate hardening and thermal softening. The pressure dependence of yield strength is brought out indirectly using the pressure-dependence of the melt temperature, unlike the usual approach of using a pre-factor of temperature dependent shear modulus (G/G_0). Melt curve and its implications are discussed in detail in Chapter 5. Due to low melting points of molecular crystals such as energetic materials and their temperature-sensitive mechanical and chemical properties, temperature is an important thermodynamic variable in constitutive modeling. Therefore, temperature changes due to conduction, elasticity and plasticity are all accounted for. An explicit expression for thermoelastic heating is derived and its importance further highlighted in Chapter 5. Since a solid to liquid phase transition is expected under large shear strains that the sucrose specimen is subject to under PSPI experiments, constitutive behavior of molten sucrose needs to be considered. However, the

current thermodynamic framework does not allow for solid-solid or solid-liquid phase transitions, which remains a task for the future.

Chapter 5

Sucrose: Simulations

5.1 Introduction

The constitutive model for sucrose described in Chapter 4 is implemented in the commercial Finite Element software, ABAQUS, through a VUMAT (user-subroutine for an Explicit analysis). This chapter details the results of the simulations and draws comparisons with experimental observations. The VUMAT algorithm is laid out in detail in Appendix A.

The flyer, target plates and the sandwiched specimen are modeled using four-noded two-dimensional plane strain elements with thermal coupling. Since shear localization is expected, mesh size of the specimen is kept smaller than the expected shear band width. Without the knowledge of expected temperature rise and shear strain-rates expected within the band, the shear band width can be estimated through the following equation:

$$\delta_{band} \approx 2\sqrt{Dt} \tag{5.1}$$

where $D = k/\rho c$ is thermal diffusivity and t is the expected duration of loading. Using material constants listed in Table 5.1. and variation of specific heat discussed in Appendix B, the thermal diffusivity of sucrose can be calculated to vary between $94 \times 10^{-9}\, m^2/s$ and $247 \times 10^{-9}\, m^2/s$. For a loading duration of about $1\, \mu s$, the shear band width is expected to lie between $0.61\, \mu m$ and $1\, \mu m$. Therefore, a mesh size of $0.25\, \mu m$, which is sufficiently smaller than the expected band width, is chosen to err on the side of caution (see Figure 5.1). For stability of the

numerical scheme, time-step is dictated by the longitudinal wave speed in sucrose and the time-scale of thermal diffusion.

$$\Delta t < \min\left(\frac{\Delta x}{c_L}, \frac{(\Delta x)^2}{2D}\right) \tag{5.2}$$

where c_L is the longitudinal wave speed and Δx is mesh size. For a mesh size of $0.25\ \mu m$, a time-step of $10^{-11} s$ obeys the stability criteria in equation (5.2) with sufficient margin for error. Simulations are carried out using a dynamic, temperature-displacement, explicit time-step. Thermal conduction is modeled even though its effects are negligible, as demonstrated below.

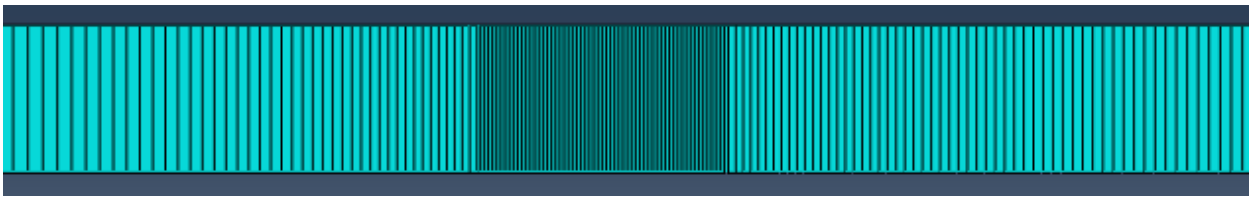

Figure 5.1 Mesh for simulation of shot PM1804. The sucrose specimen has a finer mesh size of 0.25 μm (middle of the figure) than the target plates on either side which have a mesh size increasing linearly from 0.5 μm (at the target/specimen interface) to 50 μm (at the other end)

5.2 Comparison of velocity profiles

Experimental and simulated velocity profiles at the sample/rear target plate interface are compared. The material constants used in simulations are detailed in Table 5.1. The choice of material constants is justified in Appendix B. While some of the material constants, have been obtained from literature, others have been fit to experimental data. Material parameters for the Johnson-Cook model are based on a modest search of parameter values and better fits to experimental data might be possible using a more rigorous parameter optimization approach based on minimization of least squared errors between experimental and simulated velocity profiles.

Figure 5.2 shows experimental and simulated normal velocity profiles for low-pressure shots while Figure 5.3 shows the same for high-pressure shots. Nodal values of the simulated velocity profiles are plotted on the rear surface of the specimen and multiplied by a factor of 2 to obtain free surface velocities at the rear target plate. Since compaction of the initial surface roughness of the sucrose specimen is not modeled in simulations, the initial step observed in the experiments is not seen in simulations. The rise of normal velocity to the plateau agrees very well with the experiments. For the high-pressure shots, a slight deviation from the simulated profiles is observed for normal velocities above 0.12 mm/μs, due to loading of the anvil WC plates beyond their Hugoniot Elastic Limit.

Simulated transverse velocity profiles for low and high-pressure shots are compared with experimental velocities in Figure 5.4 and Figure 5.5 respectively. It is shown that the choice of a single set of material constants can fit the transverse velocities under different experimental conditions reasonably well. Simulated profiles can capture the drop in shearing resistance of sucrose, which results when thermal softening overtakes hardening due to increasing strains and strain-rates. The rising portion of simulated transverse velocity is steeper than that observed in the experiments which indicates that the actual shear modulus value upon the arrival of shear wave is smaller than the quasi-static shear modulus value used here. As discussed in Chapter-4, shear modulus varies with temperature and pressure and such a variation is easy to incorporate into the user-subroutines. However, due to the lack of experimental data on variation of shear modulus with temperature and pressure, a constant value is employed. Good agreement between the experiments and the simulations is seen for the peak value of transverse velocities, hence the shear stresses, especially for the case of low pressures. Due to small variations in experimentally

observed shear behavior under similar set of conditions, simulated transverse velocity profiles fit some shots better than the others. The drop in shear strength is also captured very well through simulations. Simulated profiles for low-pressure experiments show a slightly delayed drop.

Table 5.1 Material constants for sucrose

ρ_0	Initial density	1580.5 $\mathrm{kg/m^3}$
Elastic Parameters		
G_0	Shear Modulus at ambient	8.58 GPa
G_θ	Temperature coefficient of shear modulus	0
G_P	Pressure coefficient of shear modulus	0
ν	Poisson's ratio	0.25
$K_{\theta 0}$	Isothermal bulk modulus at ambient	14.3 GPa
$K'_{\theta 0}$	Derivative of Bulk modulus with respect to pressure	3.75
Γ_0	Gruneisen parameter at ambient	1.09
Johnson-Cook parameters		
A	Static yield strength	500 MPa
B	Strain-hardening coefficient	500 MPa
n	Strain-hardening exponent	0.1
C	Strain-rate hardening coefficient	0.01
$\dot{\epsilon}_0$	Effective plastic strain-rate	1 $\mathrm{s^{-1}}$
m	Thermal softening exponent	0.5
θ_{tr}	Reference temperature	298 K
θ_{m0}	Melt temperature at ambient pressure	459 K
$\dot{\epsilon}^p_{lim}$	Limiting strain-rate	10^7 $\mathrm{s^{-1}}$
Thermal parameters		
c_p^*	Specific heat capacity at ambient	1244 J/kgK
k	Thermal conductivity	0.486 W/mK
α	Coefficient of thermal expansion	0.486 W/mK
P_{ref}	Reference pressure in Simon-Glatzel melt relation	0
P_0	Parameter in Simon-Glatzel melt relation	0.3 GPa
d	Parameter in Simon-Glatzel melt relation	3.25

*Simulations use the temperature-dependent specific heat capacity rather than the constant value mentioned here.

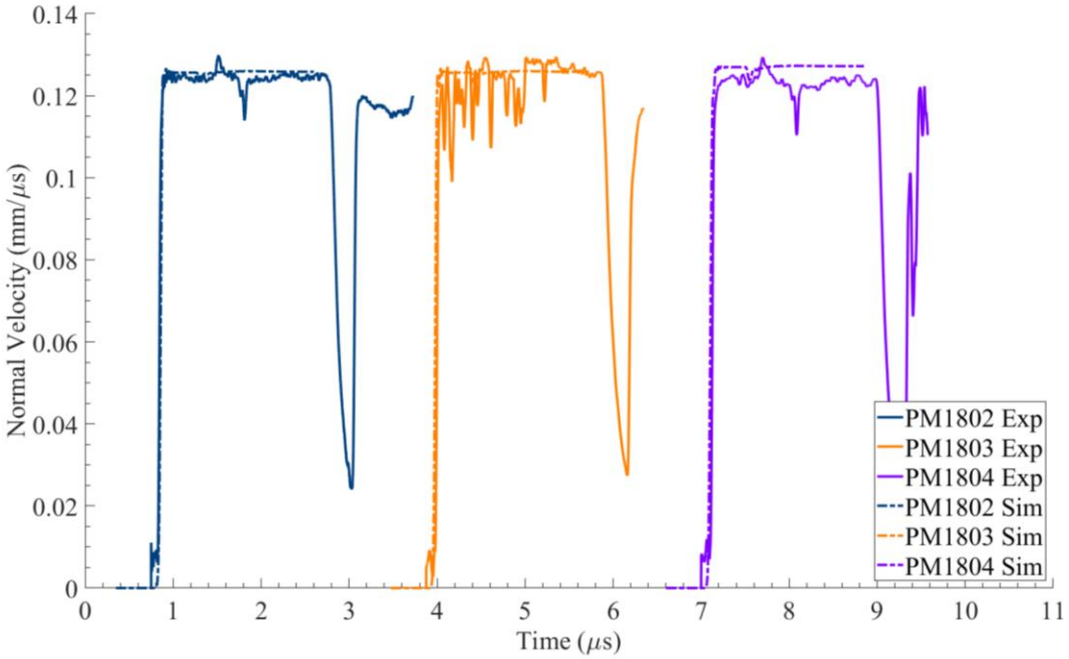

Figure 5.2 Normal velocity profiles of low-pressure shots on sucrose. Experimental profiles are shown using solid lines while the simulated profiles are represented using dashed lines

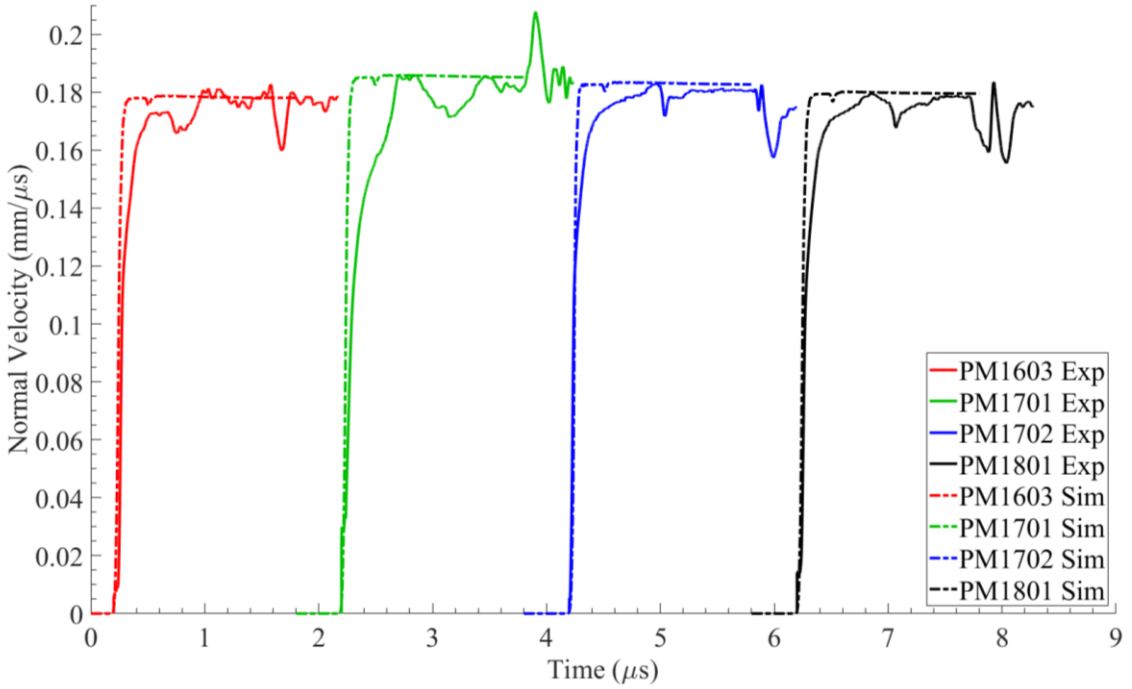

Figure 5.3 Normal velocity profiles of high-pressure shots on sucrose. Experimental profiles are shown using solid lines while the simulated profiles are represented using dashed lines

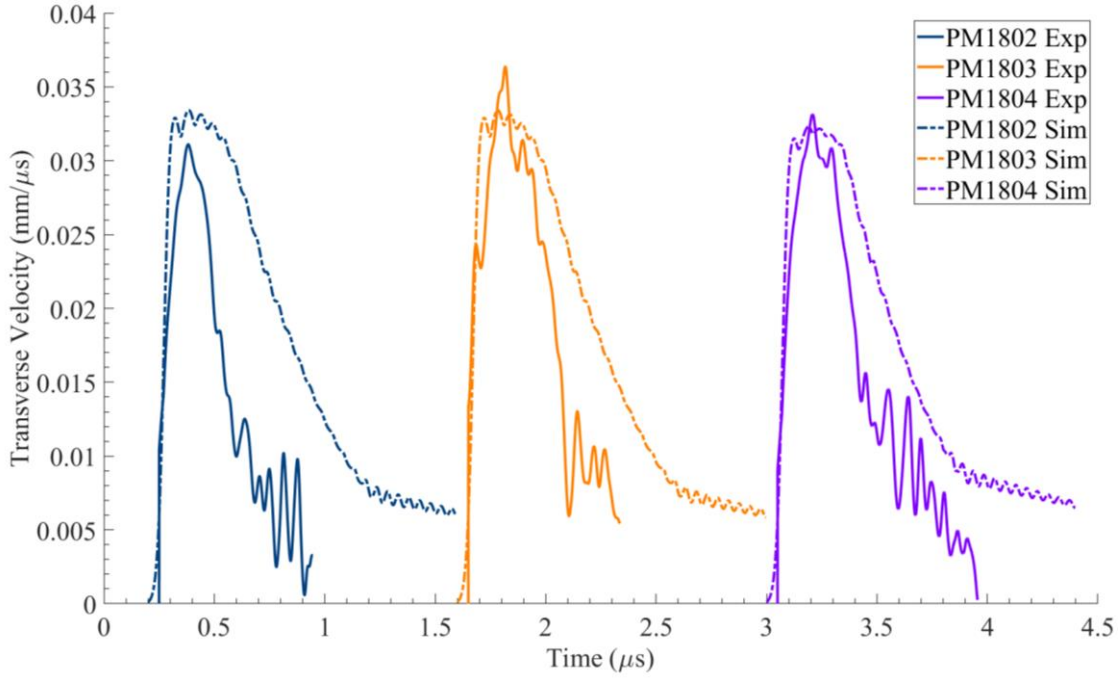

Figure 5.4 Transverse velocity profiles of low-pressure shots on sucrose. Experimental profiles are shown using solid lines while the simulated profiles are represented using dashed lines

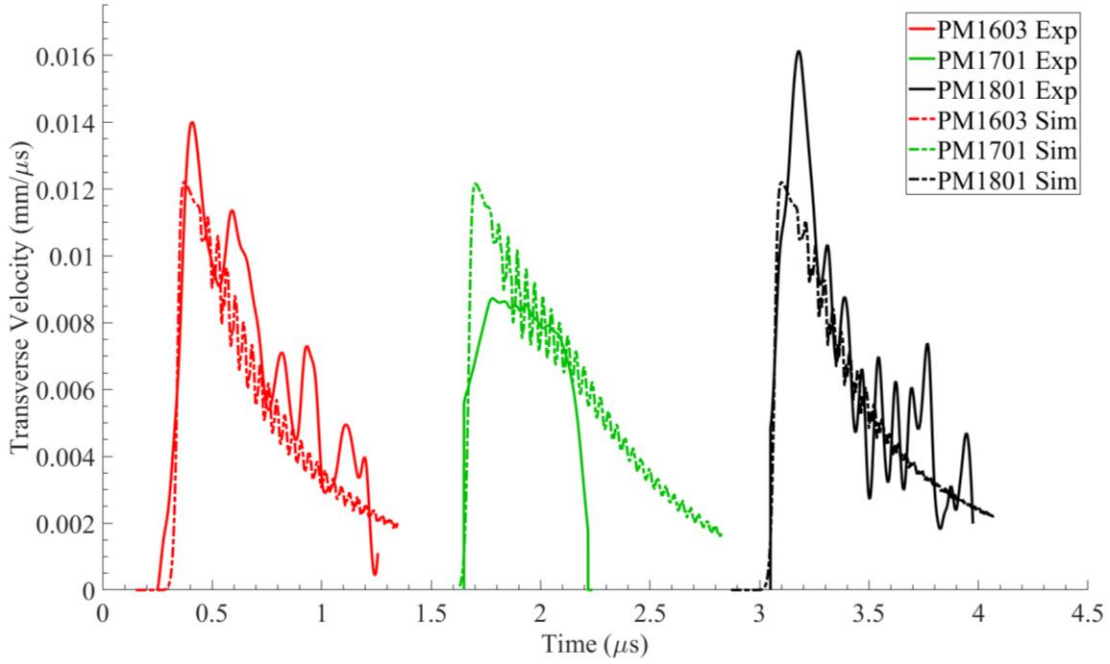

Figure 5.5 Transverse velocity profiles of high-pressure shots on sucrose. Experimental profiles are shown using solid lines while the simulated profiles are represented using dashed lines

5.3 Adiabatic Shear Localization

A drop in the shear strength of sucrose as shown by experiments and simulations is indicative of the development of localized deformation in the form of adiabatic shear bands. Temperature profiles across the specimen for a low and high-pressure case each are plotted in Figure 5.6 and Figure 5.7 respectively. Shots PM1804 and PM1603 are chosen as representative shots for low and high-pressure cases. As the specimen is compressed by the normal wave, the temperature of the specimen rises uniformly due to elastic and plastic work; the contribution of each to temperature rise is discussed further in section 5.4.1. There is a small drop in temperature at each specimen interface due to heat conduction to the bounding anvil plates. However, the temperature drop at the interfaces is so small that thermal conduction effects are practically negligible and the temperature increase in the specimen can be assumed to be the result of a purely adiabatic process. After the arrival of the shear wave, adiabatic shear localization is observed in both low and high-pressure cases. A shear band of $\sim 3.5\,\mu m$ width forms for the low-pressure case while the band width for the high-pressure case is $\sim 4.3\,\mu m$, as shown in Figure 5.6 and Figure 5.7 respectively.

For the low-pressure case, the shear wave arrives at the left specimen interface at 0.86 μs and shear localization begins at 1.16 μs. Shear localization is characterized by a sudden and steep increase in temperature and a drop in shear stress, as shown at the middle of the shear band in Figure 5.8. Normal and shear stress profiles for the element are also plotted to provide a perspective on the timeline of events. It is observed that the temperature increases initially to 370 K following the arrival of the normal wave. When the normal stress has plateaued, the

temperature in the middle of the band remains constant. After the shear wave arrives, there is a modest increase in temperature initially followed by a rapid rise after localization begins. Temperatures as high as 1136 K are predicted at the end of 2 μs.

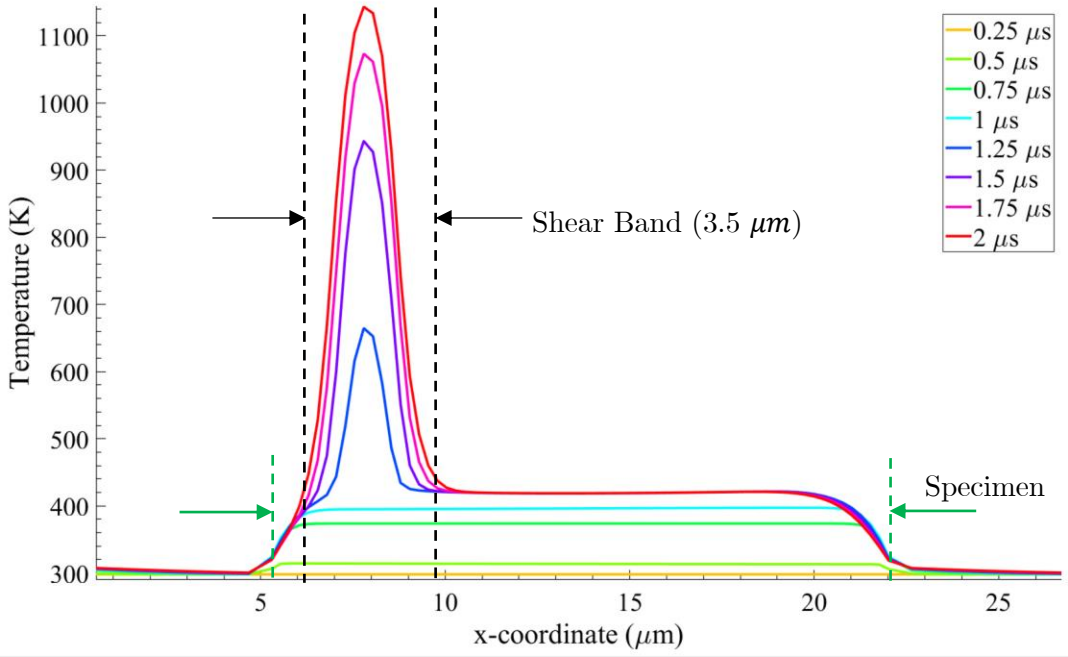

Figure 5.6 Temperature profile for shot PM1804 (low-pressure shot) plotted in deformed coodinates. The span of the specimen is indicated by green arrows. A small portion of D2 anvil steel plates on either side is also plotted to demonstrate that negligible heat conduction takes place at the specimen interfaces for the time duration considered. Note that the temperature values are plotted at integration points of each element. Temperatures are plotted at 8 different time instants from 0.25 μs to 2 μs. Time of impact is 0 μs. Normal wave arrives at the left interface of the specimen at 0.45 μs while the shear wave arrives at 0.86 μs. A uniform increase in temperature is observed across the specimen initially. A little while after the arrival of shear wave, between 1 and 1.25 μs, temperature begins to localize in a shear band. The band width is measured to be roughly 3.5 μm. Temperatures as high as 1136 K are expected within the band at 2 μs

Similarly, stress and temperature profiles are plotted in Figure 5.9 for the high-pressure shot, in the middle of the shear band. In this case, normal compression increases the

temperature substantially to a value of 594 K from the ambient, as compared to a value of 370 K for the low-pressure shot. A larger increase is expected with increasing pressure due to increase in both thermo-elastic work and thermo-viscoplastic work. It is also observed that the time duration between the arrival of shear wave and formation of shear band is only 0.11 μs compared to 0.3 μs for the low-pressure case. Therefore, localization begins earlier in time at higher pressures in PSPI experiments. However, as is the case with the low-pressure shot, the steep increase in temperature coincides with the drop in shear stress.

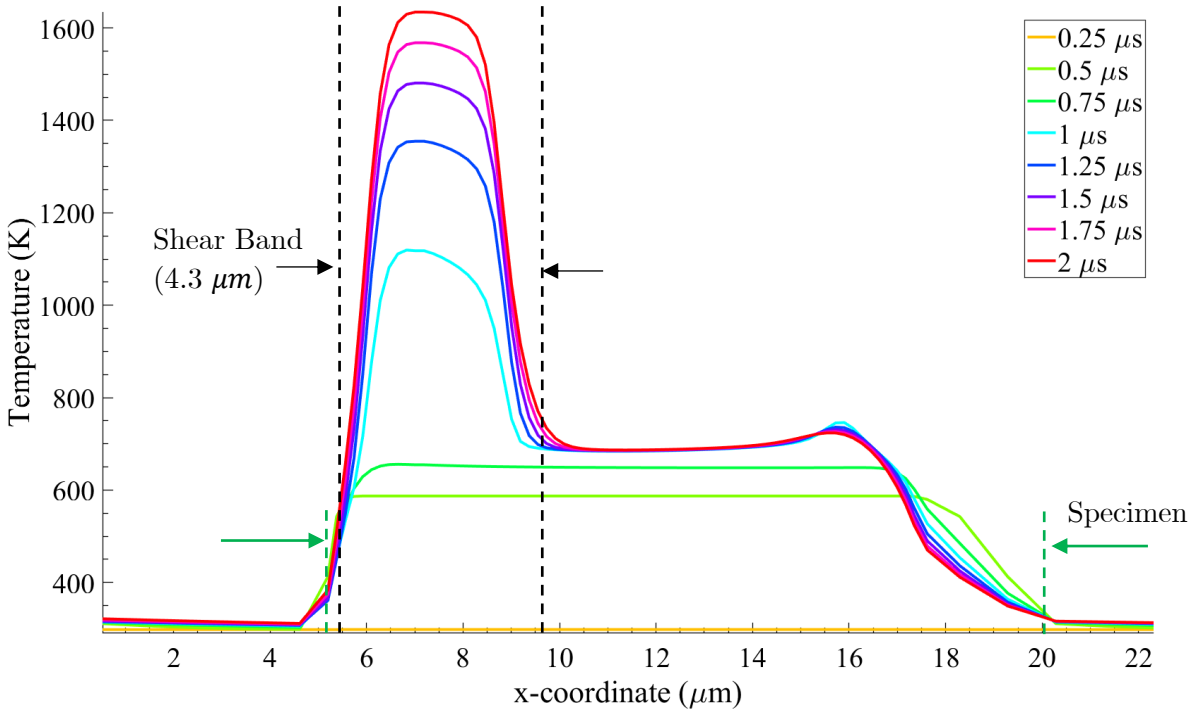

Figure 5.7 Temperature profile for shot PM1603 (high-pressure shot) plotted in deformed coordinates. The span of the specimen is indicated by green arrows. A small portion of WC anvil steel plates on either side is also plotted to demonstrate that negligible heat conduction takes place at the specimen interfaces for the time duration considered. Note that the temperature values are plotted at integration points of each element. Temperatures are plotted at 8 different time instants from 0.25 μs to 2 μs. Time of impact is 0 μs. Normal wave arrives at the left interface of the specimen at 0.38 μs while the shear wave arrives at 0.65 μs. A uniform temperature increase is observed across the specimen after the arrival of the normal wave. However, right after the arrival of shear wave, there are signs of localized temperature rise

between 0.75 μs and 1 μs, close to the left interface of the specimen. A shear band with a width of 4.3 μm eventually forms. Temperatures as high as 1634 K are expected within the shear band at 2 μs

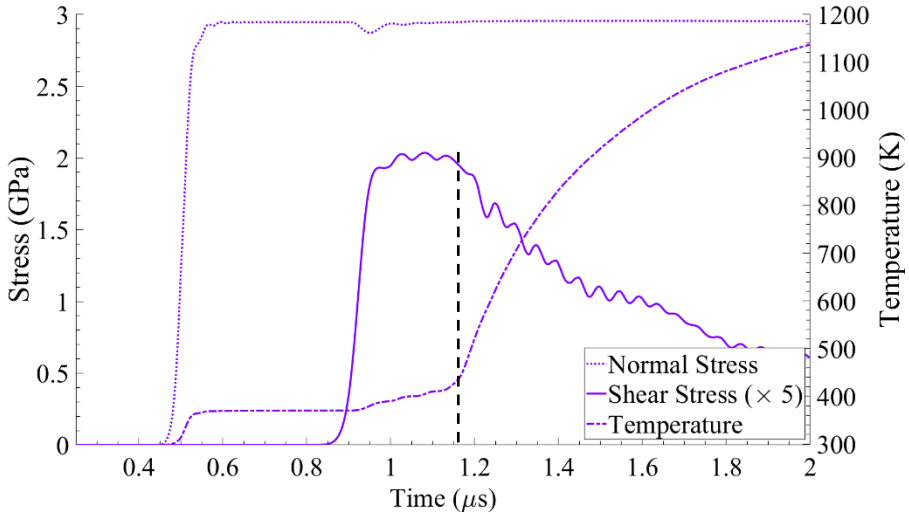

Figure 5.8 Normal and shear stress profiles at the middle of the shear band for shot PM1804 (low-pressure shot). Shear stress is scaled by a factor of 5 for better visualization. The stresses are shown on the left y-axis. Temperature profile is also plotted at the same location and its values indicated on the right y-axis. All values are plotted at the integration point of the element in the middle of the shear band. Temperature is observed to rise steeply at 1.16 μs which coincides with a drop in shear stress, indicating the onset of localization (shown using a vertical dashed black line)

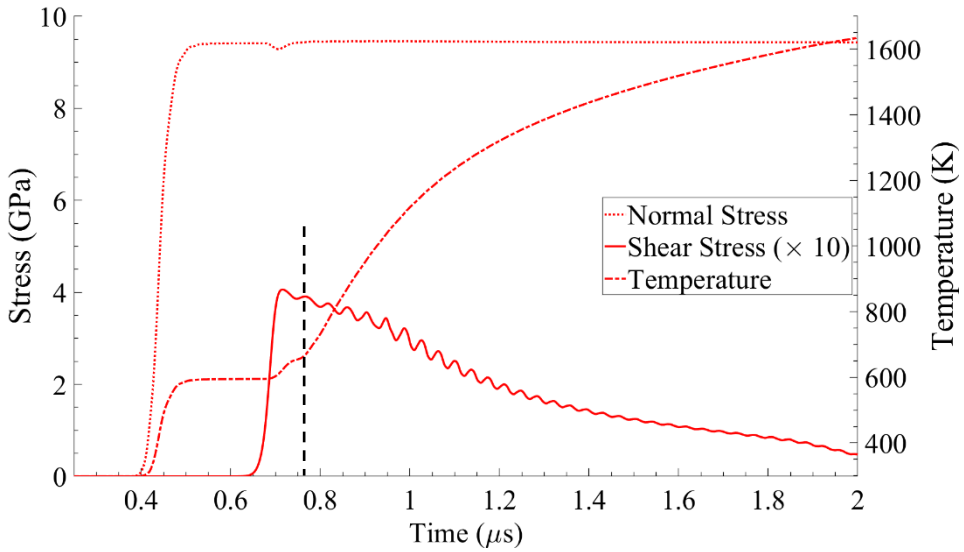

Figure 5.9 Normal and shear stress profiles at the middle of the shear band for shot PM1603 (high-pressure shot). Shear stress is scaled by a factor of 10 for better visualization. The stresses are shown on the left y-axis. Temperature profile is also plotted at the same location and its values indicated on the right y-axis. All values are plotted at the integration point of the element in the middle of the shear band. Temperature is observed to rise steeply at 0.76 μs which coincides with a drop in shear stress, indicating the onset of localization (shown using a vertical dashed black line)

5.4 Discussion

The constitutive model of sucrose presented in Chapter-4 is implemented in ABAQUS to model the PSPI experiments. Even though sucrose has been used as an energetic simulant for a long time, material models of sucrose have not been characterized for their shearing behavior under different pressure ranges. In this chapter, a material model of sucrose with a complete equation of state and a thermo-viscoplasticity model for strength is shown to adequately capture the experimentally observed shearing response. The model can be extended to simulate more complex phenomena like pore collapse or shear band formation under complex loading scenarios. Simulations show that the fall in the shear strength of sucrose is a result of a thermo-viscoplastic instability in the form of adiabatic shear bands. It is also shown that normal

compression can lead to significant temperature increase, especially at higher pressures. The contribution of thermoelastic heating to this temperature increase is significant and can affect the shearing response upon arrival of the shear wave, as discussed below. Therefore, for accurate determination of temperatures and shearing behavior under PSPI loading, a complete equation of state with a temperature-dependent specific heat capacity is required. If the constant specific heat capacity at the ambient conditions were used, much larger temperatures would be expected. It is shown that melting eventually occurs in the shear bands leading to a drop in the shearing resistance. The choice of the melt curve can significantly affect the shearing behavior, as discussed below. Accurate modeling of material behavior beyond melt requires consideration of solid-liquid phase transition, latent heat of melting and a constitutive relation for the molten liquid, especially the shear viscosity of the liquid. Lack of experimental data for molten energetic crystals or their simulants makes it difficult to validate the material models for the melt. Modeling the liquid phase, especially the pressure and temperature dependent shear viscosity, is important in simulations of phenomena such as pore-collapse. However, the attention of this study is limited to the solid phase before melt. It is assumed that beyond melt, the solid loses its strength completely while maintaining a constant limiting shear strain-rate. Such an assumption can be relaxed when better models of the phase transition to the liquid phase and shear resistance of the melt phase become available.

5.4.1 Thermoelastic work

A significant temperature increase is expected from elastic compression of sucrose, as predicted by the isentropic temperature increase in Figure 6.1 of Chapter 4. It is important to accurately model this temperature for the PSPI experiments as it significantly impacts the

subsequent material response upon the arrival of the shear wave. Some plastic work is also expected during normal compression which leads to an additional temperature rise. However, separating the thermo-elastic and thermo-viscoplastic temperature changes during normal loading a priori is not possible due to the non-linear coupling of the two effects. Since explicit expressions for heat generation due to thermo-elastic and thermo-viscoplastic effects are known, it is possible to separate the two effects in the numerical scheme. Assuming the specific heat to be constant for a given time-step, the temperature increase due to thermo-elasticity can be calculated by using equation (5.3). Such an assumption is valid for the small time-steps used here. An infinitesimal time step ensures infinitesimal changes in temperature and volume and hence infinitesimal changes in the specific heat. Therefore, the temperature change due to thermoelastic work for a time-step can be found to be:

$$\Delta\theta = \frac{\Delta q^e}{\rho c_v(\theta)} \tag{5.3}$$

where the thermo-elastic heat increment, $\Delta q^e = \dot{q}^e \Delta t$ is calculated in the deformed configuration. The simulated predictions are compared with the theoretical predictions for isentropic hydrostatic compression of a single 3D element. Perfect agreement is seen between analytical and computational results (see Figure 5.10) validates the method for separating temperature increase due to elastic and viscoplastic deformations

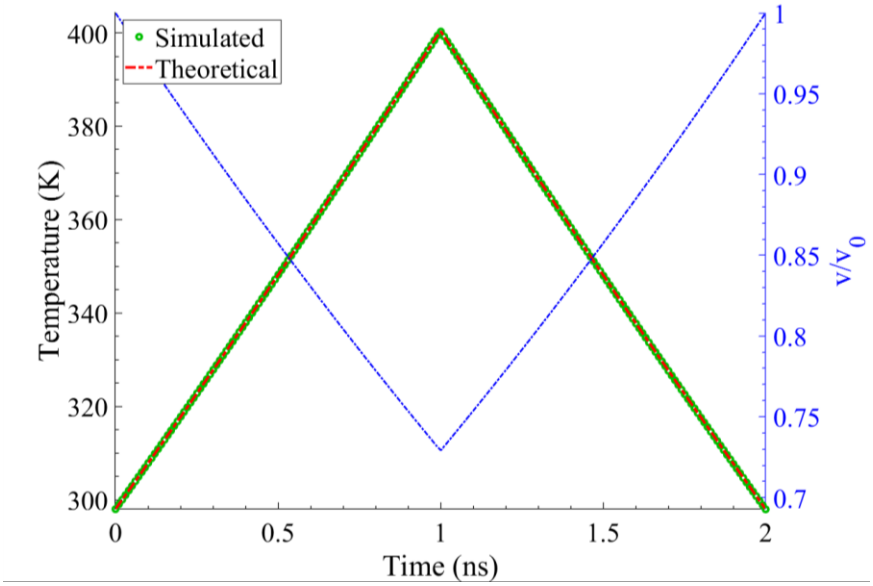

Figure 5.10 Simulated (green open circles) and theoretical (red dashed line) temperature profiles of a single 3D element subjected to a ramp volumetric strain. A minimum compression ratio (= v/v_0 = 1 - volumetric strain) of 0.73 is imposed to decrease linearly over a duration of 1 ns followed by a linear increase to the original state over a duration of another ns.

Temperature increase is plotted at the middle of shear band for low and high-pressure cases as a function of pressure in Figure 5.11 and Figure 5.12 respectively. Simulated thermoelastic temperature profiles agree well with theoretical predictions. For the low-pressure shot, the overall increase in temperature due to normal compression is 72 K; thermoelastic work contributes 42 K increase while the rest is due to viscoplastic work. For the case of large-pressure shot, thermoelastic work contributes a temperature increment of 124 K in a total increase of 296 K during normal compression. It is clear from these figures that thermo-elastic temperature increase is a significant portion of the total temperature change and hence an important component that should be included in a thermo-mechanically coupled model for energetic materials and their simulants.

5.4.2 Melt Curve

Yield strength of sucrose is a strong function of the specimen temperature and its melt temperature, which is accounted for by the $(1-\hat{\theta}^m)$ factor in the Johnson-Cook model for yield strength. However, melting point of sucrose is itself a function of pressure (thus making the shear strength of sucrose dependent on pressure). Since the thermal factor in the Johnson-Cook model is responsible for thermal softening and hence a fall in the shear strength, it is important to consider the pressure-dependence of the melting point of sucrose so that its shear behaviour can be simulated consistently for different pressures. Accurate representation of melt curve is also important for prediction of hot-spot formation. Shearing resistance of the energetic crystal drops to zero at melt, shear viscosity of the molten fluid takes over and results in a significantly reduced thermal dissipation. Hence, the melt curve dictates the amount of dissipation and hence peak hot-spot temperatures during localization. Formation of hot-spots and their transition to ignition is highly temperature-sensitive under weak shocks which emphasizes the importance of accurate prediction of melting point as a function of pressure. However, measurement of melting point for energetic crystals is difficult to measure due to associated dissociation reactions. Therefore, experimentally measured melt curves are typically replaced by empirical laws. One such law is the Lindeman Law Lindemann (1910), Ross (1969), Poirier (2000) , as discussed in Chapter-4:

$$\theta_m = \theta_{m0} \exp\left[2\Gamma_0(1-\nu) + \frac{2}{3}\ln(\nu)\right] \tag{5.4}$$

where subscript '0' indicates ambient temperature and pressure. θ_m is the melt temperature, Γ_0 is the Gruneisen parameter at ambient conditions, $\nu = \frac{v}{v_0} = \frac{\rho_0}{\rho}$ is the relative volume and ρ represents the density of the solid. Sometimes, the Lindeman Law is linearized in volume

(Kraut-Kennedy relation) or in pressure Menikoff and Sewell (2002) . However, as discussed in Menikoff and Sewell (2002) and Appendix B, the use of linearized versions for higher pressures are not very accurate. However, molecular dynamics simulations on HMX Kroonblawd and Austin (2020) show that the Lindemann Law grossly underestimates the melt temperature whereas the following Simon-Glatzel relationship (equation (5.5)) fits the molecular dynamics data very well.

$$\theta_m = \theta_{m0}\left(1 + \frac{P - P_{ref}}{P_0}\right)^{1/d} \tag{5.5}$$

Here (P_{ref}, P_0, d) are fitting parameters. Due to the lack of experimental data on the melt curve of sucrose as a function of pressure, parameters for the Simon-Glatzel fit used for HMX by Kroonblawd and Austin (2020) are employed here for sucrose. Figure 5.13 shows a comparison between the shear stress profiles based on the Simon-Glatzel melt relation and the Lindemann melt curve for low and high-pressure cases. Other material parameters are kept the same for both cases. Using the Lindemann Law results in a much smaller shear strength than that observed experimentally. This is expected since a lower melt temperature, as predicted by the Lindemann Law results in earlier melting and hence an earlier fall in shear strength. Additionally, it results in a lower overall temperature due to decreased dissipation after melt, affecting the predictions of strength and temperature. On the other hand, the Simon-Glatzel melt relation captures the experimental data much better.

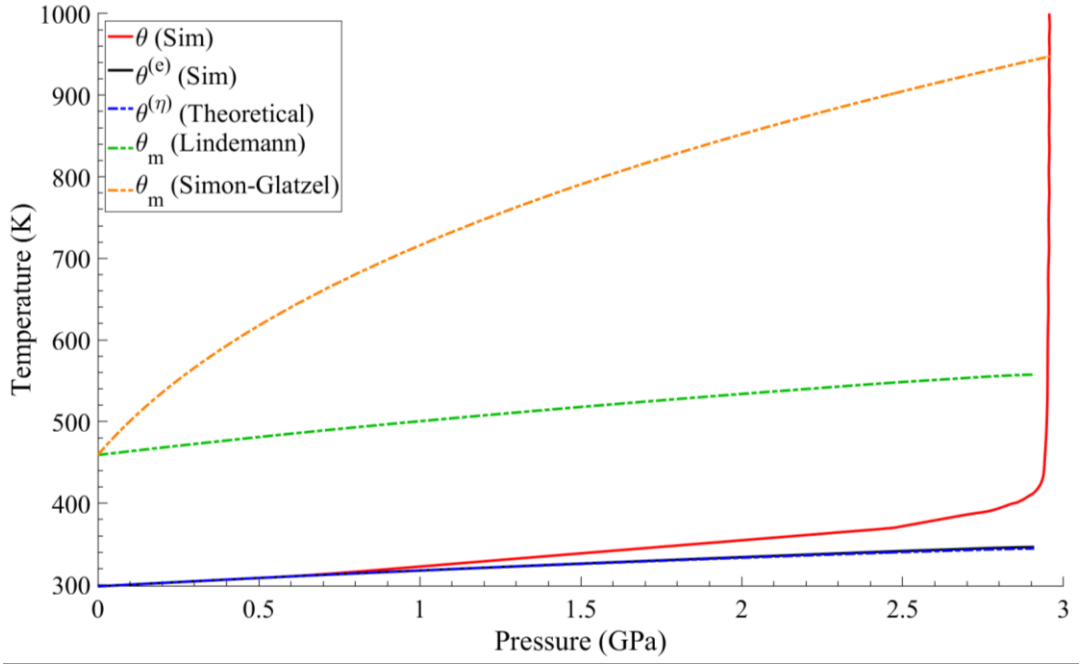

Figure 5.11 Simulated temperature profiles as a function of pressure, plotted at the middle of the shear band for shot PM1804 (low-pressure shot). θ (solid red line) shows the simulated profile using the Simon-Glatzel melting relation. A modest increase in temperature is observed as the pressure increases under compressive loading. After the pressure saturates, the temperature increases steeply due to shear loading. $\theta^{(e)}$ (solid black line) shows thermoelastic temperature increase as predicted by simulations and $\theta^{(\eta)}$ (dashed blue line) shows isentropic temperature increase predicted by theoretical calculations for the same increase in pressure. θ_m (dashed green line) shows the melt curve for Lindemann Law and θ_m (dashed orange line) shows the melt curve for Simon-Glatzel relation. The Lindemann Law predicts melting at 557 K while the Simon-Glatzel curve predicts melting at a much higher temperature of 947 K, at the same saturation pressure of 2.95 GPa

A comparison between the two melting relations is also plotted at the middle of shear bands for the low and high-pressure cases in Figure 5.11 and Figure 5.12 respectively. It is observed that for the same pressure, Lindemann Law predicts a much lower melt temperature than the Simon-Glatzel relation.

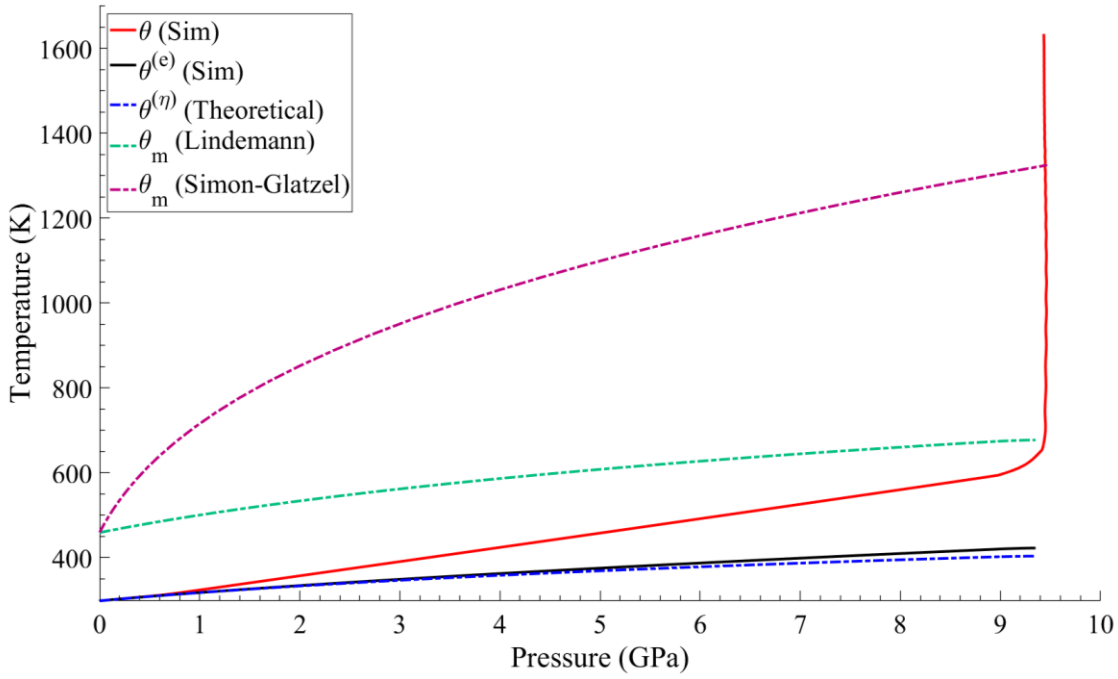

Figure 5.12 Simulated temperature profiles as a function of pressure, plotted at the middle of the shear band for shot PM1603 (high-pressure shot). θ (solid red line) shows the simulated profile using the Simon-Glatzel melting relation. A substantial increase in temperature is observed as the pressure increases under compressive loading. After the pressure saturates, the temperature increases steeply due to shear loading. $\theta^{(e)}$ (solid black line) shows thermoelastic temperature increase as predicted by simulations and $\theta^{(\eta)}$ (dashed blue line) shows isentropic temperature increase predicted by theoretical calculations for the same increase in pressure. θ_m (dashed green line) shows the melt curve for Lindemann Law and θ_m (dashed orange line) shows the melt curve for Simon-Glatzel relation. The Lindemann Law predicts melting at 677 K while the Simon-Glatzel curve predicts melting at a much higher temperature of 1325 K, at the same saturation pressure of 9.45 GPa

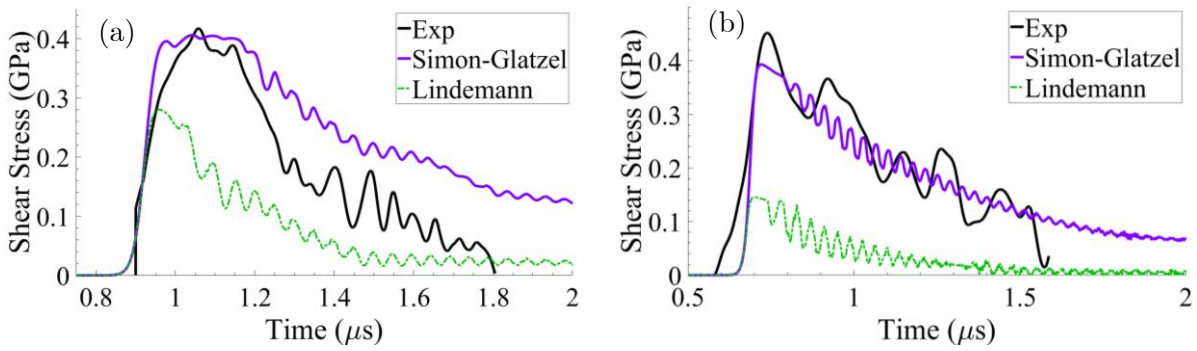

Figure 5.13 Shear stress vs time for shot (a) PM1804 (low-pressure shot), and (b) PM1603 (high-pressure shot). A comparison is drawn between the shear stress profiles obtained using Simon-Glatzel melt relation and the Lindemann melt curve, keeping all other material parameters for sucrose the same

5.5 Summary

PSPI experiments on sucrose have been simulated using the constitutive model developed in Chapter-4. For an appropriate choice of material parameters (shown in Table 5.1), simulated transverse velocity profiles fit the experimentally measured values reasonably well for both low and high-pressure shots. Adiabatic shear localization results in a fall in the shear strength of sucrose. Simulations predict peak temperatures as high as 1136 K and 1634 K within the shear band for nominal pressures of 3 GPa and 9.5 GPa respectively. Such high temperatures go beyond the melting point of sucrose at corresponding pressures. It is shown that the choice of the melt curve, i.e. melting temperature as a function of pressure, plays a significant role in deciding the shearing response of sucrose. The most widely used melting relation for energetic crystals -Lindemann law, is shown to largely under-estimate the melting point required for a good fit of simulated shear stresses to experimental observations. Therefore, an alternative melt curve given by the Simon-Glatzel relation is employed. The contributions of thermoelastic work and thermo-viscoplastic work to the total increase in temperature during normal compression

are separated numerically in the VUMAT sub-routine and validated for a simple case of a single 3D element. Thermo-elastic work due to normal compression causes significant temperature increase and is found to influence the response of sucrose specimen under subsequent shear loading. Overall, it can be concluded that it is very important to characterize the shear strength behavior, melt curve and shear viscosity of the molten phase to accurately model hot-spot temperatures of energetic crystals and their simulants. While shear strength measurements on sucrose have been made in the present study, experimental measurements of the melt curve and shear viscosity remain a missing link in the validation of its deformation behavior under high-pressures and high strain-rates. Such measurements are expected to increase confidence in simulations of complex phenomena like pore-collapse and the resulting temperature changes.

5.6 Appendix A: VUMAT Algorithm

Given: ($\boldsymbol{F}_{n+1}$, $\boldsymbol{F}_n^p, \boldsymbol{D}_n^p, \boldsymbol{T}_n, \theta_{n+1}$), find $\boldsymbol{T}_{n+1}$.

1. If $t = 0$ (dummy elastic step), there is no plastic flow, i.e.

$$\boldsymbol{F}_{n+1}^p = \boldsymbol{I} \tag{5.6}$$

$$\boldsymbol{D}_{n+1}^p = \boldsymbol{D}_n^p$$

a. Elastic deformation gradient is the overall deformation gradient.

$$\boldsymbol{F}_{n+1}^e = \boldsymbol{F}_{n+1} \tag{5.7}$$

b. Polar Decomposition of elastic deformation gradient:

$$\boldsymbol{U}_{n+1}^e = \sqrt{(\boldsymbol{F}_{n+1}^e)^T \boldsymbol{F}_{n+1}^e} \tag{5.8}$$

$$\boldsymbol{R}_{n+1}^e = \boldsymbol{F}_{n+1}^e (\boldsymbol{U}_{n+1}^e)^{-1}$$

c. Find logarithmic strain and elastic compression ratio:

$$\boldsymbol{E}_{n+1}^e = \ln(\boldsymbol{U}_{n+1}^e) \tag{5.9}$$

$$J_{n+1}^e = \frac{v_{n+1}}{v_0} = \det(\boldsymbol{F}_{n+1}^e)$$

d. The logarithmic strain is calculated from the eigenvalues of $\boldsymbol{U}^e$ using the relation:

$$\boldsymbol{E^e} = \sum_{i=1}^{3} \ln(\lambda_i^e)\, \boldsymbol{r_i} \otimes \boldsymbol{r_i} \tag{5.10}$$

e. Find Mandel stress and Cauchy Stress:

$$\boldsymbol{M^e_{n+1}} = 2G\boldsymbol{E^e_{n+1}} + \lambda\, tr(\boldsymbol{E^e_{n+1}})\boldsymbol{I} \tag{5.11}$$

$$\boldsymbol{T}_{n+1} = \frac{1}{J^e_{n+1}}\, \boldsymbol{R^e_{n+1}} \boldsymbol{M^e_{n+1}} (\boldsymbol{R^e_{n+1}})^{\boldsymbol{T}}$$

f. Update state variables. Find effective stress from deviatoric Mandel stress. Effective plastic strain remains constant in an elastic step and the effective plastic strain-rate is zero.

$$\overline{\sigma_{n+1}} = \sqrt{\frac{3}{2}}\, |\boldsymbol{M^e_{0,n+1}}| \tag{5.12}$$

$$\overline{\epsilon^p_{n+1}} = \overline{\epsilon^p_n}$$

$$\overline{\dot{\epsilon}^p_{n+1}} = 0$$

2. Else (Plastic Step).

a. For an explicit step, freeze plastic plow, i.e. assume

$$\boldsymbol{D^p_{n+1}} = \boldsymbol{D^p_n} = \frac{3}{2} \frac{\overline{\dot{\epsilon}^p_n}\, \boldsymbol{M^e_{0,n}}}{\bar{\sigma}_n} \tag{5.13}$$

If $\overline{\sigma_n} = 0$, $\boldsymbol{D^p_{n+1}} = 0$, else $\boldsymbol{D^p_{n+1}} = \frac{3}{2} \frac{\overline{\dot{\epsilon}^p_n}\, \boldsymbol{M^e_{0,n}}}{\bar{\sigma}_n}$

b. Find the plastic deformation gradient using a Forward Euler scheme for a discretized version of $\boldsymbol{\dot{F}^p = D^p F^p}$

$$\boldsymbol{F^p_{n+1}} = (\boldsymbol{I} + dt * \boldsymbol{D^p_{n+1}})\boldsymbol{F^p_n} \tag{5.14}$$

c. Since $\boldsymbol{F = F^e F^p}$, find the elastic deformation gradient:

$$\boldsymbol{F^e_{n+1}} = \boldsymbol{F}_{n+1}\left(\boldsymbol{F^p_{n+1}}\right)^{-1} \tag{5.15}$$

d. Polar decompose the elastic deformation gradient:

$$\boldsymbol{U^e_{n+1}} = \sqrt{(\boldsymbol{F^e_{n+1}})^T \boldsymbol{F^e_{n+1}}} \tag{5.16}$$

$$\boldsymbol{R^e_{n+1}} = \boldsymbol{F^e_{n+1}} (\boldsymbol{U^e_{n+1}})^{-1}$$

e. Find logarithmic strain and elastic compression ratio:

$$\boldsymbol{E^e_{n+1}} = \ln(\boldsymbol{U^e_{n+1}}) \tag{5.17}$$

$$J^e_{n+1} = \frac{v_{n+1}}{v_0} = \det\,(F^e_{n+1})$$

f. Find pressure using complete equation of state. First, calculate isothermal pressure using the 3rd order logarithmic Birch-Murnaghan equation of state:

$$P_{BM} = -\frac{K_{\theta 0}}{J^e_{n+1}} ln(J^e_{n+1}) \left[1 - \frac{K'_{\theta 0} - 2}{2} ln(J^e_{n+1})\right] \tag{5.18}$$

g. Find the integral of specific heat capacity:

$$\int_{\theta_0}^{\theta} c_v(\theta) d\theta = a_0(\theta - \theta_0) + a_1(\theta^2 - \theta_0^2) \tag{5.19}$$

h. Find pressure from the complete equation of state:

$$P_{n+1} = P_{BM} - \frac{d\phi}{dv} \int_{\tilde{\theta}_0}^{\tilde{\theta}} \tilde{c_v}(\tilde{\theta}) d\tilde{\theta} = P_{BM} + \phi(v) \frac{\Gamma_0}{v_0} \int_{\tilde{\theta}_0}^{\tilde{\theta}} \tilde{c_v}(\tilde{\theta}) d\tilde{\theta} = P_{BM} + \frac{\Gamma_0}{v_0} \int_{\theta_0}^{\theta} c_v(\theta) d\theta \tag{5.20}$$

i. Find Mandel stress and Cauchy Stress:

$$\boldsymbol{M}^{\boldsymbol{e}}_{n+1} = 2G\boldsymbol{E}^{\boldsymbol{e}}_{\boldsymbol{0},n+1} - P_{n+1} J^e_{n+1} \boldsymbol{I} \tag{5.21}$$

$$\boldsymbol{T}_{n+1} = \frac{1}{J^e_{n+1}} \boldsymbol{R}^{\boldsymbol{e}}_{n+1} \boldsymbol{M}^{\boldsymbol{e}}_{n+1} (\boldsymbol{R}^{\boldsymbol{e}}_{n+1})^{\boldsymbol{T}}$$

j. Update state variables. Find effective stress from deviatoric Mandel stress. In an explicit analysis, effective plastic is calculated using the effective plastic strain-rate from the previous increment.

$$\overline{\sigma_{n+1}} = \sqrt{\frac{3}{2}} \, |\boldsymbol{M}^{\boldsymbol{e}}_{\boldsymbol{0},n+1}| \tag{5.22}$$

$$\overline{\epsilon^p_{n+1}} = \overline{\epsilon^p_n} + \dot{\overline{\epsilon^p_n}} \Delta t$$

k. To update the effective plastic-strain rate, the value of melting temperature at the current pressure is required. This is done through the Simon-Glatzel relation:

$$\theta_{m,n+1} = \theta_{m0} \left(1 + \frac{P_{n+1} - P_{ref}}{P_0}\right)^{1/d} \tag{5.23}$$

l. If $\theta_{n+1} > \theta_{m,n+1}$, the temperature term in the Johnson-Cook Model is zero and the material loses all its shear strength, i.e. $\hat{\theta} = 1$. Find effective plastic strain-rate using the Johnson-Cook Model:

$$\left(\dot{\overline{\epsilon^p_{n+1}}}\right)_{JC} = \dot{\epsilon_0} \exp\left(\frac{1}{C}\left(\frac{\overline{\sigma_{n+1}}}{\left(A + B\left(\overline{\epsilon^p_{n+1}}\right)^n\right)\left(1 - \hat{\theta}^m_{n+1}\right)} - 1\right)\right) \tag{5.24}$$

m. Find the effective plastic strain-rate which is limited by a constant value through the following relation:

$$\frac{1}{\dot{\overline{\epsilon^p_{n+1}}}} = \frac{1}{\left(\dot{\overline{\epsilon^p_{n+1}}}\right)_{JC}} + \frac{1}{\dot{\overline{\epsilon^p_{lim}}}} \tag{5.25}$$

n. Calculate increment in plastic work converted to heat:

$$(\Delta q^p)_{n+1} = \beta \boldsymbol{T}: \boldsymbol{D^p} = \frac{\beta}{J^e_{n+1}} \boldsymbol{M^e}: \boldsymbol{D^p} = \frac{\beta}{J^e_{n+1}} \bar{\sigma}_{n+1} \overline{\dot{\epsilon^p}}_{n+1} \Delta t \tag{5.26}$$

Note that the factor of $\left(\frac{1}{J^e_{n+1}}\right)$ is required to convert the heat generated due to plastic work, from the structural configuration to the deformed configuration. Since the inelastic heat fraction is accounted for through β in the VUMAT, it should not be doubly imposed through the ABAQUS input file.

o. As a first step towards calculating thermoelastic work, find the specific heat the current time instant.

$$c_{v,n+1} = \frac{\theta^3_{n+1}}{c_0 + c_1\theta_{n+1} + c_2\theta^2_{n+1} + c_3\theta^3_{n+1}} \tag{5.27}$$

p. Find $\partial \boldsymbol{M^e}/\partial\theta$ assuming no temperature dependence of the shear modulus:

$$\left(\frac{\partial P}{\partial \theta}\right)_{n+1} = \Gamma_0 \rho_0 c_{v,n+1} \tag{5.28}$$

$$\left(\frac{\partial \boldsymbol{M^e}}{\partial \theta}\right)_{n+1} = -\left(\frac{\partial P}{\partial \theta}\right)_{n+1} J^e_{n+1}\, \boldsymbol{I} \tag{5.29}$$

q. Find $\dot{\boldsymbol{C}}^{\boldsymbol{e}}$:

$$\boldsymbol{F^e_n} = \boldsymbol{F}_n \left(\boldsymbol{F^p_n}\right)^{-1} \tag{5.30}$$

$$\boldsymbol{C^e_n} = (\boldsymbol{F^e_n})^T \boldsymbol{F^e_n} \tag{5.31}$$

$$\boldsymbol{C^e_{n+1}} = (\boldsymbol{F^e_{n+1}})^T \boldsymbol{F^e_{n+1}} \tag{5.32}$$

$$\dot{\boldsymbol{C^e_{n+1}}} = \frac{\boldsymbol{C^e_{n+1}} - \boldsymbol{C^e_n}}{\Delta t} \tag{5.33}$$

Where $\boldsymbol{F^e_n}$ is available as *defgradOld*, $\boldsymbol{F^e_{n+1}}$ as *defgradNew* and $\boldsymbol{F^p_n}$ through state variables, *stateOld*.

r. Find thermoelastic work increment:

$$(\Delta q^e)_{n+1} = \frac{1}{J^e_{n+1}} \frac{\theta_{n+1}}{2} \left(\frac{\partial \boldsymbol{M^e}}{\partial \theta}\right)_{n+1} : (\boldsymbol{C^e_{n+1}})^{-\boldsymbol{T}} \dot{\boldsymbol{C}}^{\boldsymbol{e}}_{\boldsymbol{n}} \Delta t \tag{5.34}$$

Add $(\Delta q^e)_{n+1}$ to the plastic work increment.

s. Calculate thermoelastic temperature change:

$$\theta^e_{n+1} = \theta^e_n + \frac{(\Delta q^e)_{n+1}}{\rho c_v} = \theta^e_n + \frac{J^e_{n+1}(\Delta q^e)_{n+1}}{\rho_0 c_v} \tag{5.35}$$

3. Update the specific internal energy and dissipated inelastic specific energy

5.7 Appendix B: Material Constants for Sucrose

5.7.1 Elastic Constants

5.7.1.1 Bulk Modulus

Bridgman made measurements of compression ratios of sucrose under pressures up to 3 GPa (see Table V in Bridgman (1949)). The bulk modulus and elastic modulus (assuming Poisson's ratio, $\nu = 0.25$) are shown in the table below:

Table 5.2 Elastic moduli of sucrose measured at different pressures. Bulk moduli and volumetric changes are calculated based on Table V in Bridgman (1949) .

Pressure (kg/cm^2)	Pressure (GPa)	$\frac{\Delta V}{V_0}$	Bulk Modulus (GPa)	Young's Modulus (GPa)	Shear Modulus
5,000	0.5	0.03151	15.868	23.802	9.521
10,000	1	0.05518	18.122	27.184	10.873
15,000	1.5	0.07434	20.178	30.266	12.107
20,000	2	0.09074	22.041	33.061	13.225
25,000	2.5	0.10552	23.692	35.538	14.215
30,000	3	0.11866	25.282	37.923	15.169

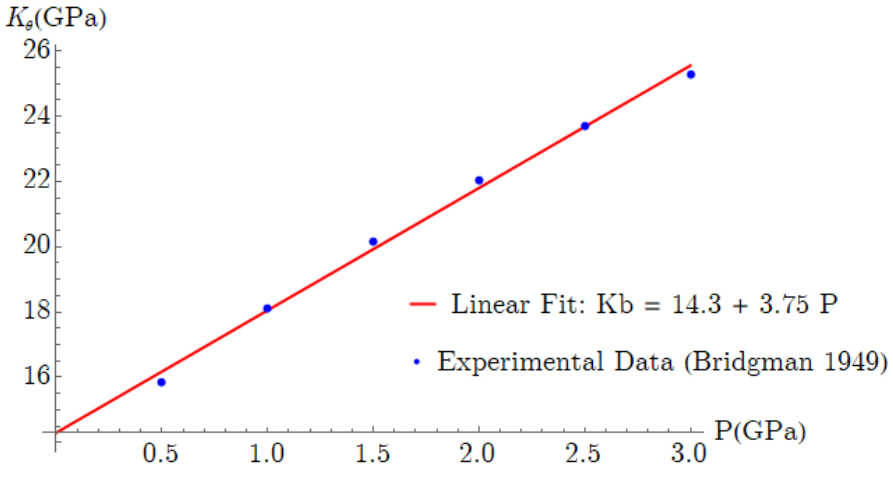

Figure 5.14 Linear fit to experimental data for isothermal bulk modulus of sucrose

Figure 5.14 indicates the pressure dependence of bulk modulus for sucrose. $K_{\theta 0} = 14.3\, GPa$ and $K'_{\theta 0} = 3.75$ are obtained using a linear fit to the experimental data. $K_{\theta 0}$ is the isothermal bulk modulus at ambient temperature and pressure while $K'_{\theta 0}$ is the first derivative of bulk modulus with respect to pressure at ambient temperature and pressure. These values are very close to the data obtained from Bridgman (1933) .

5.7.1.2 Poisson's Ratio and Young's Modulus

Trott et al. (2007) use a Poisson's ratio of 0.25 for sucrose. Using $K_{\theta 0} = 14.3\, GPa$ and $\nu = 0.25$, $E = 21.45\, GPa$ is obtained.

5.7.2 Thermal Constants

5.7.2.1Coefficient of Thermal Expansion

A mean volumetric coefficient of thermal expansion of $140.1 \times 10^{-6}\ ^{\circ}\mathrm{C}^{-1}$ is reported by Bridgman (1933) over a temperature range of $30\,^{0}C$ to $75\,^{0}C$.

5.7.2.2 Specific Heat

Specific heat capacity at constant pressure, c_p is reported by Anderson Jr et al. (1950) over a temperature range of $25\,^{0}C$ to $90\,^{0}C$. The experimental data is given in Table 5.3. In order to derive specific heat capacity at constant volume, c_v the following thermodynamic relation can be used:

$$c_p - c_v = v\theta\alpha^2 K_\theta \tag{5.36}$$

where $v = V/m$ is specific volume, α is the coefficient of thermal expansion and K_θ is the isothermal Bulk Modulus. It can be noted that the difference in c_p and c_v values is extremely small.

Table 5.3 Specific heat capacities of sucrose. c_p values are direct experimental measurements while c_v values are derived from thermodynamic constraints

Temp (K)	$c_p\left(\frac{J}{kg\,K}\right)$ (Experimentally Measured)	$c_v\ (= c_p - v\theta\alpha^2 K_\theta)$
275.6	1137.98	1087.331
281.9	1167.32	1115.513
289.7	1200.32	1147.079
296.2	1255.32	1200.885
296.8	1234.54	1179.995
296.9	1238.21	1183.646
299.4	1250.43	1195.407
301.2	1250.43	1195.076
302.8	1263.88	1208.232
313	1313.99	1256.467
320.3	1351.89	1293.026
342.4	1476.56	1413.634
362.7	1581.68	1515.024

Fitting to Debye Relation

Using a complete equation of state requires temperature dependent specific heat capacity. However, experimentally measured values are not available for the entire temperature range of interest. So, specific heat capacity is fit to the well-known Debye model of specific heat capacity.

$$c_v = \frac{9Nk}{M}\left(\frac{\theta}{\theta_D}\right)^3 \int_0^{\theta_D/\theta} \frac{x^4 e^x}{(e^x-1)^2}\,dx = 3A\left(\frac{\theta}{\theta_D}\right)^3 \int_0^{\theta_D/\theta} \frac{x^4 e^x}{(e^x-1)^2}\,dx \tag{5.37}$$

where N is the number of atoms, k is the Boltzmann constant, M is the molecular mass, θ_D is Debye temperature and $A = \frac{3Nk}{M}$. At $\theta \to 0, c_v \to 0$ and $\theta \to \infty, c_v \to fR_0/M$ where the latter asymptotic limit is referred to as the Dulong-Petit limit. $R_0 = 8.314 \frac{J}{K\ mol}$ is the universal gas constant and M is the molecular mass in kg/mol. f represents the degrees of freedom contributing to specific heat. For a monoatomic molecule, $f = 3$. However, for complex polyatomic molecules like HMX and sucrose, the number of degrees of freedom is very large. For any non-linear molecule, the total degrees of freedom is $3N$ (3 translational, 3 rotational and 3N-6 vibrational) where N is the number of atoms in the molecule. Hence, the Dulong-Petit limit of specific heat should be $\theta \to \infty, c_v \to 3NR_0/M$. However, as is noted in Menikoff and Sewell (2002) , some of the vibrational degrees of freedom corresponding to C-H bond stretching in HMX do not contribute to the specific heat capacity (as the vibrational frequencies of C-H bonds are very high and these modes are not very highly populated). Therefore, for HMX, the Dulong-Petit limit is expected to be $\theta \to \infty, c_v \to (3 \times 28 - 8)R_0/M$, where number of atoms in HMX is 28 and number of C-H bonds is 8. However, no such information is available about the vibrational frequencies C-H bonds in sucrose. So, to begin with, a conservative limit for specific heat of sucrose is assumed, i.e. as $\theta \to \infty, c_v \to \frac{135R_0}{M} = 3279 \frac{J}{kg\ K}$ ($M = 342.3\ g/mol$).

Aside: Dulong-Petit limit for monoatomic solids specifies

$$\lim_{\theta \to \infty} c_{v,molar} = 3R_0 \tag{5.38}$$

where R_0 is the universal gas constant and the molar specific heat capacity, $c_{v,molar}$ is given below:

$$c_{v,molar} = \frac{C_v}{n} \tag{5.39}$$

where C_v is the heat capacity and $n = m/M$ is the number of moles, m is mass and M is molecular mass. However, the commonly used form of specific heat is defined below:

$$c_v = \frac{C_v}{m} = \frac{C_v}{n}\frac{1}{M} = \frac{c_{v,molar}}{M} \tag{5.40}$$

Hence, the Dulong-Petit limit can be re-written as:

$$\lim_{\theta \to \infty} c_v = \frac{3R_0}{M} \tag{5.41}$$

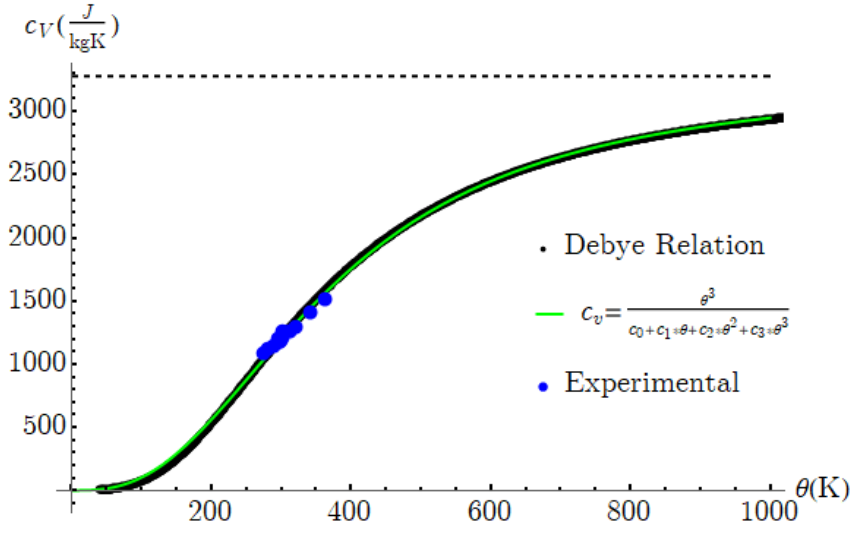

Figure 5.15 Debye model fit to experimental data for specific heat capacity at constant volume for sucrose

In the form for Debye model above, $c_v \to A \; as \; \theta \to \infty$, hence A is the Dulong-Petit limit. There are two unknown constants for a fit to experimental data in the Debye form of specific heat, i.e. A and θ_D. The Debye expression is fit to the experimental specific heat data for sucrose assuming $A = 3279 \frac{J}{kg\,K}$ as shown below in Figure 5.15. It can be noted that since the experimental data for sucrose is available only for a small range of temperatures, it would help

to know a more accurate Dulong-Petit Limit (A) for a better prediction at higher temperatures (θ >400K).

Fitting to an Empirical form: $\widetilde{c_v}(\tilde{\theta}) = \frac{\tilde{\theta}^3}{c_0+c_1\tilde{\theta}+c_2\tilde{\theta}^2+c_3\tilde{\theta}^3}$

In order to provide a simpler expression to calculate the specific heat and enable the integration of the Debye form, the specific heat is fit to an empirical form shown below, as done for HMX by Sewell and Menikoff (2004) :

$$\widetilde{c_v}(\tilde{\theta}) = \frac{\tilde{\theta}^3}{c_0 + c_1\tilde{\theta} + c_2\tilde{\theta}^2 + c_3\tilde{\theta}^3} \tag{5.42}$$

where (c_0, c_1, c_2, c_3) are constants. Such a form is chosen as it obeys the asymptotic limits at the two temperature extremes, i.e. $\widetilde{c_v}(\theta) \to \theta^3 \; as \; \theta \to 0$ and $\widetilde{c_v}(\theta) \to \frac{3R_0}{M} = \frac{1}{c_3} as \; \theta \to \infty$ (Dulong-Petit Limit). A fit to the Debye relation for specific heat capacity using the empirical form is shown in Figure 5.15. It can be seen from the plot that the empirical relation fits the Debye Model very well. The following set of parameters are used for this fit:

$$\begin{aligned} c_0 &= 7.095 \times 10^3 \frac{kgK^4}{J} \\ c_1 &= 2.230 \times 10^1 \frac{kgK^3}{J} \\ c_2 &= 4.180 \times 10^{-3} \frac{kgK^2}{J} \\ c_3 &= 3.050 \times 10^{-4} \frac{kgK}{J} \end{aligned} \tag{5.43}$$

An explicit expression for the integral of specific heat capacity with temperature is still hard to evaluate using the empirical relation for specific heat. Therefore, the integral is calculated

numerically and a quadratic polynomial is fit, as shown in Figure 15. A simple quadratic polynomial is able to fit the data very well.

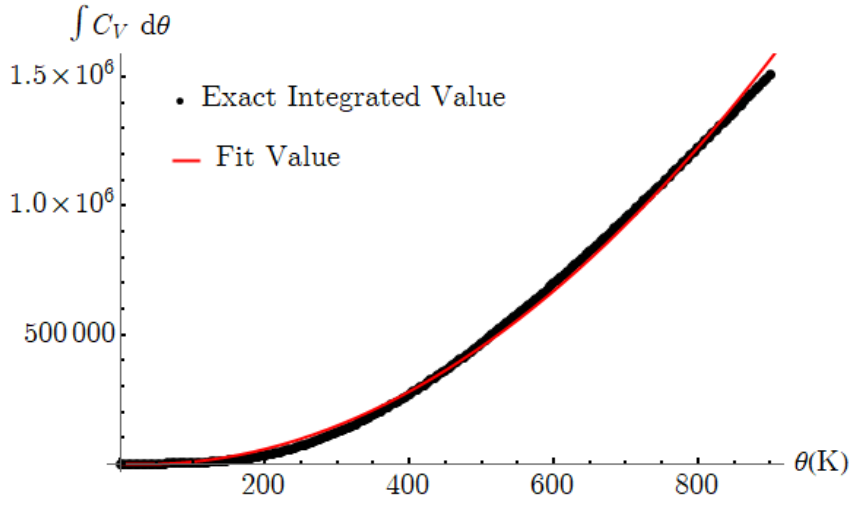

Figure 5.16 $\int_0^\theta C_v(\theta)d\theta$ is evaluated numerically (thick black curve) and fit to a quadratic function (thin red curve)

Therefore, the approximation is given as: $\int_0^\theta C_v(\theta)d\theta \approx f(\theta) = (-133.647 \times \theta + 2.082 \times \theta^2)\frac{J}{kg}$.

So, the complete Mie-Gruneisen EOS (equation (5.44)) can now be written as:

$$P(v,\theta) = P(V,\theta_0) - \frac{d\phi(v)}{dv} f\left(\frac{\theta}{\phi(v)}\right) \tag{5.44}$$

5.7.2.3 Thermal Conductivity

A thermal conductivity value of 0.486 W/m K is reported in Trott et al. (2007) .

5.7.2.4 Melting Point/Melt Curve

The melting point temperature of large organic molecules like HMX and sucrose is highly dependent on pressure. Melting is typically described by the Lindemann Law:

$$\theta_m = \theta_{m0} \exp\left[2\Gamma_0(1-\nu) + \frac{2}{3}\ln(\nu)\right] \tag{5.45}$$

where subscript '0' indicates ambient temperature and pressure. θ_{m0} is the melt temperature, Γ_0 is the Gruneisen parameter, $\nu = \frac{v}{v_0} = \frac{\rho_0}{\rho}$ is the relative volume and ρ represents the density of the solid. Lindemann Law can be linearized as follows:

$$\begin{aligned}
\theta_m &= \theta_{m0} \exp\left[2\Gamma_0(1-\nu) + \frac{2}{3}\ln(\nu)\right] \\
&= \theta_{m0} \exp\left[2\Gamma_0 \frac{\Delta v_c}{v_0} + \frac{2}{3}\ln\left(1 - \frac{\Delta v_c}{v_0}\right)\right] \\
&\approx \theta_{m0} \exp\left[2\Gamma_0 \frac{\Delta v_c}{v_0} - \frac{2}{3}\frac{\Delta v_c}{v_0}\right] \\
&= \theta_{m0} + 2\left(\Gamma_0 - \frac{1}{3}\right)\frac{\Delta v_c}{v_0} \\
&= \theta_{m0} + a\frac{\Delta v_c}{v_0}
\end{aligned} \tag{5.46}$$

Δv_c represents compressive change in volume and $a = 2\left(\Gamma_0 - \frac{1}{3}\right)$. This linearized relation is called the Kraut-Kennedy relation. Figure 5.17 shows a comparison between the Lindemann Law and Kraut-Kennedy relation and the agreement is very close for compressive strain ratios up to 0.2.

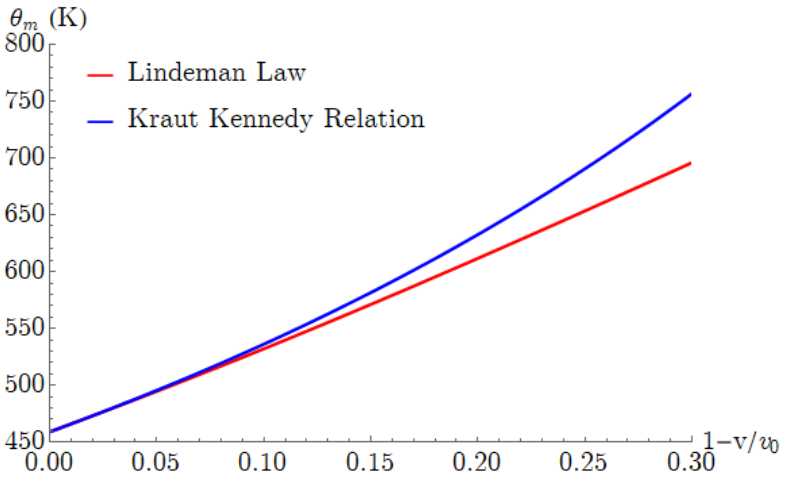

Figure 5.17 Comparison between Lindemann Law for sucrose and the linearized version (Kraut-Kennedy relation)

5.7.3 Yield Strength

Nanoindentation measurements of sucrose by Ramos and Bahr (2007) estimate a hardness of 1.5 GPa suggesting a bulk yield strength of 500 MPa, which motivates the use of $A = 500\ MPa$ in the Johnson-Cook model.

5.7.4 Gruneisen parameter

The following functional form of Gruneisen parameter is assumed as noted by Grady (2017) :

$$\Gamma(v) = \frac{\Gamma_0}{v_0} v \tag{5.47}$$

The value of Γ_0 is derived from the following thermodynamic relation to be consistent with values for other thermodynamic quantities:

$$\frac{\Gamma(v)}{v} = \frac{\alpha_v K_T}{c_v} \tag{5.48}$$

Using the above relations in equations (5.47) and (5.48), $\Gamma_0 = 1.09$ is obtained which is very close to that for HMX ($\Gamma_{0_{HMX}} = 1.1$). The integrating factor, $\phi(v)$ in equation (4.107) can now be calculated explicitly:

$$\phi(v) = \exp\left(-\int_{v_0}^{v} \frac{\Gamma(v')}{v'} dv'\right) = \exp\left(-\int_{v_0}^{v} \frac{\Gamma_0}{v_0} dv'\right) = \exp\left(\Gamma_0\left(1 - \frac{v}{v_0}\right)\right) \tag{5.49}$$

5.8 Appendix E: Parametric Study of Johnson-Cook Model

A parametric study is carried out for two important Johnson-Cook parameters: (a) thermal softening coefficient, m (Figure 5.18), and (b) strain-rate hardening coefficient, C (Figure 5.19). These parameters influence the shear stress profile the most and the magnitude of their effects is not intuitively clear. In general, it can be concluded from the Johnson-Cook expression for yield strength that increasing m and increasing C would lead to an increase in the yield strength.

Note that these parametric studies are done in the vicinity of a local minima for least squared errors, obtained for the parameters mentioned in Table 5.1. Only one parameter is varied at a time. Such a parametric study is helpful in establishing the trends quantitatively and putting bounds to the range of values to be considered for each parameter. Increasing the value of m increases the peak yield strength and delays the fall in transverse velocity, especially at low pressures. For the high-pressure shot, however, the fall in transverse velocity for $m > 0.65$ is quickened. This is expected because the melting event occurs at the peak of transverse velocity for the high-pressure shot while melting for the low-pressure shot occurs farther away from the peak, at some point along the falling region of the velocity profile. It can be said with confidence that an m value in the 0.5-0.65 range is of interest at low and high-pressures. The strain-rate

hardening coefficient, C has a much more dramatic effect for lower pressures. No drop in transverse velocity is observed for $C = 0.05$ for the low-pressure case. However, for the high-pressure case, the drop is still observed for $C = 0.05$ although the melting event is slightly delayed. It can be concluded that $C = 0.01$ is a good choice.

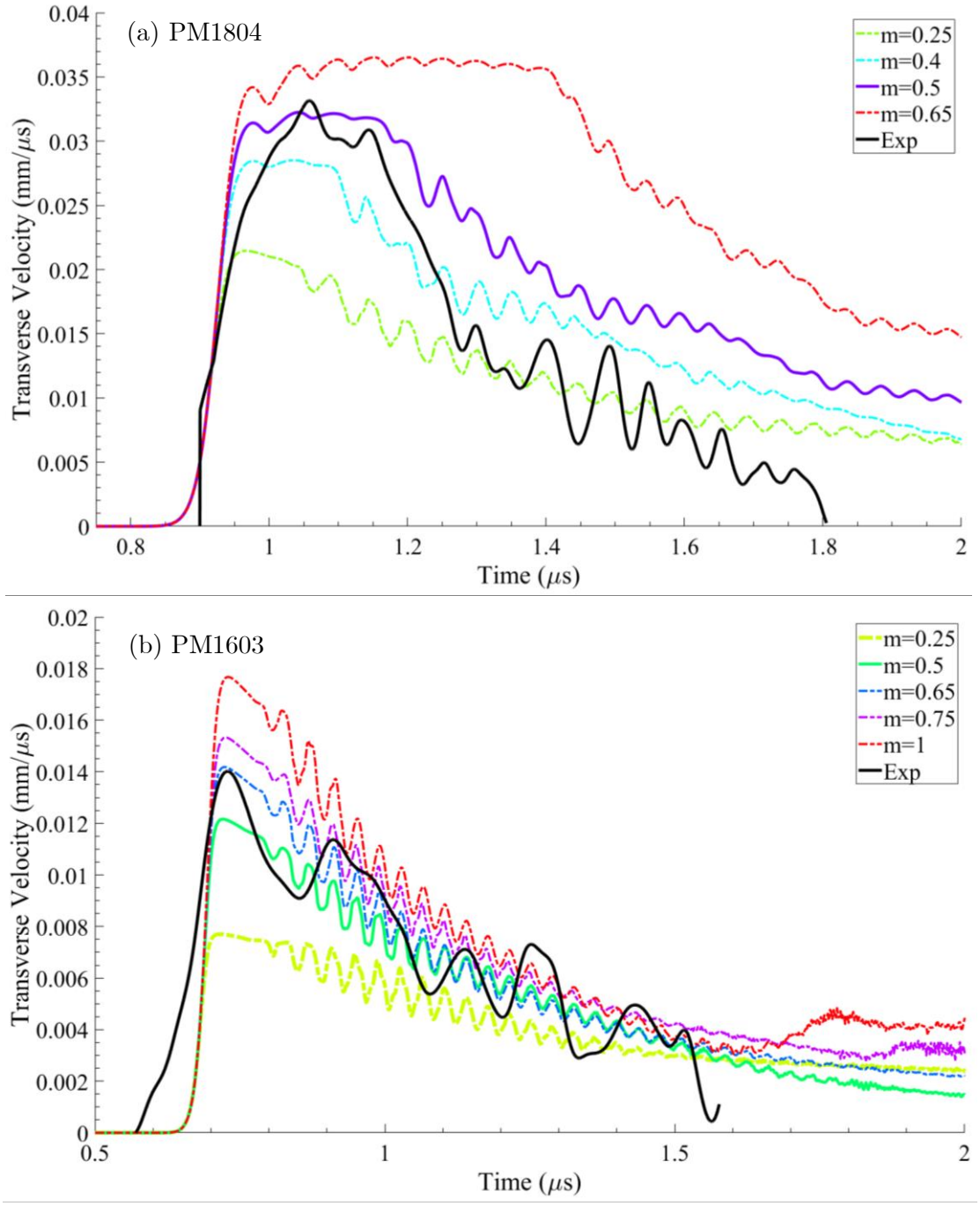

Figure 5.18 Effect of thermal softening exponent, m. (a): Low-pressure shot PM1804, (b) High-pressure shot PM1603.

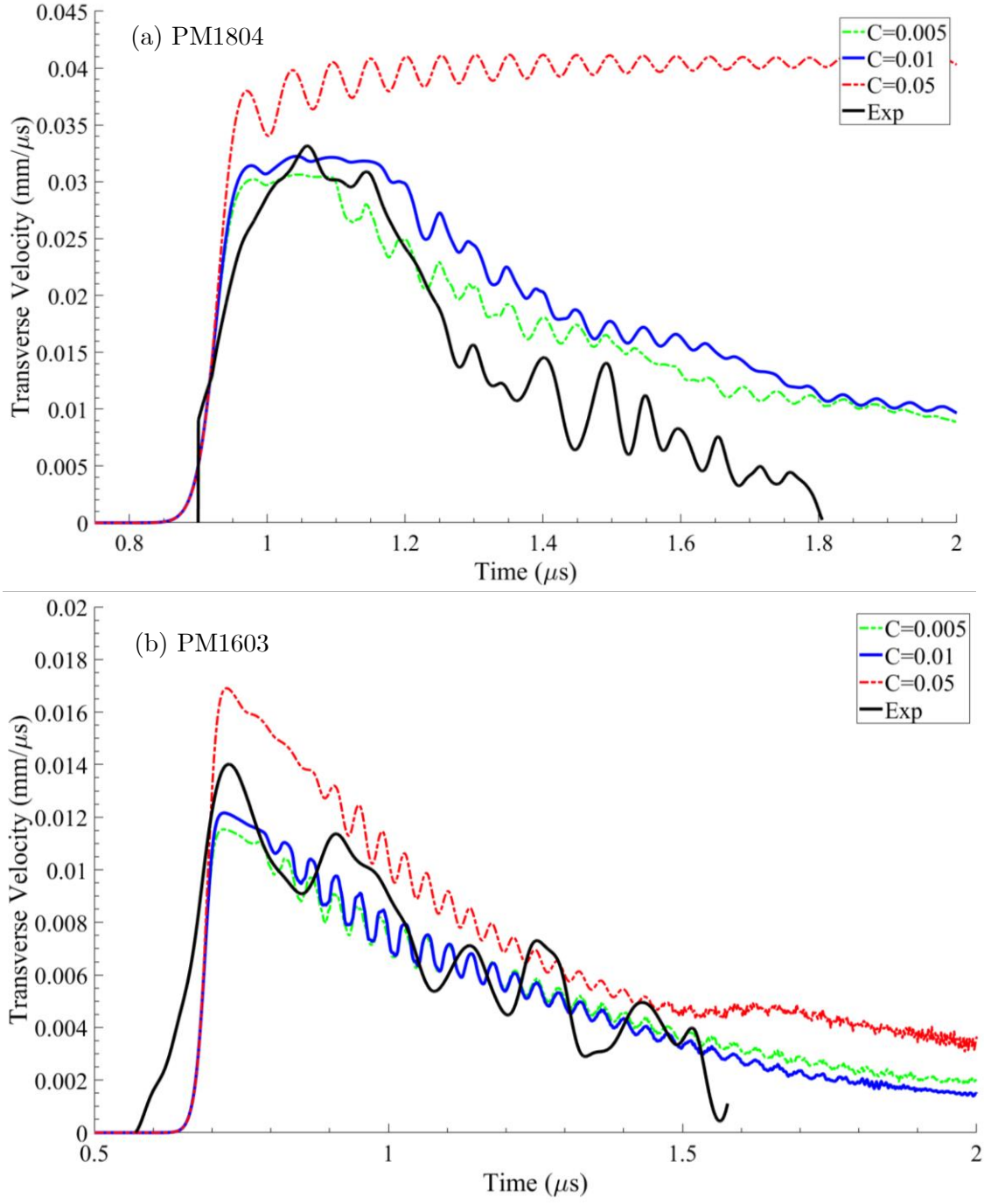

Figure 5.19 Effect of strain-rate hardening pre-factor, C (a): Low-pressure shot PM1804, (b) High-pressure shot PM1603.

Chapter 6

Polymer-Bonded Sucrose: Experiments and Simulations

6.1 Introduction

A polymer-bonded explosive (PBX) is a composite of an explosive crystal (such as HMX, RDX, PETN, etc.) and a soft elastomeric binder (such as HTPB, Estane, etc.). PBXs are used in a wide range of civil and military applications such as mining, construction, as solid fuel in rocket propellants and as explosives. Usually, the PBX consists largely of explosive crystals with a very small fraction of binder (2-10% by weight). The elastic modulus of the binder is usually about four orders of magnitude smaller than that of the explosive crystal. Consequently, the binder absorbs most of the mechanical energy imparted to the composite Wiegand and Reddingius (2005), Ravindran et al. (2016), (2017) . Since the binder takes up much of the deformation in a PBX, including a soft elastomeric binder allows for low impact sensitivity, thereby making PBXs safer to manufacture, handle and transport, while maintaining the effectiveness of the explosives.

One of the key problems confronted in the study of PBXs is the difficulty in predicting their initiation. Since the formation of hot-spots and hence the eventual initiation of PBXs is strongly related to the failure modes of PBXs, deformation and failure mechanisms of PBXs have been studied intensively for the past few decades. Due to the highly heterogenous nature of the

composite, combined with complex material behavior of the energetic crystals and the elastomeric binder, predicting the mechanical and chemical properties of PBXs has remained a major challenge. The factors affecting the deformation and failure of PBXs can be broadly categorized as external and internal. Internal factors include microstructure of the PBX, mechanical and chemical properties of the ingredients (explosive crystal and binder) and defects inside the crystal (such as voids, inclusions, impurities, dislocations and grain boundaries) or the binder. The microstructure of a PBX is further defined by characteristics such as loading density (i.e. the weight fraction of the crystals relative to the binder), crystal size, crystal morphology and distribution of crystals inside the binder matrix. The external factors comprise of the loading conditions used to deform the PBX. Loading conditions are typically described by strain-rate, pressure and temperature.

To begin with the effect of internal factors, it should be noted that the strength of the composite has been shown to vary inversely with the square root of the particle size Balzer et al. (2004) , i.e. larger crystal size leads to a weaker PBX. Similarly, a larger crystal size is associated with larger impact sensitivity. It is demonstrated by Armstrong et al. (1990) that the drop-height for 50% probability of initiation of RDX crystals varies linearly with the inverse of the square root of particle size. Effect of crystal morphology, in particular the smoothness of grains, on shock sensitivity of PBXs of RDX and HMX has been studied by van der Heijden et al. (2004) . Numerical simulations by Barua and Zhou (2011) have shown that a bimodal microstructure with spherical crystals has a larger loading capacity than microstructure with unimodal spherical or diamond-shaped crystals. For a given explosive crystal, the choice of a binder can have a significant impact on the overall mechanical behavior of the PBX. Swallowe

and Field (1982) first demonstrated the effect of different binders on sensitization of PETN crystals using drop-weight impact testing. They concluded that softer polymers with a lower glass transition temperature were less likely to sensitize the explosive crystals while polymers with high strength and low specific heat capacity were more likely to fail catastrophically and ignite the PETN crystals.

Effects of external factors such as strain-rate and temperature have been studied by several researchers. They have observed that in quasi-static and high strain-rate testing, the compressive stress drops after reaching a peak. Following the peak, the PBX exhibits strain softening. The mode of failure changes with strain-rate and temperature. It has been shown through quasi-static and split-Hopkinson bar testing that the compressive strength of PBXs increases with increasing strain-rates and decreasing temperatures Funk et al. (1996), Gray III et al. (1998), Drodge et al. (2007), Siviour et al. (2008) . In quasi-static and Kolsky-bar type tests, the dependence of the response of PBX to strain-rate and temperature comes primarily from the binder. Wiegand and Reddingius (2005) explored the effect of confinement on elastic and plastic behavior of a polymer-bonded simulant, under quasi-static strain rates. They showed an increase in elastic modulus and flow stress with increasing pressure. The primary mode of failure was found to switch from fracture and debonding, as is the case with uniaxial stress loading, to plastic flow dominated failure.

Failure of a PBX can take place in several ways, such as by fracture and by localization. Fracture can occur inside the bulk of either the crystal or binder phase, or at the interface of the binder and crystal. The latter failure is typically called delamination. At temperature above the

glass transition temperature of the binder, delamination between the binder and explosive crystals has been shown to be the primary failure mechanism in quasi-static and moderate strain-rate experiments with no confinement Siviour et al. (2008), Ravindran et al. (2016), (2017) . Fractured surfaces can rub against each other dissipating heat and resulting in localized temperature rise. If the temperature increase is sufficient, it may result in the formation of hot-spots or even localized melting. Formation of localized regions of high shear strains through adiabatic shear banding in the binder or crystal phase can cause thermal softening and eventual failure of the PBX. Shear bands are usually associated with a large increase in temperature in narrow regions which can result in hot-spots. Therefore, it is important to incorporate such effects in numerical modeling and simulations of PBXs. Another mechanism that is important to incorporate into numerical models from the perspective of hot-spot formation is collapse of voids.

Overall, an ideal numerical model of a PBX should be able to model: bulk fracture of the binder and energetic crystals, debonding, shear banding in either phase and pore collapse, while taking into account thermal dissipation associated with any deformation. Thermal dissipation can result from bulk inelasticity in the binder or crystal phase or due to friction between two sliding interfaces. Adequate thermo-mechanical models of the binder and energetic/simulant crystals need to be implemented in a finite-deformation setting. In case of shocks, it is important to account for finite elastic deformation and shock wave heating. Usually, fracture and delamination are implemented through cohesive zone modeling using suitable traction-separation laws. At the same time, it is important to model contact between grains in the undeformed microstructure and between the newly formed surfaces after fracture. Barua and Zhou

(2011) present a coupled thermal-mechanical Lagrangian framework incorporating fracture and contact modeling to simulate deformation and failure of a given microstructure of a PBX.

While much has been done on studying the compressive response of PBXs, especially under uniaxial stress conditions, mechanical response under high-pressures and high shear-strain rates has not been examined so far. Herein, PSPI experiments have been described with the aim of informing constitutive models for PBXs under multi-axial loading. Experiments have been conducted for a given microstructure of a HTPB and sucrose composite subjected to large pressures and large shear strains. ABAQUS simulations for different one-dimensional canonical structures of PBS are described based on the constitutive models of HTPB and sucrose developed in the previous chapters. A critical review of the adequacy of such modeling is presented.

6.2 Specimen Preparation

In this section, the preparation of two different samples is described: (a) a composite of sucrose grains and HTPB, and (b) sucrose grains only.

6.2.1 Preparation of composite specimen

Our aim is to prepare a 90:10 (by weight) composite sample of pure sucrose grains and HTPB on a WC/steel substrate. Desired thickness range of the specimen is 100-200 μm. Pure sucrose grains (~2 mm) are ball-milled to a smaller size. The milled crystals are sieved to obtain the required size range. An additional step of cleaning the sucrose grains using methanol can be

added here to remove small crystallites from the faces of milled crystals. First, HTPB binder is prepared as described in Chapter 2. After different components of HTPB binder are mixed together, the mixture is degassed for ~10 minutes. Approximately 80 grams of HTPB mixture is prepared, 30 grams of which is mixed with 270 grams of sucrose grains. Since the fraction of HTPB in the composite is very small, a large quantity of composite mixture needs to be made for ease of mixing. Initial mixing is done with a scoopula, followed by mixing with hands, until a uniform consistency is obtained. Remaining 50 grams of HTPB are poured into a rectangular container, to be used later for measuring Shore A hardness of the cured polymer. The composite along with the remnant HTPB are kept in the oven at 60 ^{0}C for 2 hours for partial curing. This curing is followed by pressing the composite inside a steel split mold (see Figure 6.1). The split mold is used to allow for easy removal of sample and substrate after pressing. The aluminum plate in the split mold is replaced by a thin sheet of Teflon for preparation of the composite sample. It is important to spread the partially cured composite evenly inside the mold before pressing it. The composite mixture is pressed down to a final pressure of 50 MPa using an Instron machine. The load is ramped up gradually to 50 MPa at a rate of 5 MPa/min, held for a minute before decreasing it to zero at a rate of 25 MPa/min. The slow ramp up rate allows enough time for the sucrose crystals and polymer to move around and distribute uniformly on the substrate. Partial cure of the binder gives the composite a semi-solid consistency which is adequate to press without squeezing the binder out of the composite. After pressing, the composite mixture is cured for another 12-16 hours in the oven until a Shore A hardness of 3-5 is obtained for the remnant HTPB polymer. This procedure results in a composite layer of ~2-3 mm on the substrate. The sample is polished down to the required thickness using a lapping fixture as shown in Figure 6.2. The polishing sequence involves starting with a dry 120-grit

sandpaper, followed by a 320-grit size for the last few tens of microns and finally by a 600-grit size for a smooth surface. Polishing off the last few hundred microns is tricky as the layer starts to erode at the edges. So, a layer of epoxy is put on the periphery of the sample before starting the polishing step. The epoxy ensures that the edges of the specimen layer do not fracture and also helps in achieving a uniform sample thickness.

6.2.2 Preparation of granular sucrose specimen

One PSPI shot is also done on granular sucrose for comparison. For a granular sucrose sample, the aim is to make a 100-200 μm thick layer of sucrose grains pressed together with minimum porosity. Two methods were chiefly employed in this pursuit: (a) pressing in a mold, and (b) Sucrose-Methanol Slurry (SMS) method. For the first method of pressing in the split-mold as shown in Figure 6.1. Sucrose grains are pressed at pressures up to 5 MPa. An aluminum disc polished down to 3 μm is introduced between the piston and sucrose layer to avoid sticking of sucrose to the piston. However, this method is not found to be effective for several reasons: (1) results in crushing of grains, (2) poor repeatability, as pockets of sucrose get stuck to the polished aluminum disc, and (3) a uniformly thick sample is hard to achieve. The uniformity of sucrose layer is found to depend on the initial spread of sucrose grains in the mold prior to pressing. While this method works well for making thicker layers of sucrose of the order of few mm, it is not suitable for making flat layers with a 100-200 μm thickness as required for PSPI experiments. Therefore, a new method is invented for making an extremely thin and flat layer of sucrose grains.

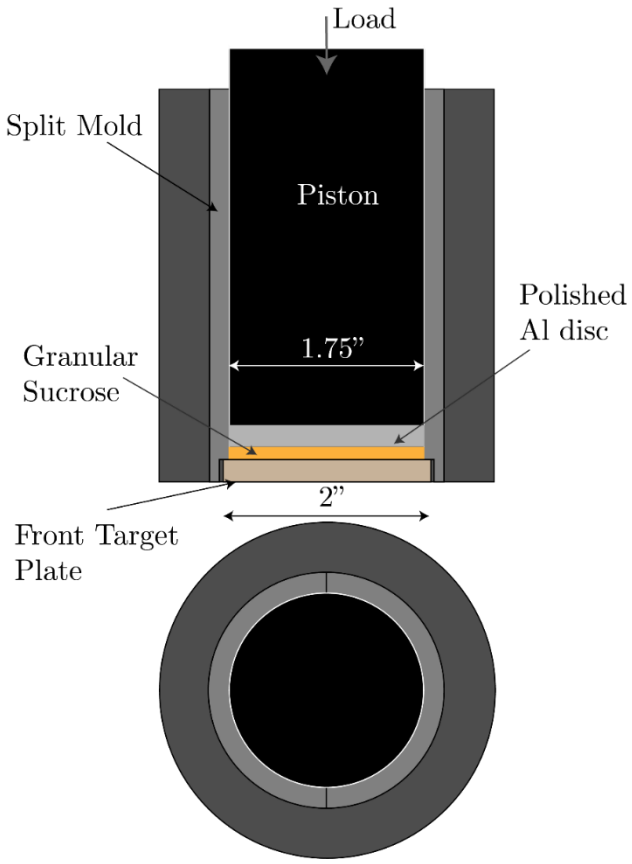

Figure 6.1 Split- Mold fixture to prepare granular sucrose sample. Top: section view. Bottom: top view

The new method is named ‘Sucrose-Methanol Slurry’ method as it involves making a slurry of sucrose grains in methanol. Just enough methanol is added to make a semi-solid slurry. The slurry is spread on the substrate and let dry for a few minutes (It is important to use a minimal amount of methanol and apply the slurry to the substrate as soon as the slurry is made). This methodology is needed to ensure that the methanol dissolves a minimal amount of sucrose. The sample is then loaded on a lapping fixture, shown in Figure 6.2. Excess thickness is polished off using the same polishing sequence as used in the preparation of the composite sample. A layer of epoxy is used on the periphery of the sample after the slurry dries. The epoxy

ensures that the edges remain intact in order to achieve extremely small thicknesses, down to 100 μm. This method has several advantages: (a) sucrose layer adheres to the substrate much more strongly than for the split-mold method, allowing the sample to be polished down to a thickness as small as a hundred microns (not possible with split-mold pressing); (b) sucrose grains adhere to each other very strongly; (c) porosity is visibly lower; (d) minimal fracture/damage is induced prior to the actual experiment; (e) use of lapping fixture enables thickness control down to a μm and ensures uniformity of thickness; (f) samples as thin as 100 μm can be made with ease; and (g) this method has a much higher repeatability than attained for the split-mold method.

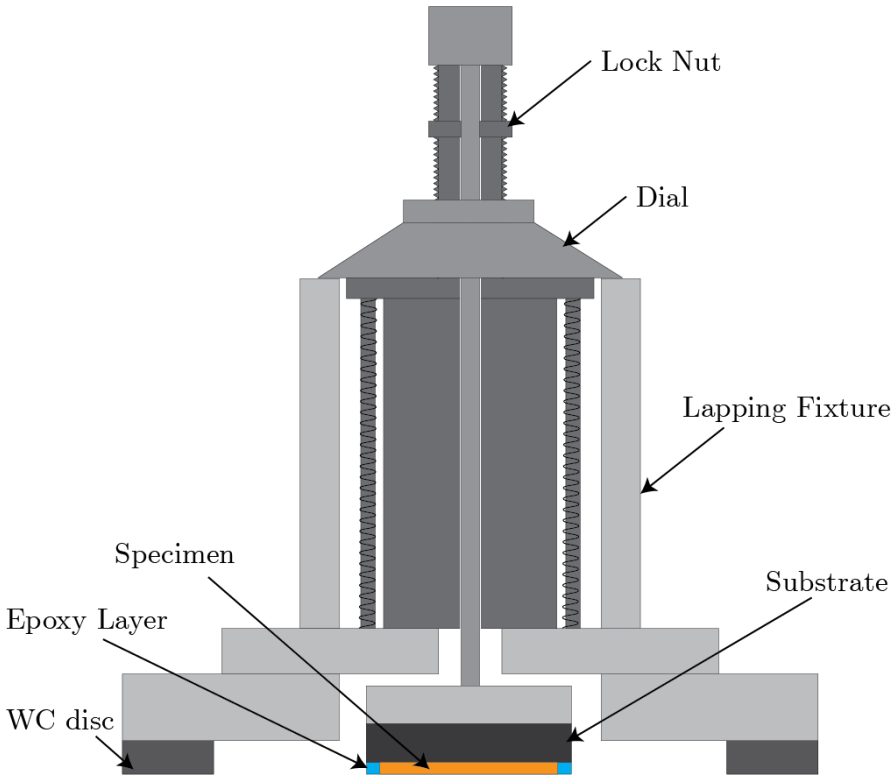

Figure 6.2 Lapping fixture used to make the granular sucrose specimen for PSPI using the Sucrose-Methanol Slurry (SMS) method. The specimen is placed flat on the polishing paper and polished for a short time to get a flat sample. The fixture along with the sample is then placed

on a flat surface and reading dial brought flush with the outer cylinder. The dial is rotated to set the thickness of the sample to be removed and locked in place using the lock nut. The polishing sequence described in the text is followed. At the end of the polishing sequence, the sample is cleaned gently of the excess sucrose and HTPB dust using an acetone dipped wipe. Note that the plate above the substrate is ensured to be flat and bonded temporarily to the substrate using Kapton tape on the periphery. The hard tungsten carbide discs (dark grey) at the bottom of the fixture ensure flatness of the sample. Since the sample thicknesses prepared are extremely small, an epoxy layer on the periphery of the sample prevents erosion of the specimen at the boundaries and ensures flatness

6.3 Experimental Results

A total of 4 PSPI shots have been conducted on the sucrose/HTPB composite. A summary of shots is provided in Table 6.1. D2 steel is used as the anvil material for low normal stress (nominally 3 GPa) shots while WC is used for high normal stress (nominally 9.5 GPa) shots. Shear strain rates of the order of 10^5 s^{-1} are obtained. One shot (PM1902) is done on a granular sucrose sample at a normal stress of 2.90 GPa and a shear strain rate of 10^5 s^{-1}.

Table 6.1 Summary of PSPI shots on sucrose/HTPB composite and granular sucrose. Shot PM1902 is done on granular sucrose. Other shots are on the composite

Shot No.	Target Material	h_S (μm)	h_F (mm)	h_{FT} (mm)	h_{RT} (mm)	θ	V_0 (m/s)	Tilt (mrad)	σ_{max} (GPa)	τ_{max} (GPa)	$\dot{\gamma}$ (s^{-1})
PM1901	D2 Steel	184	7.056	3.046	6.589	18^0	133.46	1.74	2.93	167	$1.78x10^5$
PM2001	D2 Steel	203	7.056	2.967	6.989	18^0	131.51	0.94	2.95	184.27	$1.53x10^5$
PM2002	Pure WC	114	6.554	3.020	6.252	18^0	197.83	1.26	9.73	451	$4.51x10^5$
PM2003	Pure WC	195	6.559	2.900	6.442	18^0	193.13	1.37	NA	454	$2.53x10^5$
PM1902	D2 Steel	129	7.062	2.977	6.525	18^0	132.37	0.89	2.90	346	$2.11x10^5$

h_S: sample thickness h_F: flyer thickness, h_{FT}: front target plate thickness, h_{RT}: rear target plate thickness, θ: angle of impact, V_0: impact velocity, σ_{max}: peak normal stress, τ_{max}: peak shear stress, $\dot{\gamma}$: average shear strain-rate

Normal and transverse velocity-time profiles for shots on the composite are shown in Figure 6.3 and Figure 6.4 respectively. Note that normal velocity for shot PM2003 is not plotted

since NDI trace could not be obtained for this shot. Normal velocity profiles of the low-pressure shot PM2001 and high-pressure shot PM2002 show steps before rising up to the plateau. However, another low pressure-shot, PM1901 does not show any such steps. The rise-times for shots under similar conditions (PM1901 and PM2001) are also very different ($\sim 575\, ns$ for PM1901 and $\sim 875\, ns$ for PM2001). A rise-time of $\sim 515\, ns$ is observed for the high-pressure shot, PM2002. Such variations are expected in a heterogeneous sample with extremely different properties.

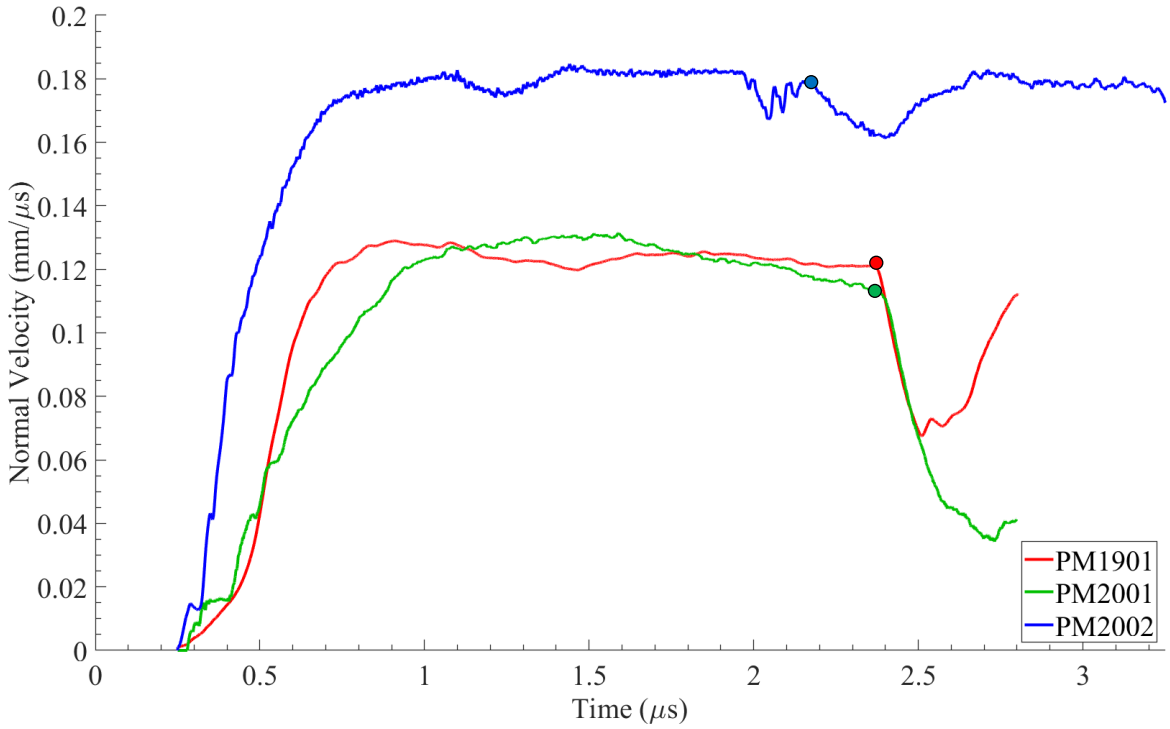

Figure 6.3 Normal velocity profiles of PSPI shots on the polymer-bonded sucrose composite. Arrival of unloading wave is marked with dots. Normal velocity profile for shot PM2003 is not available due to loss of the NDI trace for the shot

Transverse velocity profiles for both low and high-pressure shots show similar qualitative behavior, i.e. the velocity rises to a peak value before dropping down to a smaller non-zero value. However, the transverse velocity profiles for the composite are not as clean as observed for the cases of HTPB and sucrose. This is primarily due to the extremely heterogeneous nature of the sample. The portion of transverse velocities after the fall are noisier than earlier segments due to low signal to noise ratio of the TDI trace in the latter part of the deformation.

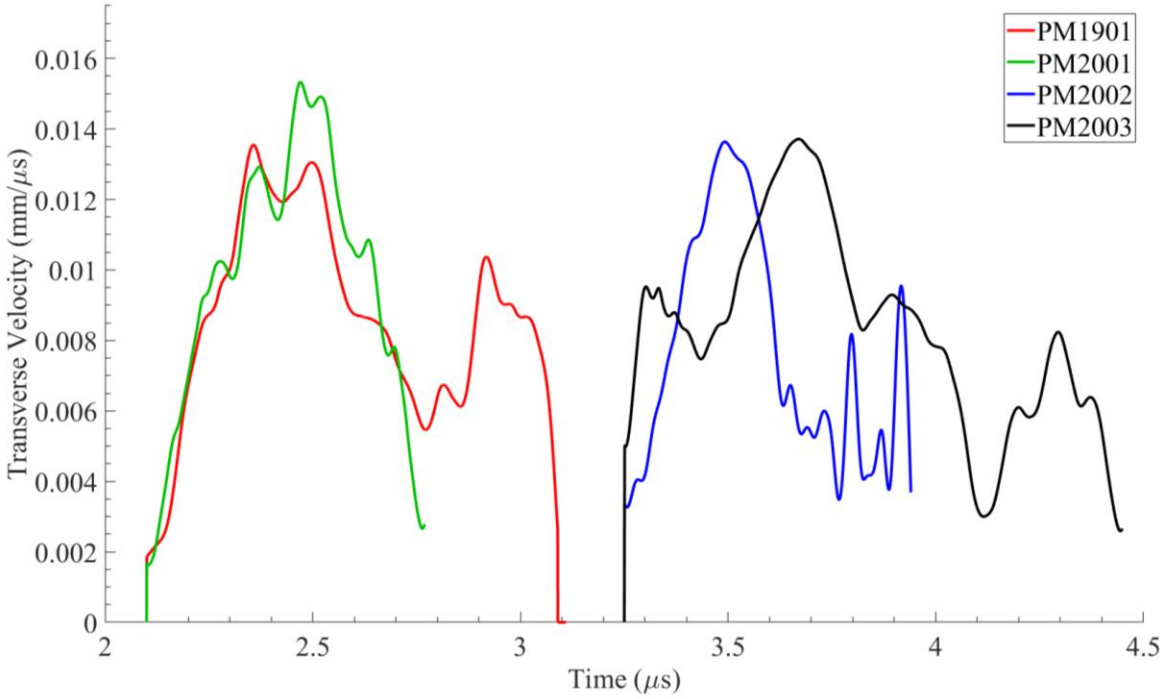

Figure 6.4 Transverse velocity profiles of PSPI shots on the polymer-bonded sucrose composite. Transverse velocities for low-pressure shots (PM1901, PM2001) are shown on the left and for high-pressure shots (PM2002, PM2003) on the right

Normal and shear stresses for the shots on the composite are plotted in Figure 6.5 and Figure 6.6. Saturation normal stress values of 2.93 GPa, 2.95 GPa and 9.73 GPa are obtained for shots PM1901, PM2001 and PM2002 respectively. Nominally, the shots can be labelled as 3 GPa and 9.75 GPa shots. For the 3 GPa shots, peak shear strengths of 167 MPa and 184.27

MPa are obtained. Similarly, the peak shear strengths of the 9.75 GPa shots are 451 and 454 MPa. Despite the heterogeneous nature of the sample, peak shear strength values are consistently repeatable and show smaller variation at larger pressures. It should also be noted that the shear strength is not completely lost after the drop as is observed in the case of sucrose. Such a loss in shear strength of the composite can have multiple complex failure mechanisms such as binder delamination, fracture and adiabatic shear band localization in the binder or sucrose. By contrast, for the case of monolithic sucrose the only suspected mode of failure is localization through shear bands.

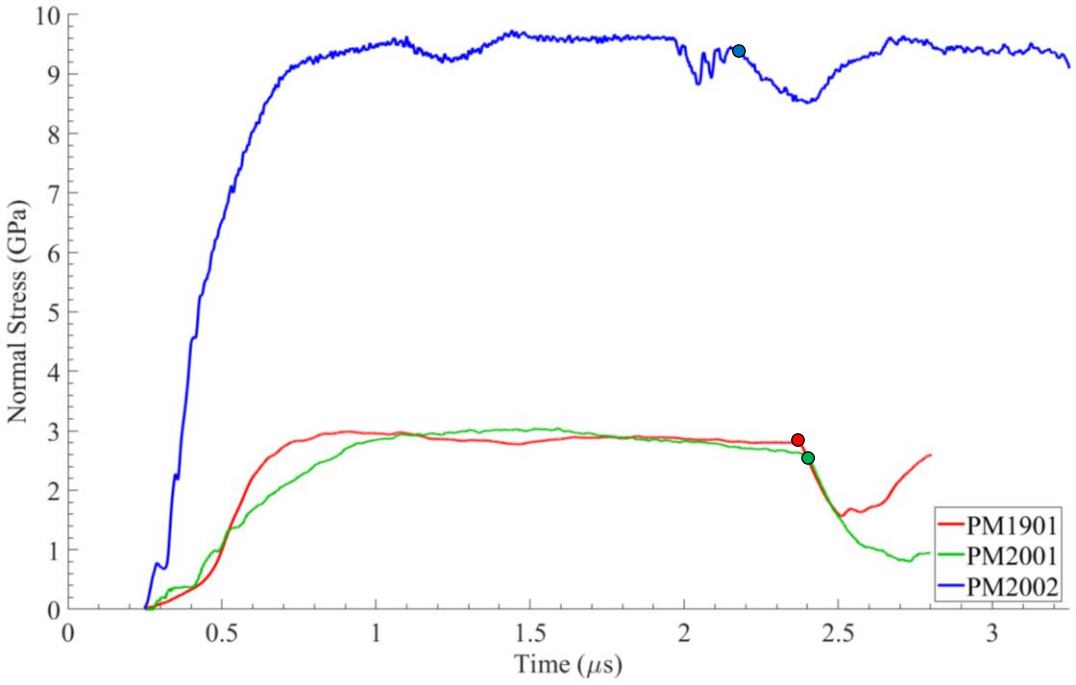

Figure 6.5 Normal stress profiles of PSPI shots on the polymer-bonded sucrose composite. Arrival of unloading waves is marked by dots. Normal stress profile for shot PM2003 is not available due to loss of the NDI trace for the shot

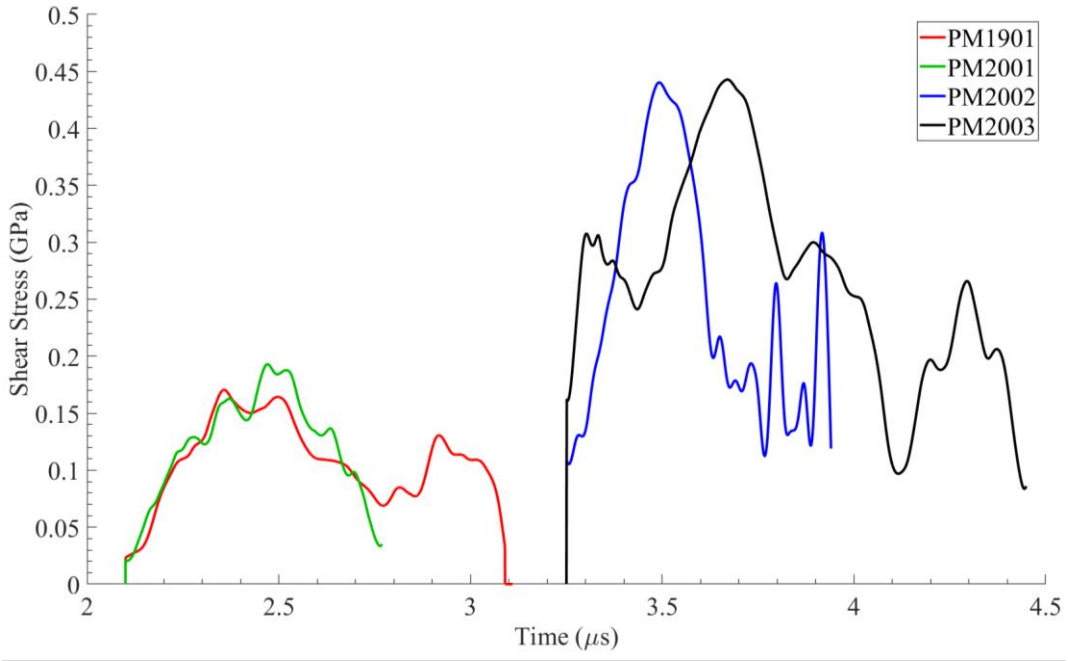

Figure 6.6 Shear stress profiles of PSPI shots on the polymer-bonded sucrose composite. Shear stresses for low-pressure shots (PM1901, PM2001) are shown on the left and for high-pressure shots (PM2002, PM2003) on the right

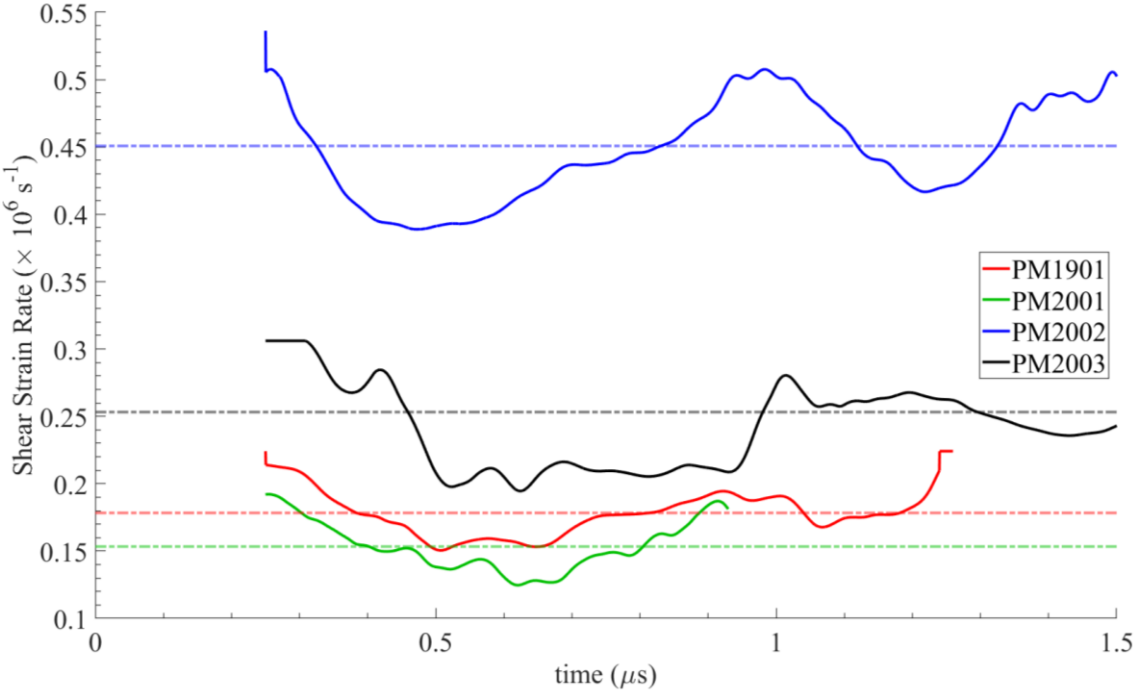

Figure 6.7 Shear strain-rates for PSPI shots on the polymer-bonded sucrose composite

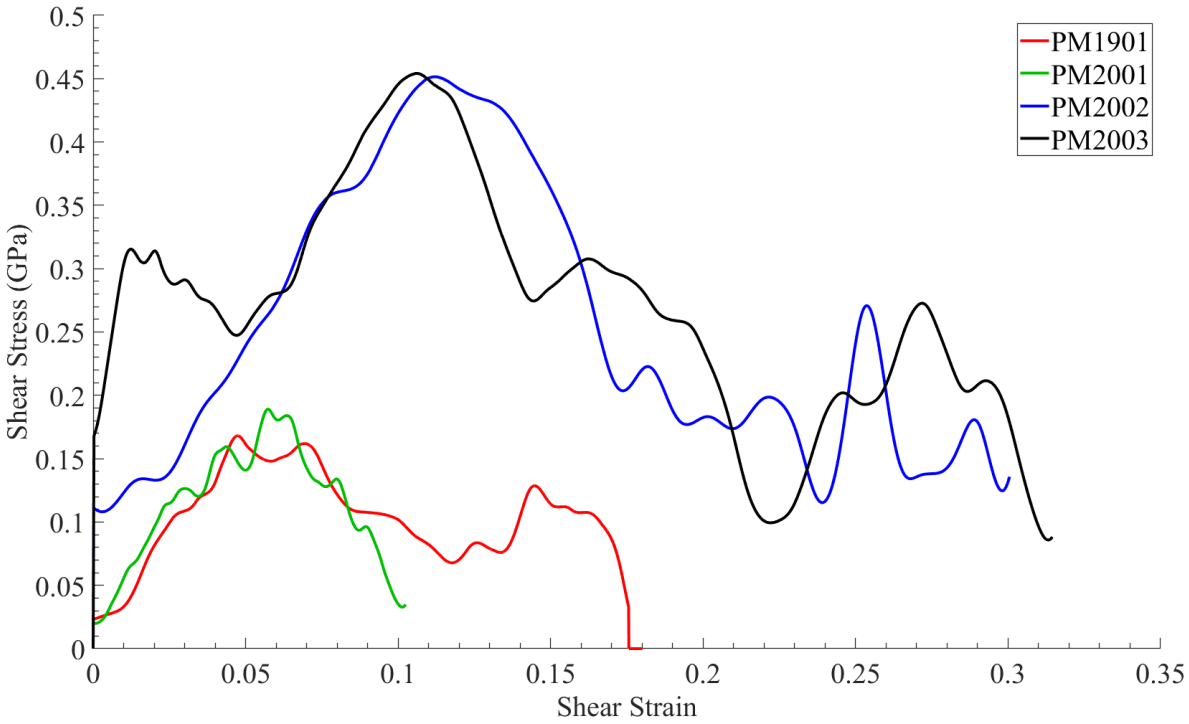

Figure 6.8 Shear stress vs shear strain plots for all PSPI shots on the polymer-bonded sucrose composite

Figure 6.7 shows the shear strain-rate plots of different shots on the composite. Note that the shear strain rates are calculated assuming that the shear strain is uniform through the thickness of the sample. As a result, the shear strain-rates are indicative of nominal values only. Shear strain-rates in the range of $\sim 1.5 \times 10^5 - 4.5 \times 10^5\ s^{-1}$ are obtained. Shear strains can be obtained by integrating the shear strain rate to obtain the shear stress versus shear strain behavior, as shown in Figure 6.8. The shear stress-strain profiles are quite repeatable for the two pressure levels. The low-pressure shots peak at a shear strain of approximately 0.05 while the high-pressure shots peak at a shear strain of about 0.1, indicating an increase in the critical failure shear strain with increasing pressures. Peak shear strength of the composite is also seen to increase with increasing normal stress, as shown in Figure 6.9. A linear fit to the

experimental data shows that an increase of 41 MPa in shear strength with every 1 GPa increase in normal stress. A comparison is drawn for shear strength of HTPB, sucrose and their composite. The pressure sensitivity of the shear strength of the composite is indicative of the dominant effect played by the binder in the composite. Also note that the shear strength of the composite is closer to that of the binder than that of sucrose even though sucrose comprises of 90% of the composite by weight. Clearly, the rule of mixtures doesn't apply in this case.

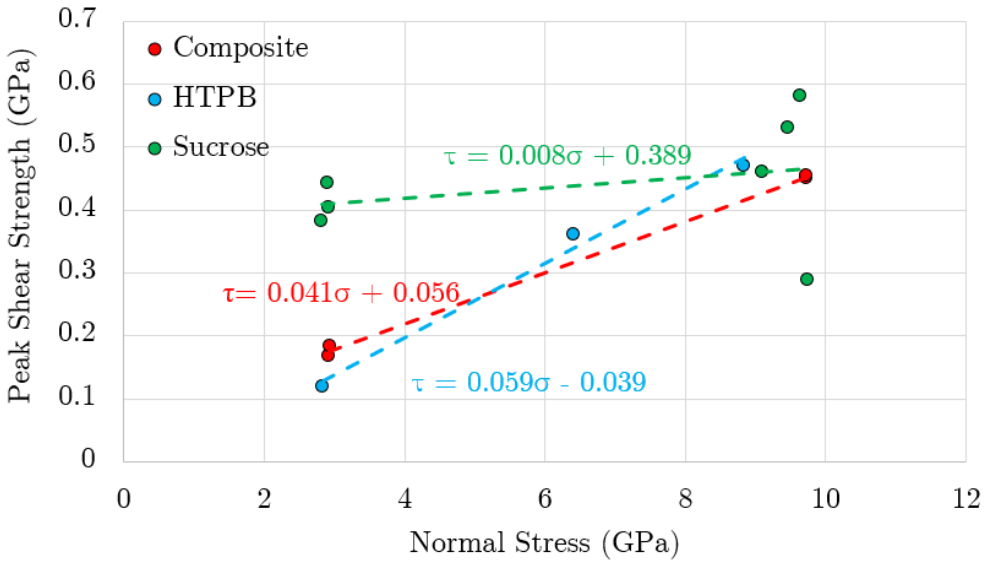

Figure 6.9 Peak shear stress versus normal stress of polymer-bonded sucrose composite, at a nominally similar shear strain rate. The dashed line indicates a linear fit to the experimental data. The equation to the linear fit is displayed on the top left. Note that the slope of the curve $\left(\frac{d\tau}{d\sigma} = 0.041\right)$ lies between that of sucrose $\left(\frac{d\tau}{d\sigma} = 0.008\right)$ and HTPB $\left(\frac{d\tau}{d\sigma} = 0.059\right)$

A better way to bring out the role of the binder in determining the dynamic shear strength of the composite is a direct comparison with a specimen with no binder, i.e. a pressing of granular sucrose only. Such a comparison between compacted granular explosives and PBXs subjected to normal loading has been made by Wang et al. (2016) using numerical simulations.

Average and localized stress and temperature fields are found to be higher for the granular explosives than for PBX. However, no analysis of shear response has been made. Moreover, there is a lack of experimental data for making direct comparisons between the shear response of granular explosives and PBXs. Therefore, a PSPI shot was done on compacted granular sucrose for the case of low normal stress. Figure 6.10 shows the normal and transverse velocity profiles of for the shot on granular sucrose. The corresponding normal and shear stresses are shown in Figure 6.11. It can be observed that the normal velocity shows an initial step corresponding to an elastic precursor, followed by a comparatively slow rise to the plateau. Shear strength of the granular pressing shows qualitatively similar behavior to that of sucrose and the composite. The shear stress rises to a peak and falls thereafter to a small but non-zero value. A mean shear strain-rate of $2.1 \times 10^5 s^{-1}$ is obtained for the shot depicted in Figure 6.12. Figure 6.13 shows the shear stress versus shear strain behavior, with the shear stress rising to a peak value of 346 MPa at a shear strain of ~ 0.05 before falling off to a lower value of ~ 80 MPa. The specimen is sheared to a strain of 0.15 before the arrival of an unloading wave from the free surface of the rear target plate.

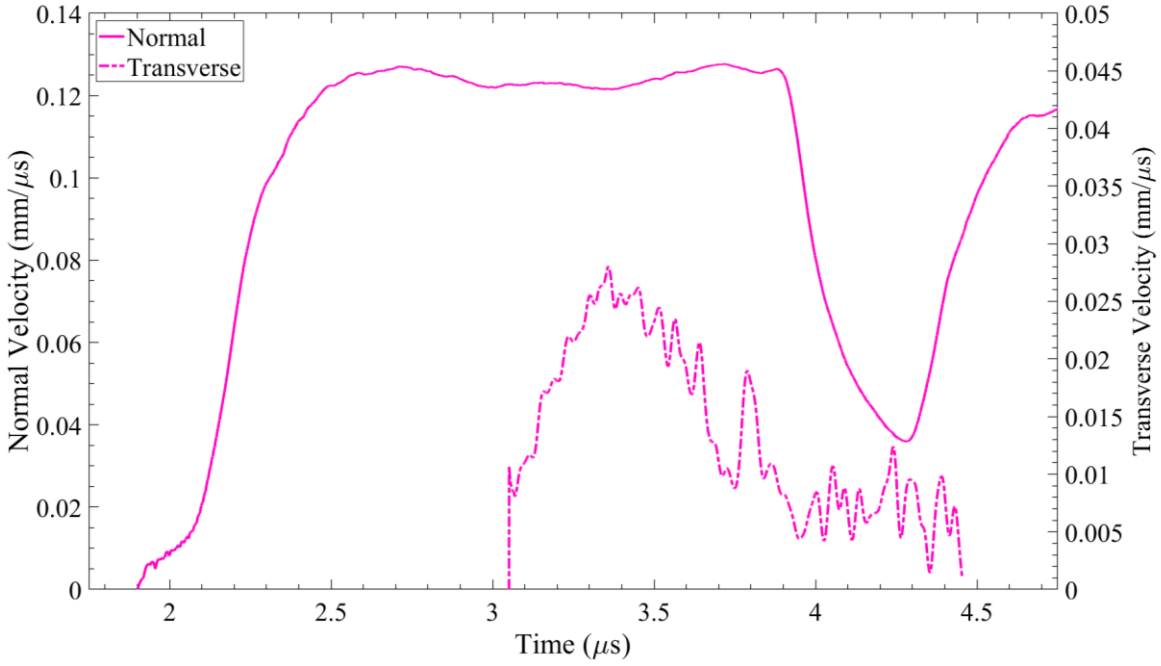

Figure 6.10 Normal and transverse velocity profiles of the PSPI shot on granular sucrose

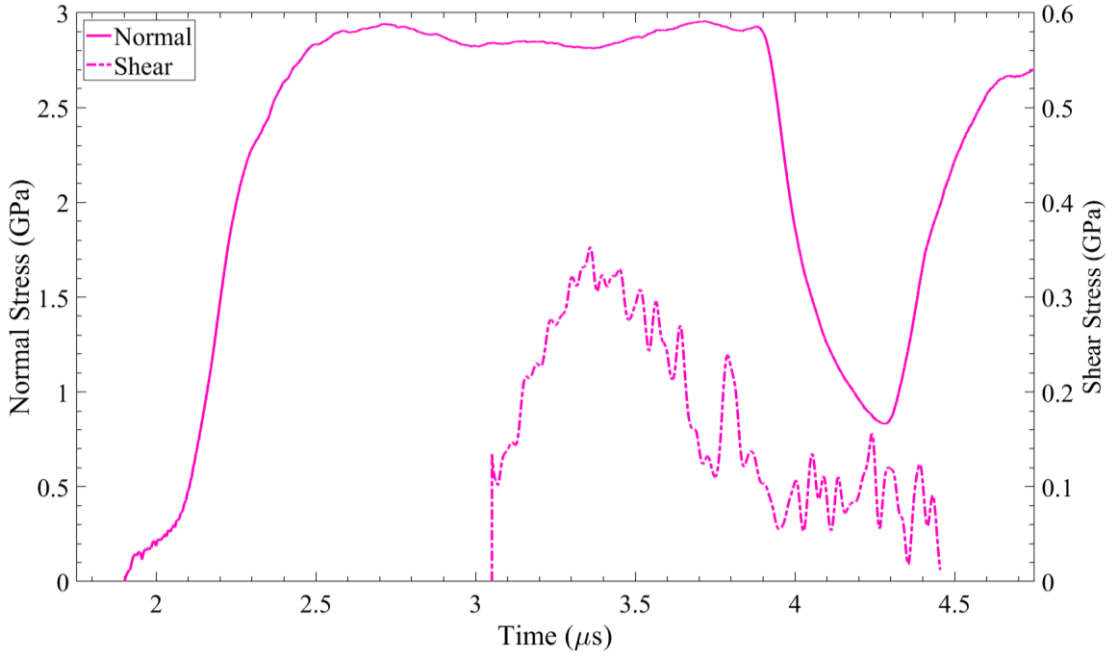

Figure 6.11 Normal and shear stress profiles of the PSPI shot on granular sucrose

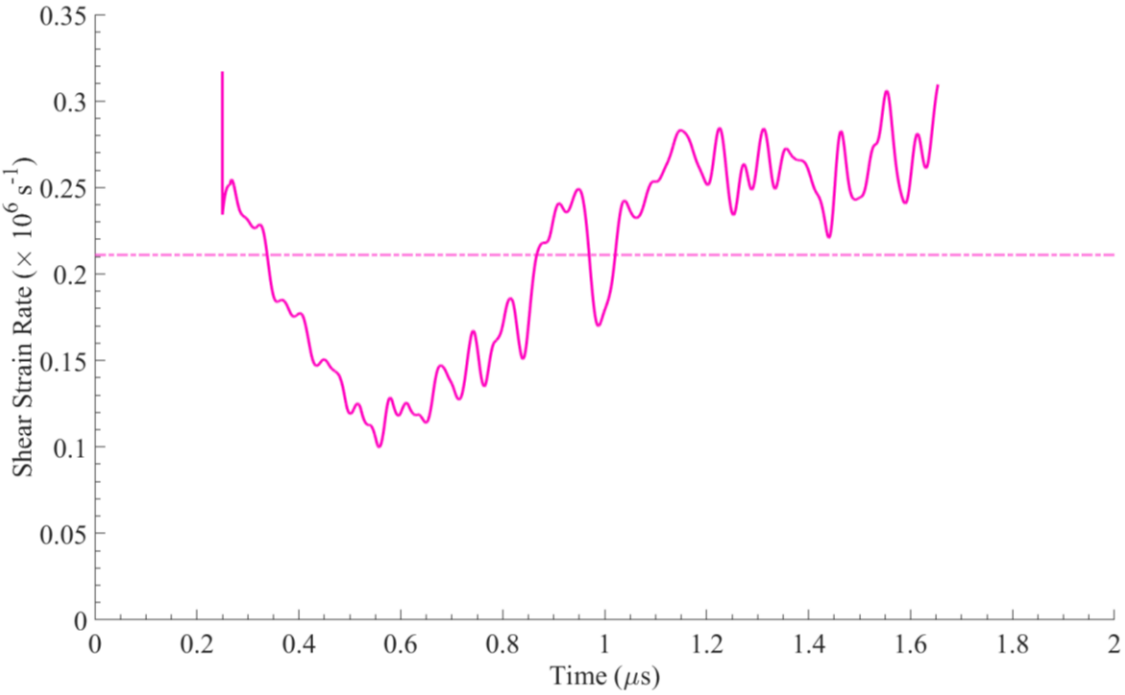

Figure 6.12 Shear strain-rate profile of shot on granular sucrose

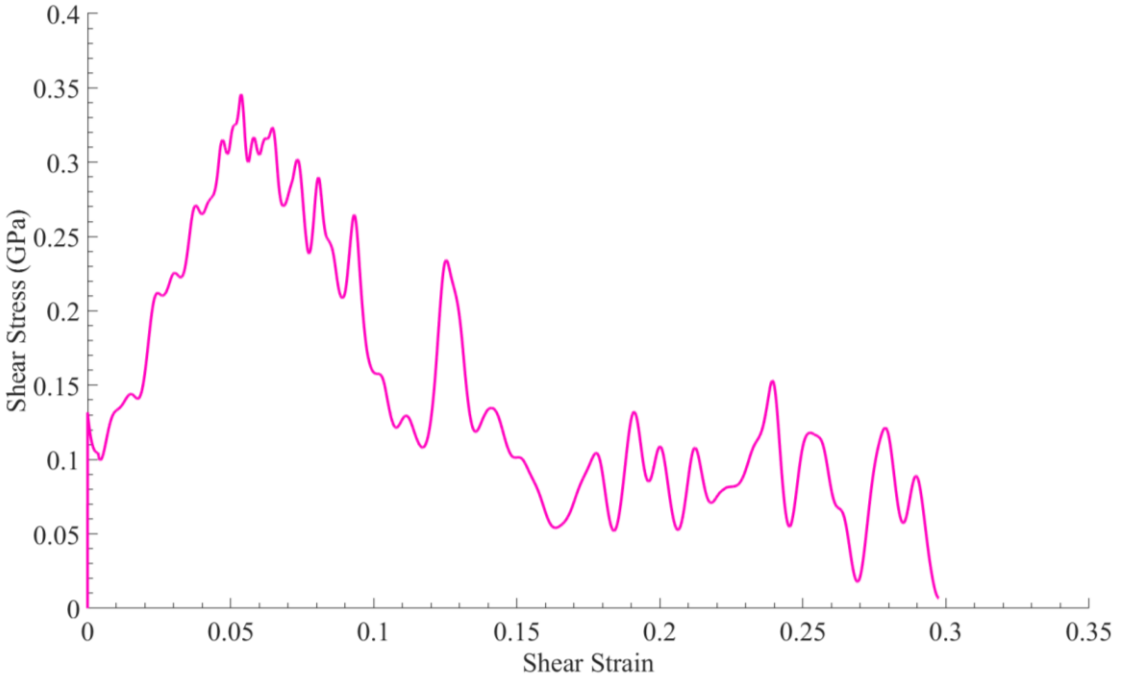

Figure 6.13 Shear stress versus shear strain plot of PSPI shot on granular sucrose

Normal stress profiles of PSPI shots on all different materials for the same nominal values of normal stress of 3 GPa are shown in Figure 6.14. The rise times of the composite and granular sucrose are comparable to each other. While granular sucrose does not show any steps, the normal responses of the composite and granular sucrose are very close to each other. HTPB, on the other hand, shows a slightly quicker rise to the plateau since no compaction is involved, as is the case with the composite and granular sucrose. The uniform sucrose specimen shows the quickest rise-time but it should be kept in mind that the specimen thickness in that case is an order of magnitude less than in the other cases.

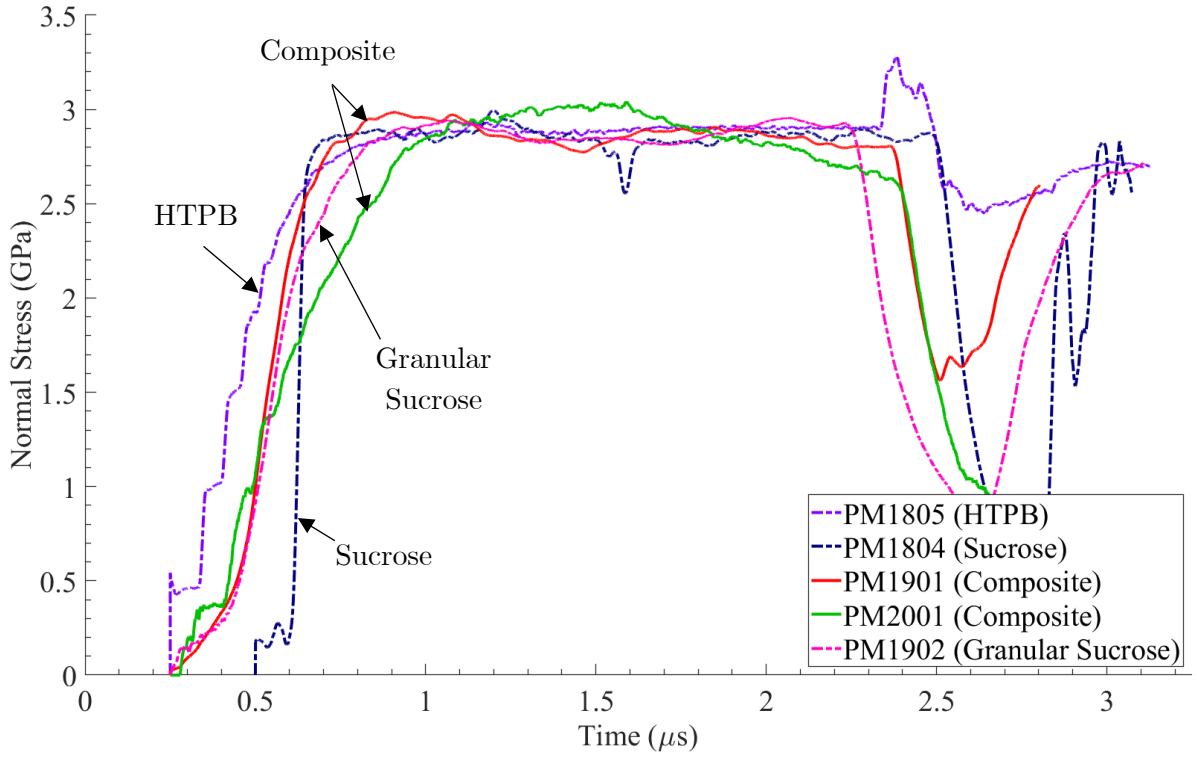

Figure 6.14 Comparison of normal stress profiles of shots on HTPB, uniform sucrose sample, polymer-bonded sucrose composite and granular sucrose

It is most instructive to compare the shear stress versus shear strain behavior of the polymer-bonded sugar with compacted granular sucrose. Such a comparison is presented in Figure 6.15. It is evident that introduction of just 10% HTPB binder into the granular pressing of sucrose can reduce its shear strength by half of its original value. The shear strength of the binder at the critical shear strain of the granular pressing of sucrose is 4 times lower than that of granular sucrose. The composite and granular sucrose exhibit a fall in shear strength at similar critical shear strain values of ~0.05.

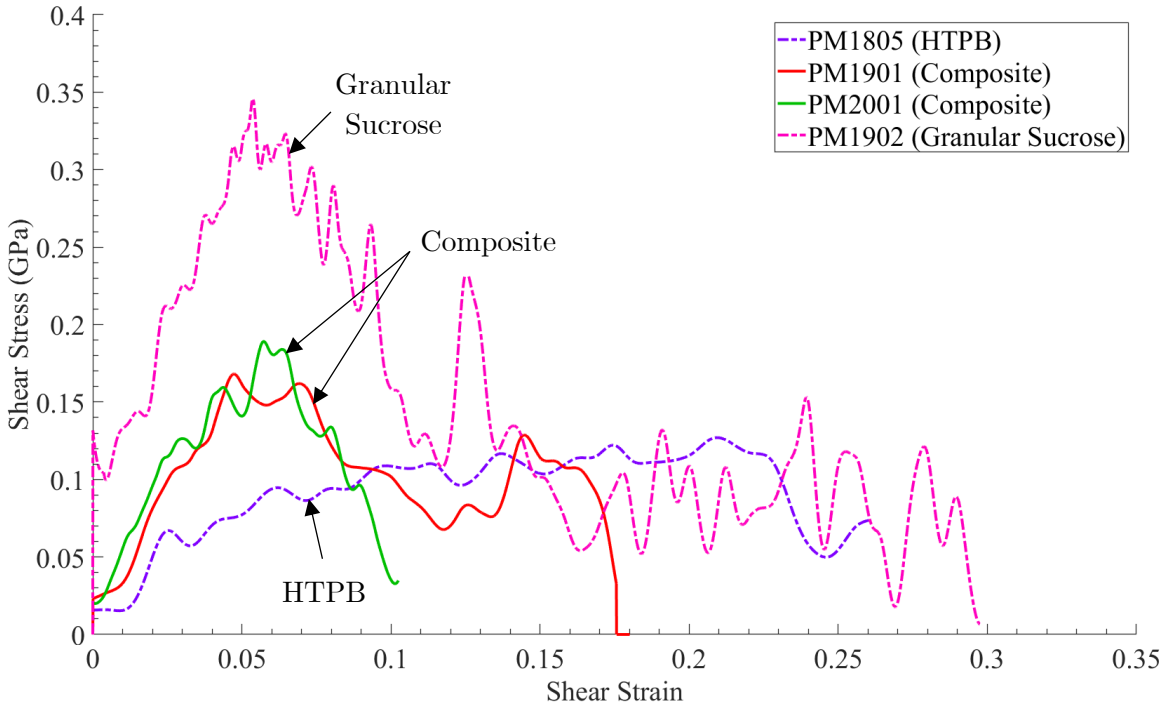

Figure 6.15 Comparison of shear stress versus shear strain behavior of granular sucrose, binder HTPB and their composite

6.4 Finite Element Simulations

ABAQUS/Explicit simulations are carried out for a canonical one-dimensional case, with a vertical laminate geometry, as shown in Figure 6.16. Three different cases are explored for the low and high-pressure shots: $n = 2, n = 5$ and $n = 11$, where n is the number of sucrose grains. In each simulation, the relative weight fraction of sucrose and HTPB is kept at a constant value of 0.9. The results are shown for a low-pressure shot and a high-pressure shot in Figure 6.17 and Figure 6.18 respectively.

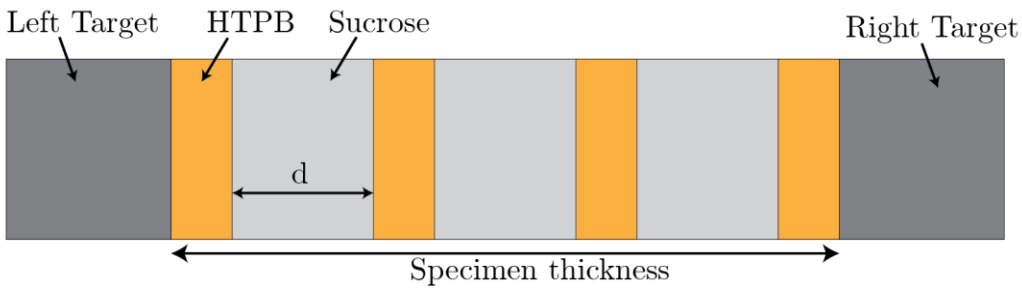

Figure 6.16 A vertical laminate composite specimen geometry used in ABAQUS/Explicit simulations. Alternating layers of HTPB and sucrose are simulated. Sucrose grain size is indicated by the parameter d while the number of layers of sucrose is n. Note that $n = 3$ is shown here only for demonstration

It can be observed that the simulated normal stress profiles show steps which indicate the large impedance mismatch between the specimen and the bounding plates. These steps are observed in some experiments, but not observed in others because of the highly heterogeneous nature of the specimen. Shear stress predictions for the low-pressure shot do not match very well with the experimentally measured values. Simulations predict large shear peak shear stresses which fall off at much later times as compared to the experimental shear stress. The fall in simulated shear stresses is the result of shear band formation in one of the sucrose grains.

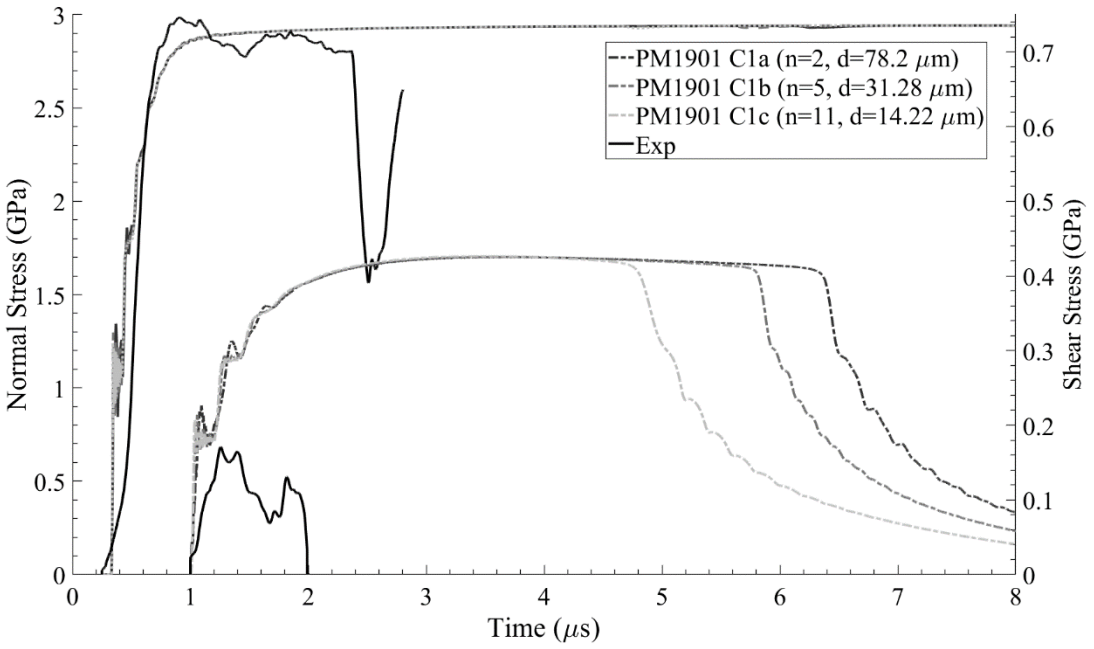

Figure 6.17 Comparison of simulated normal and shear stress profiles with experimental measurements for the low-pressure shot, PM1901 on sucrose/HTPB composite. Simulated results are plotted for 3 different grain sizes. The simulated normal stress profiles due not show any unloading due to the nature of geometry chosen (see Appendix A). Simulated shear stresses are much larger than experimentally measured

However, the simulated peak shear stresses not only exhibit a closer match to the experimental values for the high-pressure shot simulations but also display a much earlier drop in shear stress compared to their low-pressure counterparts. Such a behavior hints at the presence of other strain softening and failure mechanisms such as fracture in the binder or crystals, delamination of the binder and adiabatic shear localization in the binder. Thermal softening due to friction between fractured surfaces is also expected to contribute to the drop in strength of the composite. None of these mechanisms have been considered in the simple one-dimensional vertical laminate microstructure studied here and should be accounted for in realistic modeling of the composite. The simulations of the vertical laminate also show grain size dependence of the

onset of localization and subsequent failure of the composite. Lower grain sizes result in an earlier drop in shear strength, with the grain size dependence being stronger for the low-pressure case. Thermal diffusivity of the binder phase is lower than that of sucrose, which results in quicker temperature rise for smaller grains and hence an earlier onset of adiabatic shear band instability.

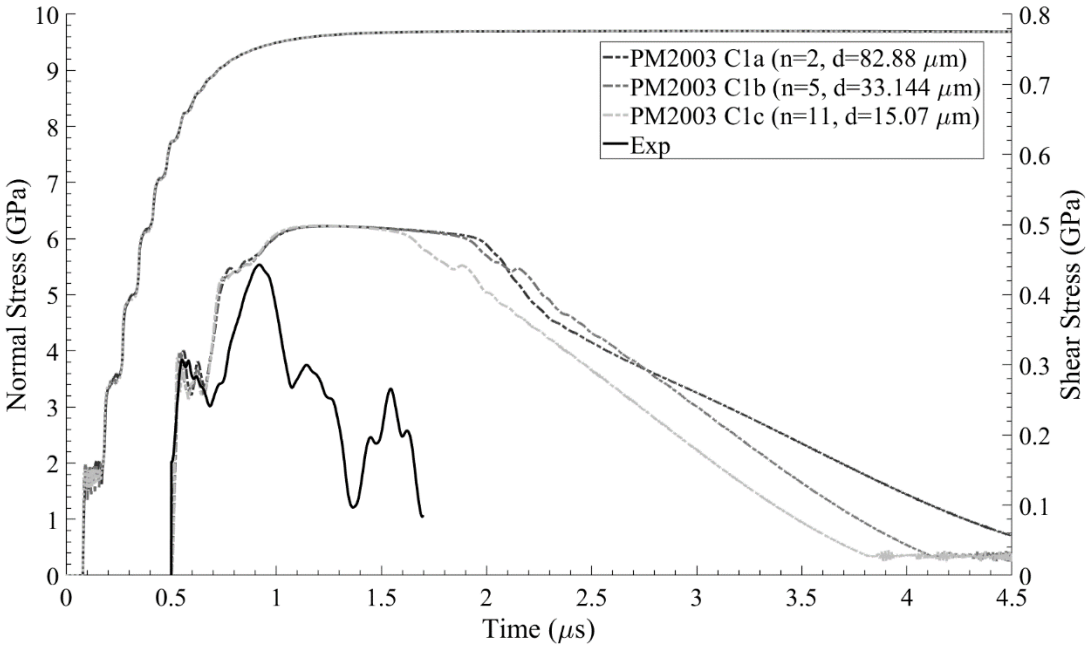

Figure 6.18 Comparison of simulated normal and shear stress profiles with experimental measurements for the low-pressure shot, PM2003 on sucrose/HTPB composite. Simulated results are plotted for 3 different grain sizes. The simulated normal stress profiles due not show any unloading due to the nature of geometry chosen (see Appendix A). Peak shear stresses are very close to experimentally measured values

6.5 Discussion

PSPI experiments are carried out on a 90:10 sucrose/HTPB composite by weight. Both normal and transverse velocity profiles display some variability under similar experimental

conditions, which is expected for such a highly heterogenous specimen. Peak shear strength of the composite exhibits dramatic normal stress dependence. Even though sucrose forms 90% of the composite, such a pressure-dependence of shear strength of the composite is closer to that of HTPB than sucrose. A comparison of shear behavior of the composite with that of granular sucrose highlights the role of the binder in determining the shearing response of the composite. It can be concluded that the binder effectively acts as a lubricant between sucrose crystals and is therefore, expected to reduce the number of hot-spots in a PBS as compared to a granular pressing of sucrose.

Shear strength of the composite shows a dramatic drop to a smaller value after accruing a certain amount of critical shear strain. Such a drop can be a result of multiple failure mechanisms like adiabatic shear band localization in the binder and crystal phases, fracture of the binder of the crystal, delamination of the binder from the crystal or friction resulting from sliding between fractured surfaces. Shearing response of a one-dimensional vertical laminate shows a closer agreement with experimental measurements under high-pressures than lower-pressures, thereby highlighting the need for including the above-mentioned failure modes into modeling. However, it should be noted that adequate experimental characterization of each failure mode is necessary before incorporating them into the modeling framework.

6.6 Appendix A: Creating ABAQUS Input file using MATLAB

Carrying out simulations of two-dimensional geometries of the composite requires a large number of mesh elements. Since the simulations are run on a regular PC, it is desired to speed

up the calculations. Reducing the length of the target plates and removing the flyer with appropriate boundary conditions facilitates the reduction in number of mesh elements. *Dashpot connector elements* of the *Cartesian* type are used to apply the velocity boundary conditions. Consider the schematic in Figure 6.19. A small thickness of target plates on either side of the specimen is retained. Dashpot connector elements are employed on both the ends. Dashpots allow the implementation of characteristic equations (discussed in Chapter 1) as described through Figure 6.19. The characteristic equations between points 1 and A and points 2 and B can be written as:

$$\sigma_1 = \rho_0 c_L (u_1 - u_0) \tag{6.1}$$

$$\tau_1 = \rho_0 c_s (v_1 - v_0) \tag{6.2}$$

$$\sigma_2 = \rho_0 c_L u_2 \tag{6.3}$$

$$\tau_1 = \rho_0 c_s v_2 \tag{6.4}$$

Using the above equations, the force transmitted by the dashpot elements and hence the damping coefficients can be calculated. The force transmitted by a dashpot is given as the damping coefficient multiplied by the difference in velocities at its two ends. For dashpot 1, the normal and shear forces can be given as $\sigma_1 a$ and $\tau_1 a$ respectively. Similarly, for dashpot 1, the normal and shear forces can be given as $\sigma_2 a$ and $\tau_2 a$ respectively. This justifies the use of dashpot elements as the equation of motion of dashpots represents the wave characteristic equations. Since the force in a cartesian dashpot connector element between two nodes 1 and 2 is given as $F_i = \sum_i C_{ij}(v_{j1} - v_{j2})$, the damping coefficients are then given as:

$$C_{11} = \rho_0 c_L a \tag{6.5}$$

$$C_{22} = \rho_0 c_s a$$

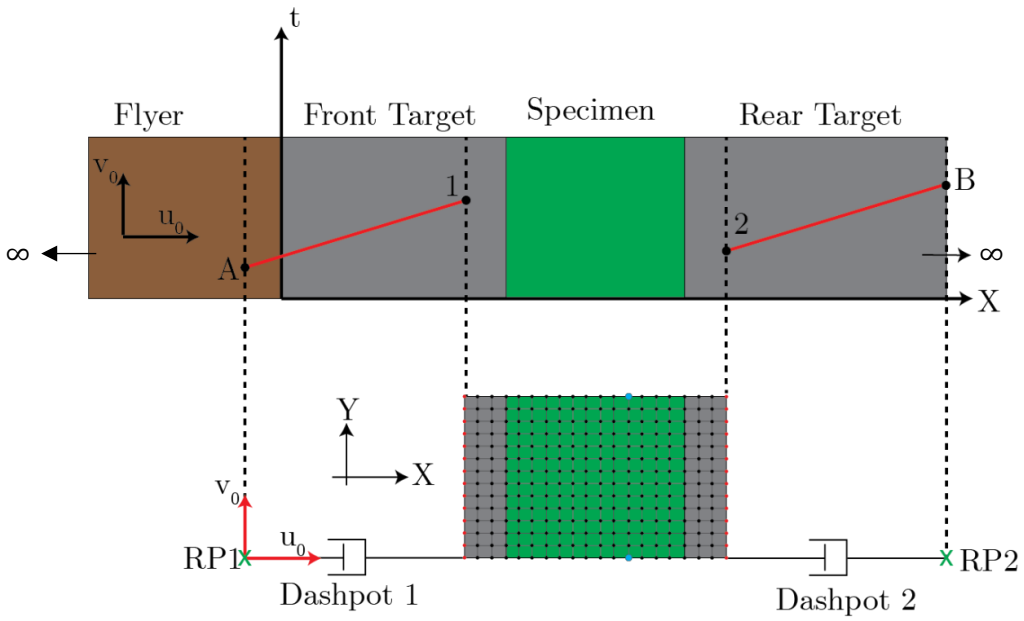

Figure 6.19 Schematic showing implementation of dashpot connector elements for simulating the composite behavior in PSPI experiments. *Top figure*: The flyer (brown) impacts the specimen (green) sandwiched between target plates (grey) with an impact velocity of u_0 in the normal direction and v_0 in the transverse direction. Wave characteristics between two pairs of points are shown as red solid lines. Since specimen behavior is not of interest after the arrival of unloading waves from the free surfaces, the flyer and rear target plate are assumed to extend to infinity. *Bottom figure*: A section of the sandwich is considered with only a portion of the target plates. The flyer is removed and replaced by a dashpot connector element on the left. Another dashpot is added to the right. Boundary conditions are applied to the reference points, RP1 and RP2. Nodes highlighted in red are all constrained to have same degrees of freedom in the X and Y directions. Vertically nearest node pairs on top and bottom faces are constrained to have same degrees of freedom in the X and Y directions. One such pair is highlighted in blue

Since boundary conditions need to be applied uniformly to all nodes highlighted in red on each face, the displacements of the two node sets are constrained to be the same using *equation constraints*. The nodes on top and bottom faces (not highlighted) are also constrained in pairs to have the same displacements in X and Y-directions and zero rotations about the Z-axis (for example, see the blue highlighted pair). However, it must be kept in mind that the nodes on the top and bottom faces need to be sorted before applying the equation constraints.

Since ABAQUS does not generate a sorted set of nodes on its own, a MATLAB code needs to be written for this purpose.

Two time-steps are used, the first to apply normal velocity and the second to apply transverse velocity along with the normal velocity. The duration of each step is decided based on the difference between the arrival times of longitudinal and shear waves at the left specimen/target-plate interface. In time-step 1, the normal velocity is applied on the left reference point. In time-step 2, the transverse velocity is applied on the reference point while keeping the normal velocity same as in time-step 1. In both the time-steps, all the degrees of freedom of the right reference point are constrained.

Since equation constraints require sorted pairs of nodes, it is easier to generate the entire input file using MATLAB. Once the geometry is created using ABAQUS, a raw input file with information about nodal coordinates, element connectivity and raw node sets is fed into the MATLAB code. The code then generates an input file with the required connector elements, equation constraints, time-step definitions and output variables. Some parts of the code were written in guidance of Prof. David Henann.

Chapter 7

High-Speed Microscopy

7.1 Introduction

In this chapter, an experimental method is reported that can, simultaneously, image the deformation fields associated with dynamic failure events at high spatial and temporal resolutions. The method is demonstrated at a temporal resolution of 250 ns and a spatial resolution of ~1 µm, while maintaining a relatively large field of view (≈ 1.11 mm x 0.63 mm). As a demonstration, the method is used to resolve the deformation field near a notch tip during initiation of an adiabatic shear instability. An ordered array of 10 µm diameter speckles deposited on the specimen surface near the notch tip helps track evolution of the deformation field. The combination of high spatial and temporal resolutions has a broad range of applications such as the study of the role of microstructural heterogeneities on initiation and propagation of dynamic failure events.

In-situ imaging of dynamic events has been of interest in experimental mechanics for a long time. High-speed imaging has been used in a wide range of disciplines to study a variety of events such as cavitation Estrada et al. (2018) , combustion Kohse-Höinghaus and Jeffries (2002), Aldén et al. (2011), Böhm et al. (2011), Sick (2013) , shock waves Rubino et al. (2017), Gori et al. (2018), Rubino et al. (2019) , adiabatic shear localization Hartley et al. (1987), Marchand and Duffy (1988), Zhou et al. (1996), Guduru, Ravichandran, et al. (2001), Guduru, Rosakis, et al.

(2001), Dodd and Bai (2012) , crack tip deformation fields Tippur and Rosakis (1991), Tippur et al. (1991), Mason et al. (1992) , twinning Kannan et al. (2018) and dynamic friction Rubino et al. (2017), Gori et al. (2018), Rubino et al. (2019) . Advancements in imaging of such dynamic events have been enabled by the rapid evolution of high-speed camera technologies over the past 70 years and the high temporal resolution that they offer. At the same time, there are several dynamic phenomena that occur not only at small time-scales but also at small length-scales, examples of which include hot-spot mechanisms in energetic materials; dynamic failure of heterogeneous materials through crack propagation; adiabatic shear bands; twinning and dynamic friction; and cavitation. Imaging such events requires high temporal and spatial resolutions simultaneously, i.e., high-speed microscopy. The importance of high-speed microscopy in advancing our understanding of dynamic response and failure of materials has been highlighted in a recent National Research Council report Council (2011) .

Significant progress has been reported in the recent literature on imaging at high spatial and temporal resolutions simultaneously. Rubino et al. (2019) reported an investigation on laboratory earthquakes in which rupture of frictional interfaces was investigated by combining high speed imaging with the digital image correlation (DIC) technique. The combination allowed them to measure the deformation and stress fields associated with shear shock waves and evolution of dynamic friction coefficient at the interface. Based on the imaging technology and magnification reported in their work, the spatial resolution of imaging can be inferred to be 27.8 μm based on the Nyquist criterion (sensor pixel pitch $p = 30$ μm, magnification =2.16). Kannan et al. (2018) reported a study on dynamic twinning in single crystal magnesium by employing high-

speed photography. They employed a 105 mm Nikon lens coupled with 2 teleconverter lenses and bellows in order to spatially resolve twin nucleation and propagation. Based on the numbers reported in their paper, imaging was done at a magnification of 5 μm per pixel, which implies a pixel-limited spatial resolution of 10 μm. Imaging at a temporal resolution of 200 ns, they measured twin tip velocities of the order of 1 km/s. Twin boundary growth values and twin tip velocities of second-generation twins that nucleate from boundaries of pre-existing twins were also reported. Estrada et al. (2018) used micro-cavitation as a rheometer to measure viscoelastic properties of polyacrylamide gel under high strain rates. A pulsed laser was used to generate cavitation, which was imaged using a Phantom v2511 high-speed camera and bright-field illumination with a halogen lamp. Images of bubble generation, collapse, and subsequent oscillations were taken at a temporal resolution of 3.7 μs. Combining bubble kinematics with a constitutive model allowed them to extract material properties of the gel in a minimally invasive manner. Ravindran et al. imaged polymer-bonded sugar (PBS) subject to high strain rate loading in order to identify deformation localization mechanisms Ravindran et al. (2016), (2017) . They employed Photron SAX2 high-speed camera at 100,000 fps along with a Navitar extension tube. They appear to have achieved a pixel-limited spatial resolution of 20 μm. Using Digital Image Correlation (DIC) to analyze the deformation field, they showed that large strain localization occurs in polymer-rich areas between crystal boundaries while the deformation of crystals is minimal.

It is clear that there is a great deal of interest in measuring deformation fields at high spatial and temporal resolutions simultaneously in order to understand the deformation response and failure mechanisms in heterogeneous materials. Here a method is presented that offers such a

capability with a temporal resolution of 250 ns, spatial resolution of 1 μm and a field of view of about 1.1 mm x 0.63mm. The following section presents the experimental setup.

7.2 Experimental Setup

A schematic of the experimental set-up is shown in Figure 7.1. The key components of the high-speed microscopy system are: (a) a high-speed camera, (b) imaging optics and (c) illumination. First, considerations that determined the choices made in assembling the experimental setup are described.

7.2.1 High-speed camera

Dynamic deformation and failure events such as adiabatic shear localization occur over times scales of a few microseconds, which necessitates a high-speed camera with framing rates of 10^6 s^{-1} or higher. As will be explained below, imaging such events also requires a sufficiently large sensor (i.e., pixel array size of 1000 x 1000 or greater) and a fine pixel pitch in order to image at an acceptable field of view combined with micron scale spatial resolution. In addition, low electronic noise of the camera is a requirement for measuring the kinematic fields through DIC or particle tracking, particularly for large deformations. Among the three most commonly used technologies for the present-day high-speed cameras are: (a) single CMOS sensor cameras, (b) gated-intensified cameras, and (c) rotating mirror cameras.

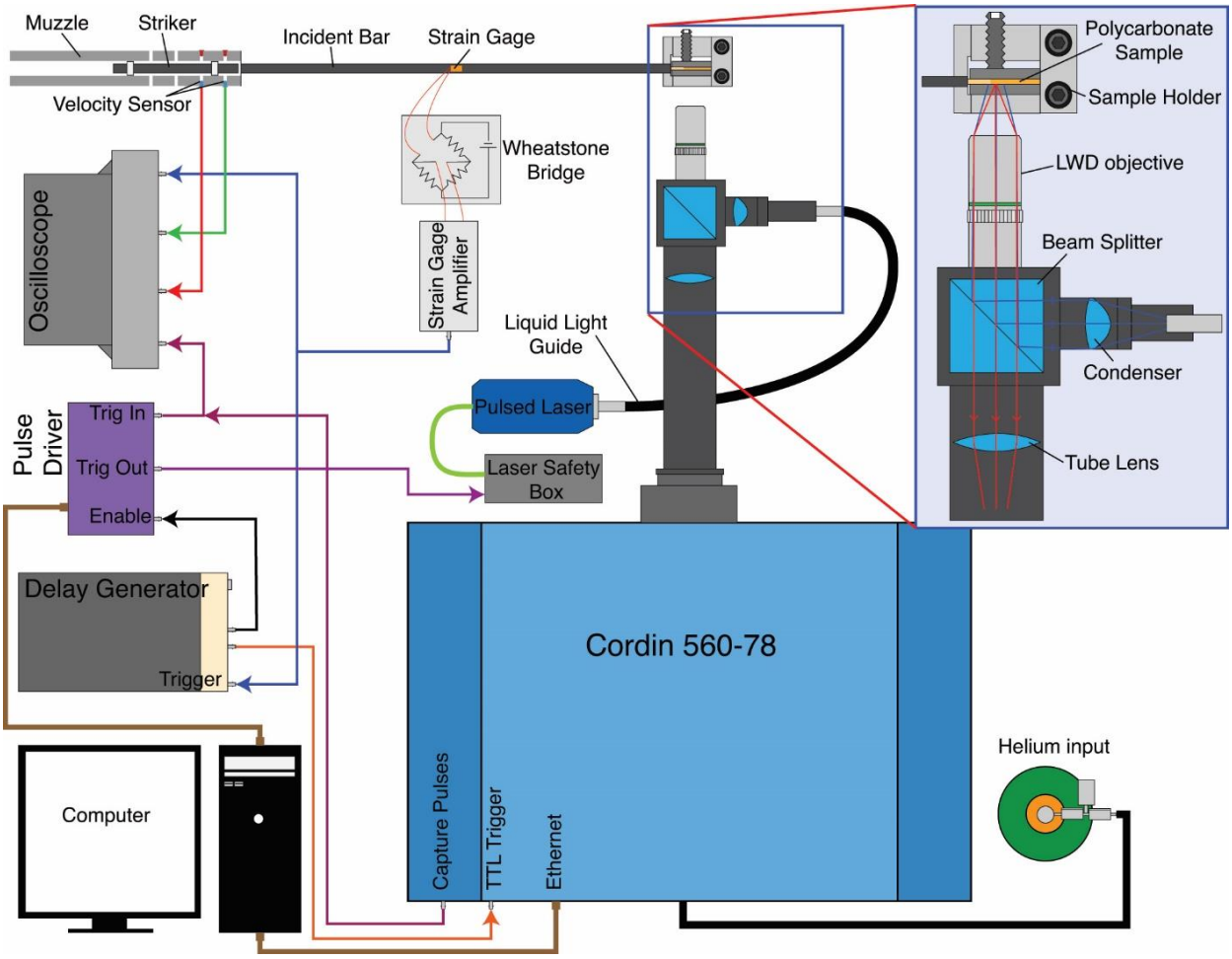

Figure 7.1 A schematic of high-speed microscope set up for imaging a sample impacted in a Kolsky bar. Key components of the system are: high-speed camera, microscope optics and the laser for illumination. Cable connections between various components are shown using arrows. The inset on the right shows the optical elements in detail. Illuminating rays are shown in blue and image forming rays in red

The single-sensor in-situ storage cameras are the most popular high-speed cameras at present. These cameras use a CMOS (complementary metal-oxide semiconductor) sensor and on-chip storage of all frames, which allows them to run at high frame rates. Depending on the read-out mechanism, these sensors can offer varying resolutions at different frame rates. Typically, the sensor resolution decreases as the framing rates go up. This loss of resolution is due to limitations on read-out speeds, i.e. the speed at which an acquired image can be transferred to the memory.

However, certain cameras offer constant resolution at all frame rates. Among the best specifications for these commercial cameras are: sensor size of 400 x 250 pixels^2, image acquisition rate of 5 million frames per second, and the number of frames collected of 128. These cameras tend to be lighter and more compact compared to the rotating mirror and gated-intensified cameras but usually have large pixel size (~30 μm) and lower sensor resolution. The sensor chip architecture also leads to lower fill factors (~37%) which can cause aliasing and inability to resolve higher spatial frequency content.

The gated-intensifier cameras consist of an image intensifier unit, coupling optics and a CCD sensor. The heart of these cameras is the image intensifier unit, which can amplify the incoming photons by a factor of over 1000. The intensification is achieved through a micro-channel plate (MCP) that amplifies the photoelectrons received from the photocathode and sends them to a phosphor screen for conversion back to photons. The intensifier comes with an added advantage of electronic gating which allows extremely small exposure durations – of the order of nanoseconds. These cameras can offer framing rates of up to a few hundred million fps with 200 ps exposures and up to 8 frames at these framing rates. However, these cameras suffer from larger noise, loss of contrast and loss of spatial resolution Tiwari et al. (2007), Pierron et al. (2011) , which are inherent to the intensification process and optical coupling in this design of high-speed cameras. As mentioned by Rubino et al. (2019) , extracting useful quantitative information like displacements and strains from images taken using an intensified CCD camera is not easy, especially to meet the stringent requirements of displacement, velocity and strain resolutions. Also,

the total number of frames is very small, which may not be sufficient for capturing the full evolution of dynamic events.

Table 7.1 A comparison of six commercially available high-speed cameras with respect to their ability to capture images at a spatial resolution of 0.5 μm. The parameters of interest are the minimum magnification required to achieve this spatial resolution and the corresponding field of view. The illumination wavelength is assumed to be 640 nm. N is the number of frames and m is the magnification for $r_{obj} = 0.5\,\mu m$

	Tech.	Max fps	N	Sensor pixel array size	Pixel pitch (μm)	MCP Res.	m	Field of View (mm^2)
1	Rotating Mirror	4 million	78	1920x1080	7.4	-	44x	0.48x0.27
2	Single CMOS sensor	5 million	180	924x768	30	-	120x	0.23x0.19
3	Single CMOS sensor	5 million	128	400x250	30	-	120x	0.1x0.06
4	Image-Intensifier	200 million	8	2000x2000	7.4	40 lp/mm or 25 μm	100x	0.15x0.15
5	Image-Intensifier	333 million	16	1360x1024	6.45	50 lp/mm or 20 μm	80x	0.11x0.08
6	Image-Intensifier	200 million	8	1360x1024	6.7	28 μm	112x	0.08x0.06

Rotating mirror cameras consist of multiple independent CCD sensors arranged equally in two 120^0 arcs, positioned radially with respect to a rotating mirror in the center. A light beam hitting the mirror is swept across each of the arcs and focused on the CCDs by relay lenses. A helium gas-turbine is used to drive the mirror at high speeds, which yields framing rates up to a few million fps. The advantage of the rotating mirror cameras is that the individual CCD sensors can be configured to have a large pixel array with a small pitch to

increase the spatial resolution (to be discussed below). On the other hand, these cameras are bulky and heavy; and their operation is much more complex than that of the other technologies.

High-speed microscopy, as the name suggests, requires integration of a high-speed camera and an optical microscope. The achievable temporal resolution of such a system is determined by the framing rate of the high-speed camera. All of the high-speed imaging technologies described above satisfy the time resolution requirements for imaging most dynamic events in solids, however they differ in the spatial resolution that can simultaneously be X achieved practically. The spatial resolution of any optical imaging system is limited either by the numerical aperture of the objective lens (diffraction limit) or the pixel size of the imaging detector (sampling limit). The former, known as the Rayleigh criterion, can be expressed as

$$r_{obj,d} = \frac{\lambda}{2\,NA} \tag{7.1}$$

where λ is the wavelength of the illuminating light and NA is the numerical aperture of the objective. On the other hand, pixel-limited spatial resolution of an imaging system can be defined using the Nyquist criterion as

$$r_{obj,p} = \frac{2p}{m} \tag{7.2}$$

where $r_{obj,p}$ is the finest feature that can be resolved, p is the pixel pitch and m is the magnification of the optical imaging system. The spatial resolution of the system is given by the larger of $r_{obj,p}$ and $r_{obj,d}$. There is a wide range of commercially available microscope objectives, which reduces the task of satisfying the Rayleigh criterion to one of proper optical design and integrating the microscopy optics with those of the high-speed camera. However, the characteristics of the imaging sensors in commercially available high-speed imaging cameras often set limits on imaging

resolution, minimum required magnification, and the field of view. Table 7.1 illustrates the trade-offs for six different commercial high-speed cameras (company names are not shown). The table presents the minimum required magnification of the optics and the achievable field of view for a target spatial resolution of 0.5 μm. Note that in the case of gated intensifier cameras, the resolution of the microchannel plate (MCP) can set the resolution limit instead of the sensor pixel pitch. From Table 7.1 it can be seen that the minimum optical magnification required for achieving a target spatial resolution and the corresponding field of view at that resolutions differ widely between the cameras considered. An optical system with a higher magnification has a correspondingly lower depth of field, which limits the allowable out of plane motion of the specimen during an experiment while still keeping it in focus. Moreover, a higher magnification objective tends to have a smaller working distance, requiring a working distance as close as a millimeter at high magnifications Such a small working distance could be impractical for the dynamically deforming specimen surfaces of interest. Thus, the combination of lowest required magnification and the largest field of view provides a practical criterion of choosing an appropriate high-speed camera.

Based on these considerations, a rotating mirror camera has been chosen in this investigation despite the complexity of its technology, operation and maintenance. The Cordin 560 rotating mirror high-speed camera employed in our setup consists of 78 independent CCD sensors. The mirror can rotate at a speed up to 16,667 revolutions per second, corresponding to framing rate of 4 million fps. Each CCD is a monochrome 14-bit sensor with a 1920 x 1080 pixel array and a pixel pitch of 7.4 μm. The camera body has approximate dimensions of 24 in x 30 in

x 26 in and weighs about 100 kg. However, since it operates as a microscope, it is necessary to be able to move it at micron-scale precision for alignment and focusing purposes. A 6-degree of freedom stage has been custom-designed and built to meet these requirements with the camera mounted on it (Figure 7.2).

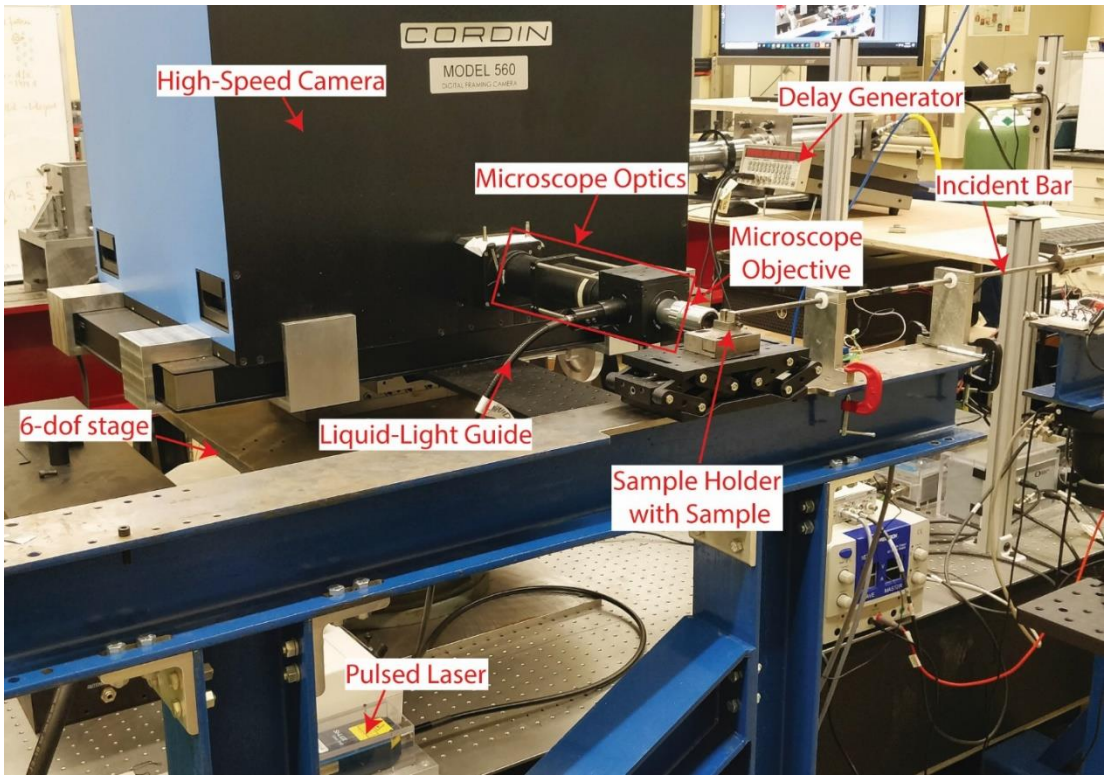

Figure 7.2 High-speed microscope set-up at Brown University. The important components of the system are highlighted in the figure above: Cordin high-speed camera mounted on a 6-dof stage, microscope optics (highlighted in red box), microscope objective, pulsed laser, the liquid light guide that carries illumination pulses from the pulsed laser to the condenser lens for in-line illumination and the delay generator that serves as the master clock to synchronize all events. The incident bar and sample holder with the sample are also shown

In addition to the above considerations, since one is often interested in imaging dynamic events, there are additional constraints on the illumination system in order to minimize motion

blur and the need to make use of the available dynamic range of the imaging sensors. Further details are discussed in the section on illumination.

7.2.2 Optics

The optical imaging system consists of a microscope that forms an image of the specimen surface on a prescribed plane at the entrance of the Cordin camera, from where it is relayed by the internal optics of the camera to the sensor plane via the rotating mirror. The microscope elements are shown in Figure 7.2. The main elements are an infinity-corrected long working distance objective and a tube lens. An in-line illumination arrangement is chosen, where the illumination light enters the optical train normal to the optical axis and is directed into the objective through a 50:50 beam splitter as shown. A liquid light guide feeds light from a laser illumination source to an aspheric condenser lens, the relative position of which with respect to the end of the light guide determines the illumination spot size on the specimen. A Koehler-type illumination can be achieved by adjusting the condenser lens position to form the image of the end of the light guide on the back focal plane of the objective. On the other extreme, a highly focused spot can be achieved by adjusting the condenser lens such that it collimates the light from the liquid light guide. In our experiments, an intermediate configuration is chosen such that the illumination spot size on the specimen surface is slightly larger than the field of view. Diffuse reflection from the specimen is collected by the objective (see inset in Figure 7.1) and a tube lens forms a real image on the prescribed plane near the entrance to the high-speed camera. A Nikon F-mount connects the microscope optics to the camera. The system has been configured for three long working distance microscope objectives: 10X, 20X and 50X. Table 7.2 shows the details of the objectives (make and model, NA and working distance), the combined magnification of the

microscope optics and the camera internal optics), spatial resolution, the limiting criterion that determines the spatial resolution (diffraction limited vs. sampling limited) and the field of view. Figure 7.3 demonstrates that the calculated spatial resolutions are indeed realized; it shows images of a resolution target with the 20X and the 50X objectives. The former is able to resolve 1 μm features and the latter can resolve 0.5 μm features. Microscope optics and illumination (described below) have been custom designed to serve the purpose of attaining large spatio-temporal resolutions simultaneously. The know-how has been shared with Cordin and the optics is now commercially available through Cordin.

Table 7.2 Comparison of different objectives used in the optical train of the high-speed microscope. All objectives are long working distance objectives. As the magnification increases, the working distance decreases and the spatial resolution increases. The 50x objective gives the highest resolution of 0.58 μm. NOTE: $m_{total} = m_{objective} \times 2/3$

Objective	NA	Working Distance	m_{total}	Spatial Resolution	Limiting Criterion	Field of View
10x Plan Apo Infinity-Corrected Long Working Distance Objective	0.28	34 mm	6.67x	2.22 μm	Pixel-Limited	2.13x1.20 mm^2
20x Plan Apo Infinity-Corrected Long Working Distance Objective	0.42	20 mm	13.33x	1.11 μm	Pixel-Limited	1.07x0.60 mm^2
50x Plan Apo Infinity-Corrected Long Working Distance Objective	0.55	13 mm	33.33x	0.58 μm	Diffraction-Limited	0.43x0.24 mm^2

7.2.3 Illumination

The combination of high temporal and spatial resolutions places severe requirements on the illumination. Since the interest is in imaging dynamic events, image blur due to object motion must be minimized. As an example, consider the case of the characteristic particle velocity within

the field of view to be of the order of 100 m/s. In order to restrict the particle displacement during optical exposure (i.e. motion blur) to be within the imaging resolution (say 1 μm), the illumination duration has to be no more than 10 ns for each frame. A pulsed laser is a convenient source for generating a sequence of such short illumination pulses. Another vital difference between normal high-speed imaging with a large field of view (of the order of a centimeter) and high-speed microscopy is that in the latter each pixel of the CCD sensor collects photons from a very small area of the specimen surface. In the system under consideration here, for a magnification of 20X, each pixel collects photons from an area of approximately 0.56 μm x 0.56 μm. In order to make use of the dynamic range of the CCD pixels and obtain sufficient image contrast, the number of photons collected by each pixel multiplied by its quantum efficiency needs to be a significant fraction of the CCD full well depth, which in our case is 44,000 electrons. Based on this number, one can calculate the power requirement on the laser source by accounting for the losses along the optical path (e.g. losses in the light guide, passing through the beam splitter twice, diffuse reflectivity of the specimen surface, collection efficiency of the objective, etc.) and the finite illumination pulse width. Such a calculation, based on a pulse width of 10 ns, shows the required power to be a few hundred Watts. The Specialized Imaging LUX640 pulsed laser source was employed to illuminate the specimen, which is a 400W pulsed laser that emits a low coherence beam at a wavelength of 640±10 nm. It is shown schematically in Figure 7.1.

7.3 Experimental Demonstration

The capability of the experimental system is demonstrated by imaging the initiation of an adiabatic shear band (ASB) from a notch tip in a polycarbonate specimen subjected to impact

loading in a Kolsky bar. ASBs are zones of intense plastic shear strain that are typically formed under high strain-rates when the increase in the strength of a material due to strain and strain-rate hardening is offset by the decrease due to thermal softening (or other softening mechanisms). ASBs have been studied extensively in a variety of materials including metals, alloys, bulk metallic glasses and polymers. Since the primary aim here is a demonstration of the experimental method, it is not our intent to provide a comprehensive review of the literature on ASB; for a more extensive list of references, see Wright and Perzyna (2003) and Dodd and Bai (2012) . However, in the context of real time imaging of ASB initiation and propagation, it is worth mentioning a few relevant reports from the literature. Broadly, there have been two streams of investigations: measurement of strain and stress fields in the vicinity of initiating and propagating ASBs Marchand and Duffy (1988), Kalthoff (1990), Ravi-Chandar (1995), Ravi-Chandar et al. (2000), Guduru, Rosakis, et al. (2001) and measurement of the corresponding temperature fields Hartley et al. (1987), Zehnder et al. (2000), Guduru, Ravichandran, et al. (2001), Guduru, Rosakis, et al. (2001), Guduru (2001) . In the former, the dimension of the typical field of view was a few centimeters with very coarse spatial resolution; consequently, the measured far field stress and strain fields corresponded to those due to the mixed mode loading of the pre-existing notch. In the absence of information on the micron-scale processes near the notch tip, it was not possible to relate these processes to the far field stress/strain measurements to formulate a rational criterion for ASB initiation. For example, in the context of edge-impact of notched plate experiments Kalthoff (1990), Ravi-Chandar (1995), Zhou et al. (1996), Ravi-Chandar et al. (2000) , it was reported that a locally mode-I crack initiated for impact velocities below a critical impact velocity and an ASB initiated above a critical impact velocity. However, as reported by Guduru, Rosakis, et al. (2001), Guduru (2001) , a careful post-experiment microscopic investigation of the specimens

that failed in mode-I showed the presence of a small initiated and arrested ASB at the notch tip (the total length of the ASB was of the order of less than a mm). Further, the local mode-I crack that propagated at an oblique angle initiated from the notch tip, not from the arrested ASB tip. In other words, even at velocities below the so-called critical velocity, an ASB initiated at the notch tip, propagated and got arrested, before the reflected waves from the specimen boundary modified the notch tip stress field to force a crack to initiate in a different mode. The lack of micron-scale spatial resolution in imaging meant that the correct sequence of events was not captured experimentally and consequently escaped modeling efforts as well. These observations provide a motivation to resolve the local strain fields near a notch tip during initiation of an ASB.

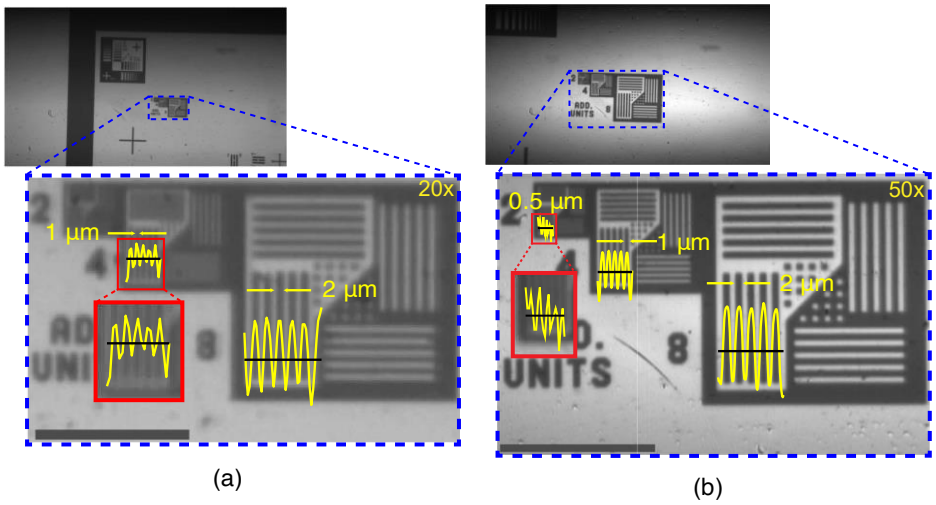

Figure 7.3 Demonstration of imaging resolution using a resolution target with groups of 2 µm, 1 µm and 0.5 µm wide lines. The images are taken using a (a) 20X, and (b) 50X objective. For each magnification, a full resolution image is shown on the left while the region of interest is outlined in a dashed blue line and a magnified view shown right below the full image. The yellow curves are variations in intensity across a group of lines. As shown in Table 7.2, the 20X objective has a calculated resolution of 1 µm, which is demonstrated by its ability to resolve the 1 µm and 2 µm wide lines. The 50X objective system has a calculated resolution of 0.58 µm, which is demonstrated by its ability to resolve the 0.5 µm wide lines. Note that the images have been cropped to show the area of interest and do not represent the entire field of view. The length of the scale bar is 50 µm in both images.

For the purposes of this study, the well-studied edge-notched plate configuration has been employed, which was impact loaded in a Kolsky bar. Polycarbonate has been chosen as the specimen material, partly motivated by a prior investigation of similar nature by Ravi-Chandar (1995) . However, a significant difference is that the specimen dimensions are much smaller than those used by Ravi-Chandar (1995) and the impactor diameter is only 6.35mm. As a result, the state of stress near the notch tip during the experimental observation is expected to be more complex than what was observed by Ravi-Chandar (1995) . However, this shortcoming was deemed to be an acceptable compromise for the purposes of demonstrating the experimental capability, while deferring a more complete study of ASB initiation on larger sized specimens to a subsequent investigation. The experiments reported here are conducted with the 20X objective.

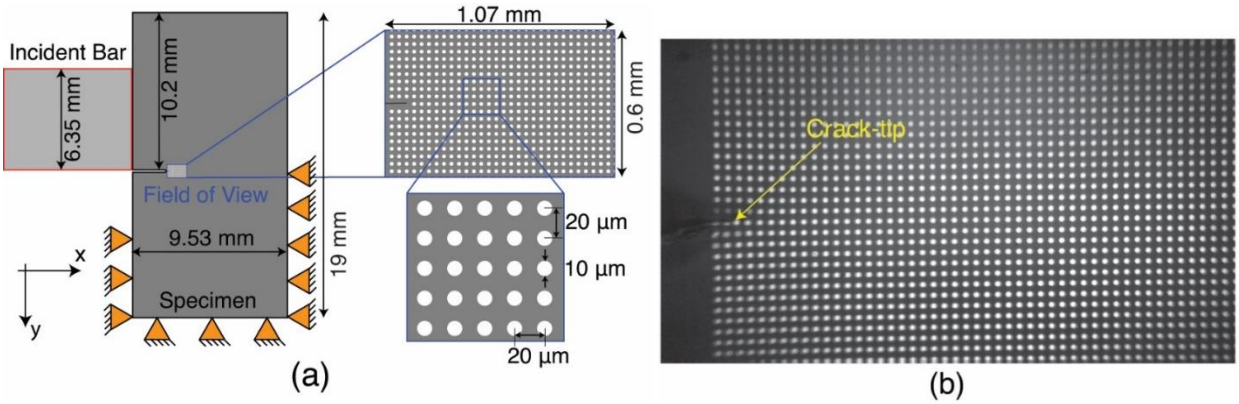

Figure 7.4 (a) Edge-on impact on the polycarbonate specimen. The specimen is fixed on the bottom half at the back to prevent rigid translation. Fixing on the bottom face and bottom half of the front face impedes rigid rotation. Lateral confinement (not shown here) is provided on both sides of the specimen plate to minimize out of plane motion. The field of view with a 20X objective is shown. 10 μmsized Cu dots, spaced 20 μm apart are used for particle tracking. (b) High-speed camera image of the specimen before the arrival of longitudinal compressive wave at the crack tip

Specimens are cut from a Lexan 9034 polycarbonate sheet and have the following dimensions: 19 mm x 9.53 mm x 1.5 mm (Figure 7.4 (a)). A pre-crack is made in the polycarbonate sample at the tip of the machined notch using a sharp razor. The specimen is constrained in a steel fixture to enforce the boundary conditions shown in Figure 7.4. An edge-on impact is carried out on the specimen using the incident bar of the Kolsky bar system. The incident bar is 6.3 mm in diameter, 61 cm in length and is made of C350 maraging steel. A striker of the same diameter and material, and a length of 15.24 cm, sends a 50 μs compressive pulse through the incident bar. The deformation field can be measured through DIC or particle tracking. For this first investigation, particle tracking has been chosen. A grid of 10 μm sized circular copper dots, with a pitch of 20 μm in both directions, was deposited on the specimen at the notch tip (Figure 7.4).

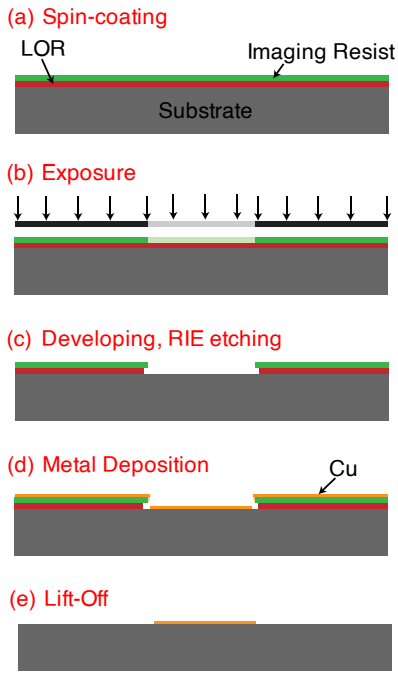

Figure 7.5 Steps for photolithography process, used to deposit Cu dots for particle tracking

The dots are deposited around the pre-crack tip using a lift-off photolithography process, as illustrated in Figure 7.5. The polycarbonate sample is cleaned with isopropanol using sonication, especially to get rid of the debris that accumulates around the notch tip after a pre-crack is made with a razor. Plasma ashing via Reactive-Ion Etching (RIE) is used to further clean the sample. The sample is spin-coated with LOR-5A photoresist followed by a hard-bake at 100 ^{0}C in an oven. Another photoresist, AZ1505A, is spin-coated on top of the previous layer and soft-baked at 95 ^{0}C. Since the glass transition temperature (T_g) of polycarbonate is very low (147 ^{0}C), baking temperatures are kept far from T_g to avoid any softening and specimen distortion. As a result, baking times have to be increased as compared to the standard baking times for silicon wafers. These temperatures and times are calibrated to yield best results. A maskless aligner, MLA150 from Heidelberg Instruments, is used to selectively expose the photoresists at a calibrated exposure intensity of 150 mJ/cm^2. The use of a maskless aligner allows flexibility to make any dot pattern on the specimen down to a size of 1 μm and avoid costs associated with making masks. The photoresist is developed using CD-26 (9 parts CD-26 and 1-part DI water) for 60 seconds, followed by a DI water rinse. An O_2 plasma de-scumming process is performed before the metal deposition process. A 200 nm thin layer of Cu is deposited using an e-beam evaporator (Kurt J.Lesker). For the final lift-off step, methanol is used in a sonicator. Since the samples are small, it is possible to do the entire process in batches.

The copper dots form a reflective foreground against the transparent polycarbonate background, providing good contrast. Even though particle tracking is used here, DIC can also be employed. DIC requires a speckle size of 3-5 pixels, that is 1.7-2.8 μm speckles with a 20x

microscope objective. Features of these sizes can be easily achieved with photolithography with a fine control over speckle size, shape and distribution for optimal image correlation.

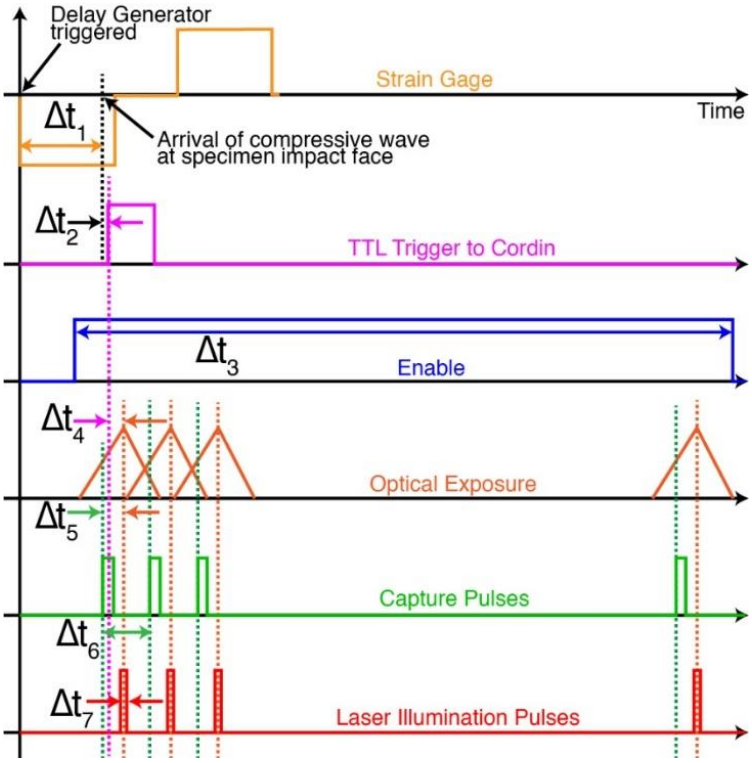

Figure 7.6 A typical timing diagram at a frame rate of 4 million fps. The incident wave is taken to arrive at the strain gage at t=0.At this instant, the strain gage triggers the Delay Generator. At t = Δt_1 ($\approx 60\ \mu s$), the compressive incident wave arrives at the specimen impact face. A 5V TTL trigger is then sent to the camera at t = $\Delta t_1 + \Delta t_2$ where Δt_2 accounts for the time delay between impact at specimen interface and the time when compressive wave first reaches the notch-tip. An Enable signal with a pulse-width of Δt_3 is sent to the Laser Pulse Driver (a unit that controls synchronization of laser illumination pulses with input pulses from the camera) before the camera is triggered. There is a time gap of Δt_4 between the TTL trigger to the camera and the alignment of the rotating mirror with the first CCD after the trigger signal is received. Due to the mirror rotation, optical exposure of each CCD is not uniform during one inter-frame time-period, which is depicted using triangular pulses. The optimal location of exposure lies at the peak of these pulses, whereby the rotating mirror is said to be aligned to the CCD. Illumination pulses need to be centered at these peaks. This is achieved by sending capture pulses from the camera to the Laser Pulse Driver in advance by a time duration of Δt_5. $\Delta t_5 = 0.185\ \mu s$ is found to work well. Δt_6 indicates the inter-frame time (=250 ns at 4 million fps). An illumination pulse width, $\Delta t_7 = 20\ ns$ is used in these experiments but this width can be brought down to 5 ns

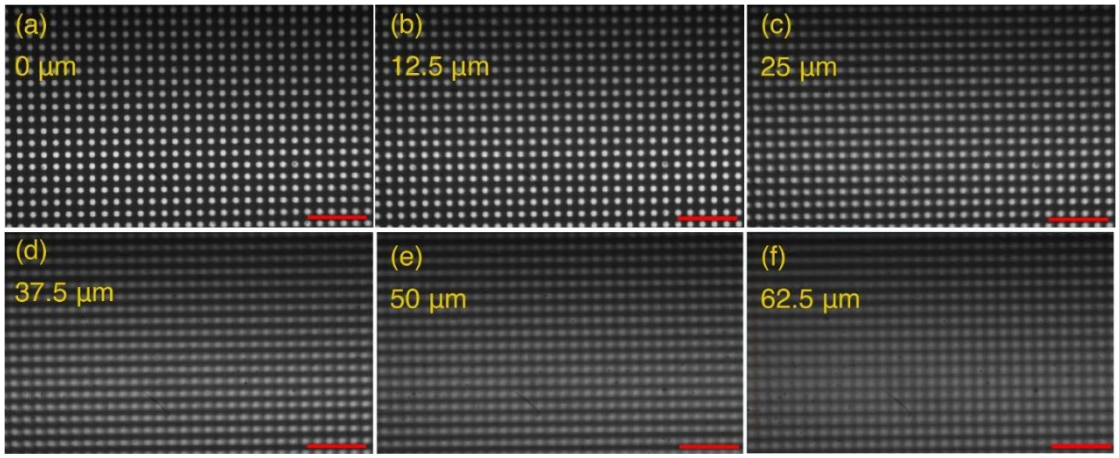

Figure 7.7 "Practical" depth of field measurements for the optics with the 20X objective using a grid pattern of circular dots. The dots are 10 µm in diameter and spaced 20 µm apart. A sample with these dots is mounted on a translation stage and moved towards the objective, starting from the focused position in (a). In (b)-(f), the sample is moved in increments of 12.5 µm to a final position of 62.5 µm away from the focused position. At this point, the image becomes blurry and the neighboring dots begin to coalesce with each other. Note that the entire field of view is not shown. A scale bar of 100 µm length is shown in red at the bottom corner of each image

7.4 Experimental Procedure

The high-speed microscopy system is set-up in conjunction with the Kolsky bar, as shown in Figure 7.2. Experimental preparation consists of aligning the impact face of the specimen with the middle of incident bar cross-section, followed by focusing the camera on the area of interest on the specimen surface. Strain gage signal from the incident bar is used to trigger the camera. An important element of the experimental procedure is to ensure that the illumination pulses are synchronized with the optimal mirror positions with respect to the CCD sensors by accounting for signal delays at many interfaces in the system. The corresponding signal timing diagram is shown in Figure 7.6. The signal from the strain gage amplifier is fed into a delay generator, which delays the signal by a known amount before sending an image acquisition trigger to the camera.

The camera sends out a sequence of capture pulses that correspond to alignment of the rotating mirror position with the CCD sensors. In practice, the capture pulses are advanced with respect to the optimal alignment by a predetermined time (Δt_5 in Figure 7.6). The capture pulses are then used to trigger a sequence of laser pulses to coincide with the optimal alignment of the mirror positions with CCD sensors.

As alluded to earlier, depth of field is an important consideration in any microscopy application, particularly in high-speed microscopy where out-of-plane movement of the specimen surface is unavoidable due to the deformation itself (i.e. the Poisson's ratio effect). In the strict sense of microscopy, the depth of field of a microscope is determined by the numerical aperture of the objective, illumination wavelength and the sensor pixel pitch Kenneth R. Spring . For the setup with the 20X objective, the depth of field can be calculated to be approximately 6 μm. This small depth of field places severe restrictions on the maximum allowed specimen thickness. It also requires that the specimen be constrained against for rigid translations in the out-of-plane direction. However, the present experimental situation is more forgiving since the need is to image the 10 μm dots instead of features at the resolution limit of ~1 μm. From Figure 7.7, it can be seen that at an out-of-plane displacement of 25 μm does not result in a significant loss in definition of the dots. At a displacement of 62.5 μm, some of the neighboring dots begin to coalesce with each other, although individual dots can still be distinguished. Consequently, 62.5 μm can be treated as the "practical" depth of field for the purposes of imaging the 10 μm dot pattern.

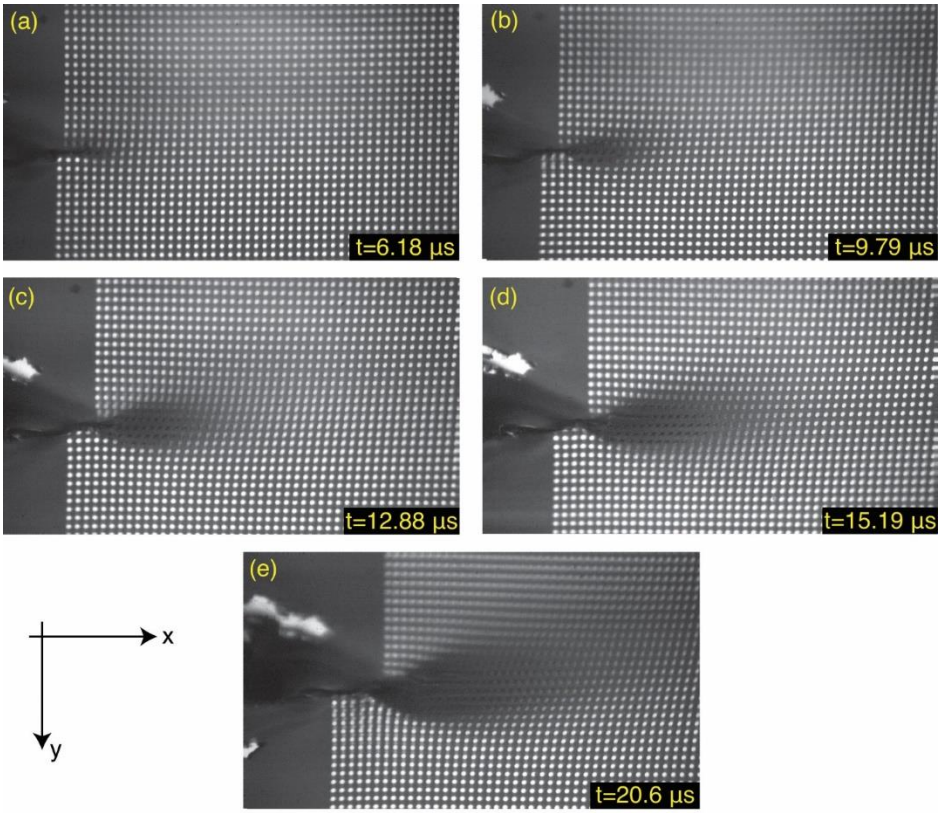

Figure 7.8 Acquired images of the notched polycarbonate plate at different times: (a) t=6.18 μs, (b) t=9.79 μs, (c) t=12.88 μs, (d) t=15.19 μs, and (e) t=20.6 μs. The images were taken at a framing rate of 3,883,495 fps. As the deformation progresses, a zone of localized plastic deformation forms ahead of the crack tip. Particle tracking is performed until t=15.19 μs. By t=20.6 μs, the top half of the specimen has moved ahead of the lower half by $\approx 120\,\mu m$, indicating the development of a large shear strain

7.5 Results and Discussion

Figure 7.8 shows a sequence of images of the dot pattern when the striker impact speed is 17.4 m/s. The images were acquired at a rate of 4 million frames/s. The sequence shows only a selected set of images, during the evolution of deformation from arrival of the loading wave and through subsequent initiation of ASB at the notch tip. A video of the event generated by collating the individual images is included in the supplemental material. Even without quantitative analysis, one can visualize the strain field evolution from the change in the slope of the lines connecting the

dots along vertical and diagonal directions in the undeformed configuration. The out of plane motion of the specimen within the notch tip plastic zone is evident through the appearance of dark regions and also through loss of focus of the dot pattern. The former can be improved by making the dots to be diffuse reflectors. The latter, which is due to the limited depth of field discussed above, can be tolerated in the present situation because it is still possible to identify the centroid of the dot through image processing.

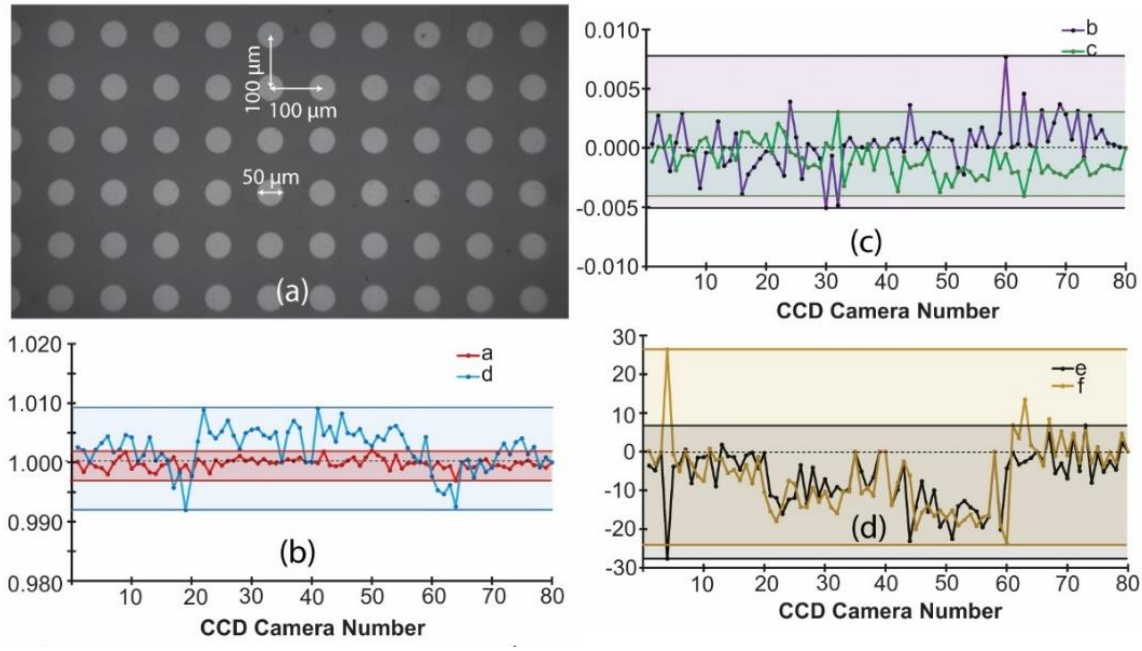

Figure 7.9 (a) Grid Pattern of circular dots used for CCD misalignment calibration. Constants for transformation matrix are shown in (b), (c) and (d). (d) shows translations in pixel coordinates

The first step in extracting the displacement and strain field from the images is to correct for slight differences in the fields of view of successive images. As noted above, the Cordin camera consists of 78 different CCD sensors. Since light is relayed through a different optical path for the formation of each image, slight differences in the extent and orientation between successive images

are expected. For more details, see Kirugulige et al. (2007) . Since the particle tracking algorithm used here is sensitive to such misalignments, it is necessary to correct the images to set the same global coordinate axes on all images. The procedure followed here is similar to that employed by Kirugulige et al. (2007) . A camera calibration is performed by imaging a static sample with a grid pattern of 50 μm circular dots, spaced 100 μm apart (see Figure 7.9 (a)). All images are thresholded and binarized, followed by locating the centroids of the dots. One of the 78 CCD images is chosen as a reference and centroid locations in the rest of the frames are tracked with respect to this reference image. It is assumed that the optical distortion of the images can be modeled as a homogeneous deformation. Therefore, the coordinates in these images can be related to the coordinates in the reference image through a transformation of the form

$$\begin{pmatrix} x_i \\ y_i \end{pmatrix} = \begin{bmatrix} a & b \\ c & d \end{bmatrix} \begin{pmatrix} x_0 \\ y_0 \end{pmatrix} + \begin{pmatrix} e \\ f \end{pmatrix} \tag{7.3}$$

where (x_i, y_i) are coordinates of deformed images, (x_0, y_0) are coordinates of the reference image, the matrix with (a, b, c, d) constants corresponds to the assumed homogeneous deformation gradient, and the vector (e, f) corresponds to in-plane rigid translation. The unknown constants are determined using least-squares minimization. A set of these unknowns is shown in Figure 7.9 (b), (c) and (d). It can be seen that the diagonal components (a, d) of the deformation gradient differ from 1 by less than 1% and the off-diagonal components (b, c), which represent the shearing deformation, are less than 0.5% for the most part. However, the rigid translations e and f are significant. Hence, a set of static images is obtained just prior to each dynamic experiment, which is used to determine the correction constants for each experiment. All experimental parameters such as the frame rate, illumination settings and delays are kept identical between the static

imaging and the actual dynamic experiment that follows immediately. The correction constants are used to perform an inverse transform in order to align each image with the reference image.

7.6 Particle Tracking

Particle tracking has been used in this study to calculate the displacement field. This tracking involves 2 steps: (a) identifying positions of particles in each image, and (b) tracking trajectories of individual particles across all frames to deduce displacements. The first step can be carried out with a pixel-scale accuracy using Gaussian fitting Cheezum et al. (2001), Abraham et al. (2009), Small and Stahlheber (2014) or radial symmetry methods Parthasarathy (2012), Liu et al. (2013) . Particles can then be tracked using nearest neighbor search, relaxation methods Baek and Lee (1996), Ohmi and Li (2000), Pereira et al. (2006) , feature vector-based methods Feng et al. (2014) and topology-based methods Patel et al. (2018) among several others. In general, average inter-particle distance is an important parameter in single particle tracking methods. It is not possible to resolve sinusoidal displacements with a period smaller than inter-particle distance according to the Nyquist criterion. Therefore, to resolve high spatial frequency content, smaller inter-particle distance and hence higher particle density are favorable. However, with smaller inter-particle distance, it becomes difficult to resolve large displacements accurately due to ambiguity in assigning new positions to identical particles. An inter-particle distance of 20 μm, which was found to be satisfactory was used here.

For the first step of locating the particles, all images are thresholded and binarized to extract regions corresponding to each particle/dot. The centroid of each particle is chosen as the

representative of its location. Due to intensity gradients across the image, a small subset of the particles cannot be thresholded in a few images. A GUI is written in MATLAB 2019a (The MathWorks Inc., Natick MA) to interactively allow for manual addition of approximate centroid locations for these particles. More accurate centroid estimates are subsequently refined by Gaussian fitting. For the second step of particle tracking, an iterative tracking scheme is adopted, i.e. the image $I_{t+\Delta t}$ is correlated to image I_t . A reference particle is chosen in all images. $I_{t+\Delta t}$ is translated and overlaid on top of I_t so that the location of reference particles in the two images matches exactly. A nearest neighbor algorithm is then used to match particles. Since the displacement between consecutive frames is substantially less than the inter-particle distance, this simple scheme works well.

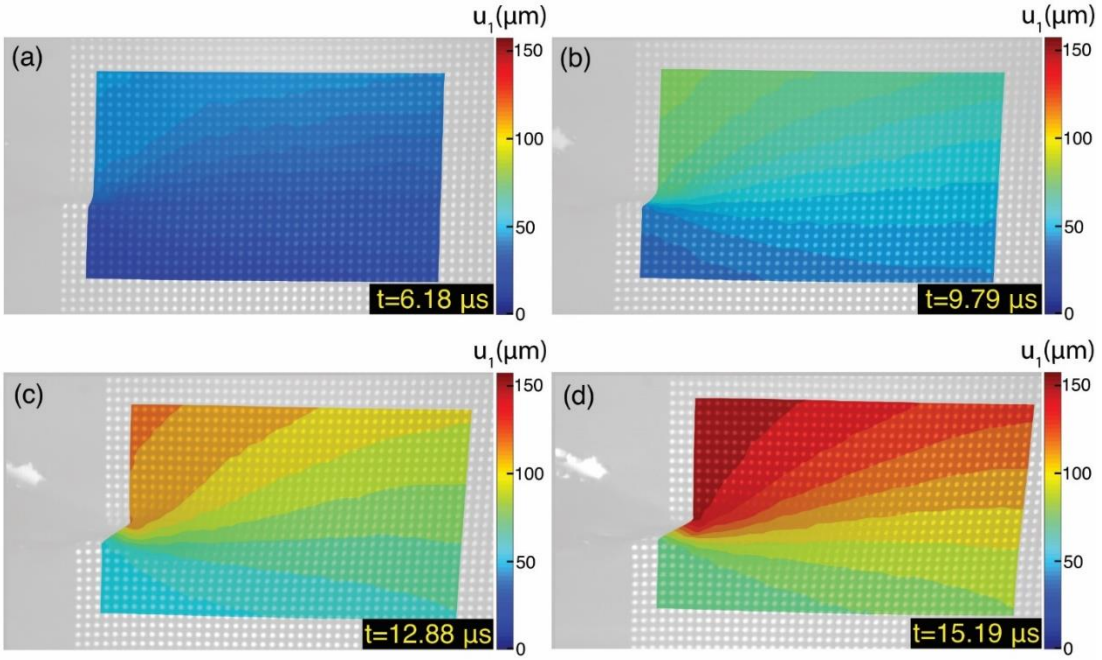

Figure 7.10 Displacement, u_1 plotted at (a) t=6.18 μs, (b) t=9.79 μs, (c) t=12.88 μs and (d) t=15.19 μs

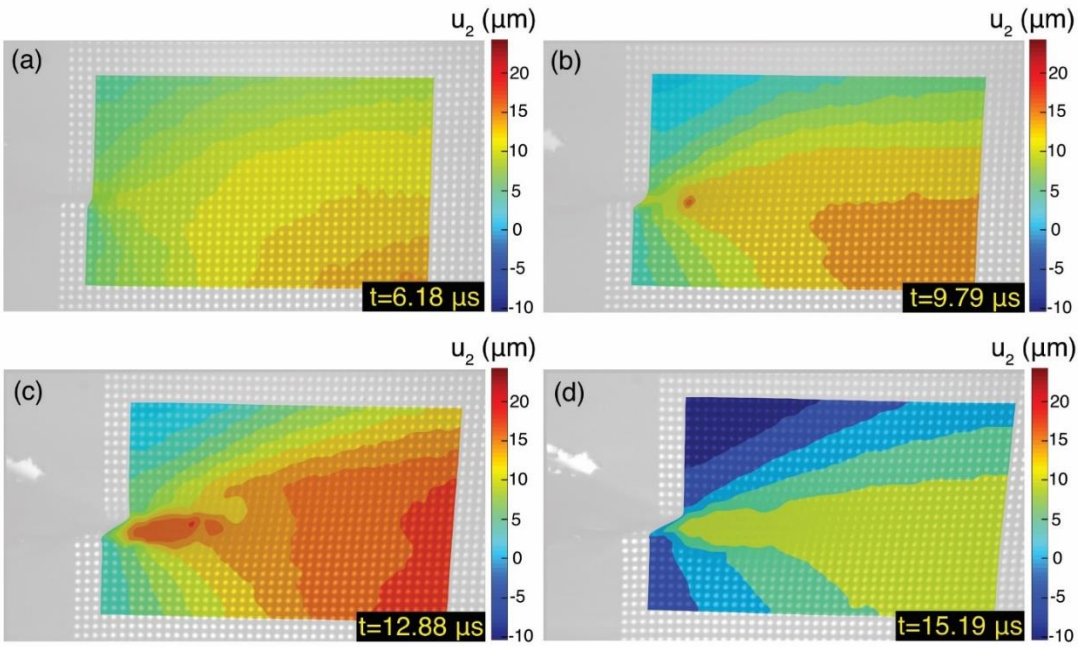

Figure 7.11 Displacementu_2 plotted at (a) t=6.18 μs, (b) t=9.79 μs, (c) t=12.88 μs and (d) t=15.19 μs

7.7 Deformation Fields

Displacements of particle centroids are determined by tracking their locations. These displacements are interpolated using a cubic, $\mathbb{C}^2$ continuous, triangulation-based polynomial. Data points are obtained every 7 pixels (3.89 μm) from the interpolated polynomial. To be able to reliably calculate gradients from the noisy displacement data, a non-local means (NLM) filter Immerkaer (1996), Fuente and Rodríguez (2003), Buades et al. (2005) is used for de-noising and smoothing the displacement fields. The NLM filter preserves sharp displacement gradients expected in and around the shear band region. The usual 'local' means filters smoothen a discrete field by taking the mean value of a group of neighboring values. This results in a lower noise level but at the cost of smoothing out sharp features. A 'non-local' means filter, on the other hand, calculates a weighted mean of field values within a search window Ω around the target location.

The weights are chosen based on the similarity of $N \times N$ neighborhoods within Ω, to the $N \times N$ neighborhood of the target location. An exponentially decreasing function is typically used to assign weights, with the weight value decreasing with a decreasing degree of similarity. The degree of smoothing is controlled using a parameter h_s that controls the rate of decay of the weighting function. In this study, the NLM filter is applied to interpolated displacement fields. Here, parameters used in filtering are: search window size Ω=7x7, data points (=81.6x81.6 μm^2), neighborhood size N=7 data points (=27.2 μm), degree of smoothing $h_s = 0.5$. The effect of NLM parameters on deformation fields is explored in detail in Appendix A and Appendix B.

The extracted u_1 and u_2 displacement fields are shown in Figure 7.10 and Figure 7.11 respectively, at four different instants of time. Note that all the deformation fields for this experiment are evaluated from t=1.55 µs to t=15.19 µs. The compressive wave first reaches the left edge of the field of view at 1.55 µs, i.e. the high-speed camera is triggered slightly in advance of the event of interest. Even though the images are recorded until t=20.6 µs, displacement field is calculated until 15.19 µs; for later times, the out of plane motion of the sample causes significant blurring of dots leading to difficulty in particle tracking, especially close to the crack-tip. It can be seen in Figs. 9and 10 that there is a pronounced concentration of displacement contours at the crack-tip which suggests large displacement gradients there, as expected. Note that u_1 displacements are significantly larger than the u_2 displacements, characteristic of the predominantly mode II loading of the notch tip. At the same time, the small specimen dimensions result in boundary wave reflections, resulting in some crack opening displacement also during the observation time window.

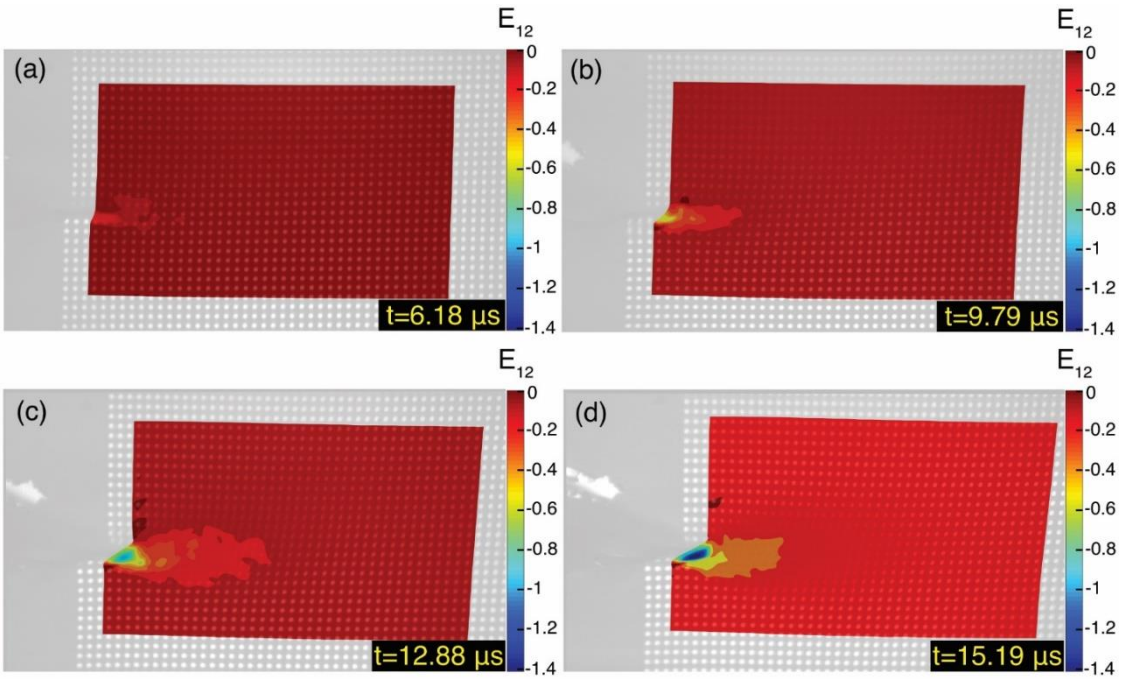

Figure 7.12 Lagrangian shear strain, E_{12} plotted at (a) t=6.18 μs, (b) t=9.79 μs, (c) t=12.88 μs and (d) t=15.19 μs

Strains are expressed in the form of a Green-Lagrange strain tensor, $\boldsymbol{E}$, which is computed from the deformation gradient $\boldsymbol{F}$ as follows:

$$\boldsymbol{F} = \boldsymbol{I} + \nabla \boldsymbol{u} \tag{7.4}$$

$$\boldsymbol{E} = \frac{1}{2}[\boldsymbol{F}^T \boldsymbol{F} - \boldsymbol{I}] \tag{7.5}$$

where $\boldsymbol{u}$ is the displacement field and $\boldsymbol{I}$ is identity tensor. Displacement gradients are found by means of a finite-difference scheme. At the boundaries, forward or backward finite difference-schemes are employed. At interior locations, a central finite-difference scheme is used. For example, the derivatives of u_1 along the x-direction are given as:

$$\frac{\partial u_1}{\partial x}(i,j,k) = \frac{u_1(i+1,j,k) - u_1(i,j,k)}{h_x} \tag{7.6}$$

$$\frac{\partial u_1}{\partial x}(i,j,k) = \frac{u_1(i,j,k) - u_1(i-1,j,k)}{h_x} \tag{7.7}$$

$$\frac{\partial u_1}{\partial x}(i,j,k) = \frac{u_1(i+1,j,k) - u_1(i-1,j,k)}{2h_x} \tag{7.8}$$

where equations (7.6), (7.7) and (7.8) show forward, backward and central difference implementations respectively. The shear strain E_{12} is the most relevant quantity for studying shear localization; its evolution is plotted in Figure 7.12. As the notch tip gets loaded by the stress waves from the impact face, a plastic zone develops at the notch tip. When the loading rate is sufficiently high, the plastic zone transitions into an ASB. A precise criterion for predicting when the transition occurs in terms of local strain and strain rate parameters is very valuable. However, it is first necessary to identify when the instability begins. A complete characterization requires knowledge of the stress field information, which cannot be obtained directly from the kinematic fields being measured here. If the high strain rate constitutive response of the material is known, the stress field can be calculated from the measured strain field, which will be presented in a future publication. Here, the presentation is limited to examining the features of the displacement field that can indicate the potential onset of the instability. At t = 6.18 μs, it can be seen that concentration of shear strain near the notch tip has already begun (Figure 7.12 (a)). The zone of intense plastic deformation evolves with time, leading to accumulation of shear strains as large as 1.4 by t = 15.19 μs.

In order to gain further insight into evolution of shear strain and possible localization near the notch tip, it is instructive to examine the deformation of dots along referential vertical lines (referred to as columns in the discussion below) at different distances from the notch tip, as illustrated in Figure 7.13 and Figure 7.14. Deformation of columns closer to the initial crack tip,

i.e. columns 4 and 5 and a column farther away from the crack tip, i.e. column 13 are plotted, to encompass the region of large shear strain. Figure 7.14 shows u_1 and E_{12} as a function of position along the vertical coordinate (y) for these columns and their evolution with time. Each line corresponds to a different time, which is color coded as shown. Strictly, the experimental data gives the values at discrete points only. However, in Figure 7.14, a smoothed curve is fit along the discrete values using a method that employs local regression with weighted linear least squares and a 2nd degree polynomial model. Points that fall outside 6 standard deviations are assigned zero weights. The extent of smoothing is controlled by a fraction f that indicates the fraction of the total number of points used for smoothing. f=0.8 is used for both u_1 and E_{12}. It is verified that this operation does not smooth out the evolution of localized band near the crack tip. Note that the smoothing is applied on top of the non-local means filter used to extract the displacement fields. However, the smoothing is applied for each point in the temporal sense, i.e. the displacement fields at each location are smoothened over time to minimize the noise in Figure 7.14. This smoothing does not affect the displacement and strain fields but is required to extract strain rates in the localized region with excessive deformation.

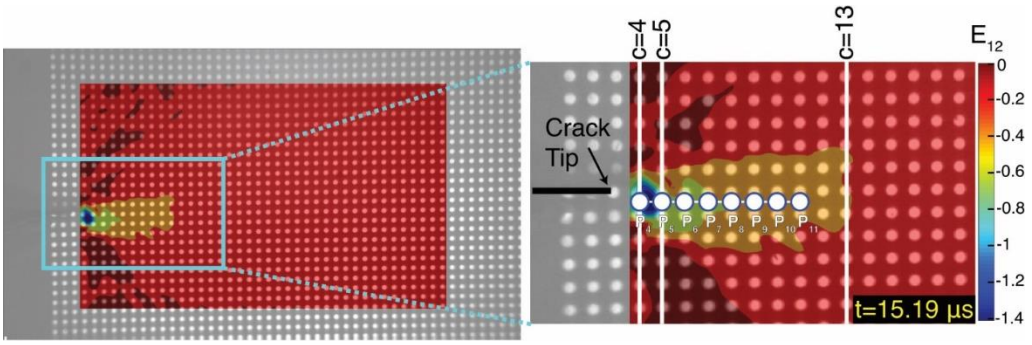

Figure 7.13 Left: shear Strain, E_{12} field at t=15.19 μs plotted on the reference undeformed image. Right: a zoomed in figure showing query locations for displacements, strains and strain rates. Deformation along columns c=4, c=5 and c=13 (vertical white lines) has been analyzed as a function of time. A straight line just ahead of the crack tip is probed for strains and strain rates, at 8 points (white circles with blue outline) labeled P_4 to P_{11} . Location of this straight line is just below the initial crack plane and corresponds, approximately, to the region of maximum shear strain. P_4 to P_{11} lie on columns of Cu dots from c=4 to c=11

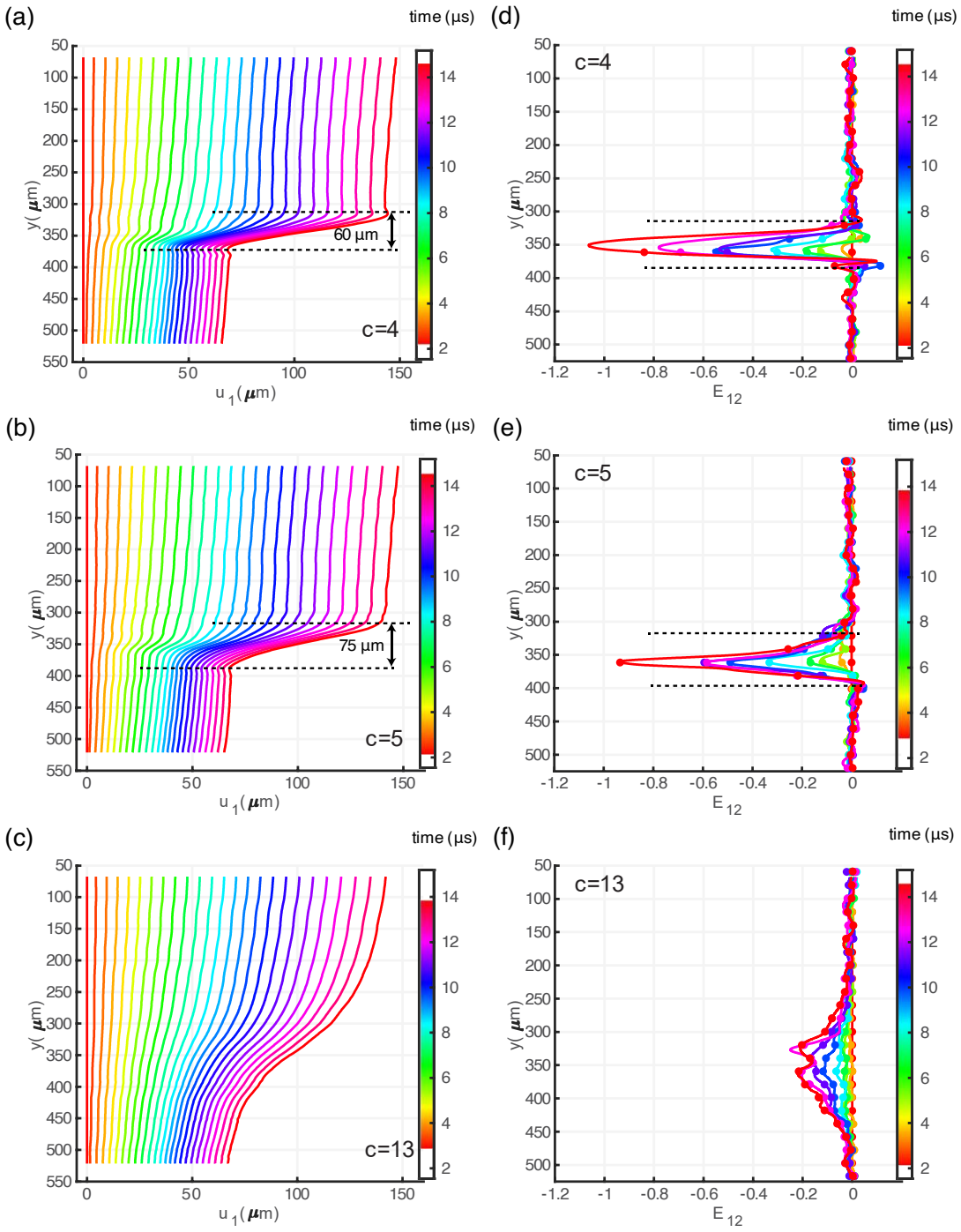

Figure 7.14 (a), (b), (c): x-displacement, u_1, profiles of columns 4, 5 and 13 respectively, from t=1.55 μs to t=15.19 μs. (d), (e), (f): Lagrangian shear strain, E_{12}, profiles of columns 4, 5 and 13 respectively, from t=1.55 μs to t=15.19 μs. The dots on shear strain profiles indicate the values measured at particle centroids. Note that the shear strain profiles are not drawn at all time instants captured, to allow for clarity in the figures. A localized region of plastic deformation is shown for columns 4 and 5 in (a), (b), (d) and (e) using dotted lines

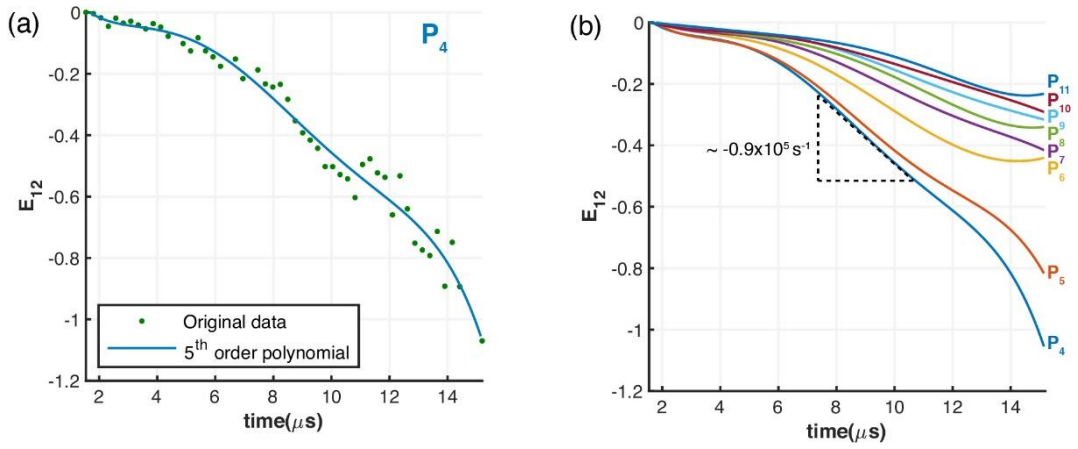

Figure 7.15 (a) E_{12} vs time at point P_4. A 5th order polynomial (blue line) is fit to the noisy data (green dots). (b) E_{12} polynomial fit curves for points P_4 to P_{11}. A distinct transition in the slopes for P_4 and P_5 is observed around 6 μs. A strain rate of $\sim -0.9 \times 10^5\ s^{-1}$ is observed for P_4 during $\sim 7-10\ \mu s$

From Figure 7.14 (a), it can be clearly seen that as time evolves, the x-displacement of the 4th column of dots (c=4) is localized in a band-like region of approximately 60 µm in width, as corroborated by the strain field shown in Figure 7.14 (d). The strain field also shows that the localized zone of intense plastic shear strain increases in width with time before the width reaches a plateau. A similar localization is observed in the adjacent column (c=5) (Figure 7.14 (b) and (e)), however with a slightly different localized bandwidth of ~75 µm and smaller peak shear strain. The width is found to increase slowly as one moves away from the notch tip until a diffused plastic zone is reached as in c = 13 (Figure 7.14 (c) and (f)). It is important to note that the accuracy of the strain values reported here is bound by the resolution limit posed by the discreteness of the measurement points (i.e., the dots). Further improvements in the resolution can be achieved by decreasing the dot diameter and the pitch.

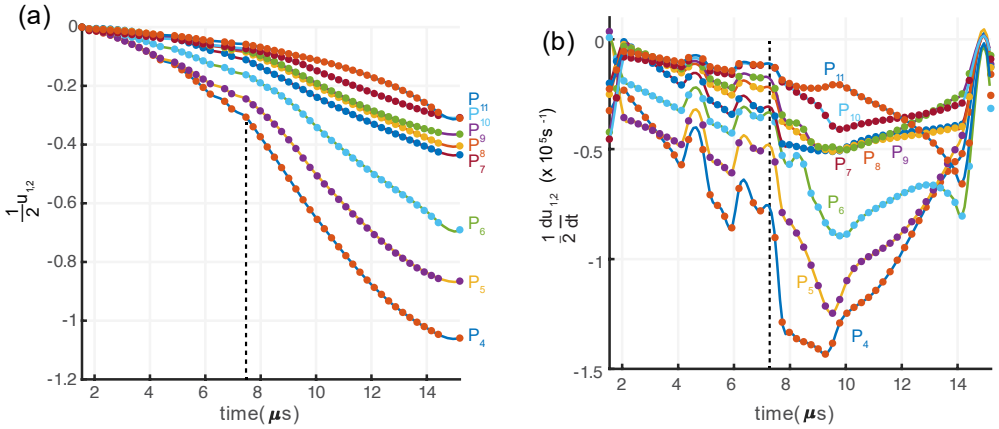

Figure 7.16 (a) $\frac{1}{2}u_{1,2}$ for points P_4 to P_{11} as a function of time. (b) $\frac{1}{2}\frac{\partial u_{1,2}}{\partial t}(\times 10^5\ s^{-1})$ for points P_4 to P_{11} as a function of time. A distinct change in strain rate is observed in both (a) and (b) at $\sim 7.25\ \mu s$, as shown by the vertical dotted line

Rate of shear strain is determined at several discrete points ahead of the crack tip, P_4 – P_{11} as shown in Figure 7.15 by first plotting E_{12} vs. time at each location. The data is noisy, particularly near the notch tip, due to errors in locating the centroids of the dots because of severe deformation as well as loss of image focus. A polynomial function is used to fit the data, which is differentiated to get the strain rate. As expected, it can be seen that points away from the crack-tip experience smaller strain-rates compared to points near the crack-tip. For P_4, there is a sharp increase in the rate of shear strain at ~6 μs, beyond which a shear strain rate as high as $0.9\text{x}10^5\ s^{-1}$ is observed. The transition can be seen better by plotting the shear strain rate. Since u_1 and $u_{1,2}$ are the dominant displacement and displacement gradients, the latter is plotted in Figure 7.16 (a). It can be seen in Figure 7.16 (a) that at around t = 7.25 μs, there is a sharp increase in the rate of change of $u_{1,2}$, which is seen more clearly in Figure 7.16 (b), which shows the evolution of the time-derivative of $u_{1,2}$ (The time-derivatives is found using a combination of forward, central and backward finite-difference schemes as described in Eq. 6-8).

The sharp increase in $\dot{u}_{1,2}$ beyond 7.25 μs is a possible kinematic signature of the onset of localization near the crack tip. Further, note that the transition to higher strain rates in Figure 7.16 (b) at points farther away from the crack tip are progressively delayed, indicating the propagation of localization. Since all measurements reported here are kinematic in nature, the discussion is limited to kinematic signatures of the onset of the localization/instability. More definitive conclusions will have to await the calculation of the stress field and the shear traction on the crack plane from the measured kinematic fields. In Figure 7.16 (b), small bumps in strain rates are observed to begin at 4 and 6 μs, which correspond to the arrival of release waves from the specimen boundaries. An unloading wave from the rear surface of the specimen eventually unloads the specimen at ~9.5 μs.

7.8 Summary and Conclusions

An experimental technique capable of capturing dynamic failure events at high spatial and temporal resolutions simultaneously has been reported. The setup can capture images at rates of up to 4 million fps with a sub-micron spatial resolution. A commercial high-speed camera (Cordin 560) is coupled with custom built optics and a high-power pulsed laser. The technique is demonstrated by imaging the deformation field near a crack tip subjected to dynamic loading to initiate an adiabatic shear band. Pre-notched polycarbonate plates are impacted on the edge in a Kolsky-bar while measuring the evolution of displacement field through an array of copper micro-dot pattern deposited on the specimen surface. Displacement and strain fields indicate localization of deformation in a 60-75 μm wide band near the crack-tip. A sharp increase in the shear strain rate appears to be a signature of the onset of localization. More broadly, it is

anticipated the technique reported here can help understand the role of micro-scale material heterogeneities in the mechanisms of fracture and failure during high strain rate loading of materials and structures.

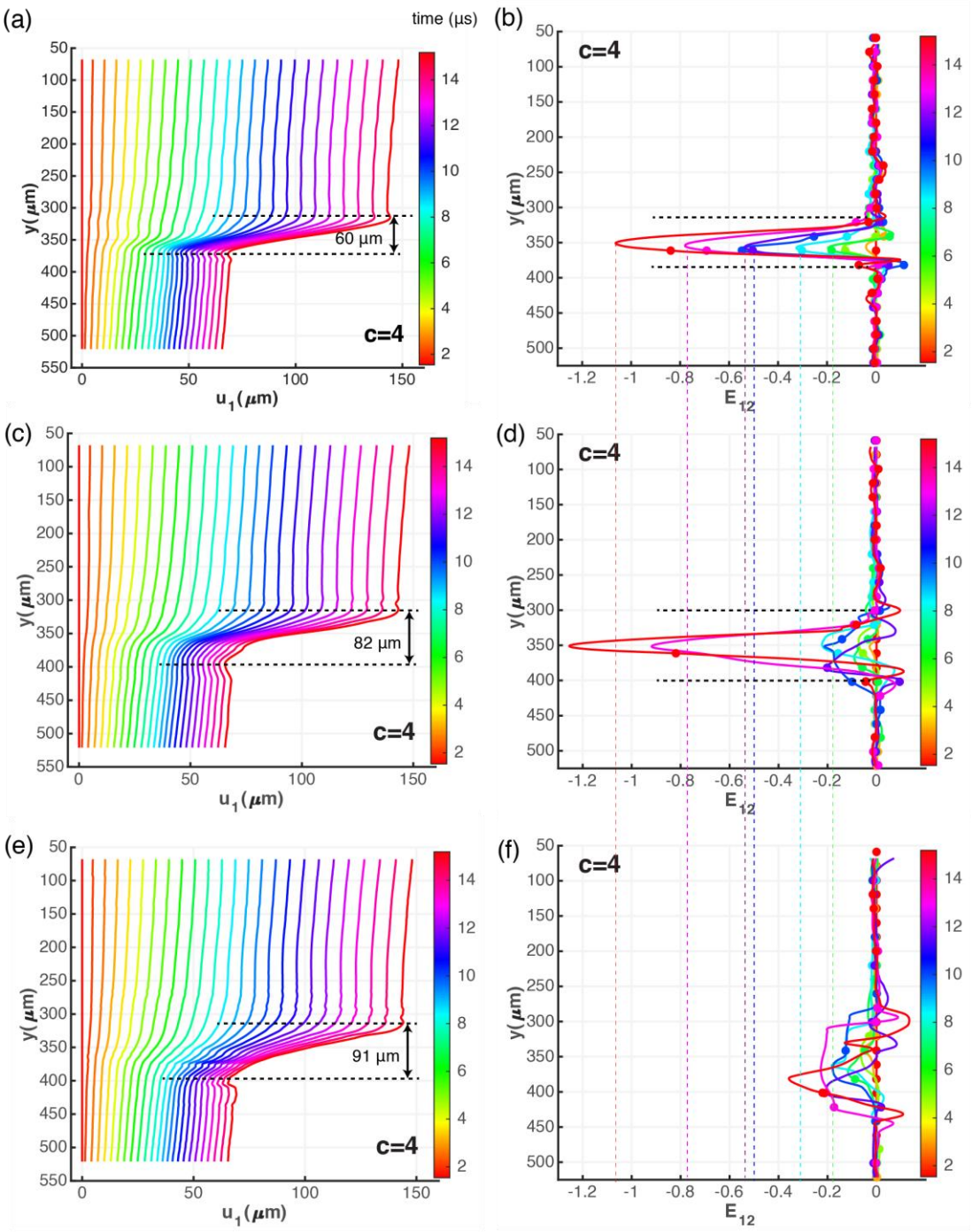

Figure 7.17 Displacement and shear strain profiles of column c=4 at different spatial resolutions. (a), (b): original resolution; (c), (d): half of original resolution; (e), (f): quarter of original resolution.

7.9 Appendix A: Effect of NLM filter

In this section, the effect of NLM filter on displacement and strain fields is explored. Following experimental observations, a shear band of width, $w_b = 60\,\mu m$ is considered. A schematic of deformation is shown in Figure 7.18. A square block of $a \times a\,\mu m^2$ is subjected to shear stress, τ. A shear band is assumed to form with the following displacement profile in the y-direction:

$$u_1 = \Delta u_1 \frac{\tanh\left(\frac{y - y_c}{a}\right) + 1}{2} \tag{1}$$

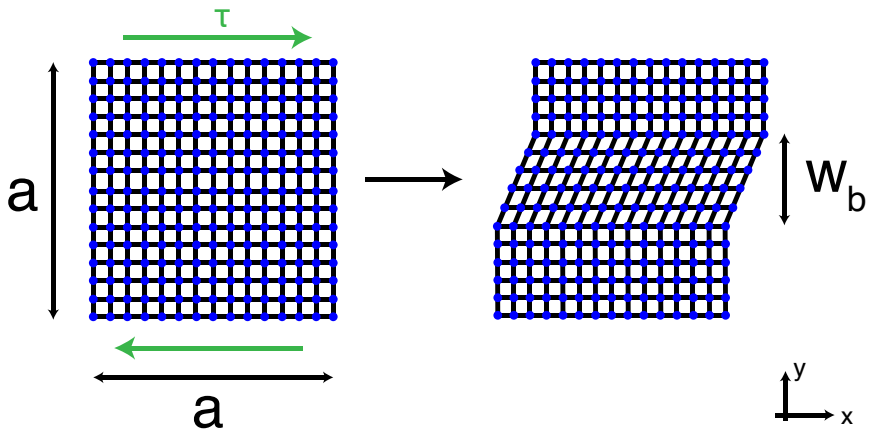

Figure 7.18 A box of $a \times a\,\mu m^2$ subject to shear, leading to the formation of a shear band of width $w_b\,\mu m$. Note that the number of grid data points shown here are just a representation, the actual numbers are different.

where y_c is the y-coordinate for the center of the shear band and a is a parameter chosen to agree with maximum shear strain observed in experiments. Δu_1 represents the displacement difference across the shear band. Note that data is available only at discrete points, as shown by blue dots in Figure 7.18. Since the interpolated displacements are sampled every 7 pixels for

experimental data, this corresponds to a data point every 3.885 μm. The shear strain for this assumed displacement profile is given as:

$$E_{12} = \frac{1}{2}\frac{\partial u_1}{\partial y} = \Delta u_1 \frac{\left(\operatorname{sech}\left(\frac{y - y_c}{a}\right)\right)^2}{4a} \tag{7.9}$$

Therefore, maximum shear strain inside the shear band is:

$$E_{12max} = \frac{\Delta u_1}{4a} \tag{7.10}$$

From experiments, it is observed that $E_{12max} \approx 1.1$ and $\Delta u_{1max} = 75\ \mu m$ (at t=15.19 μs for 4th column of particles) which gives $a = 17.05 = \frac{w_b}{3.52}$.

The prescribed displacements are filtered using an NLM filter with different values for search window size (Ω), neighborhood size ($\mathtt{N}$) and degree of smoothing ($\mathtt{h_s}$). The effect of these filter parameters is studied for different values of Δu_1. Errors in displacement and shear strain are defined below:

$$eu_1 = \frac{1}{n}\sum_{i=1}^{n} |u_{1if} - u_{1i}| \ \forall\ |y_i - y_c| \le a \tag{7.11}$$

$$eE_{12} = \frac{1}{n}\sum_{i=1}^{n} |E_{12if} - E_{12i}| \ \forall\ |y_i - y_c| \le a \tag{7.12}$$

where eu_1 and eE_{12} are errors in displacements and shear strains respectively, u_{1f} and E_{12f} represent filtered values and u_1 and E_{12} represent prescribed values.

Figure 7.19 (a) and Figure 7.19 (b) show plots for eu_1 and eE_{12} as a function of Ω for $h_s = 0.25$ and different values of N, for a given Δu_1. On the same graph, the errors are also plotted for different values of prescribed Δu_1. Variation of errors is explored for $h_s = 0.5$ and

$h_s = 1$ in Figure 7.19 (c)-(f). The following conclusions can be drawn from these graphs: (a) Displacement errors are always below 0.1 μm for the range of parameters explored. This value is smaller than the spatial resolution of the system. Therefore, the effect of filtering on displacements is negligible. (b) Shear strain errors are small but finite and increase with increasing h_s and Ω while decreasing with increasing N. (c) There is no clear dependence of displacement and shear strain errors on prescribed peak displacement value, Δu_1.

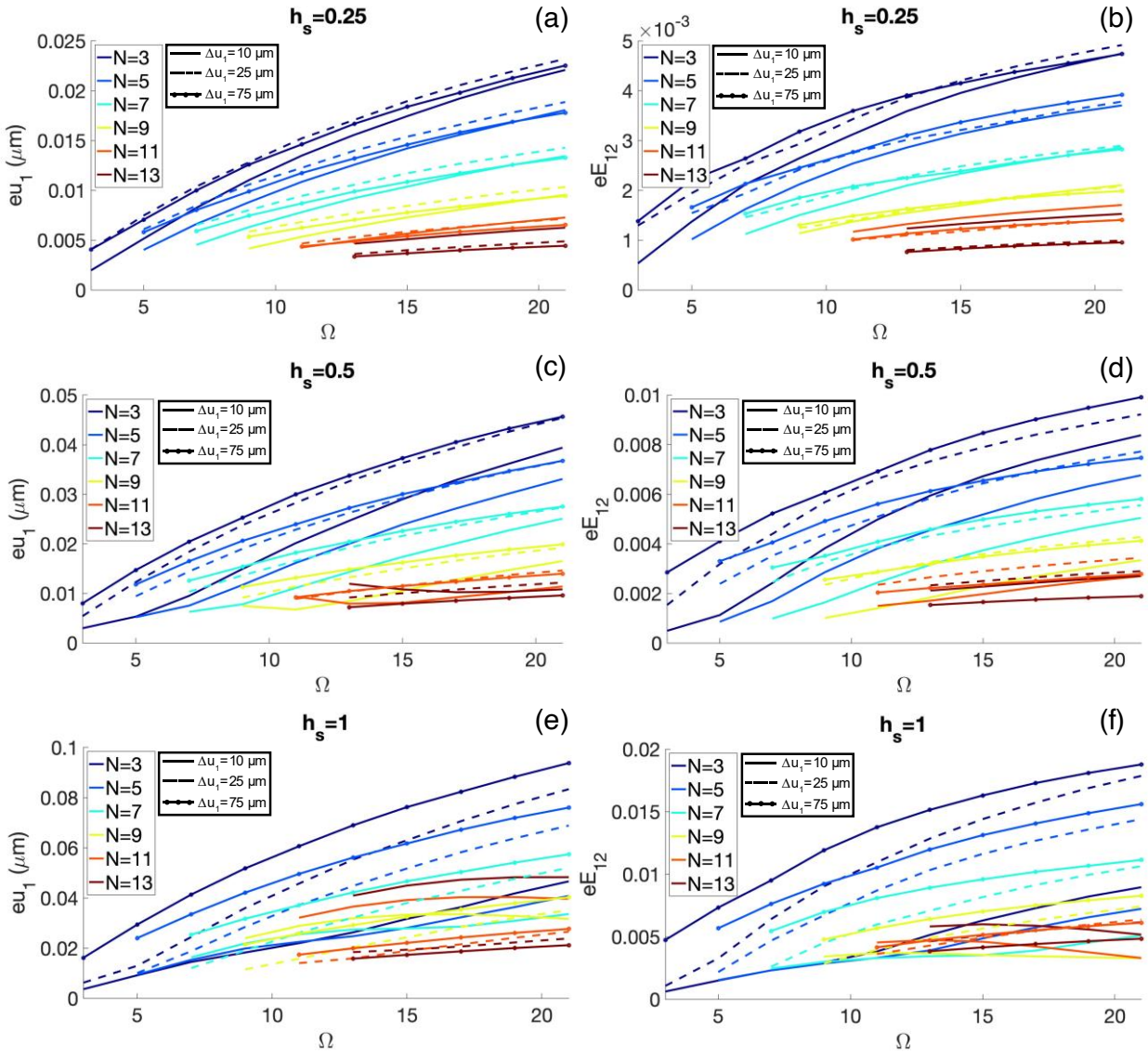

Figure 7.19 Displacement and strain errors plotted with different NLM filter parameters.

The effect of NLM filter is better illustrated through displacement and strain profiles along a vertical column of particles/points in the y-direction, as shown in Figure 7.20. The effect of search window, Ω and prescribed peak displacement, Δu_1 is explored while keeping $h_s = 0.5$ and $N = 7$ fixed. It has been shown above that absolute errors (as quantified in equation (4) and (5) and plotted in Figure 7.19) are independent of Δu_1. However, it is evident from Figure 7.20

that as the peak displacement/strain increases, errors relative to the peak values decrease, i.e. for a given set of NLM parameters, the filtered displacement and strain profiles look closer to the prescribed profiles for larger Δu_1. It can also be seen from Figure 7.20 that $\Omega = 7$, $N = 7$ and $h_s = 0.5$ should work adequately for the problem at hand. This is made clear in the next section on the effect of filtering on experimental data.

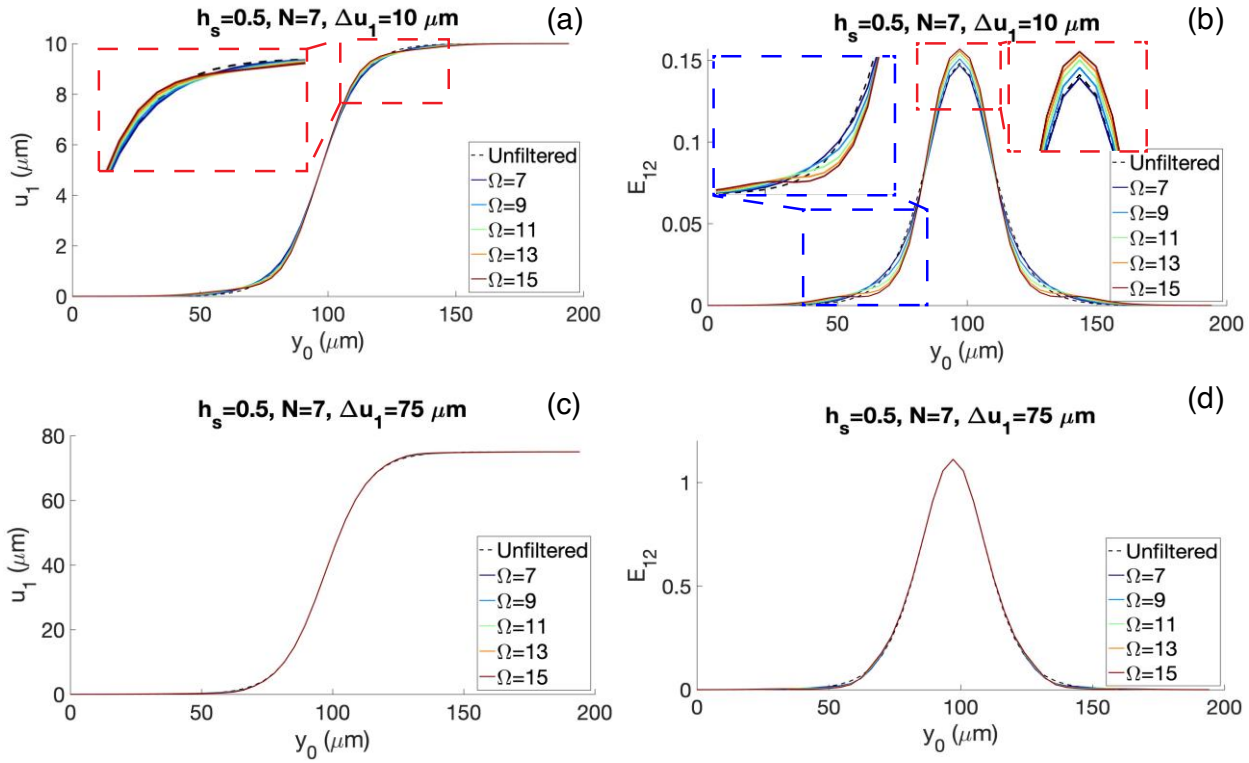

Figure 7.20 Displacement and strain contours plotted with different NLM filter parameters. (a) and (b): contours for $\Delta u_1 = 10\,\mu m$, (c) and (d): contours for $\Delta u_1 = 75\,\mu m$.

7.10 Appendix B: Effect of filtering on experimental data

Real experimental data is probed for the effect of NLM filtering. For brevity, the effect is displayed on u_1, u_2 and E_{12} contours at two time instants, $t = 6.18\,\mu s$ and $t = 15.19\,\mu s$. At

these time instants, displacements and shear strains are very close to the cases considered in Fig. S4 in the previous section. A value of 0.5 is found adequate for the degree of smoothing (h_s). Search window size (Ω) and neighborhood size (N) are varied from 7 to 15. 2D contours for some of the representative parameter combinations are given in Figure 7.21, Figure 7.22 and Figure 7.23 and compared with the unfiltered case.

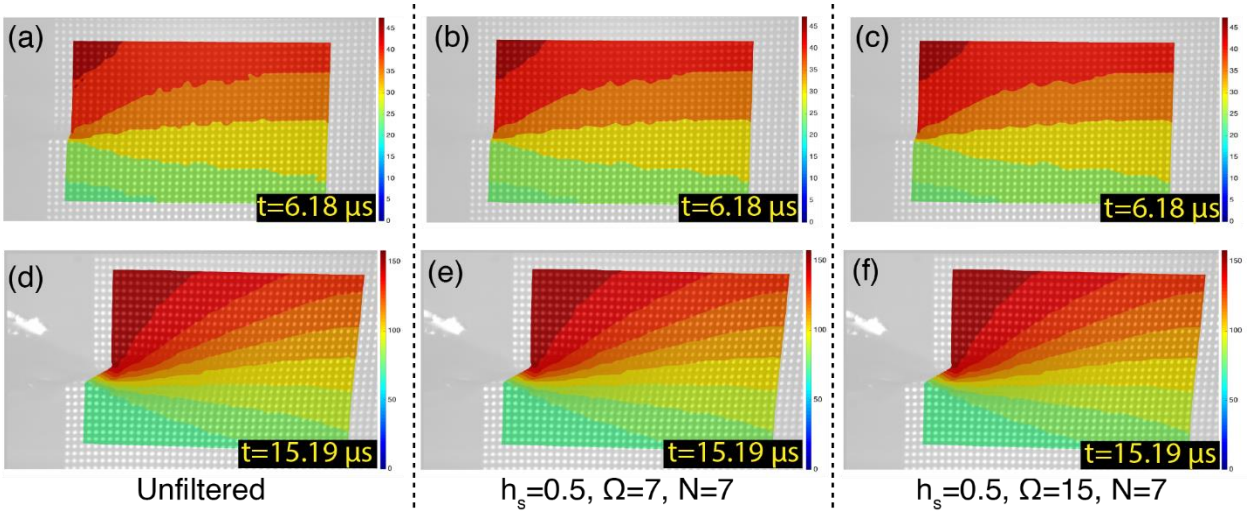

Figure 7.21 Displacements in x-direction, u_1 plotted with different NLM filter parameters at different times. (a)-(c): at time $6.18\,\mu s$, (d)-(f): $15.19\,\mu s$

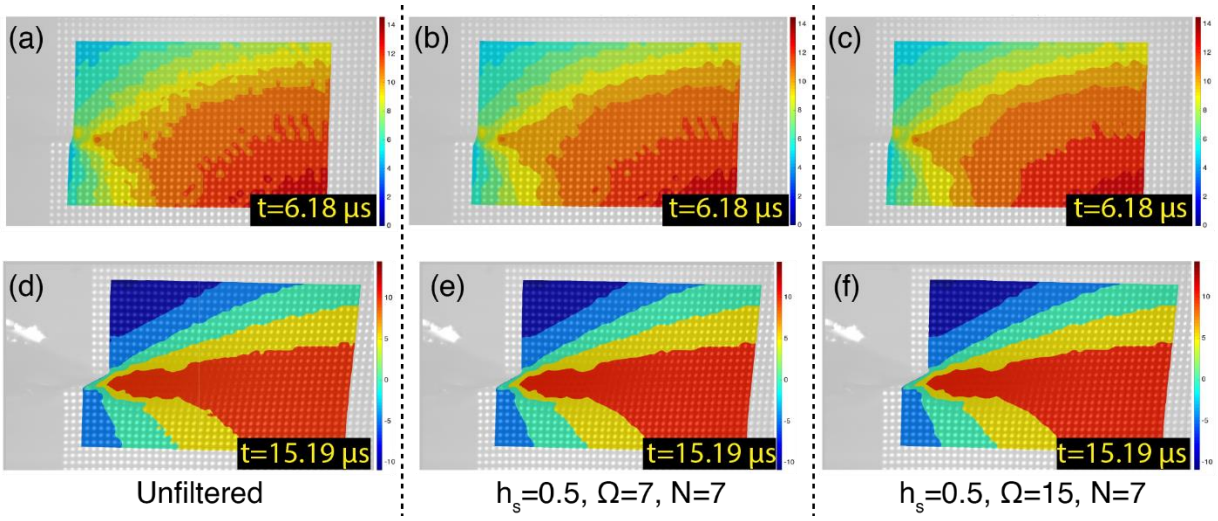

Figure 7.22 Displacements in y-direction, u_2 plotted with different NLM filter parameters at different times. (a)-(c): at time $6.18\,\mu s$, (d)-(f): $15.19\,\mu s$

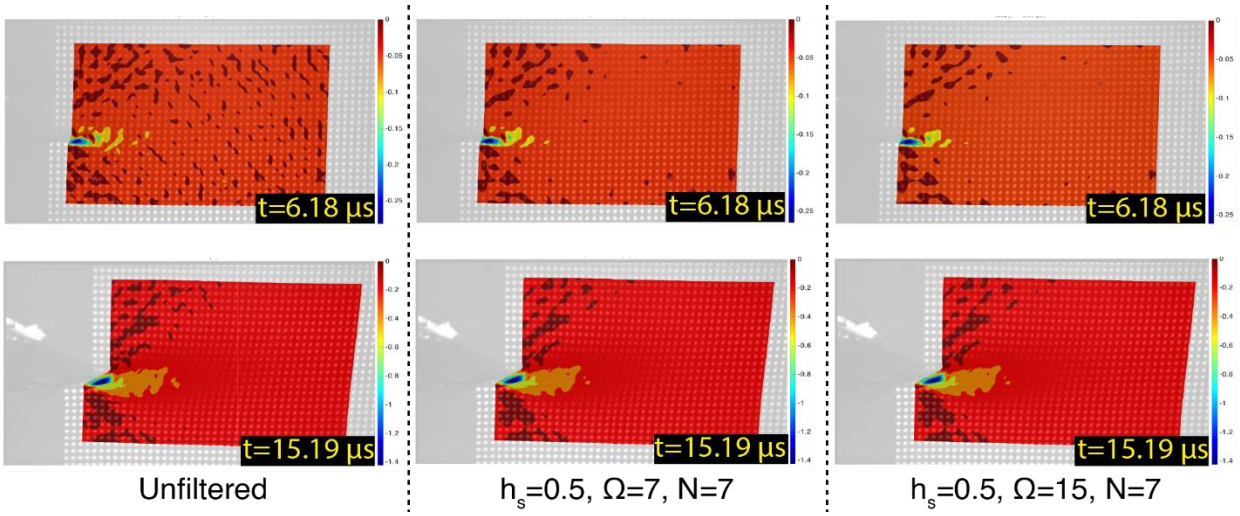

Figure 7.23 Lagrangian shear strain, E_{12} plotted with different NLM filter parameters at different times. (a)-(c): at time $6.18\,\mu s$, (d)-(f): $15.19\,\mu s$

It can be concluded from Figure 7.21, Figure 7.22 and Figure 7.23 that the NLM filter, for the values of parameters explored here, doesn't lead to any smoothing of strain gradients across the

shear band. However, it does help eliminate the noise associated with uncertainty of locating particle centroids.

Chapter 8

Summary and Future Work

Pressure shear plate impact experiments have been performed on a polymer-bonded energetic material simulant and its constituents - a simulant crystal sucrose and an elastomeric binder HTPB. Dynamic response of each of the constituents is first investigated under a range of normal stresses (3-10 GPa) and high shear strain-rates ($10^5 - 10^6\ s^{-1}$). Shear strength of HTPB shows a highly pressure-dependent behavior, with the strength increasing from 120 MPa to 470 MPa as the normal stress increases nominally from 3 GPa to 9 GPa. Peak shear strength of sucrose, on the other hand, shows a relatively weak dependence on normal stress, with its shear strength increasing merely from an average value of 410 MPa to 465 MPa as the normal stress increases from 2.9 GPa to 9.5 GPa. Such different pressure-sensitivities of the two phases of a PBS can result in a change of its deformation mechanisms at increasing pressures. Sucrose also exhibits pronounced strain softening under shear after reaching a peak value and in some cases a complete loss in shear strength.

Experimental effort on HTPB and sucrose is aimed at building suitable constitutive models to enable prediction of the constitutive response of their composite. A quasi-linear viscoelastic model with a pressure-dependent instantaneous elastic response is used to model HTPB. ABAQUS/Explicit simulation results show reasonable agreement with normal and shear stress profiles obtained from experiments. However, thermal effects are ignored in the current model, which prevents softening and localization the binder phase of a PBS. A

thermodynamically consistent framework incorporating thermo-viscoelastic effects is desired for the polymeric binder, which is a subject of future research.

A thermodynamic framework is presented for constitutive modeling of sucrose. A finite deformation thermo-mechanical model is presented, which incorporates several features. Isotropic finite strain elasticity with higher order constants is employed along with consideration of thermoelastic effects. A rate-dependent thermally-coupled plasticity law is used. For accurate modeling of the volumetric response, a complete Mie-Gruneisen equation of state with a temperature-dependent specific heat capacity is derived and used in the model. Simulations show that the dramatic drop in shear strength of sucrose is a result of localized deformation in the form of adiabatic shear bands. Shear strain localization leads to a large increase in temperature and the simulations predict eventual melting of the material within the band. Thus, the experiments show that molecular crystals can undergo adiabatic shear localization, which is a potential hot-spot mechanism. These results motivate the study the dynamic shearing resistance of actual energetic crystals through PSPI experiments.

Then, PSPI experiments are carried out on the sucrose/HTPB composite. Peak dynamic shearing resistance of the composite increases from 176 MPa to 453 MPa as the normal stress increases nominally from 3 GPa to 9.75 GPa. The shearing resistance builds up to a peak value before decreasing to a smaller non-zero value. Such a drop in the shear strength of the composite could be due to multiple factors like fracture of sucrose and/or HTPB, delamination of HTPB from sucrose crystals, adiabatic shear band localization in the HTPB binder or sucrose crystals and friction between fractured surfaces. However, exploring each of these mechanisms requires

an extensive experimental undertaking focused on studying each mechanism in isolation from others. Such an experimental effort can reveal physical insights that can inform computational simulations of the composite microstructures with realistic constraints. Such an effort is a fruitful research avenue for the future.

PSPI experiments and constitutive modeling of HTPB and sucrose lay a foundation for studying mechanisms leading to the formation of hot-spots in PBXs. However, in-situ quantitative experimental investigation of deformation fields and mechanisms of hot-spot formation remains a challenging task, particularly due to the stringent requirements placed on imaging systems to adequately resolve micron-scale features at sub-microsecond temporal resolutions. A high-speed microscopic imaging system has been built in pursuit of this goal. The capability of the system is demonstrated by imaging adiabatic shear band formation in a notched polycarbonate plate, at a temporal resolution of 250 ns and a spatial resolution of ~1 μm, while maintaining a large field of view ($\approx 1.11 \times 0.63\, \mu m$).

Bibliography

Abraham, A. V., Ram, S., Chao, J., Ward, E. & Ober, R. J. 2009. Quantitative study of single molecule location estimation techniques. *Optics Express,* 17, 23352-23373.

Aldén, M., Bood, J., Li, Z. & Richter, M. 2011. Visualization and understanding of combustion processes using spatially and temporally resolved laser diagnostic techniques. *Proceedings of the Combustion Institute,* 33, 69-97.

Anand, L. 1979. On H. Hencky's approximate strain-energy function for moderate deformations. *Journal of Applied Mechanics*.

Anand, L. 1986. Moderate deformations in extension-torsion of incompressible isotropic elastic materials. *Journal of the Mechanics and Physics of Solids,* 34, 293-304.

Anderson Jr, G., Higbie, H. & Stegeman, G. 1950. The heat capacity of sucrose from 25 to 90. *Journal of the American Chemical Society,* 72, 3798-3799.

Armstrong, R., Coffey, C., Devost, V. & Elban, W. 1990. Crystal size dependence for impact initiation of cyclotrimethylenetrinitramine explosive. *Journal of Applied Physics,* 68, 979-984.

Austin, R. A., Barton, N. R., Reaugh, J. E. & Fried, L. E. 2015. Direct numerical simulation of shear localization and decomposition reactions in shock-loaded HMX crystal. *Journal of Applied Physics,* 117, 185902.

Baek, S. & Lee, S. 1996. A new two-frame particle tracking algorithm using match probability. *Experiments in Fluids,* 22, 23-32.

Balzer, J., Siviour, C., Walley, S., Proud, W. & Field, J. 2004. Behaviour of ammonium perchlorate–based propellants and a polymer–bonded explosive under impact loading. *Proceedings of the Royal Society of London. Series A: Mathematical, Physical and Engineering Sciences,* 460, 781-806.

Barton, N. R., Knap, J., Arsenlis, A., Becker, R., Hornung, R. D. & Jefferson, D. R. 2008. Embedded polycrystal plasticity and adaptive sampling. *International Journal of Plasticity,* 24, 242-266.

Barton, N. R., Winter, N. W. & Reaugh, J. E. 2009. Defect evolution and pore collapse in crystalline energetic materials. *Modelling and Simulation in Materials Science and Engineering,* 17, 035003.

Barua, A. & Zhou, M. 2011. A Lagrangian framework for analyzing microstructural level response of polymer-bonded explosives. *Modelling and Simulation in Materials Science and Engineering,* 19, 055001.

Becker, E. & Foppl, O. 1928. *Dauerversuche zur Bestimmung der Festigkeitseigenschaften, Beziehungen zwischen Baustoffdämpfung und Verformungsgeschwindigkeit*, VDI-Verlag.

Becker, R. 2004. Effects of crystal plasticity on materials loaded at high pressures and strain rates. *International Journal of Plasticity,* 20, 1983-2006.

Beevers, C., Mcdonald, T., Robertson, J. T. & Stern, F. 1952. The crystal structure of sucrose. *Acta Crystallographica,* 5, 689-690.

Bergström, J. S. & Boyce, M. C. 1998. Constitutive modeling of the large strain time-dependent behavior of elastomers. *Journal of the Mechanics and Physics of Solids,* 46, 931-954.

Blumenthal, W., Thompson, D., Cady, C., Gray Iii, G. & Idar, D. Compressive properties of PBXN-110 and its HTPB-based binder as a function of temperature and strain rate. Proceedings of the 12th International Detonation Symposium, San Diego, CA, USA, 2002. 11-16.

Böhm, B., Heeger, C., Gordon, R. L. & Dreizler, A. 2011. New perspectives on turbulent combustion: multi-parameter high-speed planar laser diagnostics. *Flow, Turbulence and Combustion,* 86, 313-341.

Bourne, N. & Field, J. E. 1991. Bubble collapse and the initiation of explosion. *Proceedings of the Royal Society of London. Series A: Mathematical and Physical Sciences,* 435, 423-435.

Bourne, N. & Gray Iii, G. 2005. Dynamic response of binders; teflon, estane™ and Kel-F-800™. *Journal of Applied Physics,* 98, 123503.

Bourne, N. & Milne, A. 2004. Shock to detonation transition in a plastic bonded explosive. *Journal of Applied Physics,* 95, 2379-2385.

Bowden, F. P. & Yoffe, A. D. 1958. *Fast reactions in solids*, Butterworth's Scientific Publications.

Bowden, F. P. & Yoffe, A. D. 1985. *Initiation and growth of explosion in liquids and solids*, CUP Archive.

Bridgman, P. W. Compressibilities and pressure coefficients of resistance of elements, compounds, and alloys, many of them anomalous. Proceedings of the American Academy of Arts and Sciences, 1933. JSTOR, 27-93.

Bridgman, P. W. Linear Compressions to 30,000 Kg/cm2, including Relatively Incompressible Substances. Proceedings of the American Academy of Arts and Sciences, 1949. JSTOR, 189-234.

Buades, A., Coll, B. & Morel, J.-M. A non-local algorithm for image denoising. 2005 IEEE Computer Society Conference on Computer Vision and Pattern Recognition (CVPR'05), 2005. IEEE, 60-65.

Cady, C., Blumenthal, W., Gray Iii, G. & Idar, D. 2006. Mechanical properties of plastic-bonded explosive binder materials as a function of strain-rate and temperature. *Polymer Engineering and Science,* 46, 812-819.

Cawkwell, M., Sewell, T. D., Zheng, L. & Thompson, D. L. 2008. Shock-induced shear bands in an energetic molecular crystal: Application of shock-front absorbing boundary conditions to molecular dynamics simulations. *Physical Review B,* 78, 014107.

Chaudhri, M. & Field, J. E. 1974. The role of rapidly compressed gas pockets in the initiation of condensed explosives. *Proceedings of the Royal Society of London. A. Mathematical and Physical Sciences,* 340, 113-128.

Cheezum, M. K., Walker, W. F. & Guilford, W. H. 2001. Quantitative comparison of algorithms for tracking single fluorescent particles. *Biophysical Journal,* 81, 2378-2388.

Cho, H., Rinaldi, R. G. & Boyce, M. C. 2013. Constitutive modeling of the rate-dependent resilient and dissipative large deformation behavior of a segmented copolymer polyurea. *Soft Matter,* 9, 6319-6330.

Ciezak-Jenkins, J. A. & Jenkins, T. A. 2018. Mechanochemical induced structural changes in sucrose using the rotational diamond anvil cell. *Journal of Applied Physics,* 123, 085901.

Clayton, J. D. 2014. Analysis of shock compression of strong single crystals with logarithmic thermoelastic-plastic theory. *International Journal of Engineering Science,* 79, 1-20.

Clifton, R. & Jiao, T. 2015. Pressure and strain-rate sensitivity of an elastomer:(1) pressure-shear plate impact experiments;(2) constitutive modeling. *Elastomeric Polymers with High Rate Sensitivity.*

Clifton, R. & Song, S. Inverse Problem for PSPI Experiments. Bulletin of the American Physical Society, 2019.

Clifton, R. J. & Klopp, R. W. 1985. Pressure-shear plate impact testing. *Metals Handbook 8.*

Coffey, C. & Sharma, J. 2001. Lattice softening and failure in severely deformed molecular crystals. *Journal of Applied Physics,* 89, 4797-4802.

Council, N. R. 2011. *Opportunities in protection materials science and technology for future army applications*, National Academies Press.

Criscione, J. C., Humphrey, J. D., Douglas, A. S. & Hunter, W. C. 2000. An invariant basis for natural strain which yields orthogonal stress response terms in isotropic hyperelasticity. *Journal of the Mechanics and Physics of Solids,* 48, 2445-2465.

Davison, L., Horie, Y. & Graham, R. A. 2008. Shock Wave and High Pressure Phenomena. Springer.

Dear, J. & Field, J. 1988. A study of the collapse of arrays of cavities. *Journal of Fluid Mechanics,* 190, 409-425.

Dear, J., Field, J. & Walton, A. J. 1988. Gas compression and jet formation in cavities collapsed by a shock wave. *Nature,* 332, 505-508.

Desai, S., Thakore, I., Sarawade, B. & Devi, S. 2000. Effect of polyols and diisocyanates on thermo-mechanical and morphological properties of polyurethanes. *European Polymer Journal,* 36, 711-725.

Dick, J., Hooks, D., Menikoff, R. & Martinez, A. 2004. Elastic–plastic wave profiles in cyclotetramethylene tetranitramine crystals. *Journal of Applied Physics,* 96, 374-379.

Dodd, B. & Bai, Y. 2012. *Adiabatic shear localization: frontiers and advances*, Elsevier.

Drodge, D. R., Addiss, J. W., Williamson, D. M. & Proud, W. G. Hopkinson bar studies of a PBX simulant. AIP Conference Proceedings, 2007. American Institute of Physics, 513-516.

Duncan-Hewitt, W. C. & Weatherly, G. C. 1989. Evaluating the hardness, Young's modulus and fracture toughness of some pharmaceutical crystals using microindentation techniques. *Journal of Materials Science Letters,* 8, 1350-1352.

Duncan-Hewitt, W. C. & Weatherly, G. C. 1990. Modeling the uniaxial compaction of pharmaceutical powders using the mechanical properties of single crystals. II: Brittle materials. *Journal of Pharmaceutical Sciences,* 79, 273-278.

Escauriza, E., Duarte, J., Chapman, D., Rutherford, M., Farbaniec, L., Jonsson, J., Smith, L., Olbinado, M., Skidmore, J. & Foster, P. 2020. collapse dynamics of spherical cavities in a solid under shock loading. *Scientific Reports,* 10, 1-16.

Espinosa, H. 1995. On the dynamic shear resistance of ceramic composites and its dependence on applied multiaxial deformation. *International Journal of Solids and Structures,* 32, 3105-3128.

Estrada, J. B., Barajas, C., Henann, D. L., Johnsen, E. & Franck, C. 2018. High strain-rate soft material characterization via inertial cavitation. *Journal of the Mechanics and Physics of Solids,* 112, 291-317.

Feng, X., Hall, M. S., Wu, M. & Hui, C.-Y. 2014. An adaptive algorithm for tracking 3D bead displacements: application in biological experiments. *Measurement Science and Technology,* 25, 055701.

Field, J. E. 1992. Hot spot ignition mechanisms for explosives. *Accounts of Chemical Research,* 25, 489-496.

Field, J. E., Bourne, N., Palmer, S. & Walley, S. 1992. Hot-spot ignition mechanisms for explosives and propellants. *Philosophical Transactions of the Royal Society of London. Series A: Physical and Engineering Sciences,* 339, 269-283.

Fried, E. & Gurtin, M. E. 1993. Continuum theory of thermally induced phase transitions based on an order parameter. *Physica D: Nonlinear Phenomena,* 68, 326-343.

Frutschy, K. 1997. *High temperrure pressure-shear plate impact experiments on OFHC copper and pure tungsten carbide.*

Frutschy, K. & Clifton, R. 1998. High-temperature pressure-shear plate impact experiments using pure tungsten carbide impactors. *Experimental mechanics,* 38, 116-125.

Fuente, J. L. D. L. & Rodríguez, O. 2003. Dynamic mechanical study on the thermal aging of a hydroxyl-terminated polybutadiene-based energetic composite. *Journal of Applied Polymer Science,* 87, 2397-2405.

Fung, Y.-C. 2013. *Biomechanics: mechanical properties of living tissues*, Springer Science & Business Media.

Fung, Y.-C. B. 1972. Stress-strain-history relations of soft tissues in simple elongation. *Biomechanics: Its Foundations and Objectives.*

Funk, D. J., Laabs, G. W., Peterson, P. D. & Asay, B. W. Measurement of the stress/strain response of energetic materials as a function of strain rate and temperature: PBX 9501 and mock 9501. AIP Conference Proceedings, 1996. American Institute of Physics, 145-148.

Gilat, A. & Clifton, R. 1985. Pressure-shear waves in 6061-T6 aluminum and alpha-titanium. *Journal of the Mechanics and Physics of Solids,* 33, 263-284.

Gori, M., Rubino, V., Rosakis, A. & Lapusta, N. 2018. Pressure shock fronts formed by ultra-fast shear cracks in viscoelastic materials. *Nature Communications,* 9, 4754.

Grady, D. 2017. *Physics of Shock and Impact, Volume 2: Materials and Shock Response*, IOP Publishing.

Gray Iii, G., Idar, D., Blumenthal, W., Cady, C. & Peterson, P. 1998. High-and low-strain rate compression properties of several energetic material composites as a function of strain rate and temperature. Los Alamos National Lab., NM (United States).

Grunschel, S. E. 2009. *Pressure-shear plate impact experiments on high-purity aluminum at temperatures approaching melt.* Brown University.

Guduru, P., Ravichandran, G. & Rosakis, A. 2001. Observations of transient high temperature vortical microstructures in solids during adiabatic shear banding. *Physical Review E,* 64, 036128.

Guduru, P., Rosakis, A. & Ravichandran, G. 2001. Dynamic shear bands: an investigation using high speed optical and infrared diagnostics. *Mechanics of Materials,* 33, 371-402.

Guduru, P. R. 2001. *An investigation of dynamic failure events in steels using full field high-speed infrared thermography and high-speed photography.* Ph.D. PhD. Thesis, California Institute of Technology.

Hartley, K., Duffy, J. & Hawley, R. 1987. Measurement of the temperature profile during shear band formation in steels deforming at high strain rates. *Journal of the Mechanics and Physics of Solids,* 35, 283-301.

Haska, S. B., Bayramli, E., Pekel, F. & Özkar, S. 1997. Mechanical properties of HTPB-IPDI-based elastomers. *Journal of Applied Polymer Science,* 64, 2347-2354.

Haussühl, S. 2001. Elastic and thermoelastic properties of selected organic crystals: acenaphthene, trans-azobenzene, benzophenone, tolane, trans-stilbene, dibenzyl, diphenyl sulfone, 2, 2-biphenol, urea, melamine, hexogen, succinimide, pentaerythritol, urotropine, malonic acid, dimethyl malonic acid, maleic acid, hippuric acid, aluminium acetylacetonate, iron acetylacetonate, and tetraphenyl silicon. *Zeitschrift für Kristallographie-Crystalline Materials,* 216, 339-353.

Haycraft, J. J., Stevens, L. L. & Eckhardt, C. J. 2006. The elastic constants and related properties of the energetic material cyclotrimethylene trinitramine (RDX) determined by Brillouin scattering. *The Journal of Chemical Physics,* 124, 024712.

Heavens, S. & Field, J. E. 1974. The ignition of a thin layer of explosive by impact. *Proceedings of the Royal Society of London. A. Mathematical and Physical Sciences,* 338, 77-93.

Hodowany, J., Ravichandran, G., Rosakis, A. & Rosakis, P. 2000. Partition of plastic work into heat and stored energy in metals. *Experimental Mechanics,* 40, 113-123.

Hooks, D. E., Ramos, K. J. & Martinez, A. R. 2006. Elastic-plastic shock wave profiles in oriented single crystals of cyclotrimethylene trinitramine (RDX) at 2.25 GPa. *Journal of Applied Physics,* 100, 024908.

Hooks, D. E., Ramos, K. J. & Martinez, A. R. 2006. Elastic-plastic shock wave profiles in oriented single crystals of cyclotrimethylene trinitramine (RDX) at 2.25 GPa. *Journal of Applied Physics,* 100, 024908.

Hu, R., Prakash, C., Tomar, V., Harr, M., Gunduz, I. E. & Oskay, C. 2017. Experimentally-validated mesoscale modeling of the coupled mechanical–thermal response of AP–HTPB energetic material under dynamic loading. *International Journal of Fracture,* 203, 277-298.

Hu, Z., Luo, H., Bardenhagen, S., Siviour, C., Armstrong, R. & Lu, H. 2015. Internal deformation measurement of polymer bonded sugar in compression by digital volume correlation of in-situ tomography. *Experimental Mechanics,* 55, 289-300.

Idar, D., Peterson, P., Scott, P. & Funk, D. Low strain rate compression measurements of PBXN-9, PBX 9501, and mock 9501. AIP Conference Proceedings, 1998. American Institute of Physics, 587-590.

Immerkaer, J. 1996. Fast noise variance estimation. *Computer Vision and Image Understanding,* 64, 300-302.

Ionescu, M. 2005. *Chemistry and technology of polyols for polyurethanes*, iSmithers Rapra Publishing.

Jain, S., Sekkar, V. & Krishnamurthy, V. 1993. Mechanical and swelling properties of HTPB-based copolyurethane networks. *Journal of Applied Polymer Science,* 48, 1515-1523.

Jaramillo, E., Sewell, T. D. & Strachan, A. 2007. Atomic-level view of inelastic deformation in a shock loaded molecular crystal. *Physical Review B,* 76, 064112.

Jordan, J. L., Montaigne, D., Gould, P., Neel, C., Sunny, G. & Molek, C. 2016. High strain rate and shock properties of hydroxyl-terminated polybutadiene (HTPB) with varying amounts of plasticizer. *Journal of Dynamic Behavior of Materials,* 2, 91-100.

Kalthoff, J. 1990. Transition in the failure behavior of dynamically shear loaded cracks. *Applied Mechanics Reviews,* 43, S247-S250.

Kannan, V., Hazeli, K. & Ramesh, K. 2018. The mechanics of dynamic twinning in single crystal magnesium. *Journal of the Mechanics and Physics of Solids,* 120, 154-178.

Kendall, M. J. & Siviour, C. R. 2015. Experimentally simulating high rate composite deformation in tension and compression: polymer bonded explosive simulant. *Journal of Dynamic Behavior of Materials,* 1, 114-123.

Kenneth R. Spring, M. W. D. Available: https://www.microscopyu.com/microscopy-basics/depth-of-field-and-depth-of-focus [Accessed].

Kettenbeil, C., Lovinger, Z., Ravindran, S., Mello, M. & Ravichandran, G. 2020. Pressure-Shear Plate Impact Experiments at High Pressures. *Journal of Dynamic Behavior of Materials*, 1-13.

Keyhani, A., Yang, R. & Zhou, M. 2019. Novel capability for microscale in-situ imaging of temperature and deformation fields under dynamic loading. *Experimental Mechanics,* 59, 775-790.

Kim, K. S., Clifton, R. J. & Kumar, P. 1977. A combined normal-and transverse-displacement interferometer with an application to impact of y-cut quartz. *Journal of Applied Physics,* 48, 4132-4139.

Kirugulige, M. S., Tippur, H. V. & Denney, T. S. 2007. Measurement of transient deformations using digital image correlation method and high-speed photography: application to dynamic fracture. *Applied Optics,* 46, 5083-5096.

Klopp, R. W. & Clifton, R. J. 1990. Analysis of tilt in the high-strain-rate pressure-shear plate impact experiment. *Journal of Applied Physics,* 67, 7171-7173.

Kohse-Höinghaus, K. & Jeffries, J. B. 2002. *Applied combustion diagnostics.*

Kroonblawd, M. & Austin, R. 2020. Sensitivity of pore collapse heating to the melting temperature and liquid-phase shear viscosity of HMX.

Kumar, P. & Clifton, R. 1977. Optical alignment of impact faces for plate impact experiments. *Journal of Applied Physics,* 48, 1366-1367.

Lindemann, F. A. 1910. The Calculation of Molecular Vibration Frequencies. *Physik. Z.* , 609-612.

Liu, C., Rae, P. J., Cady, C. M. & Lovato, M. L. 2011. Damage & fracture of high-explosive mock subject to cyclic loading. *Mechanics of Time-Dependent Materials and Processes in Conventional and Multifunctional Materials, Volume 3.* Springer.

Liu, S.-L., Li, J., Zhang, Z.-L., Wang, Z.-G., Tian, Z.-Q., Wang, G.-P. & Pang, D.-W. 2013. Fast and high-accuracy localization for three-dimensional single-particle tracking. *Scientific Reports,* 3, 2462.

Luscher, D. J., Bronkhorst, C. A., Alleman, C. N. & Addessio, F. L. 2013. A model for finite-deformation nonlinear thermomechanical response of single crystal copper under shock conditions. *Journal of the Mechanics and Physics of Solids,* 61, 1877-1894.

Marchand, A. & Duffy, J. 1988. An experimental study of the formation process of adiabatic shear bands in a structural steel. *Journal of the Mechanics and Physics of Solids,* 36, 251-283.

Mas, E., Clements, B., Blumenthal, B., Cady, C., Gray Iii, G. & Liu, C. A viscoelastic model for PBX binders. AIP Conference Proceedings, 2002. American Institute of Physics, 661-664.

Mason, J., Lambros, J. & Rosakis, A. 1992. The use of a coherent gradient sensor in dynamic mixed-mode fracture mechanics experiments. *Journal of the Mechanics and Physics of Solids,* 40, 641-661.

Masterson, V. M. & Cao, X. 2008. Evaluating particle hardness of pharmaceutical solids using AFM nanoindentation. *International Journal of Pharmaceutics,* 362, 163-171.

Menikoff, R. 2016. Complete Mie-Gruneisen Equation of State (update). Los Alamos National Lab.(LANL), Los Alamos, NM (United States).

Menikoff, R. & Sewell, T. D. 2002. Constituent properties of HMX needed for mesoscale simulations. *Combustion Theory and Modelling,* 6, 103-125.

Meziere, Y., Akhavan, J., Stevens, G., Millett, J. & Bourne, N. The Shock Hugoniot of Hydroxy-Terminated Polybutadiene. AIP Conference Proceedings, 2004. American Institute of Physics, 99-102.

Miller, G. & Garroway, A. 2001. A review of the crystal structures of common explosives. Part I: RDX, HMX, TNT, PETN, and Tetryl. Naval Research Lab, Washington DC.

Millett, J. & Bourne, N. 2000. The deviatoric response of polymethylmethacrylate to one-dimensional shock loading. *Journal of Applied Physics,* 88, 7037-7040.

Millett, J., Bourne, N. & Akhavan, J. 2004. The response of hydroxy-terminated polybutadiene to one-dimensional shock loading. *Journal of Applied Physics,* 95, 4722-4727.

Millett, J., Bourne, N. & Barnes, N. 2002. The behavior of an epoxy resin under one-dimensional shock loading. *Journal of Applied Physics,* 92, 6590-6594.

Milne, A., Longbottom, A., Bourne, N. & Millett, J. 2007. On the unreacted Hugoniots of three plastic bonded explosives. *Propellants, Explosives, Pyrotechnics,* 32, 68-72.

Mooney, M. 1940. A theory of large elastic deformation. *Journal of Applied Physics,* 11, 582-592.

Nadal, M.-H. & Le Poac, P. 2003. Continuous model for the shear modulus as a function of pressure and temperature up to the melting point: analysis and ultrasonic validation. *Journal of Applied Physics,* 93, 2472-2480.

Neubert, H. 1963. A simple model representing internal damping in solid materials. *The Aeronautical Quarterly,* 14, 187-210.

Ohmi, K. & Li, H.-Y. 2000. Particle-tracking velocimetry with new algorithms. *Measurement Science and Technology,* 11, 603.

Parthasarathy, R. 2012. Rapid, accurate particle tracking by calculation of radial symmetry centers. *Nature Methods,* 9, 724.

Patel, M., Leggett, S. E., Landauer, A. K., Wong, I. Y. & Franck, C. 2018. Rapid, topology-based particle tracking for high-resolution measurements of large complex 3D motion fields. *Scientific Reports,* 8, 5581.

Patyk, E., Skumiel, J., Podsiadło, M. & Katrusiak, A. 2012. High-Pressure (+)-Sucrose Polymorph. *Angewandte Chemie International Edition,* 51, 2146-2150.

Pereira, F., Stüer, H., Graff, E. C. & Gharib, M. 2006. Two-frame 3D particle tracking. *Measurement Science and Technology,* 17, 1680.

Pierron, F., Cheriguene, R., Forquin, P., Moulart, R., Rossi, M. & Sutton, M. Performances and limitations of three ultra high-speed imaging cameras for full-field deformation measurements. Applied Mechanics and Materials, 2011. Trans Tech Publ, 81-86.

Pipkin, A. & Rogers, T. 1968. A non-linear integral representation for viscoelastic behaviour. *Journal of the Mechanics and Physics of Solids,* 16, 59-72.

Poirier, J.-P. 2000. *Introduction to the Physics of the Earth's Interior*, Cambridge University Press.

Poirier, J.-P. & Tarantola, A. 1998. A logarithmic equation of state. *Physics of the Earth and Planetary Interiors,* 109, 1-8.

Porter, D. 1995. *Group interaction modelling of polymer properties*, CRC Press.

Ramesh, K. & Clifton, R. 1987. A pressure-shear plate impact experiment for studying the rheology of lubricants at high pressures and high shearing rates.

Ramos, K. & Bahr, D. 2007. Mechanical behavior assessment of sucrose using nanoindentation. *Journal of Materials Research,* 22, 2037-2045.

Ravi-Chandar, K. 1995. On the failure mode transitions in polycarbonate under dynamic mixed-mode loading. *International Journal of Solids and Structures,* 32, 925-938.

Ravi-Chandar, K., Lu, J., Yang, B. & Zhu, Z. 2000. Failure mode transitions in polymers under high strain rate loading. *International Journal of Fracture,* 101, 33-72.

Ravindran, S., Tessema, A. & Kidane, A. 2016. Local deformation and failure mechanisms of polymer bonded energetic materials subjected to high strain rate loading. *Journal of Dynamic Behavior of Materials,* 2, 146-156.

Ravindran, S., Tessema, A. & Kidane, A. 2017. Multiscale damage evolution in polymer bonded sugar under dynamic loading. *Mechanics of Materials,* 114, 97-106.

Rivlin, R. & Saunders, D. 1997. Large elastic deformations of isotropic materials. *Collected papers of RS Rivlin.* Springer.

Rosakis, P., Rosakis, A., Ravichandran, G. & Hodowany, J. 2000. A thermodynamic internal variable model for the partition of plastic work into heat and stored energy in metals. *Journal of the Mechanics and Physics of Solids,* 48, 581-607.

Ross, M. 1969. Generalized Lindemann melting law. *Physical Review,* 184, 233.

Rubino, V., Rosakis, A. & Lapusta, N. 2017. Understanding dynamic friction through spontaneously evolving laboratory earthquakes. *Nature Communications,* 8, 15991.

Rubino, V., Rosakis, A. & Lapusta, N. 2019. Full-field ultrahigh-speed quantification of dynamic shear ruptures using digital image correlation. *Experimental Mechanics*, 1-32.

Sandusky, H. W., Beard, B. C., Hglancy, B. C., Elban, W. L. & Armstrong, R. W. 1993. Comparison of Deformation and Shoch Reactivity for Single Crystals of RDX and Ammonium Perchlorate. *Structure and Properties of Energetic Materials,* 296, 93-98.

Schwarz, R., Hooks, D., Dick, J., Archuleta, J. & Martinez, A. 2005. Resonant ultrasound spectroscopy measurement of the elastic constants of cyclotrimethylene trinitramine. *Journal of Applied Physics.*

Sekkar, V., Bhagawan, S., Prabhakaran, N., Rao, M. R. & Ninan, K. 2000. Polyurethanes based on hydroxyl terminated polybutadiene: modelling of network parameters and correlation with mechanical properties. *Polymer,* 41, 6773-6786.

Sekkar, V., Bhagawan, S., Prabhakaran, N., Rao, M. R. & Ninan, K. J. P. 2000. Polyurethanes based on hydroxyl terminated polybutadiene: modelling of network parameters and correlation with mechanical properties. 41, 6773-6786.

Sewell, T. D. & Menikoff, R. Complete Equation of State for β-HMX and Implications for Initiation. AIP Conference Proceedings, 2004. American Institute of Physics, 157-162.

Sharma, J., Armstrong, R., Elban, W., Coffey, C. & Sandusky, H. 2001. Nanofractography of shocked RDX explosive crystals with atomic force microscopy. *Applied Physics Letters,* 78, 457-459.

Sharma, J. & Coffey, C. Nature of ignition sites and hot spots, studied by using an atomic force microscope. AIP Conference Proceedings, 1996. American Institute of Physics, 811-814.

Sharma, J., Coffey, C., Ramaswamy, A. & Armstrong, R. Atomic force microscopy of hot spot reaction sites in impacted RDX and laser heated AP. Materials Research Society Symposium Proceedings, 1996. Materials Research Society, 257-266.

Shastry, A. V. & Hartel, R. 1996. Crystallization during drying of thin sucrose films. *Journal of Food Engineering,* 30, 75-94.

Sheffield, S., Gustavsen, R. & Alcon, R. Porous HMX initiation studies—sugar as an inert simulant. AIP Conference Proceedings, 1998. American Institute of Physics, 575-578.

Sick, V. 2013. High speed imaging in fundamental and applied combustion research. *Proceedings of the Combustion Institute,* 34, 3509-3530.

Simon, F. & Glatzel, G. 1929. Bemerkungen zur schmelzdruckkurve. *Zeitschrift für Anorganische Und Allgemeine Chemie,* 178, 309-316.

Siviour, C., Gifford, M., Walley, S., Proud, W. & Field, J. 2004. Particle size effects on the mechanical properties of a polymer bonded explosive. *Journal of Materials Science,* 39, 1255-1258.

Siviour, C. R., Laity, P. R., Proud, W. G., Field, J., Porter, D., Church, P., Gould, P. & Huntingdon-Thresher, W. 2008. High strain rate properties of a polymer-bonded sugar: their dependence on applied and internal constraints. *Proceedings of the Royal Society A: Mathematical, Physical and Engineering Sciences,* 464, 1229-1255.

Small, A. & Stahlheber, S. 2014. Fluorophore localization algorithms for super-resolution microscopy. *Nature Methods,* 11, 267.

Steinberg, D., Cochran, S. & Guinan, M. 1980. A constitutive model for metals applicable at high-strain rate. *Journal of Applied Physics,* 51, 1498-1504.

Stevens, L. L. & Eckhardt, C. J. 2005. The elastic constants and related properties of β-HMX determined by Brillouin scattering. *The Journal of Chemical Physics,* 122, 174701.

Sundaram, S. 1999. *Pressure-shear plate impact studies of alumina ceramics and the influence of an intergranular glassy phase.* Brown University.

Swallowe, G. & Field, J. E. 1982. The ignition of a thin layer of explosive by impact; the effect of polymer particles. *Proceedings of the Royal Society of London. A. Mathematical and Physical Sciences,* 379, 389-408.

Swantek, A. & Austin, J. 2010. Collapse of void arrays under stress wave loading. *Journal of Fluid Mechanics,* 649, 399-427.

Tippur, H. & Rosakis, A. 1991. Quasi-static and dynamic crack growth along bimaterial interfaces: a note on crack-tip field measurements using coherent gradient sensing. *Experimental Mechanics,* 31, 243-251.

Tippur, H. V., Krishnaswamy, S. & Rosakis, A. J. 1991. Optical mapping of crack tip deformations using the methods of transmission and reflection coherent gradient sensing: a study of crack tip K-dominance. *International Journal of Fracture,* 52, 91-117.

Tiwari, V., Sutton, M. & Mcneill, S. 2007. Assessment of high speed imaging systems for 2D and 3D deformation measurements: methodology development and validation. *Experimental Mechanics,* 47, 561-579.

Tong, W., Clifton, R. J. & Huang, S. 1992. Pressure-shear impact investigation of strain rate history effects in oxygen-free high-conductivity copper. *Journal of the Mechanics and Physics of Solids,* 40, 1251-1294.

Trott, W. M., Baer, M. R., Castaneda, J. N., Chhabildas, L. C. & Asay, J. R. 2007. Investigation of the mesoscopic scale response of low-density pressings of granular sugar under impact. *Journal of Applied Physics,* 101, 024917.

Van Der Heijden, A. E., Bouma, R. H. & Van Der Steen, A. C. 2004. Physicochemical parameters of nitramines influencing shock sensitivity. *Propellants, Explosives, Pyrotechnics,* 29, 304-313.

Wang, X., Wu, Y., Huang, F., Jiao, T. & Clifton, R. J. 2016. Mesoscale thermal-mechanical analysis of impacted granular and polymer-bonded explosives. *Mechanics of Materials,* 99, 68-78.

Wiegand, D. A. & Reddingius, B. 2005. Mechanical properties of confined explosives. *Journal of Energetic Materials,* 23, 75-98.

Williams, C., Walker, S., Lochert, I. & Clarke, S. Investigation into the interaction of dantocol in polymer bonded explosives and bonding agent development. Proceedings of the 16th Seminar on New Trends In Research of Energetic Materials, 2013. 399-406.

Williamson, D., Palmer, S. & Proud, W. Fracture studies of PBX simulant materials. AIP Conference Proceedings, 2006. American Institute of Physics, 829-832.

Wingborg, N. 2002. Increasing the tensile strength of HTPB with different isocyanates and chain extenders. *Polymer Testing,* 21, 283-287.

Winter, R. & Field, J. E. 1975. The role of localized plastic flow in the impact initiation of explosives. *Proceedings of the Royal Society of London. A. Mathematical and Physical Sciences,* 343, 399-413.

Wright, T. & Perzyna, P. 2003. Physics and Mathematics of Adiabatic Shear Bands. *Applied Mechanics Reviews,* 56, B41.

Zaug, J. Eleventh International Symposium on Detonation (Office of Naval Reserach, Arlington, VA) 1998. 498.

Zehnder, A. T., Guduru, P. R., Rosakis, A. J. & Ravichandran, G. 2000. Million frames per second infrared imaging system. *Review of Scientific Instruments,* 71, 3762-3768.

Zhou, M., Rosakis, A. & Ravichandran, G. 1996. Dynamically propagating shear bands in impact-loaded prenotched plates—I. Experimental investigations of temperature signatures and propagation speed. *Journal of the Mechanics and Physics of Solids,* 44, 981-1006.